UNIVERSITY OF CALIFORNIA SAN DIEGO

Ambient Excitation Based Model Updating for Structural Health Monitoring via Dynamic Strain Measurements

A dissertation submitted in partial satisfaction of the requirements for the degree of

Doctor of Philosophy

in

Engineering Sciences (Aerospace Engineering)

by

Benjamin L. Martins

Committee in charge:

Professor John B. Kosmatka, Chair
Professor Joel Conte
Professor Raymond de Callafon
Professor William Hodgkiss
Professor Hyonny Kim

2019

The dissertation of Benjamin L. Martins is approved, and it is acceptable in quality and form for publication on microfilm electronically:

_____

_____

_____

_____

_____

Chair

University of California San Diego

2019

TABLE OF CONTENTS

LIST OF FIGURES

LIST OF TABLES

ACKNOWLEDGEMENTS

I would like to acknowledge my advisor and Doctoral Committee Chair, Dr. John Kosmatka, for all of his advice, guidance, and support. Professor Kosmatka's expertise in structural dynamics, composite materials, finite element modeling, and structural health monitoring were fundamental to the development of the presented algorithm. His technical advice and unwavering commitment to the project provided assurance, even in the most difficult of times. Furthermore, I would like to express my sincere appreciation to my Doctoral Committee members, Professor Hyonny Kim, Professor Joel Conte, Professor William Hodgkiss, and Professor Raymond de Callafon, for the enlightening technical discussions and support throughout my Ph.D. program.

I would also like to acknowledge the fiber optic sensing group at NASA Armstrong Flight Research Center for their expertise and access to the state-of-the-art sensing systems. In particular, I would like to recognize Allen Parker, Francisco Pena, Dr. Lance Richards, and Dr. Patrick Chan for going above and beyond to share their fiber optic sensing expertise with me. Without their contributions the experimental work in this dissertation would have not been possible.

Lastly, I would like to acknowledge the California Space Grant Consortium and NASA Advanced Research Mission Directorate for their financial support of both myself and the project.

VITA

2012	Bachelor of Science, University of California San Diego
2012-2013	Teaching Assistant, University of California San Diego
2013-2018	NASA Armstrong Flight Research Center
2016	Master of Science, University of California San Diego
2019	ATA Engineering Inc.
2019	Doctor of Philosophy, University of California San Diego

PUBLICATIONS

"Health Monitoring of Aerospace Structures via Dynamic Strain Measurements", Presented at the American Institute of Aeronautics and Astronautics SciTech 2019, San Diego, California, January 2019. Manuscript Published.

"Active In-Flight Load Redistribution Utilizing Fiber-Optic Shape Sensing and Multiple Control Surfaces", NASA Technical Report: NASA/TM-2018-219741, 2018.

"Ambient Excitation Based Model Updating for Structural Health Monitoring via Dynamic Strain Measurements", Presented at the American Institute of Aeronautics and Astronautics SciTech 2018, Kissimmee, Florida, January 2018. Manuscript Published.

"Evolution of the Laser Vibrometer for Structural Dynamic Testing", Presented at the American Institute of Aeronautics and Astronautics SciTech 2017, Grapevine, Texas, January 2017. Coauthor. Manuscript Published.

"Modal Modeling via Fiber Optic Strain Sensing for Applications in Structural Health Monitoring", Presented at the American Institute of Aeronautics and Astronautics SciTech 2017, Grapevine, Texas, January 2017. Manuscript Published.

"Evaluation of Fiber Optic Strain Sensors for Applications in Structural Health Monitoring", Presented at the American Institute of Aeronautics and Astronautics SciTech 2016, San Diego, California, January 2016. Manuscript Published.

"Detecting Damage in a UAV Composite Wing Spar Using Distributed Fiber Optic Strain Sensors", Presented at the American Institute of Aeronautics and Astronautics SciTech 2015, Kissimmee, Florida, January 2015. Manuscript Published.

"Active Flight Load Alleviation Using Segmented Trailing Edge Wings on a Small UAS", Presented at the National Council of Space Grant Directors Meeting, Arlington, Virginia, February 2014

"Variations in Interlaminar Tension and Shear Strengths due to Carbon Nanotube Reinforcement in VARTM Manufactured, Polymer-Matrix, Laminated Composites", Presented at the American Institute of Aeronautics and Astronautics SciTech 2014, National Harbor, Maryland, January 2014. Manuscript Published.

FIELDS OF STUDY

Major Field: Aerospace Engineering

Studies in Structural Design and Analysis, Composite Materials, Structural Dynamics

Professor John Kosmatka

ABSTRACT OF THE DISSERTATION

Ambient Excitation Based Model Updating for Structural Health Monitoring via Dynamic Strain Measurements

by

Benjamin L. Martins

Doctor of Philosophy in Engineering Sciences (Aerospace Engineering)

University of California San Diego, 2019

Professor John B. Kosmatka, Chair

Structural health monitoring (SHM) technologies continue to be pursued for aerospace structures in the interests of increased safety and, when combined with prognosis, efficiency in life-cycle management. The current work is focused on developing and validating a method for in-situ health monitoring of aerospace structures. In particular, the current framework has been developed for use with response only vibration data using natural operating turbulence to provide the means of excitation. While the framework is general so as to work with a wide suite of sensor options, particular emphasis has been placed on fiber optic strain sensors as a lightweight, low cost, non-intrusive means of monitoring the vibration response.

At its core, the developed SHM system actively monitors a network of fiber optic strain sensors and utilizes the transient response data to calculate their associated power spectral densities

(PSD). These PSD serve as the fundamental input to the developed SHM algorithm presented in the dissertation whereby comparisons between previously correlated model PSD and the current measured PSD are made. If anomalies between the correlated model and the measured data sets are detected, the developed SHM algorithm seeks to minimize the difference via updating of structural parameters underlying the structural model of interest (in the case of the presented work, a finite element model of the structure).

The SHM algorithm itself is an adaption of a statistical least-squares minimization based in concepts of non-linear parameter estimation and model correlation. The algorithm developed uses power spectra based residual error vectors derived from distributed vibration measurements to update a structural model through statistically weighted least-squares minimization. The output of the algorithm is a correlated finite element model which inherently produces estimates of the location, type, and severity of any detected damage as well as the uncertainty associated with these estimates. Throughout the dissertation the developed algorithm was shown, both analytically and experimentally, to successfully detect, locate, and quantify damage present in a structural system.

Chapter 1: Introduction

With advancing ambitions and an aging infrastructure, the aerospace industry is at a crucial intersection where new technologies are needed to enable the development of the next generation of aerospace vehicles, as well as ensure the safety and reliability of aging assets. Structural health monitoring and damage prognosis (SHM-DP) will almost certainly be one of the technologies evolved and adapted within the aerospace community. In an effort to avoid catastrophic failures, and avoid the prohibitive costs and uncertainty associated with regular inspection and damage tolerant structural analysis, the current practice is to replace key structural components after a certain number of flight hours, regardless of the structure's integrity. Development of a reliable, in-situ, SHM-DP system will usher in the transition from time-based to condition-based maintenance, with associated advantages like advanced certification methods, improved operational efficiency, and increased safety.

These SHM-DP systems will undoubtedly have applications in extending the utility of aging metallic airframes as well as increasing the acceptance, efficiency, and reliability of newly developed composite primary structures. Before the full potential of advanced composites materials can be realized in primary aerospace structures, it is imperative that reliable SHM-DP techniques are developed, validated, and incorporated into the vehicles' structures. Successful implementation of such a SHM-DP system would lead to a paradigm shift in terms of maintenance, inspection, certification, and life-cycle management within the aerospace industry.

Structural health monitoring (SHM) is a discipline dating back decades, largely grown from the civil and mechanical engineering fields. Industries such as off-shore oil and gas first sought to advance their understanding of the structural performance of their platforms under varying oceanic conditions. The advancements made here were soon adapted to other civil structures such as

buildings and bridges. In all of these applications in-situ monitoring was straight forward using conventional sensors as any number of sensors can be easily implemented on the relatively stationary structures with little concern to the weight and/or size of the sensors. In aerospace vehicles however, the chosen sensors must be compact, easily multiplexed, and lightweight to allow for practical in-situ monitoring. Fiber optic strain sensors make an ideal candidate for in-situ monitoring, meeting all of these criteria in addition to being immune to the harsh conditions encountered by aerospace structures such as electromagnet radiation and large fluctuations in ambient operational conditions. The current work presents a SHM methodology which utilizes fiber optic strain sensors to monitor the ambient-excitation vibration response of aerospace structures and perform an in-situ structural health assessment using statistical model updating. The following sections introduce some of the key components of this methodology.

1.1 In-Situ Structural Health Monitoring System Overview

While in many fields no distinction is needed between in-situ SHM and SHM, with aerospace structures a very important distinction must be made. In fields of civil and mechanical engineering, for example, the structure or machine being evaluated is relatively stationary and thus always evaluated in their operating environments. With aerospace vehicles however, the current practice is to pull aircraft into inspection depots after a certain number of flight hours to perform comprehensive structural evaluation. Most of the SHM methods currently being developed aim to automate and in turn increase the efficiency of these depot-based inspections. While any advancements in inspection and health monitoring efficiency would be welcomed by the aviation industry, only SHM methods based on in-situ measurements would provide the capabilities to minimize or eliminate depot inspections and allow the operators to pull the vehicles from service and inspect only when needed, regardless of the number of flight hours. All of the work developed

and presented in this dissertation was done with an eye towards in-situ health monitoring, capable of yielding the most complete SHM assessment possible. Figure 1-1 provides an illustrative example of a generic multi-sensor network which could be used for SHM [1]. Sensors such as fiber optic strain sensors, represented by the yellow lines, could be incorporated into the vehicle's structure permanently to provide comprehensive in-situ inspection.

Figure 1-1: Concept of a multi-sensor based in-situ structural health monitoring sensor layout on a commercial aircraft [1].

Irrespective of whether an SHM methodology is formulated for in-situ or ground-based monitoring, there are fundamental questions all SHM methods aim to address. The most basic of these questions is whether damage is present within the structure. Once the presence of damage has been detected it is desirable to know the location of the damage, the type of damage present, and the extent of the damage. Answers to these fundamental questions formulate the inputs that would be needed to perform structural prognosis, or predict the amount of remaining life left in the structure under expected future loads. Figure 1-2 provides a schematic representation of how the proposed SHM system would utilize measurement data, as well as correlated structural models,

to answer the fundamental SHM questions which in turn provide the requisite information for prognosis [2].

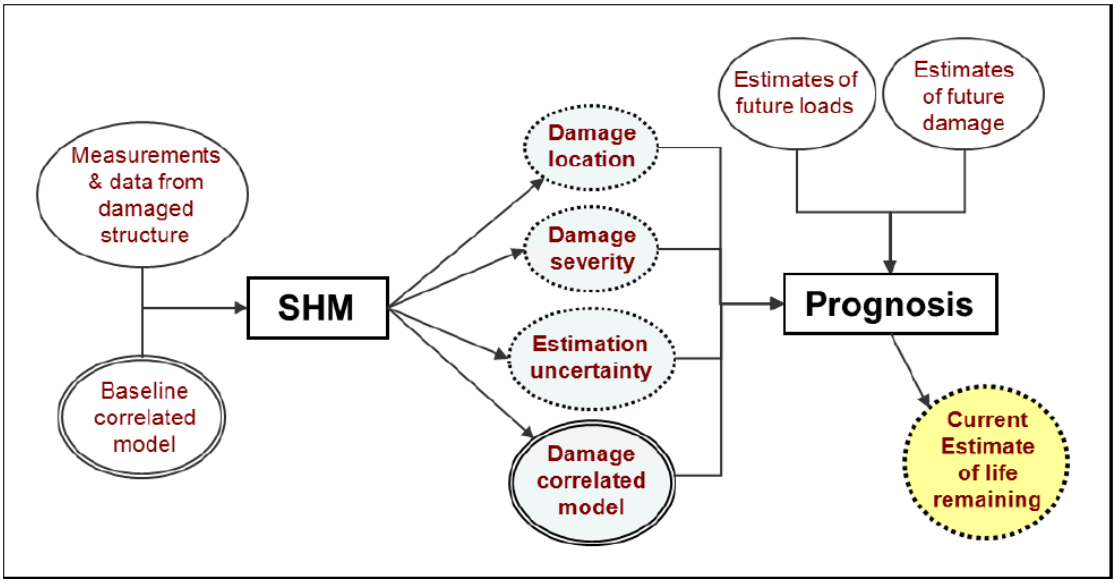

Figure 1-2: Schematic overview of a structural health monitoring and prognosis system architecture [2].

1.2 Fiber Optic Sensing Technologies

Fiber optic sensor technologies are an emerging sensing option being explored by many industries. These sensors are appealing for a multitude of applications because they are non-intrusive, lightweight, low cost, and easily multiplexed. One particularly successful application of fiber optic sensing technologies is fiber optic strain sensors (FOSS). For the past couple of decades researchers have been successfully demonstrating the ability of optical fiber, when bonded to a structural medium, to respond to changes in strain. While there are a number of methodologies being utilized for measuring strain via optical fibers, the most common type of fiber used in structural applications are Bragg grated fibers (also referred to as fiber Bragg gratings or FBG). In FBG sensors the index of refraction of the optical fiber is altered, usually using chemicals or

ultraviolet light, at various locations along the length of the fiber. The fiber is then interrogated with a laser light source. When the light encounters the Bragg gratings, a specific wavelength of the light is reflected and the rest transmitted. The wavelength of the reflected light varies based on the physical spacing of the gratings and hence can be correlated to the strain of the host structure. Figure 1-3 provides a schematic showing the grating sets of an unstrained and strained fiber [3]. Changing of the grating spacing corresponds to a change in the reflected wavelength which can be measured and correlated to structural strain, analogous to how the change in resistance in a conventional foil gauge is correlated to strain.

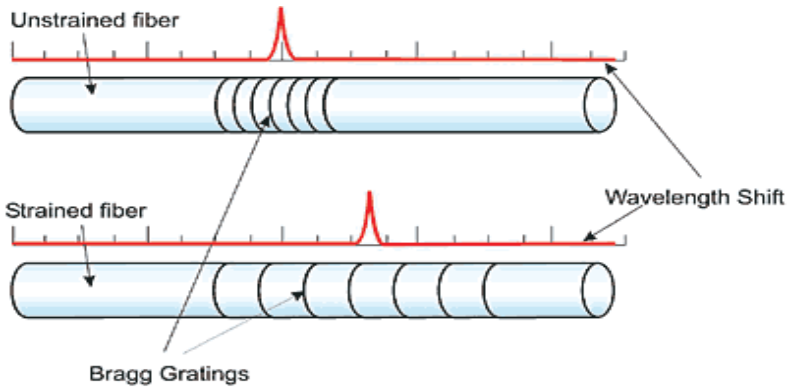

Figure 1-3: Schematic representation of the relationship between grating spacing and reflected wavelength with an FBG optical fiber [3].

A major advantage of utilizing fiber optic strain sensors is their ability to be multiplexed along a single fiber. Thousands of Bragg gratings can be etched onto a single fiber providing the possibility for high spatial resolution measurements, even over large-scale structures. Typical optical fibers used for strain sensing applications have a diameter on the order of 0.125mm (including the protective cladding), a strain sensitivity of 0.78 microstrain, a failure strain of greater than 5% elongation and a mass of 0.01g/ft (varies depending on the specific fiber and cladding combination). The lightweight, easily multiplexed fiber-optic strain sensors are an ideal

candidate for in-situ measurements as they are known to be immune to electromagnetic interference and make it possible to establish a large scale, distributed network of thousands of sensors with negligible weight penalty. Figure 1-4 shows an image of a small scale (12-foot span) unmanned aerial vehicle instrumented by the author with fiber optic strain sensors providing approximately 4000-point strain measurements on the main wings.

Figure 1-4: UAV instrumented with fiber optic strain sensors providing the possibility for in-situ health monitoring.

The expansive fiber optic network shown in Figure 1-4 can easily be extended to full-scale aerospace vehicles and encompass nearly any structural component of interest. Such sensor networks provide an ideal platform for in-situ health monitoring and the ability of such a system to perform in flight conditions has already been proven. Prior to implementation of a fiber optic

strain based SHM system, reliable techniques must be established which allow for the determination of the requisite damage features using fiber optic strain. An aircraft in its operational environment provides the perfect scenario for response only vibration-based damage features.

1.3 Vibration Based Structural Health Monitoring

Within the field of structural health monitoring a number of excitation and measurement systems have been proposed. Although SHM research spans a large number of fields, monitoring of aerospace structures poses a unique set of challenges. Aerospace structures are different than most mechanical or civil structures in that they operate in extreme and rapidly varying conditions. Furthermore, aerospace structures are, by definition, structures which are continually varying their location making in-situ monitoring by many conventional techniques very difficult and in some cases impossible.

To date most of the research attention has focused on developing SHM methods which would require aircraft to be pulled out service and inspected. Acoustics emissions, guided-wave, and vibration-based approaches garner the majority of research attention and have all been demonstrated with varying levels of success in laboratory and depot type testing environments. Acoustic emissions have been shown to locate small damage regions close to sensors on simple panels (not built-up structures), but the results cannot be implemented into structural models, thus making prognosis unattainable. Guided-wave based approaches are highly susceptible to environmental and operational variability, providing unacceptable levels of false-negative and false-positive detection events for in-situ applications. Vibration methods on the other hand show promise in detecting damage on both a local and global scale, lending themselves to prognosis and are well suited for in-situ monitoring.

Researchers have been developing vibration based SHM methodologies for both ground based and in-situ inspections. Most of these approaches have been developed around conventional sensors, such as accelerometers or laser vibrometers, which limit either the number of available sensors or the ability to perform an in-situ assessment. Distributed fiber optic strain sensors on the other hand are an ideal candidate for in-situ SHM. Adapting techniques used for in-situ inspections via accelerometers for use with FOSS will allow ambient-response, vibration-based SHM assessment to be performed in-situ on a wide variety of aerospace structures.

1.4 Summary of the Dissertation

The work presented in this dissertation is focused on developing the technologies required for implementation of an in-situ SHM system for aerospace vehicles. The SHM methodology developed utilizes a network of fiber optic strain sensors which respond to structural vibrations induced by atmospheric excitation imposed on the vehicle during the course of normal operation. The structural vibration response is calculated in terms of the power spectral density which is compared to a previously correlated finite element model (FEM) response. The FEM is updated using the latest test data to provide a statistical based parameter set of the structural parameters of interest. This updated FEM is thus used to assess the health of the current structure as well as provide the possibility for prognosis.

Coupling distributed fiber optic sensing with in-situ measurements and a model updating based SHM algorithm provides the ability to not only detect the presence of damage but also provide information on the type, location, and severity of the damage. The correlated structural models produced by the updating also allow for prognosis to be performed. Incorporation of fiber optic strain sensors provide the possibility to monitor the structural dynamics of the vehicle caused by the turbulent ambient conditions making in-situ health monitoring possible.

The remaining chapters of this dissertation are organized as follows:

- Chapter 2: Literature review covering SHM, fiber optic sensors, and statistical model updating.
- Chapter 3: Theoretical development of the SHM algorithm. This development includes modeling of the strain power spectral density response, methodology for calculating and assessing the quality of the current parameter set, and algorithmic additions to ensure efficient and precise operation.
- Chapter 4: Basic implementation and demonstration of the SHM algorithm. A simple single element (two degree of freedom) step-by-step demonstration is given. The same single element case is used to demonstrate the features, capabilities, and limitations of the algorithm.
- Chapter 5: Analytical modeling and demonstration based on a composite beam testbed. The SHM algorithm is expanded to a realistic degree of freedom set and capabilities and limitations explored. The current methodology is compared to contemporary methods as well.
- Chapter 6: Experimental work is presented which highlights the advancements in fiber optic sensing technologies developed as a result of this dissertation.
- Chapter 7: An experimental testbed is discussed which was developed for the purpose of demonstrating the proposed SHM algorithm. Experimental validation of the algorithm is performed and presented.
- Chapter 8: Conclusions are given based on the presented work highlighting the novel contributions. Recommendations are given for future advancements and development.

Chapter 2: Literature Review

For more than a century, researchers have been developing and documenting methodologies to perform non-destructive evaluation (NDE), the precursor to structural health monitoring [4]. Structural health monitoring (SHM) as a discipline has been evolving over the past four decades in an ever-increasing number of applications and industries. Largely driven by government laboratories and research universities, progress towards SHM systems have developed to the point where they are transiting from research topics to practical implementation in a number of industries [5]. With over one hundred years of research attention, there is a large amount of literature available relating to seemingly every aspect of NDE and SHM. Despite the large amount of research attention, there remains many challenges associated with successful SHM and it is clear that many of the solutions will be application specific. Within this dissertation, a number of approaches stemming from a wide spectrum of applications and industries were reviewed and considered for applications towards in-situ monitoring of aerospace structures. The following sections provide some historical context and summarize the current state-of-the-art in key areas related to the chosen SHM methodology developed in the current work.

2.1 Overview of Structural Health Monitoring

Modern SHM has largely grown from the off-shore oil industry which in the 1970's and 1980's heavily invested in technologies to monitor the structural condition of their oil drilling platforms [6]. These SHM efforts largely focused on using the vibration response of the platforms to monitor the global natural frequencies [7] and mode shapes of the structures [8]. A more advanced attempt utilized a mathematical model of the structure analyzed by the SAP IV computer program, taking into consideration the effects of mass, entrained water, soil support conditions and equipment [9]. While all of these approaches had limited successes, many were restricted by

computational and sensor limitations. Many researchers also concluded that changes in modal parameters caused by structural damage were difficult to discern from changes in the modal characteristics caused by the ever-changing boundary conditions due to soil-structural interactions as well as varying water levels in addition to changing mass loads caused by normal operations of the platforms.

Another industry credited with pioneering of in-situ health monitoring, and perhaps the most successful to date, is in the rotating machinery industry [10]. Often called condition monitoring in the rotation machinery industry, early researchers utilized vibration based methods to assess the integrity of bearings in rotating machinery [11]. The consistency of operating conditions leads to the expectation of very stable vibration responses which is in large part why condition monitoring has been so successful. Later research efforts utilized acoustic emissions to enhance the damage detection capabilities of condition monitoring for rotating machines including bearings, pumps, gearboxes and engines [12]. The developments related to rotating machinery were ultimately some of the first to transition into the aerospace industry with direct applications to monitoring turbine engines [13]. The earliest structural aerospace SHM techniques focused on load monitoring where a limited number of sensors would count the number of times a load threshold was exceeded, known as usage monitoring [14].

Most current SHM-DP research efforts with applications to aerospace structures have focused on utilizing either, ground-based (pre-flight) [15] or in-flight modal testing [16-18], ultrasonic guided waves [19, 20], or acoustic emission monitoring [21, 22], using sparse sensor arrays largely on simplified geometric structures. These methods have shortfalls that make them unrealistic for actual flight vehicles having large, complex internal structures assembled using skins, stringers, spars and frames, operating in complex, varying environments. Acoustic

emissions can locate small (extensive) damage regions close to sensors on simple panels (not built-up structures), but the results cannot be implemented into structural models, thus making prognosis unattainable [22]. Guided wave-based approaches are highly susceptible to environmental and operational variability (EOV), providing unacceptable levels of false-negative and false-positive detection events [19, 23]. Vibration based methods on the other hand show promise in detecting damage on both a local [24] and global scale [16, 25]. This ability is however highly dependent on the number and quality of the measured modes. Figure 2-1 provides a chart which summarizes the most popular SHM methodologies available in literature as well as their capabilities.

Methodology	Presence	Local vs. Global	Location	Type	Severity	Prognosis	In-Situ
Thermography	✓	Local	✓	✓	✓	✗	✗
Ultrasonics	✓	Local	✓	✓	✗	✗	✓
Vibrations	✓	Global	✓	✓	✓	✓	✓
Statics	✓	Global	✓	✗	✓	✓	✓

Figure 2-1: Summary of various SHM methodologies and their prospective capabilities.

2.2 Vibration-Based Structural Health Monitoring

Aerospace vehicles by nature operate in rapidly varying atmospheric conditions under constant load fluctuations making ambient excitation-based vibration measurements a viable option. Vibration-based measurement techniques have been used for applications in SHM since the inception of SHM [4] and the majority of literature on the topic of SHM utilizes some form of vibration data as the damage feature. Farrar et. al state that a damage feature is “some quantity extracted from the measured system response data that indicates the presence (or not) of damage in a structure” [5]. Within the field of vibration-based SHM a large number of damage features have been proposed and researched, some of the most promising are discussed in subsequent paragraphs.

The earliest vibration-based SHM research efforts sought to identify the presence or absence of damage based on changes in modal parameters such as natural frequencies and mode shapes. As early as the 1970s, Cawley and Adams were using the ratios of natural frequencies to determine the existence of damage in fiber reinforced composite panels [26, 27]. By 1980 United States Geological Survey was sponsoring research with The Aerospace Corporation to study the practicality of using mode shapes to detect structural flaws in offshore energy applications [8]. Across literature both methods, in their simplest forms, have been shown successful on simple structures subjected to testing in a laboratory setting but struggle with large scale, practical applications due low damage sensitivity, environmental and operational variability, and sparse measurement arrays [28-30].

Despite the limited success of early vibration-based SHM, researchers using shifts in frequency and mode shapes still play a role in the majority of present-day vibration-based SHM. Ganeriwala et al. extended the use of the mode shapes to calculate the modal assurance criteria matrix (MAC), where they assumed undamaged structures would provide MAC values near unity for the measured modes whereas damaged structures would decrease the orthogonality between the healthy and damaged mode shapes and hence decrease the value of the MAC [28]. Studying cracks in composite wind turbine blades, Ganeriwala et al. concluded that only very large cracks, on the order of 10% of the span or larger, could be reliably observed by changes in the MAC. Numerous other authors report similar results using modal shape based damage features such as the modal flexibility matrix [31], modal filtering [32] and changes in the operational deflection shapes [30], all of which utilize mode shapes and/or natural frequencies in the computation of the damage feature. Of the shape based damage features, those based on modal curvature [29, 33] and modal strain energies [29] show the most promise and tend to work well on single-load path beam

and truss like structures. These curvature and strain energy based features still struggle with reliably identifying and locating damage on built up structures and/or in the presence of realistic measurement noise [33].

In the 1980's and 1990's researchers began ramping up efforts to utilize all of the information gathered during a vibration test, rather than a subset of the extracted modal parameters. Ricles and Kosmatka [34] introduced the idea of utilizing residual forces in a sensitivity-based model updating scheme which is not only able to detect and locate damage but also give an assessment of the type and magnitude of the damage as well as provide an updated structural model. The utility of this method was later shown to be effective for highly damped structures [35] and was experimentally shown to reliably determine the presence of damage as well as the location and severity, where damage was defined as changes in elemental mass and stiffness of a 10 bay space truss [36]. In 2015, Oliver [2] presented significant advancements to this basic framework, where structural parameters associated with composite aerospace structures were calculated along with a statistical confidence measure of the calculated parameter set. The use of frequency response functions, rather than modal parameters, as the damage metric lead to the ability to study non-linear structural behavior.

More recently, Seyedpoor and Montazer analytically demonstrated success applying a two-stage damage detection approach based on the residual force vector [37]. In Seyedpoor and Montazer's approach, a first pass is made where potential damage elements are identified before applying a differential evolution algorithm to determine the final location and severity of any damage present. Esfandiari et al. [38] demonstrated an FRF-based model updating using incomplete transfer function data sets by supplementing the measured transfer function with natural frequency and mode shape information. While the results are only demonstrated in a

deterministic and analytical sense, the method provides independent verification of the work done by Kosmatka, Ricles, Oliver, and Napolitano [2, 34-36]. Additional work into FRF-based damage detection is also underway, such as the work by Trendafilova who looked at using the principal component analysis (PCA) technique to parse out subtle changes in the FRF caused by damage in scaled aircraft wings [39]. He and Hesheng utilize vibration transmissibility as a damage indicator for applications to civil structures [40]. While there is merit in the PCA and transmissibility techniques, the current work is focused on not only the SHM aspect but also providing an updated structural model to be used in prognosis, making methods based in model updating and system identification more appealing.

The advancements in FRF-based residual force vector methods show great promise, however, the largest obstacle for performing SHM on aerospace structures is the inability to make the requisite measurements in the structure's operating environment. The inability to measure the excitation force on aerospace vehicles in their operating environment makes it desirable to find methods that are independent of the applied dynamic excitation. The widely used methodology for response only measurements in literature is formulating a structure's frequency response in terms of its power spectral density (PSD). Researchers have begun adapting PSD derived from operational modal analysis (OMA) for applications in SHM. In 2007, Bayissa and Haritos [41] used a curvature based, response PSD to compute a damage index capable of detecting and locating damage in plate-like structures. Wang et al. [42] used the PSD to form an inner product vector based on the frequencies and mode shapes obtained via an OMA to detect the presence of damage. Following the same methodology as He and Hesheng with FRF, Li et al. [43] expanded the vibration transmissibility to be used with the PSD. Zheng, Lu and Liu [44] performed a sensitivity-based model update using information presented in analytical PSD of the moment frames being

studied. All of these approaches verified the information obtained by OMA can provide all of the requisite information for successful and meaningful SHM, however, all of them stopped short of generating the complete set of information desired by potential users of SHM technologies, namely: presence, location, type and severity of damage with the ultimate goal of providing prognostic capabilities. A more thorough review of ambient excitation based SHM is given in subsequent sections.

2.3 Dynamic Response Sensor Options

In the arena of vibration-based SHM, most researchers utilize accelerometers as a means to obtain dynamic response data. While accelerometers have been shown effective for in-situ monitoring of civil structures such as, buildings [40], bridges [45], and oil platforms [8], they can severely limit the number of available sensors for aerospace structures due to their mass loading and inability to be multiplexed [46]. Despite this limitation, they are still the backbone of most of the state-of-the-art SHM approaches [2, 30, 45]. While the use of accelerometers does not eliminate the possibility of in-situ inspection of aerospace vehicles, the mass loading associated with cabling and sensors excludes the possibility of expansive sensor networks, making damage detection and localization much more difficult.

Recently researchers have been looking into non-contact measurement techniques to avoid the problems associated with mass loading of expansive accelerometer networks. The most prominent non-contact measurement technique is laser vibrometry. A large portion of the published literature focuses on using scanning laser vibrometers for receiving guided waves in ultrasonic testing [18, 47, 48]. In 2005, Kosmatka and Valdes [49] utilized a scanning laser vibrometer system to measure the vibratory response of the Hunter UAV and correlate the response to a structural model, a keystone of the current SHM approach. A major drawback at the time was

the labor-intensive process of adhering targets to the UAV at the desired locations to ensure an adequate response signal. Recent advancements in laser doppler vibrometry have alleviated this restriction as was demonstrated by Kosmatka et al. in 2017 [50]. Oliver [2] also suggested the use of the scanning laser vibrometer for the purpose of structural dynamics based SHM and demonstrated the use of vibrometry for model correlation. While the ability of scanning laser vibrometry to successfully measure structural dynamics with high spatial resolution has been repeatedly demonstrated, it does not provide an opportunity for in-situ measurements of aerospace structures.

In addition to the acceleration and velocity-based measurements widely used for monitoring structural dynamics, researchers have also documented the use of dynamic strain measurements. Predominately starting in the late 1980's and continuing into the 1990's researchers explored the use of strain gauges for modal testing [50]. Boeing researchers published a paper in 1995 [51] in which they proposed a methodology of using a network of in-flight strain sensors to generate a strain-displacement transformation using modal data. While the purpose of the research was to ultimately characterize the real-time displacement shape of the wing, it did validate the use of dynamic strain measurements on flight hardware. The major drawback of the conventional (foil) strain gauges is their inability to be multiplexed. Since each individual sensor requires a minimum of two wires, a network of foil gauges would be on the same scale as accelerometers in terms of weight penalty, largely contributing to the lack of literature available on utilizing foil gauges for monitoring structural dynamics. It should be noted that strain gauges do however have a large following in SHM applications (utilizing quasi-static strain), as discussed in Section 2.5.

Over the last few decades fiber optic sensor technologies have undergone great advancements and as such garnered increased research attention. While there are fiber optic-based

sensors for measuring engineering parameters such as temperature, pressure, velocity, and displacement, the most common type of fiber optic sensor are strain sensors. Distributed fiber optic strain sensors are an ideal candidate for in-situ SHM [46]. They are lightweight, easily multiplexed, and immune to electromagnetic interference making them well suited for use in expansive SHM sensor networks. Several types of sensors, embedded or attached to the structure, have been proposed for SHM-DP (strain gauges, piezoelectric, electrical time-domain reflectometers), however, only those based on fiber optic technology offer the capability to perform integrated, and distributed measurements on or inside the structure, over large components and built up structures [46]. Figure 2-2 provides a summary of the candidate sensors considered in this work and their capabilities as it related to vibration-based in-situ SHM of aerospace structures.

Methodology	Multiplexing	Lightweight	Large Network	In-Situ
Accelerometers	✗	✗	✓	✓
Vibrometer	✗	✓	✓	✗
Foil S.G.	✗	✗	✓	✓
Fiber Optic S.G.	✓	✓	✓	✓

Figure 2-2: Summary of sensor options for vibration-based SHM systems.

2.4 Model Updating Based Structural Health Monitoring

While sensor type certainly plays an important role in the success of an SHM technique, equally important is the development of the data analysis strategy and damage feature selection. Within the field of vibration-based SHM, damage features range from using properties such as changes in modal parameters [42], operational deflection shapes [52], and modal curvature [53], to model updating [2, 54]. Model updating methods allow for damage to not only be detected and localized but also an estimate of the current structural parameters to be produced for use in

prognosis [2]. The ability to produce a correlated structural model and thus provide for the possibility of prognosis makes model updating based SHM the focus of the current framework.

Model updating is a term typically used within the civil engineering community to describe the process of system identification as it relates to structural systems and their models. First practiced within the electrical engineering field and later adapted by controls engineers [55], system identification is a means to preform parameter estimation for a wide range of possible applications [56]. As early as 1971 researchers were looking into ways to adapt the system identification techniques of other disciplines and apply them to structural systems [56]. Kaman Aerospace Corporation were amongst the first within the aerospace industry to explore such techniques, utilizing measured normal modes to modify the analytical mass and stiffness matrices [57].

On a high level, model updating can be subdivided into two categories, those based on deterministic methods and those relying on statistical analysis. While the current approach utilizes a statistical framework, many of the foundational works are based on deterministic methods that were later expanded to include statistical analysis. One of the key challenges in any model updating routine is to generate the requisite information for successful parameter estimation. In the 1970s and 1980s the majority of structural model updating was done using measured resonance parameters [58]. With the increase in computational power leading to larger and larger structural models, by the 1990s a need for more experimental data was realized. In 1994, Lin and Ewins were utilizing measured and modeled frequency response functions (FRF) to provide additional information beneficial towards successful structural model updating [59]. In their work, Lin and Ewins used singular value decomposition to detect changes in the system matrices (mass, stiffness and damping) using analytical mass-spring and truss systems. Along with Imgerun and Visser,

Ewins expanded on his work, utilizing beam and plate structures to perform further analytical and experimental validation [60, 61]. In these later works, Imgerun, et al. extended the existing algorithm to handle complex FRF data as well as utilize a least-squares approach to solve an overdetermined set of equations. Although some success was achieved in these experimental studies, the authors point out problems related to non-uniqueness of the overdetermined system of equations. The problem of non-uniqueness leads to the potential for incorrect, or even physically impossible, parameter sets to be identified, especially in the presence of modeling error and measurement noise [60].

Contemporary to the work of Ewins, Napolitano and Kosmatka were exploring the use of FRF data in SHM applications for a highly damped space truss system [35]. Using a residual force-based formulation, they also successfully used a least-squares solution of an overdetermined system of equations to determine the presence and magnitude of potential damage during analytical validation. In 2005, Araujo Dos Santos et al. applied an FRF-based approach to damage identification on laminated composite plates [62]. Using natural frequencies and mode shapes to generate an estimate of the measured FRF, Araujo Dos Santos numerically demonstrated that the best accuracy was achieved when dynamic expansion was performed on the measurement set, rather than reduction of the model size. A mechanism was also incorporated in Araujo Dos Santos' method which bounds the update parameters to a physically meaningful solution space [62]. While Araujo Dos Santos et al. did have some success with analytical validation, it was shown that the method suffers from model incompleteness and non-uniqueness, as concluded by the previous authors [35, 61, 62].

In order to mitigate the problem of non-uniqueness, researchers began incorporating statistics to provide a confidence measure in the estimated model parameter sets. There are two

basic approaches to stochastic model updating methods, those derived from statistics and those derived from structural mechanics. Methods derived from statistical generally seek to describe the distribution of the output parameter set based on sampling a statistical cost function. Marwala et al. included a chapter dealing with Bayesian statistics in structural dynamics in their 2017 book *Probabilistic Finite Element Model Updating Using Bayesian Statistics: Applications to Aeronautical and Mechanical Engineering* [63]. Within the book, a review of the state-of the-art literature for statistics-based methodologies are discussed and demonstrated including forward and back propagation of the stochastic parameters using Monte Carlo simulation and meta-modeling, the most common statistics-based model updating approaches. In 2017, Boulkaibet et al. expanded the use of Monte Carlo simulation to perform FE updating using Hamiltonian functions [64]. According to the authors, the major drawback of conventional Monte Carlo techniques is computational efficiency. In order to generate an estimation with statistical significance, a large number of samples must be computed. On small systems, and their corresponding models, a large number of realizations is fine but on large complex systems the sampling process is not practical. Ching, Muto and Beck first proposed the use of the Hamilton function to transform the parameter space into a simplified space for direct sampling with applications to structural health monitoring [65]. Using these modified Monte Carlo methods, which incorporate meta-modeling, the authors analytically showed that damage could be detected in large systems however false-positives and false-negatives were possible, especially in regions of sparse sensor arrays [65].

Direct search techniques are also viable techniques that have been demonstrated for SHM. In 2016, Martinez-Luengo, Kolios, and Wang did a comprehensive review of direct search statistical pattern recognition methods with specific emphasis on operational SHM of wind turbine blades [66]. In the review, Martinez-Luengo et al. considered sensors options including acoustic

emissions, thermal imaging, ultrasonic, accelerometers and strain gauges, providing benefits and drawbacks of each measurement device and suggesting statistical pattern recognition strategies. A more thorough review is given in the 2013 book by Farrar and Worden, *Structural Health Monitoring, A Machine Learning Perspective* [5].

Statistical methods derived from structural mechanics on the other hand utilize well understood engineering models and equations to incorporate the underlying physics of the structural system. Since these models utilize the underlying physics of the system, they typically require orders of magnitude fewer iterations/optimizations to achieve a solution as compared to the methods derived from statistics [2], an important feature when designing a system for real-time SHM. The vast majority of these approaches derived from structural mechanics utilize a finite element model and some form of a Bayesian least-squares minimization routine. Typically, knowledge of the parameters' statistics are needed for the formulation of the problem and in cases where they are not known the standard assumption is the distributions are Gaussian [2].

Many of the complex problems being solved by least-squares minimization are non-linear by nature and require use of linearization and iteration. One of the foundational works in linear estimation theory was published by Gura in 1968 [67] in which he describes algorithms for statistical parameter estimation of nonlinear systems, although no attempts at validation were made. Collins et al. later published a paper where Gura's framework was utilized to update the mass and stiffness matrices of a finite element model using measured natural frequencies and mode shapes [68]. Collins et al. validated the method analytically using a simple beam model as well as using a 28-element finite element model of the Saturn V rocket in conjunction with acquired test data. The method was shown to greatly improve the predicted frequencies and mode shapes of model, which after updating closely matched the experimental values [68].

In 1982, Tarantola and Valette derived an alternative approach to mechanics based statistical model updating [69]. Tarantola and Valette's work approached the problem of general parameter estimation from the perspective of maximizing the posterior parameter distribution while simultaneously minimizing the error in the system equations. Their method was validated analytically on a series of systems in which they concluded that their least-squares framework was valid for discrete and continuous systems, that are underdetermined as well as overdetermined, for both linear and nonlinear problems. They state that using the prior parameter covariance matrix allows for the computation of a stable solution for otherwise unstable problems [69].

While the foundational works for statistics-based model updating were rooted in system identification and parameter estimation literature, primarily associated with controls and electrical engineering, by the 1990's researchers were extending their use to SHM. In 1992, Ricles and Kosmatka [34] applied statistical parameter estimation to damage detection using measured modal properties along the same lines as Collins et al. had previously proposed [68]. In their work, Ricles and Kosmatka updated the mass and stiffness matrices of an analytical space truss model using simulated measured mode shapes and frequencies via the Bayesian updating framework. Follow-on work later provided experimental validation of the method, providing excellent agreement between the measured modal parameters and the updated model parameters for the same space truss system previously analyzed [36].

More recently, in his dissertation, Oliver [2] adapted the parameter estimation framework developed by Tarantola and Valette [69] to perform a least-squares parameter estimation based on the residual force vector demonstrated by Ricles and Kosmatka [34]. Oliver showed the robustness of the method, both analytically and experimentally, using acceleration-based FRF data obtained via laboratory testing. In addition to successfully updating finite elements models, Oliver also

noted that the estimation uncertainty in the updated parameter estimations is qualified with a confidence measurement in the form of the parameter covariance matrix, a major advantage of the approach adopted in the current work.

2.5 Strain-Based Structural Health Monitoring

Traditional foil resistance strain gauges comprise the overwhelming majority of strain-based SHM approaches available in literature. Credited with independently and simultaneously inventing foil gauges circa 1938 were professors Arthur Ruge and Edward Simmons at MIT and Caltech, respectively [70]. In the time since their inception, foil gauges have dominated nearly all aspects of static structural testing, model validations, load calibrations as well as countless other uses. Within the area of aerospace structures, strain gauges were used for in-flight loads monitoring at NASA as early as 1960 [71]. In his work at NASA, Ward utilized foil strain gauges to monitor the static and vibratory loads of vertical take-off and landing (VTOL) aircraft during typical flight profile cycles. With the strain gauges, he was able to determine the static root bending moment as well as the vibratory response at various flight conditions [71].

Early applications of strain-based SHM focused on identifying fatigue cracking by monitoring the resistance changes associated with fatigue damage. In 1966, Harting published an article in *Experimental Mechanics* summarizing the experience of Boeing in developing cumulative fatigue damage strain gauge monitoring systems [72]. In his work, Harting cites a 1959 internal Boeing document which notes the permanent increase in the resistance of a foil gauge subjected to fatigue loading, attributed to microcracking or work hardening in the gauge wire. Harting concluded that by controlling the microcracking and/or work hardening of the gauge material, the total fatigue life of a structure could be directly correlated to the total resistance change of the strain gauge. Harting was able to experimentally demonstrate the effectiveness of

this approach on a cantilever beam. His experiments showed structures subjected to consistent type of variation of loading or stationary random processes could be successfully monitored. Major drawbacks of this approach however included the requirement that each gauge is specifically developed and correlated for the structural material at hand as well as the requirement that the fatigue gauge be placed in the location of fatigue damage [72]. The requirement that strain gauges must be nearly collocated to a damaged region have been a common drawback noted by numerous researchers attempting to use static strain as a damage indicator.

Despite the underlying issue related to the sparsity of potential damage indicator sites associated with using static strain measurements, research persist and researchers sought out more advanced approaches to overcome the limited sensor count using static strain as the damage feature. By 1996, Sanayei et al. developed a parameter estimation scheme around a static strain framework [73]. By using subsets of applied static forces and measured strains, Sanayei developed an error function based on the difference between the analytical and measured strain values. The strain error function was linearized using a first-order Taylor series expansion before the structural parameter set is updated using a sensitivity based least-square approach. In their article, Sanayei et al. provided two noise free analytical examples on a truss and frame system. Their approach correctly identified the desired structural stiffness parameter sets in 17 of the 20 cases studied. The authors postulated that in the remaining three cases the combination of applied loads and strain locations selected lead to ill-conditioned sets of equations and better choices of loads and locations would avoid these ill conditionings [73]. A follow-up work by Sanayei and Saletnik utilize the same truss and frame models to perform an error analysis where using heuristic method they eliminated the use of load and strain locations which lead to large output errors [74]. While the

authors utilize a Monte Carlo analysis to verify their analytical results improved using the identified subset of forces and strains, no experimental validation was attempted.

The method proposed by Sanayei [73] was analytically demonstrated on constant strain beam and truss elements however the authors neglect to mention how such measurements could be readily obtained on any set of elements desired. The advent of fiber optic strain sensors provides a possible means of providing high density strain measurements for SHM. As early as 1999, researchers at NASA were evaluating these fiber optic sensors on a surrogate F/A-18 for vehicle health management on the X-33 [75]. While Schweikhard et al. reported success in integrating the fiber optic sensors and system into the flight vehicle, ultimately the swept-wavelength tunable laser of the fiber optic interrogation system proved to be too sensitive for aggressive flight environments only operating intermittently [75].

In spite of the laser shortcomings in the fiber optic sensing system, NASA continued researching the use of fiber optic strain sensors for SHM applications, characterizing their performance in a 2004 paper [76]. Using the improvements made in a series of ground-based experiments, NASA Armstrong successfully demonstrated flight testing of their fiber optic sensing systems in 2008 on a General Atomics Predator-B aircraft and again in 2010 on an AeroVironment Global Observer. In both cases, thousands of point strain measurements were taken in real-time using a few fiber optic sensing cables. While the main objectives were to validate the FOSS system's ability to reliably monitor strain in a flight environment, the authors note the potential application to future SHM efforts [77]. Additional NASA work published by Pena et al. in 2018 provided further validation of the FOSS system to not only successfully monitor real-time strain distributions in-flight but also use the on-board computational power to utilize the strain for other real-time objectives (in this case wing deformation estimations and shape control) [78].

While fiber optic strain sensors are undoubtedly the future for high density, in-flight, strain measurements, the fundamental question in regards to SHM is what engineering parameter will ultimately be used to indicate damage. As previously mentioned, early approaches utilized static strain measurements [72, 73, 79] and derived structural loads as the damage metric [80]. While these methods do work well for simple, heavily instrumented structures, they are not practical on large scale aerospace vehicles. Relying on static strain requires a damage event to be nearly collocated with a strain sensor in order for the event to be detected [72]. In order to supplement the information provided by a finite number of strain sensors, researchers began looking to damage indicators derived from structural dynamics.

Analogous to the work done with accelerometers, the most basic of these dynamic strain based approaches rely on frequency shifts to detect the possible presence of damage [81]. While frequency shifts can provide an indication of the presence of damage, the type, severity, and location of such damage cannot be obtained making it an undesirable method. Additionally, changes in frequency can also be attributed to changes in environmental and/or boundary conditions as well as mass (i.e. fuel or payload) changes and are not a reliable damage feature. More advanced approaches have looked into using modal strain energy [82], residual strain-mode shapes [53], and modal curvatures [83]. All of these methods seek to characterize the vibrational shape of the structure in some form and look for changes in such shape. Most of these changes are quantified using a damage indicator of some sort. The use of strain, rather than displacement traditionally used in such approaches, also has the associated advantage of not having to differentiate to obtain the modal curvature. In 2015, Martins and Kosmatka preformed a review of several such modal curvature based methods using dynamic strain measurements [33]. The results of the studies showed that such methods were able to detect and locate damage on simple beam

like structures under ideal conditions but struggled with complex geometries where a relatively large damage event far away from a sensor might have a negligible impact on the modal strain-energy and/or curvature. Furthermore, methods based on these shape parameters do not allow for an estimate of the type and severity of detected damage to be obtained.

More recently researchers have looked to adapt the model updating based SHM for use with dynamic strain data. In addition to providing estimates of the type, location, and severity of detected damage, model updating techniques based in structural dynamics also allow for variations in mass and damping [84], a feature omitted using static strains as suggested by Sabayeu et at.[73]. While the amount of research literature involving model updating SHM using dynamic strain measurements is limited, few researchers have begun working in the area. In 2010, Esfandiari et al. utilized incomplete strain measurements to generate FRF and perform deterministic model updating for SHM applications [84]. Using elemental level sensitivities of the FRF, successful parameter estimation was analytically performed on truss and frame structures demonstrating the utility of the method. While the method was successfully demonstrated, the incomplete modal data lead to a dependency on extracted modal parameters (natural frequencies and mode shapes) to estimate the FRF. This estimation process introduces a potential for large errors to be introduced into the residual FRF formulation providing the possibility of false-positives and false-negative detection events. Follow-up work by Esfandiari in 2014 improved the sensitivity formulation using a least-squares solution [85]. In his 2014 work, Esfandiari also points out that at different sensor locations and frequency ranges the magnitude of the sensitivity may vary by orders of magnitude. To combat this important point, a sensitivity weighting technique is presented based on the second norm of the sensitivity vectors. Using the previously developed frame and truss models, the method was again analytically shown to be robust to changes in the mass and stiffness matrix,

presumably caused by an unknown damage event. The combination of expansive dynamic strain measurement systems with model updating based SHM provides the possibility for successful in-situ SHM of large-scale aerospace structures and as such is the focus of the current work.

2.6 Ambient Excitation Structural Health Monitoring

Ambient excitation SHM grew largely out of necessity and convenience in monitoring of civil infrastructure. The ability to utilize environmental excitation to monitor a structure means that SHM can be continually performed without limiting the utility of the structure. The underlying principles of ambient excitation based SHM stem from the field of operational modal analysis (OMA). The discipline of OMA dates back hundreds of years and is associated with the first scientific studies of mechanical vibrations [86]. Although literature exists related to OMA dating back to the 1930s, experimental modal analysis techniques have dominated the modal testing domain since its inception circa 1950. With the increase in computation power and sensor quality, OMA has seen significant advancements in application and implementation starting in the 1990s [86].

Just like in experimental modal analysis (EMA), OMA can be used to extract system parameters in both the time and frequency domains. Since the input force is not measured and is instead assumed to be of flat, board frequency spectrum (sufficiently higher than the modes of interest), cross-correlations and power spectra between response sensors pairs are calculated. The ability of each sensor to act as the "reference" and/or "roving" sensor provides the opportunity for much more information to be extracted from an OMA than with an EMA which typically uses a single (or few) reference (input) sensor locations [87]. The most common representation of the modal data in OMA is using the power spectral density (PSD) to represent the frequency domain behavior of the object under test using response only measurements. Using these PSD, researchers

have begun applying many of the techniques discussed in previous sections relating to vibration-based SHM via FRF to in-situ SHM. Many of the same features and drawbacks of each of the methods already discuss hold true when performing an OMA versus an EMA. In light of this, only a brief summary of some of the most recent work related to ambient excitation based SHM is given below.

The overwhelming majority of OMA based SHM literature is focused on system identification techniques to extract modal parameters (frequency, damping, and mode shapes) to be compared between health and (potentially) damaged states. In 2012, Reynders published a comprehensive review of system identification methods for OMA covering the state-of-the-art approaches [88] and in 2014 Rainieri published a book on OMA with applications towards civil structures [89]. In 2015, Siesakul et al. extended the OMA system identification capabilities by using sub-Nyquist sampled acceleration response signals to accurately estimate the natural frequencies and damping ratios of modes nearly 70 percent below the Nyquist rate [90]. This could be particularly useful in applications involving optical frequency domain reflectometry based optical strain sensing which suffers from sampling rate limitations [91]. Literature discussing more advanced methods for OMA based SHM is extremely limited at the present time with most advanced SHM methods are being developed using conventional EMA. Although some researchers have transitioned over to model-updating SHM using PSD rather than FRF for increased parameter sensitivity [92], these approaches are still laboratory based where the FRF is computed using input-output information before using the FRF and input information in the computation of the PSD [93]. Removal of the reliance on the FRF for vibration-based model updating SHM is one of the key steps to in-situ inspection of aerospace vehicles and as such a focus of the current work.

Chapter 3: Theoretical Development

Future SHM techniques that provide the possibility of damage prognosis will almost certainly rely on a multi-level framework that requires a correlated analytical model of the damaged structure along with extensive future load predictions and material degradation models. The focus of the current work is to develop the primary framework which provides an assessment of the presence, location, type, and severity of damage present in a structure as well as a measure of the confidence in the damage estimation while maintaining the ability to provide current safety margins of the structure (assuming expected future loads are known). This is achieved by developing a correlated analytical model of the damaged structure, where the damage locations and altered properties are identified. In order to achieve these expectations, strain-based, in-situ, SHM techniques will require that aircraft use ambient excitation, or onboard excitation, to perform a response only structural health assessment. As such, correlated analytical models will be required to transition from the standard frequency response functions (FRF) widely used in dynamic testing to a response only method. To this end, in the current framework, the power spectral density (PSD) is used to determine a structure's frequency response using dynamic strain data.

In the current chapter, a closed-form solution for the PSD is first calculated in the displacement domain. A transformation matrix is then defined to transform the displacement PSD to the strain domain. In order to produce an updated correlated model, a cost function is formulated which seeks to minimize a residual error vector between measured (damaged) PSD and their previously healthy analytical responses using an inverse-problem formulation. The non-linear cost function is locally linearized using a Taylor series expansion which allows the algorithm to determine an updated set of system parameters in a closed-form, iterative, fashion. The procedure for calculating the PSD and formulating the cost function are given in the following sections.

3.1 Dynamic System Description

The foundation of the current work is formed by developing an analytical model of a structure which relates the structural parameters of interest to the structure's strain-based spectral response. In the current work, it is assumed that the parameters of interest include the physical mass, stiffness, and/or damping properties of the structural system, thus the physically correct connectivity is maintained. In order to derive such an analytical model, the equations of motion are given in the displacement domain $\{x\}$ as [94]:

$$[M(r)]\{\ddot{x}(t)\}+[C(r)]\{\dot{x}(t)\}+[K(r)]\{x(t)\}=\{f(t)\} \tag{3-1}$$

where $[M(r)]$, $[C(r)]$, and $[K(r)]$ are the system mass, damping and stiffness matrices, respectively and $f(t)$ is the transient forcing function which is dependent on time (t). These system matrices depend on the structural parameters of interest (r) which are sensitive to damage. In order to transform the equation of motion into the frequency domain, a harmonic forcing function is defined as:

$$\{f(t)\}=\{F(\omega)\}e^{j\omega t} \tag{3-2}$$

where $\{F(\omega)\}$ is the spectral representation of the forcing function that depends on the angular frequency ω. Assuming the harmonic forcing function causes a harmonic response, the displacement response can be written as:

$$\{x(t)\}=\{X(\omega)\}e^{j\omega t}. \tag{3-3}$$

Taking the first and second time derivatives of (3-3) yields:

$$\{\dot{x}(t)\} = j\omega\{X(\omega)\}e^{j\omega t} \tag{3-4}$$

and

$$\{\ddot{x}(t)\} = -\omega^2\{X(\omega)\}e^{j\omega t}\,. \tag{3-5}$$

Substituting equations (3-2) through (3-5) into (3-1) and canceling out the complex exponential term yields the equation of motion for a dynamic system in the frequency domain:

$$\{F(\omega)\} = \left(-\omega^2[M(r)] + j\omega[C(r)] + [K(r)]\right)\{X(\omega)\}\,. \tag{3-6}$$

Defining the transfer function $[H(r,\omega)]$ between the input force $\{F(\omega,T)\}$ and the response $\{X(r,\omega,T)\}$ over record length T:

$$\{X(r,\omega,T)\} = [H(r,\omega)]\{F(\omega,T)\} \tag{3-7}$$

with:

$$[H(r,\omega)] = \left(-\omega^2[M(r)] + j\omega[C(r)] + [K(r)]\right)^{-1}. \tag{3-8}$$

Further, defining the term in the parenthesis as the dynamic stiffness matrix $[Z(r,\omega)]$:

$$[Z(r,\omega)] = \left(-\omega^2[M(r)] + j\omega[C(r)] + [K(r)]\right) = [H(r,\omega)]^{-1}. \tag{3-9}$$

Equation (3-8) allows for the computation of the transfer function as a function of frequency and the structural parameters of interest. While the transfer function model is of practical importance and widely used in structural dynamic testing and system identification, it requires explicit knowledge of the excitation force which produced the structural response and hence is not

well suited for in-situ SHM of aerospace vehicles in their operational environment. To this end, the Wiener-Khinchin relationship is used to express the power spectral density matrix (PSD) of the system displacements by making use of the system transfer functions.

3.2 Power Spectral Density Matrix

Derived from signal processing, the power spectrum of a time series describes the distribution of power in the signal by decomposing the signal into the frequency components composing that signal. Assuming a stationary signal, the power spectral density (PSD) of a signal can be used to denote the spectral energy distribution found in the signal per unit time. In regards to structural dynamic testing, the PSD is useful because it allows the spectral characteristics of a vibrating system to be determined without explicit knowledge of the input force. Furthermore, the PSD of a system can be related to the transfer function and in turn the dynamic stiffness matrix and structural update parameters.

By the Wiener-Khinchin theorem [95], the PSD can be related to the transfer function starting with the definition of the power spectral density of a time series:

$$[S_{xx}(r,\omega)] = \lim_{T\to\infty} \frac{1}{T} E\left[\left\{ X(r,\omega,T) \right\}^{*} \left\{ X(r,\omega,T) \right\}^{T} \right] \tag{3-10}$$

where the ( )* denotes the complex conjugate of a function ( ) and $E[\ ]$ is the expectation operator. Substituting equation (3-7) into (3-10) and recognizing that the transpose of a product of matrices equals to the product of their transposes in reverse order (i.e., $(AB)^T = B^T A^T$) yields the PSD in terms of the transfer function and input force:

$$[S_{xx}(r,\omega)] = \lim_{T\to\infty} \frac{1}{T} E\left[[H(r,\omega)]^{*} \{F(\omega,T)\}^{*} \{F(\omega,T)\}^{T} [H(r,\omega)]^{T} \right]. \tag{3-11}$$

Utilizing the fact that the transfer function is deterministic and does not depend on the period allows it to be brought out of both the expectation operator as well as the limit such that:

$$[S_{xx}(r,\omega)] = [H(r,\omega)]^{*} \lim_{T\to\infty} \frac{1}{T} E\left[\{F(\omega,T)\}^{*}\{F(\omega,T)\}^{T}\right][H(r,\omega)]^{T} \tag{3-12}$$

Recognizing that the inner term in (3-12) has the exact form as the definition of the PSD defined in equation (3-10) allows for the PSD of the excitation force to be defined by:

$$[S_{ff}(\omega)] = \lim_{T\to\infty} \frac{1}{T} E\left[\{F(\omega,T)\}^{*}\{F(\omega,T)\}^{T}\right]. \tag{3-13}$$

Finally, substituting equation (3-12) into (3-13) provides the analytical PSD of the system of interest in the displacement domain:

$$[S_{xx}(r,\omega)] = [H(r,\omega)]^{*}[S_{ff}(\omega)][H(r,\omega)]^{T}. \tag{3-14}$$

The result of (3-14) is that the displacement (and in turn acceleration or velocity) response PSD of any system can be expressed in terms of the transfer function of the system and the PSD of the input force. An underlying assumption throughout this work is that the input force is a broad-spectrum excitation (i.e. white noise or impulse response) and as such the PSD of the input force can be assumed constant or explicitly defined.

3.3 Strain Based Power Spectral Density Matrix

The power spectral density matrix of the system strains can be determined using the power spectral density matrix of the system displacements along with appropriate strain-displacement relations. This strain-displacement transformation allows for direct comparison between

experimentally measured PSD obtained via dynamic strain measurements and the model PSD. The most general form of this transformation can be written as:

$$\{\varepsilon\} = \left[B(r)\right]\{X\} \tag{3-15}$$

where $\{\varepsilon\}$ are the strains at the fiber-optic measurement locations, $\{X\}$ are the system nodal displacements in the frequency domain, and $\left[B(r)\right]$ is the strain-displacement transformation matrix that could depend upon the system structural parameters (r). In the current development, the finite element method is used to generate [B], but this transformation matrix could also be developed experimentally. The measured strain transfer function can be written by substituting equation (3-7) into equation (3-15) resulting in:

$$\left\{\varepsilon(r,\omega,T)\right\} = \left[H_{\varepsilon}(r,\omega)\right]\left\{F(\omega,T)\right\} \tag{3-16}$$

where

$$\left[H_{\varepsilon}(r,\omega)\right] = \left[B(r)\right]\left[H(r,\omega)\right]. \tag{3-17}$$

The strain PSD is defined based on the displacement PSD given in (3-10) as:

$$\left[S_{\varepsilon\varepsilon}(r,\omega)\right] = \lim_{T\to\infty}\frac{1}{T}E\left[\left\{\varepsilon(r,\omega,T)\right\}^{*}\left\{\varepsilon(r,\omega,T)\right\}^{T}\right]. \tag{3-18}$$

Substituting equation (3-16) into equation (3-18), and recognizing that the transfer function does not depend on the record length result in:

$$\left[S_{\varepsilon\varepsilon}(r,\omega)\right] = \left[H_{\varepsilon}(r,\omega)\right]^{*}\lim_{T\to\infty}\frac{1}{T}E\left[\left\{F(\omega,T)\right\}^{*}\left\{F(\omega,T)\right\}^{T}\right]\left[H_{\varepsilon}(r,\omega)\right]^{T} \tag{3-19}$$

and recognizing that the inner term is the definition of the input-force PSD, the strain PSD is found to be:

$$\left[S_{\varepsilon\varepsilon}(r,\omega)\right]=\left[H_{\varepsilon}(r,\omega)\right]^{*}\left[S_{ff}(\omega)\right]\left[H_{\varepsilon}(r,\omega)\right]^{T}. \tag{3-20}$$

Finally, comparing equation (3-20) to equation (3-14), it is clear that the strain PSD can be written in terms of the displacement PSD using the strain-displacement transformation as:

$$\left[S_{\varepsilon\varepsilon}(r,\omega)\right]=\left[B(r)\right]\left[S_{xx}(r,\omega)\right]\left[B(r)\right]^{T}. \tag{3-21}$$

Equation (3-21) can now be used to generate analytical, strain-based, PSD which are functions of the desired structural parameters to be updated (r) and frequency (ω). It should also be noted that the strain PSD is an $N_{\varepsilon DOF}$ x $N_{\varepsilon DOF}$ matrix where $N_{\varepsilon DOF}$ is the number of strain locations which the model is evaluated at. The diagonal terms of the strain PSD correspond to the auto-power spectral density of a particular strain location with itself whereas the off-diagonal terms correspond to cross-power spectra between strain sensor pairs. The strain PSD matrix is organized such that the i^{th} column corresponds to the auto and cross spectra calculated using strain location i as the reference location. In light of this, there are $N_{\varepsilon DOF}$ possible reference points which can be used in the formulation of the strain PSD. This large number of possible reference points is a major advantage of using the PSD rather than conventional FRF based model updating methods. The large number of possible reference points provides the opportunity for the damage detection algorithm to evaluate each reference point, ultimately leading to a statistical assessment of the probability of the identified damage parameters of being correct. This point will be discussed in detail in subsequent chapters.

3.4 Formulation of the Objective Function

With the analytical, strain-based PSD model now fully developed, a framework to update the analytical model to correlate with experimental measurements is developed. At its core, the SHM framework seeks to minimize the error between the measured strain PSD and the model strain PSD in a least-squares sense. To this end, a cost function has been developed which aims to minimize the error between the two PSD at discrete frequency lines via a parameter updating scheme. In order to derive the terms associated with the identified cost function it is useful to define some parameters. Throughout the course of this development any analytical (or modeled) strain PSD will be denoted as [*W*], i.e.:

$$[W(r,\omega)] = [S_{\varepsilon\varepsilon}(r,\omega)]_{analytical}\,. \tag{3-22}$$

Likewise, measured strain PSD will be denoted with a tilde:

$$[\tilde{S}(\omega)] = [S_{\varepsilon\varepsilon}(\omega)]_{measured}\,. \tag{3-23}$$

To maximize the likelihood of accurate damage detection, it is desirable to select discrete frequency lines with high signal-to-noise ratios at which the modeled and measured responses are compared. The methodology for selecting these frequency lines is discussed in subsequent sections. For the current discussion it suffices to note that these discrete frequency lines will be denoted with a subscript *k*, i.e. $\omega \to \omega_k$. The residual error between the modeled and measured strain-based PSD is defined as [*R*] where:

$$\underbrace{\left[R(r,\omega_k)\right]}_{\text{Residual Error}} = \underbrace{\left[W(r,\omega_k)\right]}_{\substack{\text{Modeled}\\ \text{Response}}} - \underbrace{\left[\tilde{S}(\omega_k)\right]}_{\substack{\text{Measured}\\ \text{Response}}}. \tag{3-24}$$

As previously discussed, the PSD can be calculated with respect to any measurement location where the i^{th} reference location corresponds to the i^{th} column of the PSD matrix. In this regard, the residual error will be minimized with respect to the i^{th} reference location at a time within the SHM framework. The algorithm can also be run over a set of reference locations, providing a statistical basis for the identified damage parameters. Restating equation (3-24) in terms of the vector quantities relating to the i^{th} reference location (column) yields:

$$\left\{R_i(r,\omega_k)\right\} = \left\{W_i(r,\omega_k)\right\} - \left\{\tilde{S}_i(\omega_k)\right\}. \tag{3-25}$$

It is clear that when the residual error vector defined in (3-25) goes to zero the measured PSD equals the modeled PSD at the discrete frequency lines and hence a candidate set of parameters (r) have been identified.

To account for the uncertainty present in both the model and measurement responses, a Bayesian framework has been adopted for the least-squares minimization of the residual error vector given in equation (3-25). The adopted Bayesian cost function was first developed by Tarantola and Valette [69] who proposed it for the purpose general parameter estimation. Oliver [2] later adapted the formulation for FRF based SHM. As stated by Tarantola and Valette, the goal of the framework is to identify an estimate $\{\hat{r}\}$ of the true $\{\tilde{r}\}$ update parameter vector which maximizes the posterior probability distribution and simultaneously satisfies the underlying system of equations (in this case the residual error vector) [69]. The cost function $J(\hat{r})$ is thus comprised of two parts, $J_R(\hat{r})$ which corresponds to minimizing the residual error vector and $J_r(\hat{r})$ which corresponds to maximizing the posterior parameter distribution such that:

$$J(\hat{r}) = J_R(\hat{r}) + J_r(\hat{r}) \tag{3-26}$$

with

$$J_R(\hat{r}) = \{R(\hat{r})\}^T [S_{RR}(\hat{r})]^{-1} \{R(\hat{r})\} \tag{3-27}$$

and

$$J_r(\hat{r}) = \left(\{\hat{r}\} - \{\hat{r}_o\}\right)^T [S_{r_o r_o}]^{-1} \left(\{\hat{r}\} - \{\hat{r}_o\}\right). \tag{3-28}$$

Minimizing $J_R(\hat{r})$ corresponds to minimizing the residual error vector or minimizing the difference between the analytical and measured PSD at the chosen frequency line set. The matrix quantity in (3-27), $[S_{RR}(\hat{r})]$, corresponds to the covariance matrix of the residual error vector. This covariance matrix accounts for uncertainty present in each term of the residual error vector and serves as a weighting parameter. The inverse of the covariance matrix implies that parameters with the largest (co)variance (most uncertainty) are weighted the least in the cost function and the parameters with the least uncertainty given the most weight.

The second terms comprising the cost function, given in (3-28), comes from the definition of a Gaussian distribution. From probability theory, for a Gaussian distribution for $\{\hat{r}\}$ with a mean value of $\{\hat{r}_o\}$, the posterior parameter distribution is given as [96]:

$$p(\hat{r}) = Ce^{-\frac{1}{2}\left(\{\hat{r}\} - \{\hat{r}_o\}\right)^T \left[S_{r_o r_o}\right]^{-1} \left(\{\hat{r}\} - \{\hat{r}_o\}\right)} \tag{3-29}$$

where C is a constant, $\{\hat{r}_o\}$ is the initial parameter set, and $[S_{r_o r_o}]$ is the covariance matrix of the update parameters in their initial state. It is clear from (3-29) that maximizing the posterior parameter distribution (maximizing the probability of the identified parameters being correct)

corresponds to minimizing the term contained within the negative exponential of (3-29). Tarantola and Valette showed that simultaneously satisfying the governing equations while maximizing the posterior probability is equivalent to a generalized, regularized, least-squares minimization solution where the least-squares weighting terms correspond to the covariance matrices of the residual error vector and initial parameter estimates, respectively [69].

3.5 Residual Error Covariance Matrices

While the residual error vector relationship given in (3-25) holds in principle, in practice the system being modeled will not behave deterministically and have some inherent randomness associated with the measurements. In order to account for this stochastic behavior, the relationship between the measured and modeled PSD is represented as:

$$\left\{\tilde{S}_i(\omega_k)\right\} = \left\{W_i(\tilde{r},\omega_k)\right\} + \left\{e(\omega_k)\right\} + \left\{v(\omega_k)\right\} \tag{3-30}$$

where the tilde over the update parameter vector r denotes they are the "true" (but unknown) damage parameters which minimize the residual error vector. Furthermore, $\left\{e(\omega_k)\right\}$ is the (deterministic) irreducible analytical model error and $\left\{v(\omega_k)\right\}$ is zero mean additive noise present on the measurement signal. If the noise were known to be of nonzero mean, the offset is accounted for by adding the mean value to the deterministic error vector. It is assumed that the random quantities $\{r\}$ and noise $\left\{v(\omega_k)\right\}$ follow a Gaussian distribution and hence can be fully characterized by their mean and covariance.

In order to calculate the covariance of the residual error vector, the error is evaluated at the current linearization point (β) and starts with the definition of covariance:

$$\left[S_{RR}\right]_i = E\left[\left(\{R_i(r_\beta,\omega_k)\} - E\left[\{R_i(r_\beta,\omega_k)\}\right]\right)\ldots \left(\{R_i(r_\beta,\omega_k)\} - E\left[\{R_i(r_\beta,\omega_k)\}\right]\right)^T\right] \tag{3-31}$$

with

$$E\left[\{R_i(r_\beta,\omega_k)\}\right] = E\left[\{W_i(r_\beta,\omega_k)\} - \{\tilde{S}_i(\omega_k)\}\right]. \tag{3-32}$$

Note that the term $\hat{r}_\beta$ is in anticipation for the need to linearize the cost function in order to find the least-squares solution and corresponds to the update parameter set $\hat{r}$ linearized at the β linearization point.

Recognizing $\{W_i\}$ is deterministic, (3-32) can be rewritten as:

$$E\left[\{R_i(r_\beta,\omega_k)\}\right] = \{W_i(r_\beta,\omega_k)\} - E\left[\{\tilde{S}_i(\omega_k)\}\right]. \tag{3-33}$$

Starting from the definition of the measurement PSD given in (3-30), the expected value of the measurement set can be derived as:

$$E\left[\{\tilde{S}_i(\omega_k)\}\right] = E\left[\{W_i(\tilde{r},\omega_k)\} + \{e(\omega_k)\} + \{v(\omega_k)\}\right]. \tag{3-34}$$

By the distributive property of expectations:

$$E\left[\{\tilde{S}_i(\omega_k)\}\right] = E\left[\{W_i(\tilde{r},\omega_k)\}\right] + E\left[\{e(\omega_k)\}\right] + E\left[\{v(\omega_k)\}\right]. \tag{3-35}$$

Recognizing both $\{W_i(\tilde{r},\omega_k)\}$ and $\{e(\omega_k)\}$ are deterministic and $\{v(\omega_k)\}$ is assumed Gaussian with mean zero, (3-35) can be simplified as:

$$E\left[\{\tilde{S}_i(\omega_k)\}\right] = \{W_i(\tilde{r},\omega_k)\} + \{e(\omega_k)\}. \tag{3-36}$$

Combining (3-36) and (3-33) yields:

$$E\left[\{R_i(r_\beta,\omega_k)\}\right] = \{W_i(r_\beta,\omega_k)\} - \{W_i(\tilde{r},\omega_k)\} - \{e(\omega_k)\} \tag{3-37}$$

and in turn:

$$\{R_i(r_\beta,\omega_k)\} - E\left[\{R_i(r_\beta,\omega_k)\}\right] = \{W_i(\tilde{r},\omega_k)\} + \{e(\omega_k)\} - \{\tilde{S}_i(\omega_k)\}. \tag{3-38}$$

Substituting in the definition of the measured PSD given in (3-30) to (3-38) and simplifying:

$$\{R_i(r_\beta,\omega_k)\} - E\left[\{R_i(r_\beta,\omega_k)\}\right] = -\{v(\omega_k)\}. \tag{3-39}$$

Using the result of (3-39), the residual error covariance matrix can be expressed as:

$$\left[S_{RR}\right]_i = E\left[\{v(\omega_k)\}\{v(\omega_k)\}^T\right] = \left[S_{vv}\right]_i. \tag{3-40}$$

Equation (3-40) yields the final result which is that the covariance of the residual error is equal to the covariance of the noise present in the measurement.

3.6 Least-Squares Minimization of the Cost Function

The strain PSD based model updating problem is solved when a parameter set $\{\hat{r}\}$ is identified which minimizes the residual-error based cost function $J(\hat{r})$. In order to find such a parameter set for an overdetermine system of equations, it is desirable to implement a least-square minimization approach. For clarity, the cost function as given in (3-26) is repeated in its expanded form as:

$$J(\hat{r}) = \{R(\hat{r})\}^T [S_{RR}(\hat{r})]^{-1} \{R(\hat{r})\} + \left(\{\hat{r}\} - \{\hat{r}_o\}\right)^T [S_{r_o r_o}]^{-1} \left(\{\hat{r}\} - \{\hat{r}_o\}\right). \tag{3-41}$$

The least-squares solution is found by taking the variation of $J(\hat{r})$ with respect to $\{\hat{r}\}$ and setting the result equal to zero:

$$\delta J(\hat{r}) = \{\delta \hat{r}\} \left\{ \frac{\partial J}{\partial \hat{r}} \right\} = 0. \tag{3-42}$$

Recognizing that the variation of $\hat{r}$ is non-zero, equation (3-42) can be rewritten as:

$$\left\{ \frac{\partial J_R(\hat{r})}{\partial \hat{r}} \right\} + \left\{ \frac{\partial J_r(\hat{r})}{\partial \hat{r}} \right\} = 0. \tag{3-43}$$

Looking at the first term in (3-43):

$$\left\{ \frac{\partial J_R(\hat{r})}{\partial \hat{r}} \right\} = \frac{\partial}{\partial \hat{r}} \left(\{R(\hat{r})\}^T [S_{RR}(\hat{r})]^{-1} \{R(\hat{r})\} \right). \tag{3-44}$$

Since $\{R\}$ has an explicit dependency on $\{\hat{r}\}$ chain rule must be invoked yielding:

$$\left\{ \frac{\partial J_R(\hat{r})}{\partial \hat{r}} \right\} = 2 \left[\frac{\partial R(\hat{r})}{\partial \hat{r}} \right] \left[S_{RR} \right]^{-1} \{R(\hat{r})\} \tag{3-45}$$

where the matrix $\left[\frac{\partial R(\hat{r})}{\partial \hat{r}} \right]$ is the derivative of the residual error vector with each update parameter forming a column of the matrix. Furthermore, it is assumed the variation of the covariance with respect to $\hat{r}$ is negligible. For the p^{th} parameter:

$$\left\{ \frac{\partial R(\hat{r})}{\partial \hat{r}_p} \right\} = \frac{\partial}{\partial \hat{r}_p} \left(\{W_i(\hat{r}, \omega_k)\} - \{\tilde{S}_i(\omega_k)\} \right) = \left\{ \frac{\partial W_i(\hat{r})}{\partial \hat{r}_p} \right\}. \tag{3-46}$$

Stacking the result of (3-46) column wise yields the parameter sensitivity matrix:

$$\left[\frac{\partial R(\hat{r})}{\partial \hat{r}}\right] = \left[\left\{\frac{\partial W_i(\hat{r})}{\partial \hat{r}_1}\right\} \vdots \left\{\frac{\partial W_i(\hat{r})}{\partial \hat{r}_2}\right\} \vdots \cdots \vdots \left\{\frac{\partial W_i(\hat{r})}{\partial \hat{r}_n}\right\}\right]. \tag{3-47}$$

For the second term in (3-43) the derivative can be calculated directly as:

$$\left\{\frac{\partial J_r(\hat{r})}{\partial \hat{r}}\right\} = 2\left[S_{r_o r_o}\right]^{-1}\left(\{\hat{r}\} - \{\hat{r}_o\}\right). \tag{3-48}$$

Combining the results of (3-45) through (3-48) and substituting into (3-43) results in:

$$\left[\frac{\partial W_i(\hat{r})}{\partial \hat{r}}\right]^T \left[S_{RR}(\hat{r})\right]^{-1}\left\{\{W_i(\hat{r},\omega_k)\} - \{\tilde{S}_i(\omega_k)\}\right\} + \left[S_{r_o r_o}\right]^{-1}\left(\{\hat{r}\} - \{\hat{r}_o\}\right) = 0. \tag{3-49}$$

In order to achieve the desired explicit form which allows the set of parameters $\{\hat{r}\}$ to be determined in an iterative fashion a linearization of $\{W_i(\hat{r},\omega_k)\}$ must be performed. Calculating a Taylor series expansion of (3-49) about the initial point $\{\hat{r}_o\}$ and keeping terms up to first order terms yields:

$$\{W_i(\hat{r},\omega_k)\} \cong \{W_i^*(\hat{r}_o,\omega_k)\} + \left[\frac{\partial W_i(\hat{r},\omega_k)}{\partial \hat{r}}\right]\Bigg|_{\hat{r}_o}\left(\{\hat{r}\} - \{\hat{r}_o\}\right) \tag{3-50}$$

where the $\{W_i^*(\hat{r}_o,\omega_k)\}$ term corresponds to the linearized model PSD at the initial point expanded about the current linearization point $\{\hat{r}_\beta\}$:

$$\{W_i^*(\hat{r}_o,\omega_k)\} \cong \{W_i(\hat{r}_\beta,\omega_k)\} + \left[\frac{\partial W_i(\hat{r},\omega_k)}{\partial \hat{r}}\right]\Bigg|_{\hat{r}_\beta} \left(\{\hat{r}_o\} - \{\hat{r}_\beta\}\right). \tag{3-51}$$

Substituting (3-51) and (3-50) into (3-49) and grouping all terms relating to $\{\hat{r}\}$ on the left hand side produces:

$$\begin{aligned}
&\left[\left[S_{r_o r_o}\right]^{-1} + \left[\frac{\partial W_i(\hat{r})}{\partial \hat{r}}\right]^T\Bigg|_{\{\hat{r}_\beta\}} \left[S_{RR}(\hat{r}_o)\right]^{-1} \left[\frac{\partial W_i(\hat{r})}{\partial \hat{r}}\right]^T\Bigg|_{\{\hat{r}_o\}}\right]\{\hat{r}\} = \cdots \\
&\left[\left[S_{r_o r_o}\right]^{-1} + \left[\frac{\partial W_i(\hat{r})}{\partial \hat{r}}\right]^T\Bigg|_{\{\hat{r}_\beta\}} \left[S_{RR}(\hat{r}_o)\right]^{-1} \left[\frac{\partial W_i(\hat{r})}{\partial \hat{r}}\right]^T\Bigg|_{\{\hat{r}_o\}}\right]\{\hat{r}_o\} + \cdots \\
&\left[\frac{\partial W_i(\hat{r})}{\partial \hat{r}}\right]^T\Bigg|_{\{\hat{r}_\beta\}} \left[S_{RR}(\hat{r}_o)\right]^{-1} \{\tilde{S}_i(\omega_k)\} - \cdots \\
&\left[\frac{\partial W_i(\hat{r})}{\partial \hat{r}}\right]^T\Bigg|_{\{\hat{r}_o\}} \left[S_{RR}(\hat{r}_o)\right]^{-1} \left(\{W_i(\hat{r}_\beta,\omega_k)\} + \left[\frac{\partial W_i(\hat{r})}{\partial \hat{r}}\right]\Bigg|_{\{\hat{r}_\beta\}} \left(\{\hat{r}_o\} - \{\hat{r}_\beta\}\right)\right)
\end{aligned} \quad . \tag{3-52}$$

Defining the inverse of the term pre-multiplying $\{\hat{r}\}$ as $[Q]$ such that:

$$[Q] = \left[\left[S_{r_o r_o}\right]^{-1} + \left[\frac{\partial W_i(\hat{r})}{\partial \hat{r}}\right]^T\Bigg|_{\{\hat{r}_\beta\}} \left[S_{RR}(\hat{r}_o)\right]^{-1} \left[\frac{\partial W_i(\hat{r})}{\partial \hat{r}}\right]\Bigg|_{\{\hat{r}_o\}}\right]^{-1} . \tag{3-53}$$

Equation (3-52) can now be rewritten with the update parameter set $\{\hat{r}\}$ isolated on the left-hand side, as desired:

$$\{\hat{r}\} = \{\hat{r}_o\} + [Q]\left(\left[\frac{\partial W_i(\hat{r})}{\partial \hat{r}}\right]^T\Bigg|_{\{\hat{r}_\beta\}} [S_{RR}(\hat{r}_o)]^{-1} \ldots \left(\{\tilde{S}_i(\omega_k)\} - \left(\{W_i(\hat{r}_\beta, \omega_k)\} + \left[\frac{\partial W_i(\hat{r})}{\partial \hat{r}}\right]\Bigg|_{\{\hat{r}_\beta\}} \left(\{\hat{r}_o\} - \{\hat{r}_\beta\}\right)\right)\right)\right) \tag{3-54}$$

Recognizing equation (3-54) will be implemented iteratively, where the system of equations at the current iteration step will be linearized at the previous iteration estimate $\left(\{\hat{r}_\beta\}_{j+1} = \{\hat{r}\}_j\right)$, equations (3-53) and (3-54) can be rewritten in their final iterative form as:

$$[Q]_{j+1} = \left[\left[S_{r_o r_o}\right]^{-1} + \left[\frac{\partial W_i(\hat{r}_j)}{\partial \hat{r}}\right]^T [S_{RR}(\hat{r}_o)]^{-1} \left[\frac{\partial W_i(\hat{r}_o)}{\partial \hat{r}}\right]\right]^{-1} \tag{3-55}$$

and

$$\{\hat{r}\}_{j+1} = \{\hat{r}_o\} + [Q]_{j+1}\left(\left[\frac{\partial W_i(\hat{r}_j)}{\partial \hat{r}}\right]^T [S_{RR}(\hat{r}_o)]^{-1} \ldots \left(\{\tilde{S}_i(\omega_k)\} - \left(\{W_i(\hat{r}_j, \omega_k)\} + \left[\frac{\partial W_i(\hat{r}_j)}{\partial \hat{r}}\right]\left(\{\hat{r}_o\} - \{\hat{r}_j\}\right)\right)\right)\right). \tag{3-56}$$

Equations (3-55) and (3-56) can thus be solved iteratively using any number of stopping criteria. The criteria used in the current work was chosen to be the error between the analytical PSD response $\{W_i(\hat{r}, \omega_k)\}$ and measured PSD response $\{\tilde{S}_i(\omega_k)\}$ is below the predefined threshold (i.e. $\{R_i(\hat{r}, \omega_k)\} < \varepsilon$) as well as the change of parameters between iterations is below another predefined threshold. These stopping criteria will be discussed in detail in subsequent chapters when the algorithm is implemented. Once convergence has been achieved $\{\hat{r}\}_{j+1}$ becomes

the posterior parameter estimate of the effective damage parameters $\{r^*\}$ and $\left[Q\right]_{j+1}$ the posterior parameter covariance matrix $\left[S_{r^*r^*}\right]$.

The reader is reminded that the "*i*" subscript corresponds to the i^{th} reference DOF used to calculate the PSD. The SHM algorithm can be repeated using each available DOF in the model/measurement sets (or any subset of these DOF). Performing the parameter updating with respect to numerous reference DOF allows the statistics of the identified parameter set to be calculated and a confidence interval on the parameter set to be obtained.

3.7 Damage Scale Factors

Up to this point, the vector of update parameters $\{\hat{r}\}$ has been defined in general terms. In practice, the vector of update parameters can include material properties (stiffness, density, thickness, etc.), section geometry (area, inertia, etc.), or combined properties, for example the structural stiffness (*EI*). While it is possible to use any system parameters in the updating scheme, their orders of magnitude difference in value and sensitivity weights the solution space disproportionally in the direction of the larger parameters. In order to normalize the update equations ((3-55) and (3-56)) damage scale factors are introduced. Using bending stiffness as an example of an update parameter, the damage scale factor can be related to the physical parameter by:

$$\bar{EI}_n = EI_n \delta_{EI_n} \tag{3-57}$$

where the $\bar{EI}_n$ denotes the correlated posterior bending stiffness of the n^{th} element, EI_n is the healthy effective parameter, δ_{EI_n} is the n^{th} element bending stiffness damage scale factor. It is thus

observed that a damage scale factor of one indicates the algorithm did not identify a change in that particular parameter for that particular element. Likewise, a damage scale factor equal to zero would denote a complete loss of that parameter caused by the damage event. Equivalent statements of damage scale factors can be similarly expressed for density and torsional stiffness as:

$$\bar{\rho}_n = \rho_n \delta_{\rho_n} \tag{3-58}$$

and

$$\bar{GJ}_n = GJ_n \delta_{GJ_n}, \tag{3-59}$$

respectively.

These damage scale factors are inserted into the analytical model during the finite element formulation of the system matrices. Once the vector of updated damage scale factors has been determined by the SHM algorithm, they can be multiplied by their respective healthy parameter to yield the updated damage parameters in engineering units. Henceforth, reference to the vector $\{\hat{r}\}$ will imply a vector of damage scale factors which must be multiplied by their respective parameter values to yield the true updated parameter in engineering units. Equation (3-60) is an example of update parameter vector $\{\hat{r}\}$ written in terms of a set of damage scale factors:

$$\{\hat{r}\} = \begin{Bmatrix} \delta_{EI_1} & \cdots & \delta_{EI_n} & \delta_{GJ_1} & \cdots & \delta_{GJ_n} & \delta_{\rho_1} & \cdots & \delta_{\rho_n} \end{Bmatrix}^T. \tag{3-60}$$

3.8 Batch Data Processing

This damage scale factor optimization problem requires the minimization of a cost function which has an infinite number of possible solutions. While best efforts have been made to obtain the optimal solution (in a statistical sense, maximizing the posterior probability) there is no assurance the converged solution is the true, or unique, solution. Maximizing the amount of information available to the algorithm creates an overdetermined system of equations and assists in obtaining a realistic solution to the parameter updating process.

Under the current framework this update information is obtained by sampling the measured and analytical PSD at discrete frequency lines ω_k . Each "*k*" frequency line contributes two pieces of information per strain sensor location (real and imaginary component of the PSD). In order to generate sufficient information to ensure a successful parameter update it is desirable to "batch-stack" the information contained in each frequency line and process all of the information simultaneously. When batch stacking the quantities in practice, the zero values corresponding to the imaginary portion of the auto-power spectra must be removed. This is necessary to allow for the inversion of the residual error covariance matrix and is done in all instances of the use of this algorithm.

In the current development, batch-stacked quantitates will be denoted with an underbar (_). It is also noted that the batch-stacking process requires the selection of discrete frequency lines, removing the dependency of ω_k on all batched-stacked vectors and matrices. In order to provide clarity, examples of batch-stacked quantities used in the updating process and their respective sizes are listed below:

Analytical PSD:

$$\left\{\underline{W}_i\left(\hat{r}\right)\right\} = \begin{Bmatrix} \mathrm{Re}\left(\left\{W_i\left(\hat{r},\omega_1\right)\right\}\right) \\ \mathrm{Im}\left(\left\{W_i\left(\hat{r},\omega_1\right)\right\}\right) \\ \mathrm{Re}\left(\left\{W_i\left(\hat{r},\omega_2\right)\right\}\right) \\ \mathrm{Im}\left(\left\{W_i\left(\hat{r},\omega_2\right)\right\}\right) \\ \vdots \\ \mathrm{Re}\left(\left\{W_i\left(\hat{r},\omega_{N_\omega}\right)\right\}\right) \\ \mathrm{Im}\left(\left\{W_i\left(\hat{r},\omega_{N_\omega}\right)\right\}\right) \end{Bmatrix}_{(2xN_{dof}\,xN_\omega)x1} \tag{3-61}$$

where N_{dof} is the number of degrees of freedom in the analytical model and N_ω is the number of selected frequency lines.

Experimental PSD:

$$\left\{\underline{\tilde{S}}_i\right\} = \begin{Bmatrix} \mathrm{Re}\left(\left\{\tilde{S}_i\left(\omega_1\right)\right\}\right) \\ \mathrm{Im}\left(\left\{\tilde{S}_i\left(\omega_1\right)\right\}\right) \\ \mathrm{Re}\left(\left\{\tilde{S}_i\left(\omega_2\right)\right\}\right) \\ \mathrm{Im}\left(\left\{\tilde{S}_i\left(\omega_2\right)\right\}\right) \\ \vdots \\ \mathrm{Re}\left(\left\{\tilde{S}_i\left(\omega_{N_\omega}\right)\right\}\right) \\ \mathrm{Im}\left(\left\{\tilde{S}_i\left(\omega_{N_\omega}\right)\right\}\right) \end{Bmatrix}_{(2xN_{dof}\,xN_\omega)x1} \tag{3-62}$$

Residual Error Covariance Matrix (Noise Covariance):

$$\left[\underline{S}_{RR}\right]=\begin{bmatrix} \mathrm{Re}\left(\left[S_{RR}(\omega_1)\right]\right) & [0] & \cdots & [0] & [0] \\ [0] & \mathrm{Im}\left(\left[S_{RR}(\omega_1)\right]\right) & \cdots & [0] & [0] \\ \vdots & \vdots & \ddots & \vdots & \vdots \\ [0] & [0] & \cdots & \mathrm{Re}\left(\left[S_{RR}(\omega_{N_\omega})\right]\right) & [0] \\ [0] & [0] & \cdots & [0] & \mathrm{Im}\left(\left[S_{RR}(\omega_{N_\omega})\right]\right) \end{bmatrix}_{(2xN_{dof}xN_\omega)x(2xN_{dof}xN_\omega)} \tag{3-63}$$

Parameter Sensitivity Matrix:

$$\left[\frac{\partial \underline{W}_i(\hat{r})}{\partial \hat{r}}\right]=\left[\left\{\frac{\partial \underline{W}_i(\hat{r})}{\partial \hat{r}_1}\right\} \quad \left\{\frac{\partial \underline{W}_i(\hat{r})}{\partial \hat{r}_2}\right\} \quad \cdots \quad \left\{\frac{\partial \underline{W}_i(\hat{r})}{\partial \hat{r}_{N_{\hat{r}}}}\right\}\right]_{(2xN_{dof}xN_\omega)xN_{\hat{r}}} \tag{3-64}$$

where $N_{\hat{r}}$ is the number of update parameters.

Residual Error Covariance Matrix (Noise Covariance):

$$\left[\underline{S}_{r_o r_o}\right]=\begin{bmatrix} S_{r_1 r_1} & 0 & 0 & 0 \\ 0 & S_{r_2 r_2} & 0 & 0 \\ 0 & 0 & \ddots & \vdots \\ 0 & 0 & \cdots & S_{r_{N_{\hat{r}}} r_{N_{\hat{r}}}} \end{bmatrix}_{N_{\hat{r}}xN_{\hat{r}}} \tag{3-65}$$

Using these batch-stacked quantities, the iterative equations given in (3-55) and (3-56) can be restated in batch-stacked form as:

$$[Q]_{j+1}=\left[\left[\underline{S}_{r_o r_o}\right]^{-1}+\left[\frac{\partial \underline{W}_i(\hat{r}_j)}{\partial \hat{r}}\right]^T\left[\underline{S}_{RR}(\hat{r}_o)\right]^{-1}\left[\frac{\partial \underline{W}_i(\hat{r}_o)}{\partial \hat{r}}\right]\right]^{-1} \tag{3-66}$$

and

$$\{\hat{r}\}_{j+1} = \{\hat{r}_o\} + [Q]_{j+1}\left(\left[\frac{\partial \underline{W}_i(\hat{r}_j)}{\partial \hat{r}}\right]^T [\underline{S}_{RR}(\hat{r}_o)]^{-1} \cdots \left(\{\tilde{\underline{S}}_i(\omega_k)\} - \left(\{\underline{W}_i(\hat{r}_j, \omega_k)\} + \left[\frac{\partial \underline{W}_i(\hat{r}_j)}{\partial \hat{r}}\right]\left(\{\hat{r}_o\} - \{\hat{r}_j\}\right)\right)\right)\right) \tag{3-67}$$

The next chapter covers the use of these equations via an algorithm walk-through along with several validation and comparison studies.

3.9 Improved Convergence Techniques

With the theory of the algorithm established, two approaches are included for improving convergence rate and accuracy. These approaches are (a) frequency line updating, and (b) step-size restriction.

3.9.1 Frequency Line Updating

The first approach for improving convergence and accuracy is the optional updating of the frequency lines at which the analytical and measured PSD are evaluated. The algorithm is setup such that a predefined (and fixed) set of frequency lines can be used on which the parameter estimation is performed. Alternatively, a set of PSD peaks and the relative amplitudes at which to obtain the frequency line set can be defined. When the latter is used, a vector of PSD peaks $\{\Psi\}$, and a vector of the ratios of the magnitude of the analytical PSD to peak magnitude $\{\Upsilon\}$ at which to extract the frequency lines are defined. The PSD values of the measured data are fixed and hence the corresponding frequency lines of the measurement set are not updated. The values corresponding to the analytical PSD however are updated at each iteration to maintain their

magnitude with respect to their PSD peak. Figure 3-1 shows two neighboring PSD peaks at an arbitrary iteration step.

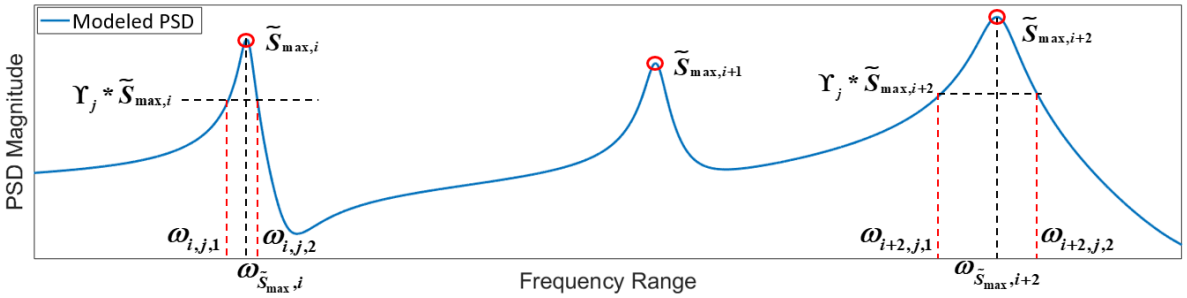

Figure 3-1: Automatic frequency line selection schematic.

To summarize for clarity, if frequency line updating is selected the peaks to include in the updating are identified. The example depicted in Figure 3-1 shows a PSD containing three possible peaks, *i*, *i+1* and *i+2*. If, for example, the peaks *i* and *i+2* (perhaps *i+1* has a poor signal-to-noise or in the presented figure a low amplitude) are to be used, the input vector would be:

$$\{\Psi\} = \{i \quad i+2\}. \tag{3-68}$$

In this case, a vector of ratios of peak magnitude at which to extract the desired frequencies would also need to be provided. In order to keep Figure 3-1 as clutter free as possible, only one update ratio is selected in the current example. In practice, one could define as many frequency ratios as desired and assemble them into a vector such that:

$$\{\Upsilon\} = \{\Upsilon_j\} \tag{3-69}$$

where is it noted that the ratios of the peaks given in $\{\Upsilon\}$ must vary between 0 and 1 and in practice should be further restricted from these extremes. Using the natural frequencies of the system, the

algorithm searches the neighborhood of the modes included in $\{\Psi\}$ to find the peak values of the model PSD. Each of these peak values are multiplied by the vector of magnitude ratios to yield the target amplitude of the PSD. The algorithm then finds the index of these target amplitudes and identifies the nearest corresponding frequencies. Figure 3-1 provides a graphical example of the process using the vectors given in equations (3-68) and (3-69).

As discussed, the inputs into the frequency line selection routine are $\{\Psi\}$ and $\{\Upsilon\}$ and what is returned is a vector of candidate frequencies. For each mode and amplitude ratio input to the routine, two possible frequencies could be returned:

$$\{\omega_k\} = \begin{Bmatrix} \omega_{i,j,1} & or & \omega_{i,j,2} \\ \omega_{i+2,j,1} & or & \omega_{i+2,j,2} \end{Bmatrix}. \tag{3-70}$$

Out of the two candidate frequencies returned, the algorithm discards the point which lies between the analytical and measurement data and instead uses the points outside of the set of modal peaks. Figure 3-2 shows a single set of peaks corresponding to a single mode of the analytical and the measured (damaged) PSD. Choosing frequency lines which lie in region 2 correspond to points were the residual error can be minimized without the correct set of parameters being identified and as such should be avoided. The main reason region 2 can lead to erroneous solutions is that the incorrect parameter set will be "closer" in the solution space than the true parameters, visually this can be thought of as the intersection of the modeled and measured curves in Figure 3-2.

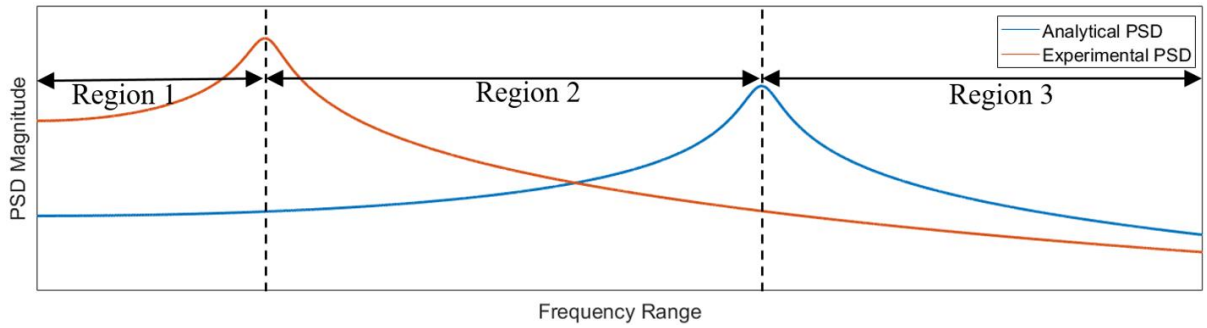

Figure 3-2: Optimal (regions 1 and 3) and sub-optimal (region 2) candidate frequency line selection ranges.

If only one mode and one frequency line was selected in region 2 it is likely the algorithm would identify an incorrect parameter set that is associated with the two PSD's overlapping at that frequency. Although adding additional lines helps to avoid this problem, any lines in region 2 decreases the algorithms ability to move to the true solution. With regard to which of the candidate frequency lines given in (3-70) the algorithm uses, they are selected such that region between the modeled and measured PSD is avoided. This is done by comparing the analytical and measured PSD peaks in $\{\Psi\}$. In the present example, given in Figure 3-2, this corresponds to choosing analytical frequency lines in region 3, or the frequencies on the right side of the peak in Figure 3-2 and measurement frequencies in region 1.

3.9.2 Stepsize Restriction Factor

The second approach for improving convergence and accuracy is the stepsize restriction factor, $\Delta r_{\max}$. During the updating routine, especially as the solution space becomes more complex, disproportional parameter sensitivities can cause some parameters to artificially vary rapidly. This artificial variation tends to "makeup" for the true parameter change associated with parameters having smaller sensitives, meaning some parameters in the solution have overshot their values to compensate for other parameters which have not reached their true damage levels. When this

happens, it usually results in converged parameter sets in which the model PSD does not exactly correlate with the measurement data and in many cases the identified parameters are non-physical. In order to combat the problem of "runaway" parameters, a stepsize restriction factor has been implemented in the algorithm.

When the stepsize restriction factor (q) is in use, the algorithm calculates the change in each parameter, at each iteration step, such that:

$$\Delta r_{j+1} = \max\left(abs\left(\left\{\hat{r}\right\}_{j+1} - \left\{\hat{r}\right\}_{j} \right) \right). \tag{3-71}$$

If Δr_{j+1} exceeds the predefined $\Delta r_{\max}$ an adaptive stepsize is implemented and the updated parameter set at iteration $j+1$ is recalculated to adhere to the limiting stepsize as:

$$\left\{\hat{r}\right\}_{j+1} = \left\{\hat{r}\right\}_{j} + \frac{1}{q}\left(\left\{\hat{r}\right\}_{j+1} - \left\{\hat{r}\right\}_{j} \right) \tag{3-72}$$

where,

$$q = \frac{\Delta r_{j+1}}{\Delta r_{\max}} + 1. \tag{3-73}$$

After each step, the stepsize restriction factor is reset to have a value of one, insuring the fastest possible convergence while implementing the restriction on only the iterations which exceed the defined criteria.

Chapter 4: Analytical Implementation and Validation – Simple System

In order to utilize the theory developed in Chapter 3, an example problem is explored. The sample problem utilizes a single Timoshenko beam element in order to provide the reader insight into the algorithm's operation while validating the proposed method. The chapter begins with a summary of the algorithm, highlighting key points related to the inputs, iteration procedure, and outputs of the algorithm. A baseline problem is then established which is used for a step-by-step demonstration of the algorithm, including displayed values for the full input set of the algorithm at each step. Pseudo experimental data representing the damaged system is generated using the analytical model. The remainder of the chapter is dedicated to studying the algorithm's performance under variations from the baseline problem including, changes in damping, type and magnitude of damage, selection of frequency lines, and noise.

4.1 Summary of the Algorithm

In order to provide clarity in the analyses performed in the remainder of the dissertation, a step-by-step outline of the inner workings of the algorithm is given below.

4.1.1 Algorithm Inputs

- Initial damage scale factor vector (Initially set to equal the undamaged parameter value, {1}):

$$\{\hat{r}_o\}$$

- System matrices as a function of update parameters:

$$[M(\hat{r})],\ \ [C(\hat{r})],\ \ [K(\hat{r})]$$

- Choice of reference degree-of-freedom(s):

$$\{i\}$$

- Initial damage scale factor covariance matrix:

$$\left[S_{r_o r_o}\right]$$

- Residual error covariance matrix:

$$\left[S_{RR}\right]$$

- Set of initial frequency lines:

$$\omega_k, \quad k = 1, 2, ..., N_\omega$$

or

Vector of ratios of magnitude of model PSD to peak magnitude at which to define frequency lines at:

$$\{\Upsilon\}$$

- Measured PSD vector(s) for the i^{th} reference DOF, sampled and batch-stacked over the chosen frequency lines:

$$\left\{\underline{\tilde{S}}_i\right\}$$

- Choice of location(s) within elements at which strain(s) is(are) calculated:

$$\xi, \quad \zeta \quad and \quad \eta$$

4.1.2 Iterative Procedure (For the j^{th} iteration where j = 0,1, 2,…)

1. Create the analytical model PSD from the system matrices and strain transformation matrix, evaluated at $\left\{\hat{r}_j\right\}$, referenced to DOF *i* and batch-stack over frequency lines using (3-9), (A-24) and (3-61):

$$\left\{\underline{W}_i\left(\hat{r}_j\right)\right\}.$$

2. Update the frequencies corresponding to the frequency lines of the analytical model PSD by finding the value in the PSD vector such that:

$$\widehat{W}_i\left(\hat{r}_j, \omega_{k_j}\right) = abs\left(W_i\left(\hat{r}_j, \omega_{k_j}\right)\right)\Upsilon_k$$

where Υ is the percent of the peak magnitude at which to sample the analytical PSD. The corresponding frequency ω_{k_j} is found by taking the first point in the particular peak region greater than or equal to $\widehat{W}_i\left(\hat{r}_j, \omega_{k_j}\right)$ for regions of positive slope or the last point in the region greater than or equal to $\widehat{W}_i\left(\hat{r}_j, \omega_{k_j}\right)$ for regions of negative slope. Once noise is considered there is an additional layer of screening the frequencies undergo but that will be discussed where relevant.

3. Compute batch-stacked parameter sensitivity matrix using (3-64) and second order central difference [97]:

$$\left[\frac{\partial \underline{W}_i(\hat{r}_j)}{\partial \hat{r}}\right].$$

4. Evaluate residual error covariance matrix at $\left\{\hat{r}_j\right\}$ and batch-stack according to (3-63) as:

$$\left[\underline{S}_{RR}\right].$$

5. Compute the quantity $\left[Q\right]_{j+1}$ from (3-66):

$$\left[Q\right]_{j+1} = \left[\left[\underline{S}_{r_o r_o}\right]^{-1} + \left[\frac{\partial \underline{W}_i(\hat{r}_j)}{\partial \hat{r}}\right]^T \left[\underline{S}_{RR}(\hat{r}_o)\right]^{-1}\left[\frac{\partial \underline{W}_i(\hat{r}_o)}{\partial \hat{r}}\right]\right]^{-1}.$$

6. Compute the updated parameter estimate from (3-67):

$$\left\{\hat{r}\right\}_{j+1} = \left\{\hat{r}_o\right\} + \left[Q\right]_{j+1}\left(\left[\frac{\partial \underline{W}_i(\hat{r}_j)}{\partial \hat{r}}\right]^T \left[\underline{S}_{RR}(\hat{r}_o)\right]^{-1}\left(\left\{\tilde{\underline{S}}_i(\omega_k)\right\} - \left(\left\{\underline{W}_i(\hat{r}_j, \omega_k)\right\} + \left[\frac{\partial \underline{W}_i(\hat{r}_j)}{\partial \hat{r}}\right]\left(\left\{\hat{r}_o\right\} - \left\{\hat{r}_j\right\}\right)\right)\right)\right).$$

7. Scale the parameter stepsize (if required) via the defined stepsize restriction factor such that:

$$\left\{\hat{r}\right\}_{j+1} = \left\{\hat{r}\right\}_j + \frac{1}{q}\left(\left\{\hat{r}\right\}_{j+1} - \left\{\hat{r}\right\}_j\right).$$

8. Check for convergence of both the parameter set and the error such that:

$$\Delta r = \max\left(\left|\hat{r}_{j+1} - \hat{r}_j\right|\right) < \alpha$$

and

$$Error = norm_2\left(\left\{\underline{\tilde{S}}_i\right\} - \left\{\underline{W}_i\left(\hat{r}_{j+1}\right)\right\}\right) < \beta$$

where α and β are predefined convergence tolerances. The iteration loop is broken when either Δr or $Error$ drops below the pre-defined threshold. There are several possible outcomes which are autonomously determined:

   a. If $\Delta r < \alpha$ and $Error < \beta \rightarrow$ Solution has converged and the error is within the specified tolerance, break iteration loop.
   b. If $\Delta r > \alpha$ and $Error > \beta \rightarrow$ Increase *j* by 1 and start the iteration process again.
   c. If $\Delta r > \alpha$ and $Error < \beta \rightarrow$ Increase *j* by 1 and start the iteration process again.
   d. If $\Delta r < \alpha$ and $Error > \beta \rightarrow$ Solution has converged to incorrect answer, break iteration loop, change input parameter(s) and rerun algorithm.

9. Repeat input and iteration process for all $\{i\}$ desired reference DOF.

4.1.3 Converged Algorithm Outputs

- Updated damaged scale factors for each for the *i* reference DOF used:

$$\left\{\hat{r}\right\}_{i,j+1} \rightarrow \left\{\hat{r}_d\right\}_i$$

- Updated damaged scale factor uncertainty estimate for the *i* reference DOF:

$$diag\left(\left[Q\right]_{i,j+1}\right)\rightarrow\left\{\sigma_r^2\right\}_i$$

- Calculated converged parameter statistics over all *i* reference DOF:

$$E\left(\left\{\hat{r}_d\right\}\right)=mean\left(\left\{\hat{r}_d\right\}_i\right)$$
$$\text{var}\left(\left\{\hat{r}_d\right\}\right)=E\left(\left(\left\{\hat{r}_d\right\}-E\left(\left\{\hat{r}_d\right\}\right)\right)^2\right)$$

- Updated, correlated finite element system model:

$$\left[M(\hat{r}_d)\right],\quad\left[C(\hat{r}_d)\right],\quad\left[K(\hat{r}_d)\right]$$

4.2 Algorithm Walk-Through using Timoshenko Beam Element

The operation of the SHM algorithm is now demonstrated through a simple one beam element system. In the current study, a thin-walled composite beam was modeled as a single, two-node Timoshenko beam element. The basic premise of the SHM algorithm is that system matrices derived from the application of the finite element method are used to produce a model-PSD equation in which the desired update parameters are represented as variables. For the current example, bending in a single plane is considered leading to a displacement and rotation DOF at each node. These displacements at the root and tip of the cantilever beam element are denoted in Figure 4-1 as v_0 and v_l, respectively, and rotations likewise represented by θ_0 *and* θ_l.

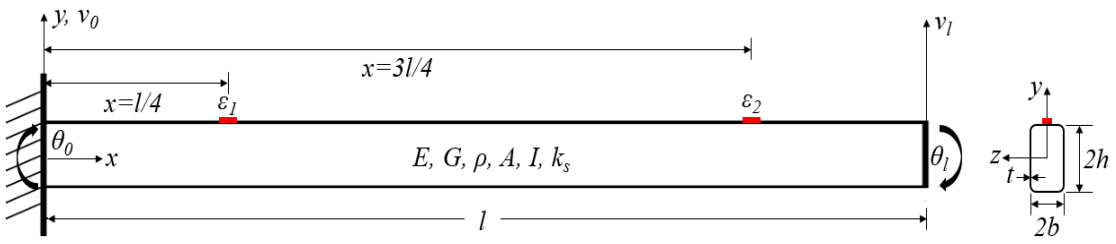

Figure 4-1: Thin-walled composite cantilever beam represented by a single Timoshenko beam element. The diagram on the left shows the span of the beam along with the chosen locations at which the strains have been evaluated. The diagram on the right shows the thin-wall (*t*) cross section of the beam which was used to calculate the section properties.

The system matrices for the beam element were developed using standard Timoshenko beam finite element modeling practices, as shown in Appendix A. Since the auto power spectral density is a real-valued function, two strain locations where defined within the single element to allow the algorithm to utilize real and imaginary components of the PSD in the update procedure. This system is assumed to contain two potential update parameters, bending stiffness (EI) and density (ρ). In this initial implementation it is assumed that the density is known and the single update parameter EI will be solved for. The robustness of the algorithm to correctly identify various levels of damage causing changes in both density and bending stiffness parameters will be discussed in subsequent sections. Throughout the walk-through presented, the analysis was performed to machine precision although only three significant figures are shown.

4.2.1 Baseline (Healthy) System Description

In anticipation of the build up to the experimental testbed, the baseline system properties have been chosen to match those of the experimental setup discussed in Chapter 7. A detailed discussion of the development of the beam's properties is given in Chapter 7 and is not of consequence for the current discussion. The cross section of the beam is uniform and the section properties were calculated using the geometry given in Figure 4-1 and listed in Table 4-1.

Table 4-1: Baseline system parameters

l (in)	b (in)	h (in)	t (in)	A (in^2)	I (in^4)	k_s	E (lb/in^2)	G (lb/in^2)	ρ ($lb\text{-}sec^2/in^4$)
92	0.5	1	0.04	0.2428	0.1336	0.65	4.42E+06	2.90E+06	1.20E-04

Using this single element, the vector of update parameters was formulated in accordance with equation (3-60) as:

$$\{\hat{r}\} = \begin{Bmatrix} \delta_{EIy_1} \\ \delta_{\rho_1} \end{Bmatrix}. \tag{4-1}$$

Using these damage scale factors and the baseline parameters, the system matrices are:

$$[M] = \frac{2.68x10^{-3}\delta_{\rho_1}}{\left(1.83x10^{-3}\delta_{EI_1}+1\right)^2}\begin{bmatrix} \left(1.12x10^{-6}\delta_{EI_1}{}^2+1.28x10^{-3}\delta_{EI_1}+3.72x10^{-1}\right) & \cdots \\ \left(1.28x10^{-5}\delta_{EI_1}{}^2+1.54x10^{-2}\delta_{EI_1}+4.82\right) & \left(1.28x10^{-5}\delta_{EI_1}{}^2+1.54x10^{-2}\delta_{EI_1}+4.82\right) \\ & \left(2.37x10^{-4}\delta_{EI_1}{}^2+2.58x10^{-1}\delta_{EI_1}+80.68\right) \end{bmatrix} \tag{4-2}$$

$$[K] = \frac{1}{\left(1.83x10^{-3}\delta_{EI_1}+1\right)}\begin{bmatrix} 9.11\delta_{EI_1} & -419.1\delta_{EI_1} \\ -419.1\delta_{EI_1} & 6426\delta_{EI_1}\left(1.83x10^{-3}\delta_{EI_1}+4\right) \end{bmatrix} \tag{4-3}$$

The beam damping matrix was developed using experimentally measured values as (see Appendix B for details):

$$[C] = \begin{bmatrix} 1.74x10^{-3} & 1.83x10^{-2} \\ 1.83x10^{-2} & 5.09x10^{-1} \end{bmatrix}. \tag{4-4}$$

Note: In general, the damping matrix can be a function of the structural parameters and allowed to vary within the algorithm. For the duration of the dissertation the damping is assumed to be constant.

The dynamic stiffness matrix, expressed in the displacement domain as a function of frequency and the update parameters, is calculated by substituting equations (4-2), (4-3) and (4-4) into (3-9). The result of this calculation is quite large even for this simple system and thus the details are omitted. In order to compute the underlying PSD matrix in the strain domain, the strain-displacement transformation matrix must be defined for the particular system. As previously mentioned, the strain was evaluated at two locations along the beam's span to allow for calculation of a complex valued PSD and demonstrate the full capabilities of the algorithm. The strain-displacement transformation matrix given in (A-21) is rewritten to reflect the reduced coordinates and parameters present in the current beam model as:

$$\{B_n\}^T = \frac{1}{92\left(1.83x10^{-3}\delta_{EI_1}+1\right)}\begin{Bmatrix}(-6+12\xi)\zeta \\ 92(-2+6\xi+1.83x10^{-3}\delta_{EI_1})\zeta\end{Bmatrix} \tag{4-5}$$

where $\xi = x/l$ and $\zeta = y/l$.

This transformation matrix was evaluated at two distinct locations within the beam's cross section as given in Table 4-2.

Table 4-2: Evaluated strain locations on the beam.

x_1 (in)	y_1 (in)	x_2 (in)	y_2 (in)
23.00	1.00	69.00	1.00

Stacking each of these strain locations row-wise yields a strain-displacement transformation matrix of size 2x2 given in terms of the update parameters as:

$$[B]=\begin{bmatrix} \dfrac{-5.16}{\left(26.60\delta_{EI_1}+1.46x10^4\right)} & \dfrac{\left(5.33\delta_{EI_1}-1.46x10^3\right)}{\left(4.90x10^2\delta_{EI_1}+2.68x10^5\right)} \\ \dfrac{5.16}{\left(26.60\delta_{EI_1}+1.46x10^4\right)} & \dfrac{\left(5.33\delta_{EI_1}+7.28x10^3\right)}{\left(4.90x10^2\delta_{EI_1}+2.68x10^5\right)} \end{bmatrix} \tag{4-6}$$

Lastly, recognizing that in the baseline (healthy) system description the damage scale factors serving as the update parameters are equal to 1, i.e. $\delta_{EI_1}\to 1 \quad and \quad \delta_{\rho_1}\to 1$, allows for the calculation of the baseline PSD matrix in the strain domain. Using equation (3-14) and (A-24) in conjunction with (4-2) through (4-6) allows for the calculation of the PSD as a function of frequency. Assuming a uniform white noise excitation, acting independently on each degree of freedom, the input force PSD was chosen as:

$$\left[S_{ff}\right]=\begin{bmatrix} 1 & 0 \\ 0 & 1 \end{bmatrix}. \tag{4-7}$$

Plotting the resulting baseline PSD as a function of frequency yields:

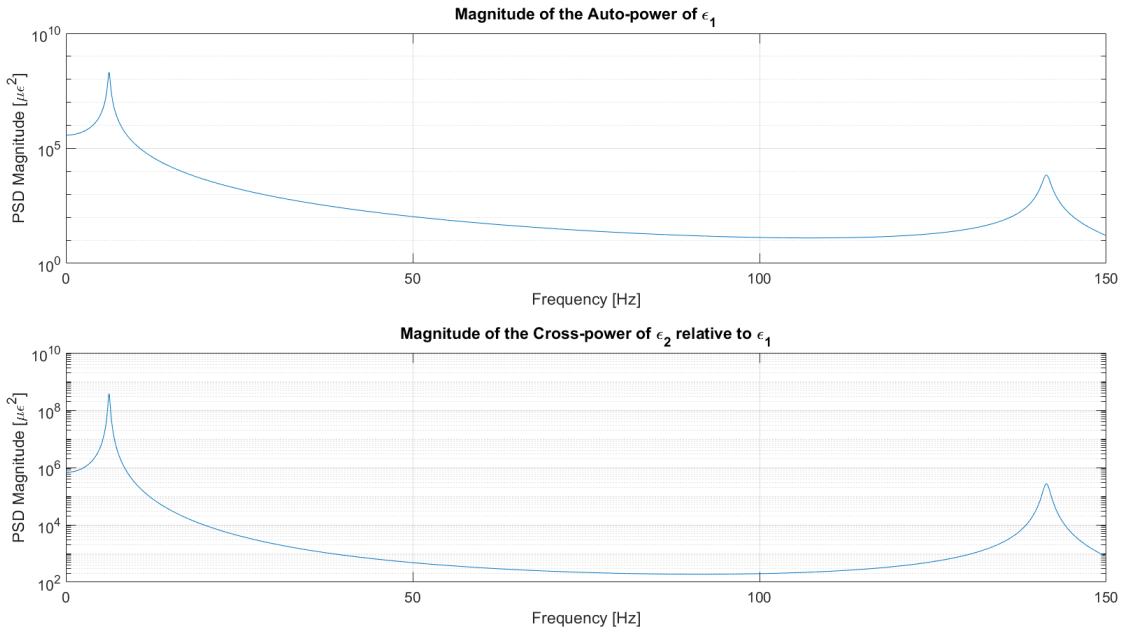

Figure 4-2: Baseline power spectral density for the system shown in Figure 4-1.

The upper plot in Figure 4-2 represents the auto power spectral density of strain location one calculated with respect to itself. The lower plot represents the response at strain location two relative to location one. It is observed that the magnitude of the response for the second mode is several orders of magnitude lower than the first mode. For the sake of a clear and concise example, the information related to the second mode will be neglected and the frequency range will be limited to 0Hz to 10Hz. With that in mind, the current walk through can be thought of as a lower bound in terms of performance with the recognition that in more complex systems all available information will be utilized. Figure 4-3 shows the real and imaginary components of the plots of Figure 4-2 over this restricted frequency domain.

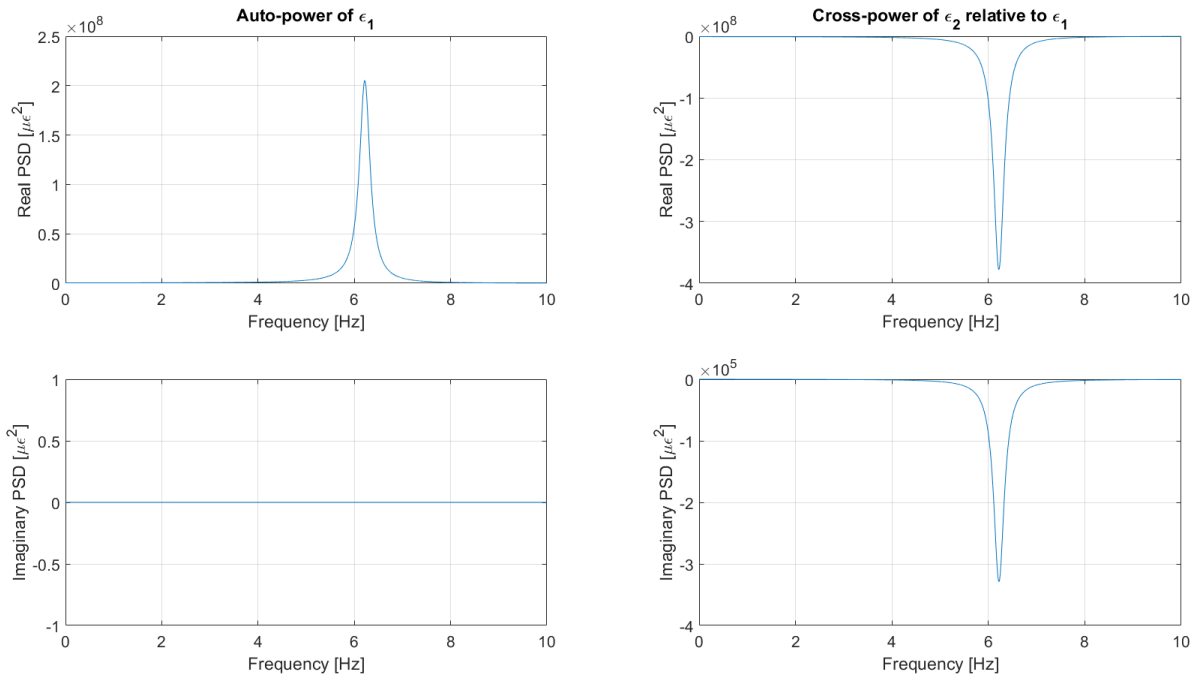

Figure 4-3: Baseline power spectral density for the system shown in Figure 4-1.

In order to implement the algorithm, the initial damage scale factor covariance matrix and residual error covariance matrix must be assigned. In the case of the initial damage scale factor covariance matrix, the variance of the parameters must be estimated using prior information or engineering judgement. In the current walk-through it is assumed that the initial parameters are statistically independent and their standard deviations are equal to ten percent of their initial values $\left(S_{rr} = (0.10)^2 = 0.01\right)$:

$$\left[S_{r_o r_o}\right] = \begin{bmatrix} 0.01 & 0 \\ 0 & 0.01 \end{bmatrix}. \tag{4-8}$$

In regards to the residual error covariance matrix, it was shown in Chapter 3 that the residual error covariance is equal to the measurement noise covariance. To this end, it is currently assumed that the standard deviation of the measurement data is equal to 0.01% of the root-mean-

square averaged over the chosen frequency lines. This is a reasonable approximation because the frequency lines chosen will be in areas of high coherence which undoubtedly will correspond to areas of high signal-to-noise ratios. Since under this formulation of the residual error covariance obviously depends on the chosen frequency lines, the residual error covariance matrix will be given in the appropriate sections of the dissertation.

Although not used in the algorithm operation, the normal (undamped) modes of the baseline system were calculated yielding the first two frequencies and mode shapes of the single element beam in the baseline configuration. Carrying out the eigenvalue calculation on the mass and stiffness matrices yields the system's natural frequencies as:

$$\begin{aligned} \omega_1 &= 6.22 Hz \\ \omega_2 &= 141.37 Hz \end{aligned} \tag{4-9}$$

and the undamped mode shapes can be found from the eigenvectors to be:

$$\begin{aligned} \{\phi_1\} &= \begin{Bmatrix} 1 \\ 0.0173 \end{Bmatrix} \\ \{\phi_2\} &= \begin{Bmatrix} 1 \\ -0.0732 \end{Bmatrix} \end{aligned} . \tag{4-10}$$

4.2.2Damaged System Description

With the baseline (healthy) system defined, the data associated with the damaged configuration is simulated by varying the damage scale factors (while assuming unknown within the algorithm). For the initial algorithm walk through, only the bending stiffness is allowed to vary and the density is assumed to be fixed. Subsequent sections will relax this assumption. For the current damage case, the parameters and strain locations given for the baseline system in Table

4-1 are used with a damaged bending stiffness set to 90 percent, i.e. $\delta_{EI_1} = 0.9 \quad and \quad \delta_{\rho_1} = 1$. Utilizing the same input force PSD given in (4-7), the damaged PSD is plotted as a function of frequency as shown in Figure 4-4.

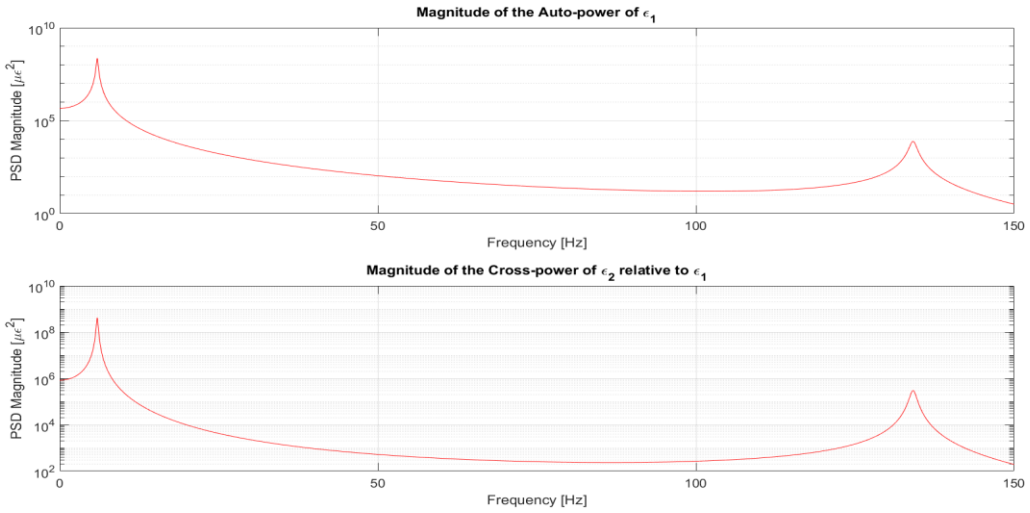

Figure 4-4: Power spectral density for the damaged system shown in Figure 4-1.

The upper plot in Figure 4-4 represents the auto power spectral density of strain location one calculated with respect to itself. The lower plot represents the cross-power spectra of the response at strain location two relative to location one. As with the baseline PSD discussed in section 4.2.1, the second mode is being omitted from the analysis and the frequency range limited from 0Hz to 10Hz. Decomposing the magnitude plots in Figure 4-4 into their real and imaginary components yields the plots given in Figure 4-5 over the restricted domain.

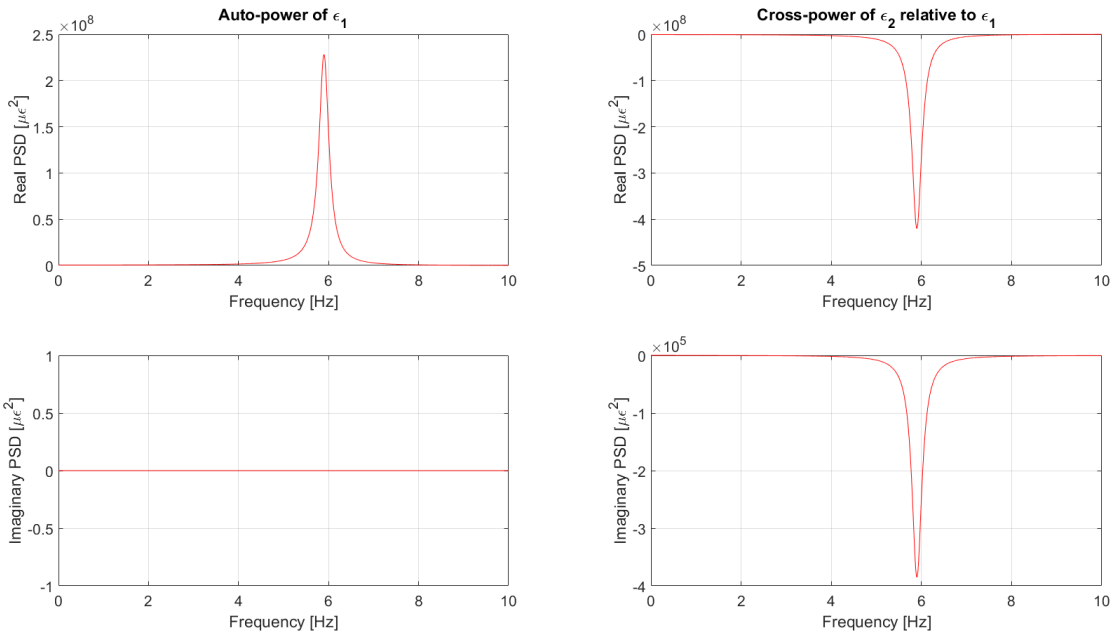

Figure 4-5: Power spectral density for the damaged system shown in Figure 4-1.

Performing a normal modal analysis of the damaged system yields the first two undamped natural frequencies and mode shapes of the single element beam. Carrying out the eigenvalue calculation on the mass and stiffness matrices yields the system frequencies to be:

$$\begin{aligned} \omega_1 &= 5.90 Hz \\ \omega_2 &= 134.13 Hz \end{aligned} \tag{4-11}$$

and the corresponding undamped mode shapes are:

$$\begin{aligned} \{\phi_1\} &= \begin{Bmatrix} 1 \\ 0.0173 \end{Bmatrix} \\ \{\phi_2\} &= \begin{Bmatrix} -1 \\ 0.0732 \end{Bmatrix} \end{aligned}. \tag{4-12}$$

Thus, the current damage case has caused a reduction in the undamped natural frequencies of 5.13% and 5.12%, respectively. The effects of damage on the mode shapes is negligible for these first two modes.

4.2.3 Step-by-Step Implementation

With the healthy and damaged systems described a basic implementation of the algorithm is performed. For this basic implementation all of the steps given in Section 4.1 are explicitly stated to allow the reader to follow the analysis. This basic implementation is procedurally exactly the same as the more complex systems studied in the remainder of this chapter and the dissertation as a whole.

In practice, before implementation of the algorithm would commence a model of the baseline structure will have already been developed and correlated, referred to herein as the "healthy" configuration. After this correlation has been completed and the model response matches the measured response of the baseline structure it is assumed some event occurs which has caused a change in the system response, as measured by the continually monitoring SHM system. This new set of measurements, which show a change in the structure's behavior, are recorded and denoted the "damaged" response. A plot of the modeled healthy response and "measured" damage responses are given in Figure 4-6. This modeled and measured PSD serve as the fundamental inputs to the damage detection algorithm.

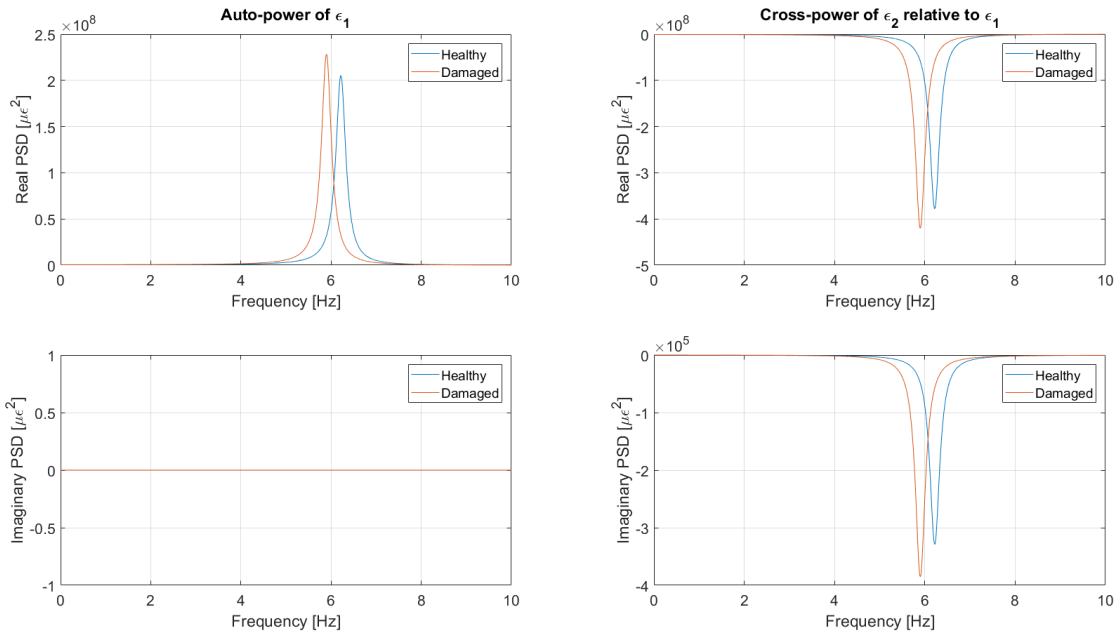

Figure 4-6: Overlay of the healthy system response model and damage system response measurement.

In order for the algorithm to begin, a set of frequency lines at which to perform the initial PSD sampling and residual error calculations must be defined. It is recommended that at least one frequency line be selected on each of the healthy and damaged PSD peaks. It is further suggested that no frequency lines are chosen which lie in between the two peaks as previously discussed. As the algorithm progresses through iterations the frequency line(s) corresponding to the model equations are updated each time the linearization point is updated and thus some of these initial frequency lines will change over the course of the algorithm's iterations. A thorough discussion of frequency line selection and updating is given in Section 3.9 and the reader is referred there for a detailed explanation. For brevity, in the present example where all of the terms are explicitly written out, the minimum of two frequency lines were selected. These two frequencies at this point were chosen somewhat arbitrarily to correspond to half the magnitude of each of the respective PSD peaks. For the current system parameters these frequencies correspond to 5.76Hz for the

damaged PSD and 6.35Hz for the model PSD. The plots in Figure 4-6 are repeated in Figure 4-7 over a narrower frequency range with the inclusion of the selected frequency lines, referred to synonymously as “analysis lines”.

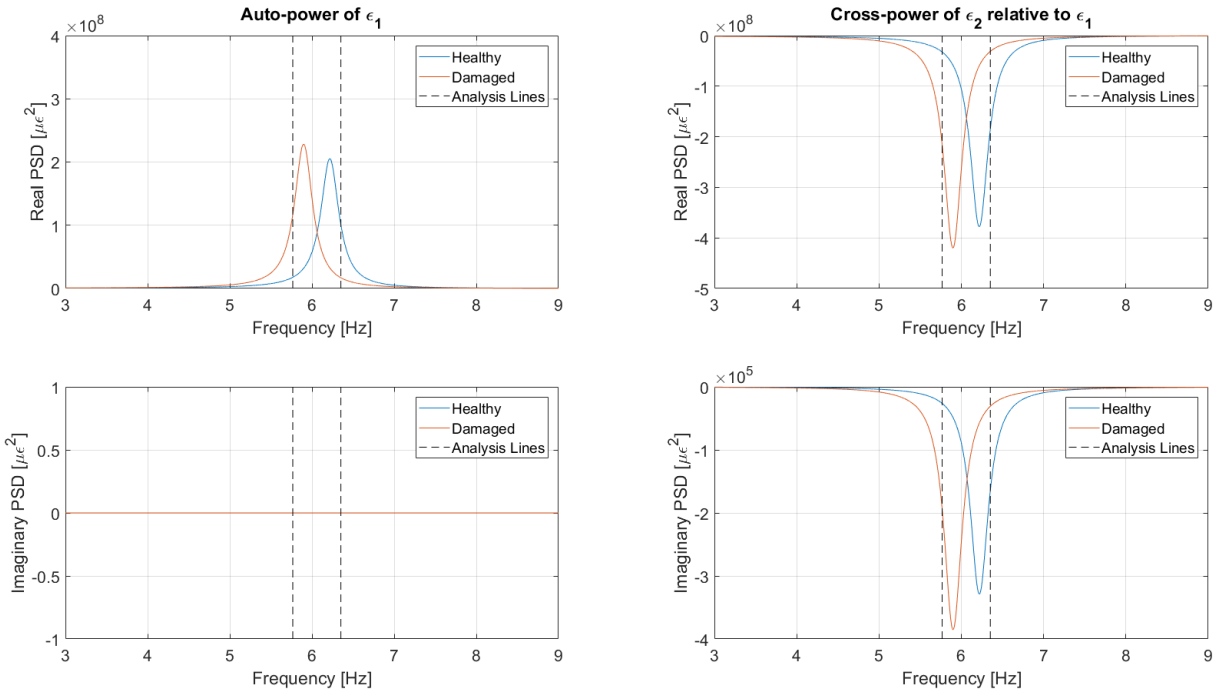

Figure 4-7: Overlay of the healthy system’s modeled response and damaged system’s measured response as well as the two analysis frequency lines chosen for this demonstration.

The algorithm is run until a set of predefined stopping criteria are met. These stopping criteria are currently set such that the change in the update parameters is less than 0.01% of their initial values, i.e.:

$$\Delta \hat{r}_{j+1} < \frac{0.01\left(mean\left(\{\hat{r}_o\}\right)\right)}{100}$$

and the two-norm of the error between the healthy and damaged PSD, evaluated at the chosen frequency lines for the current iteration, must be less the 0.01% of the mean value of the model PSD evaluated at the initial parameter set, i.e.:

$$Error_{j+1} < \frac{0.01\left(mean\left(\left\{W\left(\hat{r}_o\right)\right\}\right)\right)}{100}.$$

Algorithm Inputs:

- Initial damage scale factor:

$$\left\{\hat{r}_o\right\} = \left\{1\right\}$$

- System matrices as a function of update parameter (restated from equations (4-2) thru (4-4) in terms of the update parameters $\hat{r}$) :

$$\left[M\left(\hat{r}\right)\right] = \frac{2.68x10^{-3}}{\left(1.83x10^{-3}\hat{r}+1\right)^2}\begin{bmatrix}\left(1.12x10^{-6}\hat{r}^2+1.28x10^{-3}\hat{r}+3.72x10^{-1}\right) & \left(1.28x10^{-5}\hat{r}^2+1.54x10^{-2}\hat{r}+4.82\right) \\ \left(1.28x10^{-5}\hat{r}^2+1.54x10^{-2}\hat{r}+4.82\right) & \left(2.37x10^{-4}\hat{r}^2+2.58x10^{-1}\hat{r}+80.68\right)\end{bmatrix} \quad \ldots$$

$$\left[K(\hat{r})\right] = \frac{1}{\left(1.83x10^{-3}\hat{r}+1\right)}\begin{bmatrix} 9.11\hat{r} & -419.1\hat{r} \\ -419.1\hat{r} & 6426\hat{r}\left(1.83x10^{-3}\hat{r}+4\right)\end{bmatrix}$$

$$\left[C(\hat{r})\right] = \begin{bmatrix}1.74x10^{-3} & 1.83x10^{-2} \\ 1.83x10^{-2} & 5.09x10^{-1}\end{bmatrix}$$

- Strain-displacement transformation matrix as a function of update parameter (from equation (4-5)):

$$\left[B(\hat{r})\right] = \begin{bmatrix} \dfrac{-5.16}{\left(2.66x10^{1}\hat{r} + 1.46x10^{4}\right)} & \dfrac{\left(5.33\hat{r} - 1.46x10^{3}\right)}{\left(4.90x10^{2}\hat{r} + 2.68x10^{5}\right)} \\ \dfrac{5.16}{\left(2.66x10^{1}\hat{r} + 1.46x10^{4}\right)} & \dfrac{\left(5.33\hat{r} + 1.46x10^{3}\right)}{\left(4.90x10^{2}\hat{r} + 2.68x10^{5}\right)} \end{bmatrix}$$

- Choice of reference degree of freedom:

$$i = 1$$

- Initial damage scale factor covariance matrix:

$$\left[S_{r_o r_o}\right] = \left[0.01\right]$$

- Set of initial frequency lines:

$$\left\{\omega_{k_o}\right\} = \begin{Bmatrix} 5.76 \\ 6.35 \end{Bmatrix} Hz = \begin{Bmatrix} 36.20 \\ 39.90 \end{Bmatrix} rad/sec$$

Iteration One (j=0):

- Generate model PSD evaluated at current set of update parameters and frequencies lines using (A-23) and (3-22):

$$\left[W\left(\omega = 36.20 rad/sec\right)\right]_o = \begin{bmatrix} 1.74x10^7 + 0i & -3.19x10^7 + 2.58x10^4 i \\ -3.19x10^7 - 2.58x10^4 i & 5.86x10^7 + 0i \end{bmatrix}$$

$$\left[W\left(\omega = 39.90 rad/sec\right)\right]_o = \begin{bmatrix} 1.02x10^8 + 0i & -1.88x10^8 + 1.67x10^5 i \\ -1.88x10^8 - 1.67x10^5 i & 3.47x10^8 + 0i \end{bmatrix}$$

- Extract measured PSD values at current set of frequencies lines:

$$\left[\tilde{S}_{\varepsilon\varepsilon}\left(\omega = 36.20 rad/sec\right)\right]_o = \begin{bmatrix} 1.13x10^8 + 0i & -2.09x10^8 + 1.87x10^5 i \\ -2.09x10^8 - 1.87x10^5 i & 3.83x10^8 + 0i \end{bmatrix}$$

$$\left[\tilde{S}_{\varepsilon\varepsilon}\left(\omega = 39.90 rad/sec\right)\right]_o = \begin{bmatrix} 1.71x10^7 + 0i & -3.15x10^7 + 3.11x10^4 i \\ -3.15x10^7 - 3.11x10^4 i & 5.82x10^7 + 0i \end{bmatrix}$$

- Generate the batch-stacked model PSD vector:

$$\left\{\underline{W}\right\}_o = \begin{Bmatrix} 1.74x10^7 \\ -3.17x10^7 \\ -2.58x10^4 \\ 1.02x10^8 \\ -1.88x10^8 \\ -1.67x10^5 \end{Bmatrix}$$

Note that the zero values corresponding to the imaginary portion of the auto-power spectra have been removed from the batch-stacking to allow for the inversion of the residual error covariance matrix, as discussed in Chapter 3.

- Generate the batch-stacked measured PSD vector:

$$\left\{\underline{\tilde{S}}\right\}_o = \begin{Bmatrix} 1.13x10^{8} \\ -2.09x10^{8} \\ -1.87x10^{5} \\ 1.71x10^{7} \\ -3.15x10^{7} \\ -3.11x10^{4} \end{Bmatrix}$$

- Compute the batch-stacked parameter sensitivity matrix using a second order central difference approximation of uniform step +/- $1x10^{-6}$:

$$\left[\frac{\partial \underline{W}_o(\hat{r})}{\partial \hat{r}}\right] = \begin{bmatrix} -2.28x10^{8} \\ 4.18x10^{8} \\ 3.63x10^{5} \\ 2.33x10^{9} \\ -4.29x10^{9} \\ -3.65x10^{6} \end{bmatrix}$$

- Calculate residual error covariance matrix using frequency line set:

$$[S_{RR}] = \begin{bmatrix} 6.58x10^{7} & 0 & 0 & 0 & 0 & 0 \\ 0 & 2.22x10^{8} & 0 & 0 & 0 & 0 \\ 0 & 0 & 179.68 & 0 & 0 & 0 \\ 0 & 0 & 0 & 6.58x10^{7} & 0 & 0 \\ 0 & 0 & 0 & 0 & 2.22x10^{8} & 0 \\ 0 & 0 & 0 & 0 & 0 & 179.68 \end{bmatrix}$$

- Generate the posterior value of $[Q]_{j+1}$ using (3-66):

$$[Q]_1 = \left[4.14x10^{-12}\right]$$

- Calculate the updated value of the damage parameter set using (3-67):

$$\{\hat{r}_1\} = \{0.959\}$$

- Calculate the change in $\{\hat{r}\}$ and the residual error at the current iteration:

$$\Delta\hat{r} = \max\left(abs\left(\{\hat{r}_1\} - \{\hat{r}_o\}\right)\right) = \max\left(abs\left(0.959 - 1\right)\right) = 0.041$$

$$Error = norm_2\left(\left\{\underline{\tilde{S}}\right\}_o - \left\{\underline{W}\right\}_o\right) = norm_2\left(\begin{Bmatrix} 1.13x10^8 \\ -2.09x10^8 \\ -1.87x10^5 \\ 1.71x10^7 \\ -3.15x10^7 \\ -3.11x10^4 \end{Bmatrix} - \begin{Bmatrix} 1.74x10^7 \\ -3.17x10^7 \\ -2.58x10^4 \\ 1.02x10^8 \\ -1.88x10^8 \\ -1.67x10^5 \end{Bmatrix}\right) = 2.69x10^8$$

- Check for convergence:

$$\left(\Delta\hat{r}_1 = 0.041\right) > 1x10^{-4}$$

and

$$\left(Error_1 = 2.69x10^8\right) > 117.82$$

Where the value of the error convergence criteria was determined as the mean value of the model PSD evaluated at the initial parameter set over the frequency range of 0Hz to 10Hz.

$\rightarrow$ Solution has not converged, increment j and repeat iteration procedure

Iteration Two (j=1):

- Identify the half magnitude frequency lines using the updated model PSD:

$$\left\{\omega_{k_1}\right\} = \begin{Bmatrix} 5.76 \\ 6.22 \end{Bmatrix} Hz = \begin{Bmatrix} 36.20 \\ 39.09 \end{Bmatrix} rad/sec$$

- Generate model PSD evaluated at current set of update parameters and frequencies lines using (A-23) and (3-22):

$$\left[W\left(\omega = 36.20 rad/sec\right)\right]_1 = \begin{bmatrix} 3.19x10^7 + 0i & -5.85x10^7 + 4.93x10^4 i \\ -5.85x10^7 - 4.93x10^4 i & 1.07x10^8 + 0i \end{bmatrix}$$

$$\left[W\left(\omega = 39.09 rad/sec\right)\right]_1 = \begin{bmatrix} 1.07x10^8 + 0i & -1.97x10^8 + 1.79x10^5 i \\ -1.97x10^8 - 1.79x10^5 i & 3.64x10^8 + 0i \end{bmatrix}$$

- Extract measured PSD values at current set of frequencies lines:

$$\left[\tilde{S}_{\varepsilon\varepsilon}\left(\omega = 36.20 rad/sec\right)\right]_1 = \begin{bmatrix} 1.13x10^8 + 0i & -2.09x10^8 + 1.87x10^5 i \\ -2.09x10^8 - 1.87x10^5 i & 3.83x10^8 + 0i \end{bmatrix}$$

$$\left[\tilde{S}_{\varepsilon\varepsilon}\left(\omega = 39.09 rad/sec\right)\right]_1 = \begin{bmatrix} 3.16x10^7 + 0i & -5.84x10^7 + 5.64x10^4 i \\ -5.84x10^7 - 5.64x10^4 i & 1.08x10^8 + 0i \end{bmatrix}$$

- Generate the batch-stacked model PSD vector:

$$\left\{\underline{W}\right\}_1 = \begin{Bmatrix} 3.19x10^7 \\ -5.85x10^7 \\ -4.93x10^4 \\ 1.07x10^8 \\ -1.97x10^8 \\ -1.79x10^5 \end{Bmatrix}$$

- Generate the batch-stacked measured PSD vector:

$$\left\{\underline{\tilde{S}}\right\}_1 = \begin{Bmatrix} 1.13x10^{8} \\ -2.09x10^{8} \\ -1.87x10^{5} \\ 3.16x10^{7} \\ -5.84x10^{7} \\ -5.64x10^{4} \end{Bmatrix}$$

- Compute the batch-stacked parameter sensitivity matrix using a second order central difference approximation of uniform step +/- $1x10^{-6}$:

$$\left[\frac{\partial \underline{W}_1(\hat{r})}{\partial \hat{r}}\right] = \begin{bmatrix} -5.46x10^{8} \\ 1.00x10^{9} \\ 8.95x10^{5} \\ 2.49x10^{9} \\ -4.59x10^{9} \\ -3.98x10^{6} \end{bmatrix}$$

- Calculate residual error covariance matrix using frequency line set:

$$\left[S_{RR}\right]_1 = \begin{bmatrix} 6.93x10^{7} & 0 & 0 & 0 & 0 & 0 \\ 0 & 2.34x10^{8} & 0 & 0 & 0 & 0 \\ 0 & 0 & 190.75 & 0 & 0 & 0 \\ 0 & 0 & 0 & 6.94x10^{7} & 0 & 0 \\ 0 & 0 & 0 & 0 & 2.34x10^{8} & 0 \\ 0 & 0 & 0 & 0 & 0 & 190.75 \end{bmatrix}$$

- Generate the posterior value of $[Q]_{j+1}$ using (3-66):

$$[Q]_2 = \left[3.63x10^{-12}\right]$$

- Calculate the updated value of the damage parameter set using (3-67):

$$\{\hat{r}_2\} = \{0.923\}$$

- Calculate the change in $\hat{r}$ and the residual error at the current iteration:

$$\Delta\hat{r}_2 = \max\left(abs\left(\hat{r}_2 - \hat{r}_1\right)\right) = \max\left(abs\left(0.923 - 0.959\right)\right) = 0.036$$

$$Error_2 = norm_2\left(\left\{\underline{\tilde{S}}\right\}_1 - \left\{\underline{W}\right\}_1\right) = norm_2\left(\begin{Bmatrix} 1.13x10^8 \\ -2.09x10^8 \\ -1.87x10^5 \\ 3.16x10^7 \\ -5.84x10^7 \\ -5.64x10^4 \end{Bmatrix} - \begin{Bmatrix} 3.19x10^7 \\ -5.85x10^7 \\ -4.93x10^4 \\ 1.07x10^8 \\ -1.97x10^8 \\ -1.79x10^5 \end{Bmatrix}\right) = 2.33x10^8$$

- Check for convergence:

$$\left(\Delta\hat{r}_2 = 0.036\right) > 1x10^{-4}$$

and

$$\left(Error_2 = 2.33x10^8\right) > 117.82$$

$\rightarrow$ Solution has not converged, increment j and repeat iteration procedure

Iteration Three (j=2):

- Identify the half magnitude frequency lines using the updated model PSD:

$$\left\{\omega_{k_2}\right\} = \begin{Bmatrix} 5.76 \\ 6.11 \end{Bmatrix} Hz = \begin{Bmatrix} 36.20 \\ 38.37 \end{Bmatrix} rad/sec$$

- Generate model PSD evaluated at current set of update parameters and frequencies lines using (A-23) and (3-22):

$$\left[W\left(\omega = 36.20 rad/sec\right)\right]_2 = \begin{bmatrix} 6.47x10^7 + 0i & -1.19x10^8 + 1.04x10^5 i \\ -1.19x10^8 - 1.04x10^5 i & 2.18x10^8 + 0i \end{bmatrix}$$

$$\left[W\left(\omega = 38.37 rad/sec\right)\right]_2 = \begin{bmatrix} 1.11x10^8 + 0i & -2.05x10^8 + 1.90x10^5 i \\ -2.05x10^8 - 1.90x10^5 i & 3.78x10^8 + 0i \end{bmatrix}$$

- Extract measured PSD values at current set of frequencies lines:

$$\left[\tilde{S}_{\varepsilon\varepsilon}\left(\omega = 36.20 rad/sec\right)\right]_2 = \begin{bmatrix} 1.13x10^8 + 0i & -2.09x10^8 + 1.87x10^5 i \\ -2.09x10^8 - 1.87x10^5 i & 3.83x10^8 + 0i \end{bmatrix}$$

$$\left[\tilde{S}_{\varepsilon\varepsilon}\left(\omega = 38.37 rad/sec\right)\right]_2 = \begin{bmatrix} 6.48x10^7 + 0i & -1.20x10^8 + 1.13x10^5 i \\ -1.20x10^8 - 1.13x10^5 i & 2.20x10^8 + 0i \end{bmatrix}$$

- Generate the batch-stacked model PSD vector:

$$\left\{\underline{W}\right\}_2 = \begin{Bmatrix} 6.47x10^7 \\ -1.19x10^8 \\ -1.04x10^5 \\ 1.11x10^8 \\ -2.05x10^8 \\ -1.90x10^5 \end{Bmatrix}$$

- Generate the batch-stacked measured PSD vector:

$$\left\{\underline{\tilde{S}}\right\}_2 = \begin{Bmatrix} 1.13x10^{8} \\ -2.09x10^{8} \\ -1.87x10^{5} \\ 6.48x10^{7} \\ -1.20x10^{8} \\ -1.13x10^{5} \end{Bmatrix}$$

- Compute the batch-stacked parameter sensitivity matrix using a second order central difference approximation of uniform step +/- $1x10^{-6}$:

$$\left[\frac{\partial \underline{W}_2(\hat{r})}{\partial \hat{r}}\right] = \begin{bmatrix} -1.45x10^{9} \\ 2.66x10^{9} \\ 2.44x10^{6} \\ 2.64x10^{9} \\ -4.86x10^{9} \\ -4.29x10^{6} \end{bmatrix}$$

- Calculate residual error covariance matrix using frequency line set:

$$\left[S_{RR}\right]_2 = \begin{bmatrix} 8.54x10^{7} & 0 & 0 & 0 & 0 & 0 \\ 0 & 2.89x10^{8} & 0 & 0 & 0 & 0 \\ 0 & 0 & 239.13 & 0 & 0 & 0 \\ 0 & 0 & 0 & 8.54x10^{7} & 0 & 0 \\ 0 & 0 & 0 & 0 & 2.89x10^{8} & 0 \\ 0 & 0 & 0 & 0 & 0 & 239.13 \end{bmatrix}$$

- Generate the posterior value of $[Q]_{j+1}$ using (3-66):

$$[Q]_3 = \left[3.18x10^{-12}\right]$$

- Calculate the updated value of the damage parameter set using (3-67):

$$\{\hat{r}_3\} = \{0.902\}$$

- Calculate the change in $\hat{r}$ and the residual error at the current iteration:

$$\Delta\hat{r}_3 = \max\left(abs\left(\hat{r}_3 - \hat{r}_2\right)\right) = \max\left(abs\left(0.902 - 0.923\right)\right) = 0.021$$

$$Error_3 = norm_2\left(\left\{\underline{\tilde{S}}\right\}_2 - \left\{\underline{W}\right\}_2\right) = norm_2\left(\begin{Bmatrix} 1.13x10^8 \\ -2.09x10^8 \\ -1.87x10^5 \\ 6.48x10^7 \\ -1.20x10^8 \\ -1.13x10^5 \end{Bmatrix} - \begin{Bmatrix} 6.47x10^7 \\ -1.19x10^8 \\ -1.04x10^5 \\ 1.11x10^8 \\ -2.05x10^8 \\ -1.90x10^5 \end{Bmatrix}\right) = 1.41x10^8$$

- Check for convergence:

$$\left(\Delta\hat{r}_3 = 0.021\right) > 1x10^{-4}$$

and

$$\left(Error_3 = 1.41x10^8\right) > 117.82$$

$\rightarrow$ Solution has not converged, increment j and repeat iteration procedure

Iteration Four (j=3):

- Identify the half magnitude frequency lines using the updated model PSD:

$$\left\{\omega_{k_3}\right\} = \begin{Bmatrix} 5.76 \\ 6.03 \end{Bmatrix} Hz = \begin{Bmatrix} 36.20 \\ 37.93 \end{Bmatrix} rad/sec$$

- Generate model PSD evaluated at current set of update parameters and frequencies lines using (A-23) and (3-22):

$$\left[W\left(\omega = 36.20 rad/sec\right)\right]_3 = \begin{bmatrix} 1.08x10^8 + 0i & -1.99x10^8 + 1.78x10^5 i \\ -1.99x10^8 - 1.78x10^5 i & 3.65x10^8 + 0i \end{bmatrix}$$

$$\left[W\left(\omega = 37.93 rad/sec\right)\right]_3 = \begin{bmatrix} 1.14x10^8 + 0i & -2.10x10^8 + 1.97x10^5 i \\ -2.10x10^8 - 1.97x10^5 i & 3.87x10^8 + 0i \end{bmatrix}$$

- Extract measured PSD values at current set of frequencies lines:

$$\left[\tilde{S}_{\varepsilon\varepsilon}\left(\omega = 36.20 rad/sec\right)\right]_3 = \begin{bmatrix} 1.13x10^8 + 0i & -2.09x10^8 + 1.87x10^5 i \\ -2.09x10^8 - 1.87x10^5 i & 3.83x10^8 + 0i \end{bmatrix}$$

$$\left[\tilde{S}_{\varepsilon\varepsilon}\left(\omega = 37.93 rad/sec\right)\right]_3 = \begin{bmatrix} 1.09x10^8 + 0i & -2.00x10^8 + 1.88x10^5 i \\ -2.00x10^8 - 1.88x10^5 i & 3.69x10^8 + 0i \end{bmatrix}$$

- Generate the batch-stacked model PSD vector:

$$\left\{\underline{W}\right\}_3 = \begin{Bmatrix} 1.08x10^8 \\ -1.99x10^8 \\ -1.78x10^5 \\ 1.14x10^8 \\ -2.10x10^8 \\ -1.97x10^5 \end{Bmatrix}$$

- Generate the batch-stacked measured PSD vector:

$$\left\{\underline{\tilde{S}}\right\}_3 = \begin{Bmatrix} 1.13x10^{8} \\ -2.09x10^{8} \\ -1.87x10^{5} \\ 1.09x10^{8} \\ -2.00x10^{8} \\ -1.88x10^{5} \end{Bmatrix}$$

- Compute the batch-stacked parameter sensitivity matrix using a second order central difference approximation of uniform step +/- $1x10^{-6}$:

$$\left[\frac{\partial \underline{W}_3(\hat{r})}{\partial \hat{r}}\right] = \begin{bmatrix} -2.71x10^{9} \\ 4.98x10^{9} \\ 4.65x10^{6} \\ 2.74x10^{9} \\ -5.03x10^{9} \\ -4.50x10^{6} \end{bmatrix}$$

- Calculate residual error covariance matrix using frequency line set:

$$\left[S_{RR}\right]_3 = \begin{bmatrix} 1.24x10^{8} & 0 & 0 & 0 & 0 & 0 \\ 0 & 4.18x10^{8} & 0 & 0 & 0 & 0 \\ 0 & 0 & 351.70 & 0 & 0 & 0 \\ 0 & 0 & 0 & 1.24x10^{8} & 0 & 0 \\ 0 & 0 & 0 & 0 & 4.18x10^{8} & 0 \\ 0 & 0 & 0 & 0 & 0 & 351.70 \end{bmatrix}$$

- Generate the posterior value of $[Q]_{j+1}$ using (3-66):

$$[Q]_4 = \left[2.79x10^{-12}\right]$$

- Calculate the updated value of the damage parameter set using (3-67):

$$\{\hat{r}_4\} = \{0.899\}$$

- Calculate the change in $\hat{r}$ and the residual error at the current iteration:

$$\Delta\hat{r}_4 = \max\left(abs\left(\hat{r}_4 - \hat{r}_3\right)\right) = \max\left(abs\left(0.899 - 0.902\right)\right) = 0.0019$$

$$Error_4 = norm_2\left(\left\{\underline{\tilde{S}}\right\}_3 - \left\{\underline{W}\right\}_3\right) = norm_2\left(\begin{Bmatrix} 1.13x10^8 \\ -2.09x10^8 \\ -1.87x10^5 \\ 1.09x10^8 \\ -2.00x10^8 \\ -1.88x10^5 \end{Bmatrix} - \begin{Bmatrix} 1.08x10^8 \\ -1.99x10^8 \\ -1.78x10^5 \\ 1.14x10^8 \\ -2.10x10^8 \\ -1.97x10^5 \end{Bmatrix}\right) = 1.58x10^7$$

- Check for convergence:

$$\left(\Delta\hat{r}_4 = 0.0019\right) > 1x10^{-4}$$

and

$$\left(Error_4 = 1.58x10^7\right) > 117.82$$

$\rightarrow$ Solution has not converged, increment j and repeat iteration procedure

Iteration Five (j=4):

- Identify the half magnitude frequency lines using the updated model PSD:

$$\left\{\omega_{k_4}\right\} = \begin{Bmatrix} 5.76 \\ 6.03 \end{Bmatrix} Hz = \begin{Bmatrix} 36.20 \\ 37.93 \end{Bmatrix} rad/sec$$

Note that to the precision shown these frequencies are the same as those given for iteration four. The evaluation of the modeled and measured PSD are carried out to computer precision and the subsequent values given are obtained using the exact frequency lines identified to machine precision.

- Generate model PSD evaluated at current set of update parameters and frequencies lines using (A-23) and (3-22):

$$\left[W\left(\omega = 36.20 rad/sec\right)\right]_4 = \begin{bmatrix} 1.13x10^8 + 0i & -2.09x10^8 + 1.87x10^5 i \\ -2.09x10^8 - 1.87x10^5 i & 3.83x10^8 + 0i \end{bmatrix}$$

$$\left[W\left(\omega = 37.93 rad/sec\right)\right]_4 = \begin{bmatrix} 1.14x10^8 + 0i & -2.11x10^8 + 1.97x10^5 i \\ -2.11x10^8 - 1.97x10^5 i & 3.88x10^8 + 0i \end{bmatrix}$$

- Extract measured PSD values at current set of frequencies lines:

$$\left[\tilde{S}_{\varepsilon\varepsilon}\left(\omega = 36.20 rad/sec\right)\right]_4 = \begin{bmatrix} 1.13x10^8 + 0i & -2.09x10^8 + 1.87x10^5 i \\ -2.09x10^8 - 1.87x10^5 i & 3.83x10^8 + 0i \end{bmatrix}$$

$$\left[\tilde{S}_{\varepsilon\varepsilon}\left(\omega = 37.93 rad/sec\right)\right]_4 = \begin{bmatrix} 1.14x10^8 + 0i & -2.09x10^8 + 1.87x10^5 i \\ -2.09x10^8 - 1.87x10^5 i & 3.88x10^8 + 0i \end{bmatrix}$$

- Generate the batch-stacked model PSD vector:

$$\{\underline{W}\}_4 = \begin{Bmatrix} 1.13x10^{8} \\ -2.09x10^{8} \\ -1.87x10^{5} \\ 1.14x10^{8} \\ -2.11x10^{8} \\ -1.97x10^{5} \end{Bmatrix}$$

- Generate the batch-stacked measured PSD vector:

$$\{\underline{\tilde{S}}\}_4 = \begin{Bmatrix} 1.13x10^{8} \\ -2.09x10^{8} \\ -1.87x10^{5} \\ 1.14x10^{8} \\ -2.11x10^{8} \\ -1.97x10^{5} \end{Bmatrix}$$

- Compute the batch-stacked parameter sensitivity matrix using a second order central difference approximation of uniform step +/- $1x10^{-6}$:

$$\left[\frac{\partial \underline{W}_4(\hat{r})}{\partial \hat{r}}\right] = \begin{bmatrix} -2.85x10^{9} \\ 5.25x10^{9} \\ 4.91x10^{6} \\ 2.74x10^{9} \\ -5.05x10^{9} \\ -4.52x10^{6} \end{bmatrix}$$

- Calculate residual error covariance matrix using frequency line set:

$$[S_{RR}]_4 = \begin{bmatrix} 1.30x10^8 & 0 & 0 & 0 & 0 & 0 \\ 0 & 4.39x10^8 & 0 & 0 & 0 & 0 \\ 0 & 0 & 369.51 & 0 & 0 & 0 \\ 0 & 0 & 0 & 1.30x10^8 & 0 & 0 \\ 0 & 0 & 0 & 0 & 4.39x10^8 & 0 \\ 0 & 0 & 0 & 0 & 0 & 369.51 \end{bmatrix}$$

- Generate the posterior value of $[Q]_{j+1}$ using (3-66):

$$[Q]_5 = \left[2.76x10^{-12} \right]$$

- Calculate the updated value of the damage parameter set using (3-67):

$$\{\hat{r}_5\} = \{0.900\}$$

- Calculate the change in $\hat{r}$ and the residual error at the current iteration:

$$\Delta\hat{r}_5 = \max\left(abs\left(\hat{r}_5 - \hat{r}_4\right)\right) = \max\left(abs\left(0.900 - 0.899\right)\right) = 5.23x10^{-6}$$

$$Error_5 = norm_2\left(\left\{\underline{\tilde{S}}\right\}_4 - \left\{\underline{W}\right\}_4\right) = norm_2\left(\begin{Bmatrix} 1.13x10^8 \\ -2.09x10^8 \\ -1.87x10^5 \\ 1.14x10^8 \\ -2.11x10^8 \\ -1.97x10^5 \end{Bmatrix} - \begin{Bmatrix} 1.13x10^8 \\ -2.09x10^8 \\ -1.87x10^5 \\ 1.14x10^8 \\ -2.11x10^8 \\ -1.97x10^5 \end{Bmatrix}\right) = 4.34x10^4$$

- Check for convergence:

$$\left(\Delta\hat{r}_5 = 5.23x10^{-6}\right) < 1x10^{-4}$$

and

$$\left(Error_5 = 4.34x10^{4}\right) > 117.82$$

$\rightarrow$ Solution has not converged, increment j and repeat iteration procedure

Note that although the criteria for $\Delta\hat{r}$ has been met, the error criteria has not been satisfied and thus iterations continue.

Iteration Six (j=5):

- Identify the half magnitude frequency lines using the updated model PSD:

$$\left\{\omega_{k_5}\right\} = \begin{Bmatrix} 5.76 \\ 6.03 \end{Bmatrix} Hz = \begin{Bmatrix} 36.20 \\ 37.93 \end{Bmatrix} rad/sec$$

Note that to the precision shown these frequencies are the same as those given for iteration five. The evaluation of the modeled and measured PSD are carried out to computer precision and the subsequent values given are obtained using the exact frequency lines identified to machine precision.

- Generate model PSD evaluated at current set of update parameters and frequencies lines using (A-23) and (3-22):

$$\left[W\left(\omega = 36.20 rad/sec\right)\right]_5 = \begin{bmatrix} 1.13x10^8 + 0i & -2.09x10^8 + 1.87x10^5 i \\ -2.09x10^8 - 1.87x10^5 i & 3.83x10^8 + 0i \end{bmatrix}$$

$$\left[W\left(\omega = 37.93 rad/sec\right)\right]_5 = \begin{bmatrix} 1.14x10^8 + 0i & -2.11x10^8 + 1.97x10^5 i \\ -2.11x10^8 - 1.97x10^5 i & 3.88x10^8 + 0i \end{bmatrix}$$

- Extract measured PSD values at current set of frequencies lines:

$$\left[\tilde{S}_{\varepsilon\varepsilon}\left(\omega = 36.20 rad/sec\right)\right]_5 = \begin{bmatrix} 1.13x10^8 + 0i & -2.09x10^8 + 1.87x10^5 i \\ -2.09x10^8 - 1.87x10^5 i & 3.83x10^8 + 0i \end{bmatrix}$$

$$\left[\tilde{S}_{\varepsilon\varepsilon}\left(\omega = 37.93 rad/sec\right)\right]_5 = \begin{bmatrix} 1.14x10^8 + 0i & -2.09x10^8 + 1.87x10^5 i \\ -2.09x10^8 - 1.87x10^5 i & 3.88x10^8 + 0i \end{bmatrix}$$

- Generate the batch-stacked model PSD vector:

$$\left\{\underline{W}\right\}_5 = \begin{Bmatrix} 1.13x10^8 \\ -2.09x10^8 \\ -1.87x10^5 \\ 1.14x10^8 \\ -2.11x10^8 \\ -1.97x10^5 \end{Bmatrix}$$

- Generate the batch-stacked measured PSD vector:

$$\left\{\underline{\tilde{S}}\right\}_5 = \begin{Bmatrix} 1.13x10^8 \\ -2.09x10^8 \\ -1.87x10^5 \\ 1.14x10^8 \\ -2.11x10^8 \\ -1.97x10^5 \end{Bmatrix}$$

- Compute the batch-stacked parameter sensitivity matrix using a second order central difference approximation of uniform step +/- $1x10^{-6}$:

$$\left[\frac{\partial \underline{W}_5(\hat{r})}{\partial \hat{r}}\right] = \begin{bmatrix} -2.85x10^{9} \\ 5.25x10^{9} \\ 4.91x10^{6} \\ 2.74x10^{9} \\ -5.05x10^{9} \\ -4.52x10^{6} \end{bmatrix}$$

- Calculate residual error covariance matrix using frequency line set:

$$[S_{RR}]_5 = \begin{bmatrix} 1.30x10^{8} & 0 & 0 & 0 & 0 & 0 \\ 0 & 4.39x10^{8} & 0 & 0 & 0 & 0 \\ 0 & 0 & 369.51 & 0 & 0 & 0 \\ 0 & 0 & 0 & 1.30x10^{8} & 0 & 0 \\ 0 & 0 & 0 & 0 & 4.39x10^{8} & 0 \\ 0 & 0 & 0 & 0 & 0 & 369.51 \end{bmatrix}$$

- Generate the posterior value of $[Q]_{j+1}$ using (3-66):

$$[Q]_6 = \left[2.76x10^{-12}\right]$$

- Calculate the updated value of the damage parameter set using (3-67):

$$\{\hat{r}_6\} = \{0.900\}$$

- Calculate the change in $\hat{r}$ and the residual error at the current iteration:

$$\left(\Delta\hat{r}_6 = 4.72x10^{-11}\right) < 1x10^{-4}\ \Delta\hat{r}_6 = \max\left(abs\left(\hat{r}_6 - \hat{r}_5\right)\right) = \max\left(abs\left(0.900 - 0.900\right)\right) = 4.72x10^{-11}$$

$$Error_6 = norm_2\left(\left\{\underline{\tilde{S}}\right\}_5 - \left\{\underline{W}\right\}_5\right) = norm_2\left(\begin{Bmatrix} 1.13x10^8 \\ -2.09x10^8 \\ -1.87x10^5 \\ 1.14x10^8 \\ -2.11x10^8 \\ -1.97x10^5 \end{Bmatrix} - \begin{Bmatrix} 1.13x10^8 \\ -2.09x10^8 \\ -1.87x10^5 \\ 1.14x10^8 \\ -2.11x10^8 \\ -1.97x10^5 \end{Bmatrix}\right) = 0.391$$

- Check for convergence:

$$\left(\Delta\hat{r}_6 = 4.72x10^{-11}\right) < 1x10^{-4}$$

and

$$\left(Error_6 = 0.391\right) < 117.82$$

$\rightarrow$ Solution has converged, break iteration.

Converged Algorithm Outputs:

- Number of iterations to convergence: 6
- Updated damage scale factors:

$$\left\{\hat{r}_d\right\} = \left\{\delta_{EI_1}\right\} = \left\{0.900\right\}$$

- Correlated damaged system matrices:

$$\left[M(\hat{r}_d)\right] = \begin{bmatrix} 9.96x10^{-4} & 1.29x10^{-2} \\ 1.29x10^{-2} & 2.16x10^{-1} \end{bmatrix}$$

$$\left[K(\hat{r}_d)\right] = \begin{bmatrix} 8.19 & -376.58 \\ -376.58 & 2.31x10^{4} \end{bmatrix}$$

$$\left[C(\hat{r}_d)\right] = \begin{bmatrix} 1.74x10^{-3} & 1.83x10^{-2} \\ 1.83x10^{-2} & 5.09x10^{-1} \end{bmatrix}$$

- Updated scale factor error (relative to known true value $\{\tilde{r}_d\}$):

$$\left| \frac{\left(\{\tilde{r}_d\} - \{\hat{r}_d\}\right)}{\{\tilde{r}_d\}} \right| x100 = 1.23x10^{-14}\%$$

Figure 4-8 provides a concise graphical summary of the iterative procedure. In the upper two plots of Figure 4-8 the real (left) and imaginary (right) portions of the PSD are shown for both the healthy and damaged system configurations. The black dashed lines correspond to the initial frequency lines selected for evaluation whereas the red line is the updated frequency line calculated from the current model PSD half magnitude point for the current iteration (*j=6* as shown). Curves corresponding to the model PSD at each iteration step are also shown on the plots and listed in the legend. The last four iterations are difficult to distinguish because they so closely overlay the damaged PSD, as desired.

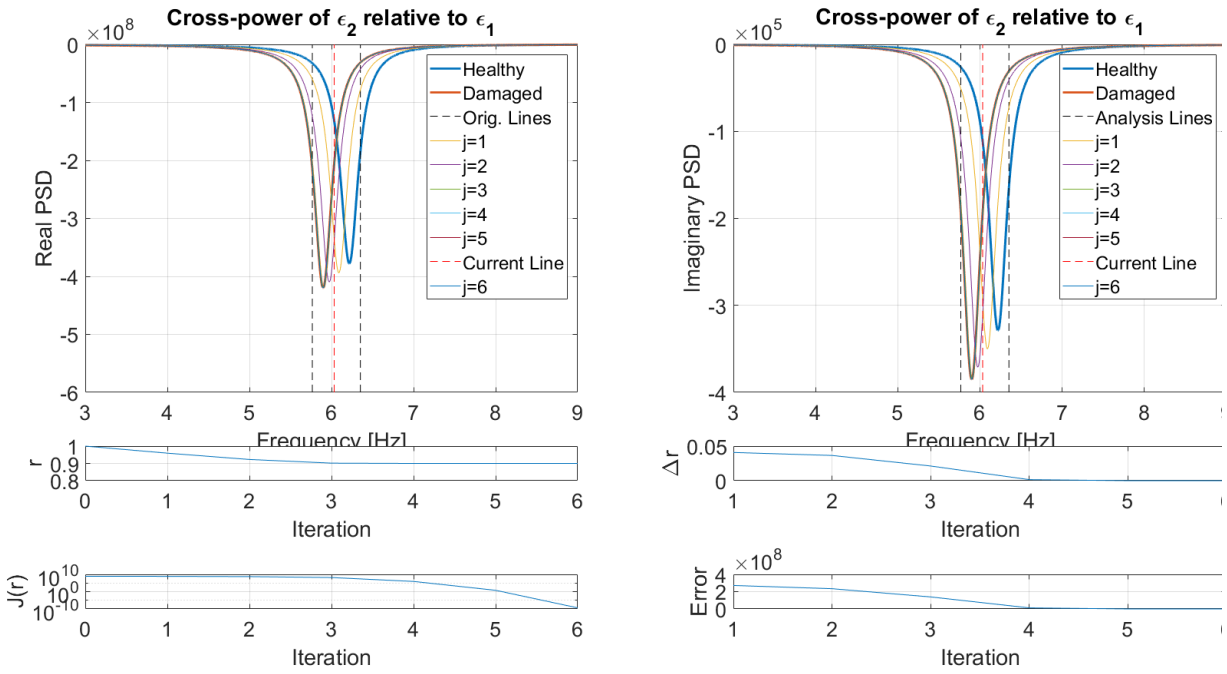

Figure 4-8: Plots tracking the progression of the iteration scheme. Clockwise from upper left: (1) Real PSD containing the healthy, damaged and iteration PSD as well as the initial and updated frequency lines; (2) Imaginary PSD containing the healthy, damaged and iteration PSD as well as the initial and updated frequency lines; (3) Plot of the change in update parameter vs. iteration; (4) Plot of the 2-norm of the error vs. iteration; (5) Plot of the cost function value vs. iteration; (6) Plot of the update parameter value vs. iteration.

The lower four plots are perhaps more pertinent in regards to assessing the quality of the converged solution. The plot in the middle row, left column, shows the evolution of the update parameter "*r*" as the iterative procedure is carried out. It is seen that the first three iterations produce relatively large changes in *r* whereas the last four are really just refining the solution further. This trend is repeated in the middle right figure which shows the change in the update parameter between successive iterations. In the bottom row of Figure 4-8 on the left, the value of the cost function being minimized is plotted for the current iteration's parameter value. It is seen that the function value is continually decreasing with the number of iterations, ultimately reaching a minimum at the converged parameter value as desired. Likewise, the 2-norm of the error vector is plotted in the lower right and goes to zero as the solution converges.

4.3 Effects of Damping

With the inner workings of the algorithm now documented, the robustness of the method to varying parameters is demonstrated. System damping can vary greatly from one system to another and as a result a SHM algorithm should be robust to handle both lightly and heavily damped systems. In the previous section, the values of the damping matrix were taken to match those calculated from experimental testing of a beam resembling that used in the current development. For the sake of demonstrating the robustness of the algorithm to a range of damping values, the same procedure will be repeated using a lightly damped case and a heavily damped case. The damping values used were set to be an order of magnitude higher and lower than the respective damping used in Section 4.2.

4.3.1 Light Generalized Viscous Damping

The system described in Section 4.2 is also used in the current demonstration with the one exception, the damping matrix will be reduced by an order of magnitude, resulting in a system damping matrix of:

$$[C] = \begin{bmatrix} 1.74x10^{-4} & 1.83x10^{-3} \\ 1.83x10^{-3} & 5.09x10^{-2} \end{bmatrix}. \tag{4-13}$$

As expected, this reduction in damping causes an increase in the peaks of the PSD and a decrease in the peak width. A narrow frequency band of the PSD for the lightly damped healthy and damaged PSD is given in Figure 4-9.

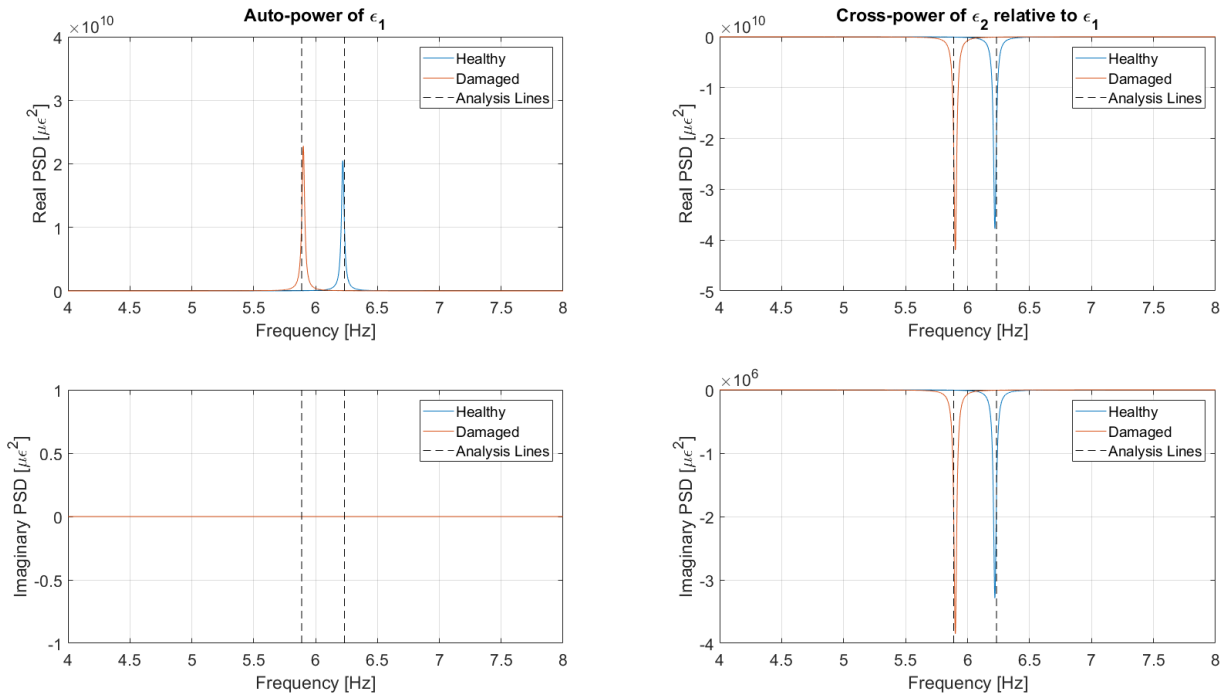

Figure 4-9: Overlay of the healthy system response model and damage system response measurement for the lightly damped system.

After examination of Figure 4-9, it is clear that the half magnitude points of the PSD have shifted and the frequency lines chosen in the previous example are no longer valid. Using the same selection criteria outlined previously, new frequency lines are selected and the algorithm is repeated. The input parameters and converged solution outputs are given below.

Algorithm Inputs:

- Initial damage scale factors:

$$\{\hat{r}_o\} = \{1\}$$

- System matrices as a function of update parameters:

$$\left[M(\hat{r})\right]=\frac{2.68x10^{-3}}{\left(1.83x10^{-3}\hat{r}+1\right)^{2}}\begin{bmatrix}\left(1.12x10^{-6}\hat{r}^{2}+1.28x10^{-3}\hat{r}+0.372\right) & \cdots\\ \left(1.28x10^{-5}\hat{r}^{2}+1.54x10^{-2}\hat{r}+4.82\right) & \\ \left(1.28x10^{-5}\hat{r}^{2}+1.54x10^{-2}\hat{r}+4.82\right) & \\ \left(2.37x10^{-4}\hat{r}^{2}+2.58x10^{-1}\hat{r}+80.68\right) & \end{bmatrix}$$

$$\left[K(\hat{r})\right]=\frac{1}{\left(1.83x10^{-3}\hat{r}+1\right)}\begin{bmatrix}9.11\hat{r} & -419.1\hat{r}\\ -419.1\hat{r} & 6426\hat{r}\left(1.83x10^{-3}\hat{r}+4\right)\end{bmatrix}$$

$$\left[C(\hat{r})\right]=\begin{bmatrix}1.74x10^{-4} & 1.83x10^{-3}\\ 1.83x10^{-3} & 5.09x10^{-2}\end{bmatrix}$$

- Strain-Displacement transformation matrix as a function of update parameters:

$$\left[B(\hat{r})\right]=\begin{bmatrix}\dfrac{-5.16}{\left(2.66x10^{1}\hat{r}+1.46x10^{4}\right)} & \dfrac{\left(5.33\hat{r}-1.46x10^{3}\right)}{\left(4.90x10^{2}\hat{r}+2.68x10^{5}\right)}\\ \dfrac{5.16}{\left(2.66x10^{1}\hat{r}+1.46x10^{4}\right)} & \dfrac{\left(5.33\hat{r}+7.28x10^{3}\right)}{\left(4.90x10^{2}\hat{r}+2.68x10^{5}\right)}\end{bmatrix}$$

- Choice of reference degree of freedom:

$$i=1$$

- Initial damage scale factor covariance matrix:

$$\left[S_{r_o r_o}\right]=\left[0.01\right]$$

- Set of initial frequency lines:

$$\left\{\omega_{k_o}\right\} = \begin{Bmatrix} 5.8875 \\ 6.2335 \end{Bmatrix} Hz$$

Converged Algorithm Outputs:

- Number of iterations to convergence: 28
- Updated damage scale factors:

$$\left\{\hat{r}_d\right\} = \left\{\delta_{EI_1}\right\} = \left\{0.900\right\}$$

- Correlated damaged system matrices:

$$\left[M(\hat{r}_d)\right] = \begin{bmatrix} 9.96x10^{-4} & 1.29x10^{-2} \\ 1.29x10^{-2} & 2.16x10^{-1} \end{bmatrix}$$

$$\left[K(\hat{r}_d)\right] = \begin{bmatrix} 8.19 & -376.58 \\ -376.58 & 2.31x10^{4} \end{bmatrix}$$

$$\left[C(\hat{r}_d)\right] = \begin{bmatrix} 1.74x10^{-4} & 1.83x10^{-3} \\ 1.83x10^{-4} & 5.09x10^{-2} \end{bmatrix}$$

- Updated scale factor error (relative to known true value $\left\{\tilde{r}_d\right\}$):

$$\left|\frac{\left(\left\{\tilde{r}_d\right\} - \left\{\hat{r}_d\right\}\right)}{\left\{\tilde{r}_d\right\}}\right| x100 = 9.87x10^{-14}\%$$

Figure 4-10 graphically depicts the iterative process associated with the lightly damped case. At first glance it appears as though the decrease in damping caused the algorithm to converge slower. In actuality, the algorithm converges more slowly because of the lack of overlap between the health and damaged PSD at the start of the algorithm. When this occurs the sensitivity of the model PSD with respect to the frequencies on the damaged PSD are essentially zero meaning there is less information to drive the residual error vector to zero.

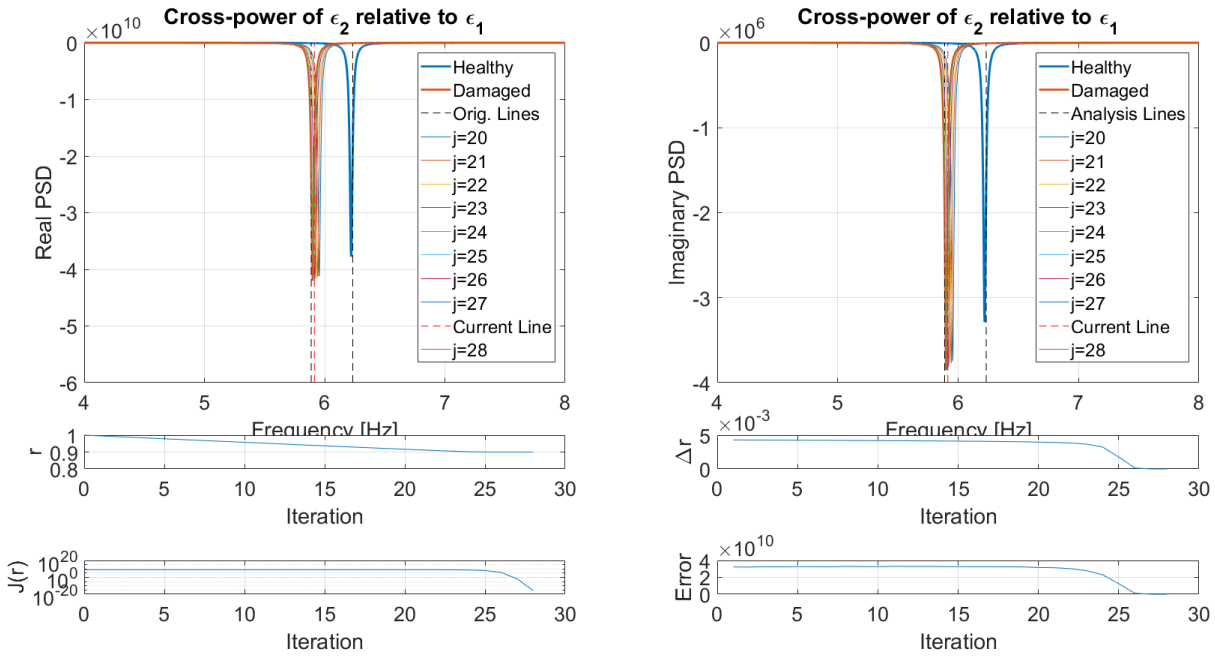

Figure 4-10: Plots tracking the progression of the iteration scheme. Clockwise from upper left: (1) Real PSD containing the healthy, damaged and iteration PSD as well as the initial and updated frequency lines; (2) Imaginary PSD containing the healthy, damaged and iteration PSD as well as the initial and updated frequency lines; (3) Plot of the change in update parameter vs. iteration number; (4) Plot of the 2-norm of the error vs. iteration number; (5) Plot of the cost function value vs. iteration number; (6) Plot of the update parameter value vs. iteration.

As the two signals begin to overlap the rate of convergence increases as shown in Figure 4-10. This same phenomenon occurs when the amount of damage increases and thus the model and damaged PSD begin with little to no overlap. Adding more frequency lines aids in the

convergence rate and will be studied in subsequent sections. As the systems being monitored become more complex overlapping of the healthy and damaged PSD will also be more likely and thus the lack of overlapping is not of great concern.

4.3.2 Heavy Generalized Viscous Damping

The system described in Section 4.2 will again be used here with the one exception, the damping matrix will be increased by an order of magnitude, resulting in a system damping matrix of:

$$[C] = \begin{bmatrix} 1.74x10^{-2} & 1.83x10^{-1} \\ 1.83x10^{-1} & 5.09 \end{bmatrix} \tag{4-14}$$

As expected, this increase in damping causes a decrease in the peaks of the PSD and an increase in the peak width. A narrow frequency band of the PSD for the heavily damped healthy and damaged PSD is given in Figure 4-11.

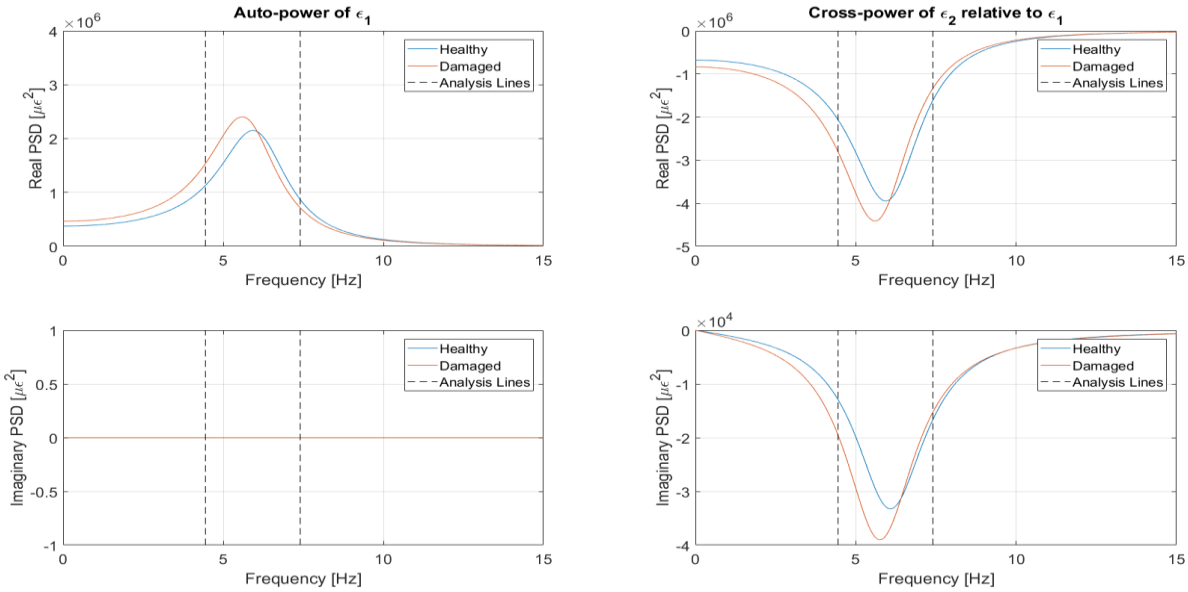

Figure 4-11: Overlay of the healthy system response model and damage system response measurement for the heavily damped system.

The input parameters and converged solution outputs are given below.

Algorithm Inputs:

- Initial damage scale factors:

$$\{\hat{r}_o\} = \{1\}$$

- System matrices as a function of update parameters:

$$[M(\hat{r})] = \frac{2.68x10^{-3}}{\left(1.83x10^{-3}\hat{r}+1\right)^2}\begin{bmatrix} \left(1.12x10^{-6}\hat{r}^2+1.28x10^{-3}\hat{r}+3.72x10^{-1}\right) & \left(1.28x10^{-5}\hat{r}^2+1.54x10^{-2}\hat{r}+4.82\right) \\ \left(1.28x10^{-5}\hat{r}^2+1.54x10^{-2}\hat{r}+4.82\right) & \left(2.37x10^{-4}\hat{r}^2+2.58x10^{-1}\hat{r}+80.68\right) \end{bmatrix} \quad \ldots$$

$$[K(\hat{r})] = \frac{1}{\left(1.83x10^{-3}\hat{r}+1\right)}\begin{bmatrix} 9.11\hat{r} & -419.1\hat{r} \\ -419.1\hat{r} & 6426\hat{r}\left(1.83x10^{-3}\hat{r}+4\right) \end{bmatrix}$$

$$[C(\hat{r})] = \begin{bmatrix} 1.74x10^{-2} & 1.83x10^{-1} \\ 1.83x10^{-1} & 5.09 \end{bmatrix}$$

- Strain-Displacement transformation matrix as a function of update parameters:

$$[B(\hat{r})] = \begin{bmatrix} \frac{-5.16}{\left(2.66x10^{2}\hat{r}+1.46x10^{4}\right)} & \frac{\left(5.33\hat{r}-1.46x10^{3}\right)}{\left(4.90x10^{2}\hat{r}+2.68x10^{5}\right)} \\ \frac{5.16}{\left(2.66x10^{1}\hat{r}+1.46x10^{4}\right)} & \frac{\left(5.33\hat{r}+7.28x10^{3}\right)}{\left(4.90x10^{2}\hat{r}+2.68x10^{5}\right)} \end{bmatrix}$$

- Choice of reference degree of freedom:

$$i = 1$$

- Initial damage scale factor covariance matrix:

$$\left[S_{r_o r_o} \right] = \left[0.01 \right]$$

- Set of initial frequency lines:

$$\left\{ \omega_{k_o} \right\} = \begin{Bmatrix} 4.008 \\ 7.177 \end{Bmatrix} Hz$$

Converged Algorithm Outputs:

- Number of iterations to convergence: 4
- Updated damage scale factors:

$$\left\{ \hat{r}_d \right\} = \left\{ \delta_{EI_1} \right\} = \left\{ 0.900 \right\}$$

- Correlated damaged system matrices:

$$\left[M(\hat{r}_d) \right] = \begin{bmatrix} 9.96x10^{-4} & 1.29x10^{-2} \\ 1.29x10^{-2} & 2.16x10^{-1} \end{bmatrix}$$

$$\left[K(\hat{r}_d) \right] = \begin{bmatrix} 8.19 & -376.58 \\ -376.58 & 2.31x10^{4} \end{bmatrix}$$

$$\left[C(\hat{r}_d) \right] = \begin{bmatrix} 1.74x10^{-2} & 1.83x10^{-1} \\ 1.83x10^{-1} & 5.09 \end{bmatrix}$$

- Updated scale factor error (relative to known true value $\{\tilde{r}_d\}$):

$$\left|\frac{\left(\{\tilde{r}_d\}-\{\hat{r}_d\}\right)}{\{\tilde{r}_d\}}\right| x100 = 1.41x10^{-11}\%$$

Just as with the lightly damped case, in the heavily damped case it appears at first glance that increasing the damping increases the rate of convergence of the solution. This is again an artifact of the amount of overlap between the modeled and damaged PSD at the start of the iterations. In this particular case the value of the update parameter overshot its target and was able to come back to the correct solution, as shown in the middle left plot of Figure 4-12, demonstrating the algorithm's robustness.

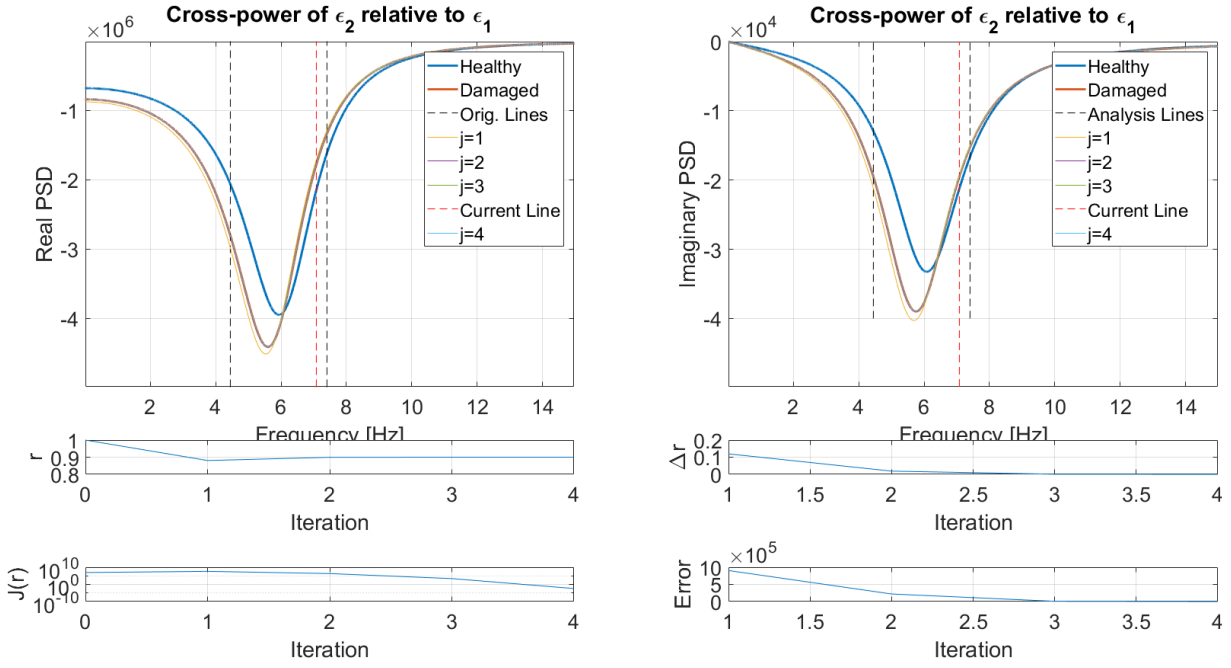

Figure 4-12: Plots tracking the progression of the iteration scheme. Clockwise from upper left: (1) Real PSD containing the healthy, damaged and iteration PSD as well as the initial and updated frequency lines; (2) Imaginary PSD containing the healthy, damaged and iteration PSD as well as the initial and updated frequency lines; (3) Plot of the change in update parameter vs. iteration; (4) Plot of the 2-norm of the error vs. iteration; (5) Plot of the cost function value vs. iteration; (6) Plot of the update parameter value vs. iteration.

The two previous examples showing the extreme cases of heavily and lightly damped systems demonstrate the algorithm's ability to identify the correct damage scale factor over a multitude of damping characteristics. The examples also demonstrate that in an extreme damage case, where the model and damaged PSD do not have any initial overlap, the algorithm is still capable of successfully converging to the correct solution.

4.4 Effects of Damage Magnitude and Type

While the first few sections have considered only a single damage variable and a single damage level, the SHM algorithm must be robust to various damage types and severities. In this section, a study has been conducted which tracks the algorithm's ability to identify the correct damage parameters over a number of damage types and severities. In particular, in Section 4.4.1 the bending stiffness related damage scale factor previously studied is varied over a range of damage scenarios. These same damage scale factors are repeated in Section 4.4.2, this time allowing the material density to vary and holding the bending stiffness fixed. Lastly, combinations of damage scale factors are studied, allowing density and bending stiffness to vary simultaneously. The system previously defined in Section 4.2 is again used here to study these variations. The specific damage parameters used in each case are explicitly stated in their respective sections.

4.4.1 Varying Levels of Bending Stiffness Damage

The current study utilizes the same system and parameters defined in Section 4.2 with varying levels of the bending stiffness damage scale factor $\left(\delta_{EI}\right)$. The model PSD equations were evaluated over a range of 0Hz to 10Hz with a stepsize restriction factor of 0.25 in all cases (*q=0.25*, as discussed in Section 3.9.2). The reader is reminded that the stepsize is automatically adjusted at each iteration based on a stepsize restriction factor chosen. Table 4-3 below provides the true value

of the damage scale factor as well as the initial frequency lines used to start the iterations. Also listed in Table 4-3 are the converged damage scale factor, number of iterations to reach convergence, and the percent error between the actual and converged damage scale factor given by:

$$\%Error = \frac{\left|\delta_{EI} - \delta_{\hat{r}_d}\right|}{\delta_{EI}} x100 \tag{4-15}$$

Table 4-3: Damaged system parameters, initial frequency lines, and converged solution parameters.

Damage Level (%)	δ_{EI}	$\omega_{1,0}$ (Hz)	$\omega_{2,0}$ (Hz)	Converged Solution	Iterations	Error (%)
0.1	0.999	6.0834	6.3516	0.9990	3	3.33E-14
1	0.99	6.0518	6.3516	0.9900	3	1.68E-13
5	0.95	5.9254	6.3516	0.9500	5	9.35E-14
10	0.9	5.7670	6.3516	0.9000	6	1.73E-13
25	0.75	5.2525	6.3516	0.7500	10	1.78E-13
50	0.5	4.2592	6.3516	0.5000	17	1.11E-14
75	0.25	2.9747	6.3516	0.2500	26	8.88E-14
90	0.1	1.8298	6.3516	0.1000	34	8.33E-14
95	0.05	1.2377	6.3516	0.0500	38	4.16E-14
99	0.01	0.4368	6.3516	0.0100	41	1.73E-14
99.9*	0.001	0.0800	6.3516	0.0010	38	0

* = Utilized adaptive step size control

It is worth noting that all of the starting frequency lines shown in Table 4-3 correspond to the half magnitude point of the damaged and model PSD, respectively, with the exception of the largest damage case. For this 99.9% damage case the half magnitude point corresponds to 0.061Hz at which the iteration scheme does not converge. Somewhat arbitrarily, this particular frequency line was moved to 0.080Hz at which point the solution converges to the exact solution, i.e. a zero

percent error as shown. In practice the algorithm would not be subjected to such an extreme, non-physical, scenario however the result was included to provide mathematical completeness in the results set. In practice, large damage in a single element would have a much smaller impact on the overall PSD and not drive the natural frequency to a near zero value.

The anticipated trend shown in Table 4-3 is that the number of iterations increases as the amount of damage increases. This increase in the number of iterations is due to the fact that there is physically more space separating the initial model PSD and the damaged measurement PSD and as such take more steps for convergence to be achieved. This rate of convergence is also dependent on the convergence criteria used, initial frequency lines, and maximum stepsize allowed. In light of these variables, the convergence rate is not meant to represent an absolute algorithm performance but instead capture a general trend. This convergence rate versus amount of damage is graphically shown in Figure 4-13.

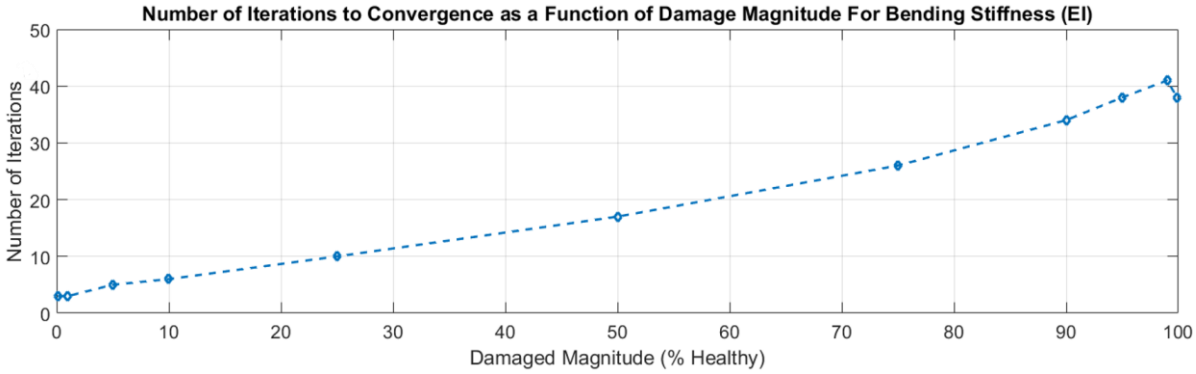

Figure 4-13: Number of iterations to convergence vs. damage magnitude for variations in bending stiffness.

The general trend is clearly that the increase in damage magnitude creates an increase in the number of iterations required to achieve convergence but has no measurable effect on the converged parameter error. The only outlier in the convergence rate trend line is that last (and

largest) damage case. While it is unclear why in this particular case a large magnitude damage converged faster than a smaller damage case, it is known that there are several factors that influence the convergence rate. One of the most profound factors are the initial frequency lines chosen. For all of the other damage scenarios studied the frequency lines were chosen to be at the half magnitude point of the signals. Perhaps the arbitrary frequency line chosen away from this point for the last damage scenario explains this deviation.

Another deviation in the 99.9% damage case was that the adaptive stepsize control, discussed in Section 3.9.2, was triggered during the updating routine. In the current study, the maximum allowable step size is 0.25. When the calculated iteration step is larger than this value a stepsize correction factor is implemented and the system parameters at the current iteration are scaled using equation (3-72) to ensure the solution converges smoothly rather than jumping around the solution space. A plot of the stepsize correction factor versus iteration number for the largest damage case is given in Figure 4-14.

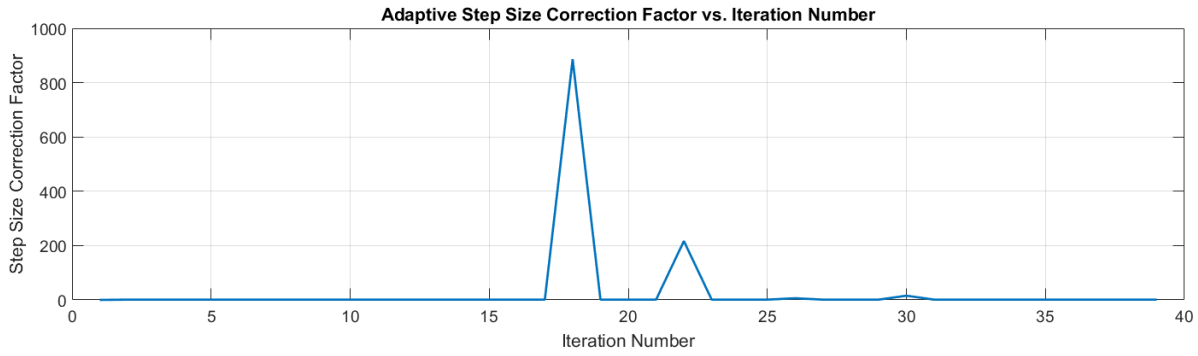

Figure 4-14: Adaptive step size correction factor used in obtaining convergence for the 99.9% damage case.

A stepsize correction factor of one is equivalent to the system taking its natural step, meaning no correct was necessary for that iteration. This is the case for the vast majority of the

iterations used in the solution of the 99.9% damage case. There were however four instances where utilizing a stepsize correction factor of one caused the solution to diverge and hence without these stepsize correction factors the solution would likely not have converged or converged to an incorrect solution. Further evidence of this divergent behavior is given in Figure 4-15.

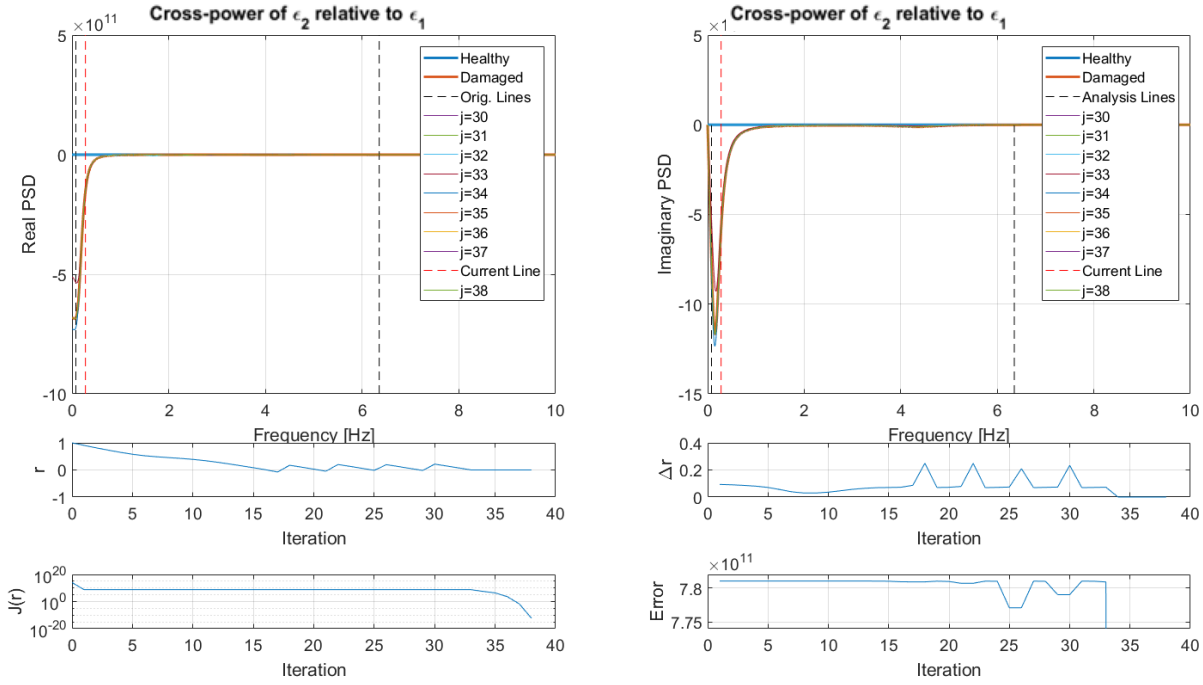

Figure 4-15: Plots tracking the progression of the iteration scheme for the 99.9% damage case. Clockwise from upper left: (1) Real PSD containing the healthy, damaged and iteration PSD as well as the initial and updated frequency lines; (2) Imaginary PSD containing the healthy, damaged and iteration PSD as well as the initial and updated frequency lines; (3) Plot of the change in update parameter vs. iteration; (4) Plot of the 2-norm of the error vs. iteration; (5) Plot of the cost function value vs. iteration; (6) Plot of the update parameter value vs. iteration.

Looking at the middle and lower right plots of Figure 4-15, it is observed that as the change in step size (Δr) increases rapidly, the error also increases. These sudden and sharp increases lead to incorrect or diverging solutions and are the reason for the stepsize control. As the solution space

becomes more complicated (more variables) this stepsize control will be imperative to ensure proper convergence.

4.4.2 Varying Levels of Density Damage

Up until this point in the analysis it has been assumed that the density of the material has remained constant and only the bending stiffness is changing. In real structures there may be variations in density that occur which need to be differentiated from changes in stiffness in order to ensure the correct solution is reached. For aerospace structures, this change in density may occur due to thermal expansion, fuel burn, or impact resulting in loss of material, just to name a few scenarios. In order to directly compare the effects of changes in density to changes in stiffness, it is now assumed that the stiffness is constant and only the density is allowed to vary. Again, the maximum Δr was set to be 0.25 for all cases. At a level of 0.25, the stepsize restriction factor was not needed for any of the variations in density studied. The same variations used for the stiffness study are used for density and are listed in Table 4-4.

Table 4-4: Damaged system parameters, initial frequency lines, and converged solution parameters for the density variation studies.

Damage Level (%)	δ_ρ	Frequency Range (Hz)	$\omega_{1,0}$ (Hz)	$\omega_{2,0}$ (Hz)	Converged Solution	Iterations	Error (%)
0.1	0.999	0-10	6.0834	6.3522	0.9990	3	3.33E-14
1	0.99	0-10	6.0834	6.3818	0.9900	3	1.23E-13
5	0.95	0-10	6.0834	6.5179	0.9500	5	4.67E-14
10	0.9	0-10	6.0834	6.6995	0.9000	6	8.64E-14
25	0.75	0-10	6.0834	7.3539	0.7500	10	5.92E-14
50	0.5	0-20	6.0834	9.0517	0.5000	17	2.22E-14
75	0.25	0-20	6.0834	12.9417	0.2500	26	2.22E-14
90	0.1	0-30	6.0834	20.8773	0.1000	33	0.00E+00
95	0.05	0-40	6.0834	30.1306	0.0500	37	4.14E-14
99	0.01	0-90	6.0834	71.7633	0.0100	41	5.20E-14
99.9	0.001	0-200	6.0834	206.2568	0.0010	46	3.32E-04

Like Table 4-3, Table 4-4 also provides information related to the initial frequency lines used, the converged solution value, number of iterations to convergence and converged solution error. As was the case for the variations in stiffness, the magnitude of the damage only impacts the number of iterations to convergence and not the converged solution error. A trend line showing the number of iterations to convergence versus the damage magnitude is shown in Figure 4-16.

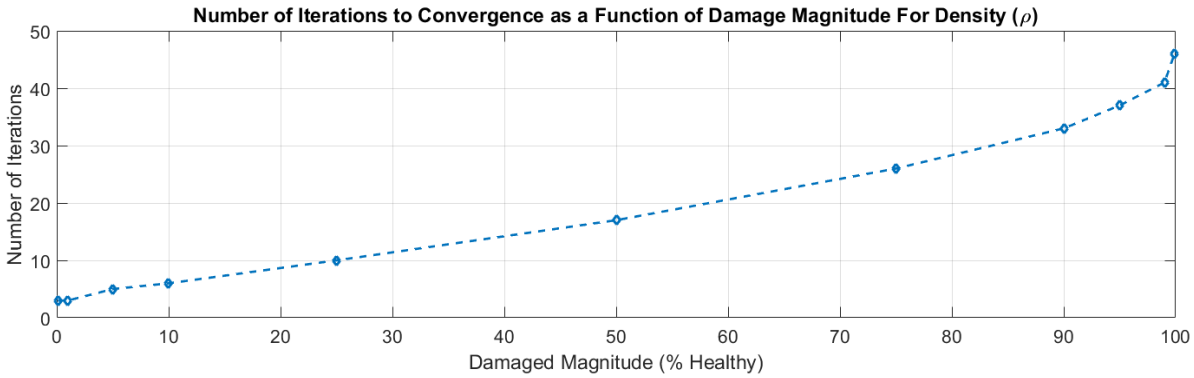

Figure 4-16: Number of iterations to convergence vs. damage magnitude for variations in density.

4.4.3 Combined Damage Studies – Varying Density and Stiffness Simultaneously

A more rigorous test of the algorithm's performance capabilities was explored by expanding the solution space to multiple dimension. A particularly challenging set of circumstances is when both the density and stiffness change simultaneously as a decrease in density shifts the PSD to higher frequencies whereas a decrease in stiffness shifts to lower frequencies. This implies that a simultaneous decrease in both density and stiffness could cause little to no change in the system's natural frequencies. A reliable SHM algorithm should be robust enough to reliably determine whether a system is undamaged or has damage in multiple parameters which result in a relatively small change in the PSD. A wide range of damage cases were studied

in which the density (mass) and bending stiffness are varied simultaneously, the results of these studies are presented in Table 4-5.

Table 4-5: Damaged system parameters, initial frequency lines, and converged solution parameters.

δ_{EI}	δ_{ρ}	Δr Limit	Frequency Range (Hz)	$\omega_{1,0}$ (Hz)	$\omega_{2,0}$ (Hz)	δ_{EI} Converged	δ_{ρ} Converged	Iterations	Mean Error (%)
0.999	1	0.25	0-10	6.0834	6.3516	0.9990	1.0000	3	1.88E-12
0.9		0.25	0-10	5.7670	6.3516	0.9000	1.0000	7	1.63E-12
0.75		0.25	0-10	5.2525	6.3516	0.7500	1.0000	10	2.22E-14
0.25		0.25	0-10	2.9747	6.3516	0.2500	1.0000	14	5.33E-13
0.1		0.25	0-10	1.8298	6.3516	0.1000	1.0000	15	4.39E-13
0.001		0.10	0-10	0.0610	6.3516	0.0010	1.0000	25	1.70E-13
0.999	0.5	0.25	0-10	6.0834	9.0534	0.9990	0.5000	14	2.13E-12
0.9		0.25	0-10	6.0834	8.6059	0.9000	0.5000	13	7.06E-13
0.75		0.25	0-10	6.0834	7.8783	0.7500	0.5000	10	1.94E-12
0.25		0.10	0-10	4.1254	6.3516	0.2500	0.5000	16	4.72E-13
0.1		0.05	0-10	2.5043	6.3516	0.1000	0.5000	35	4.39E-05
0.001		0.10	0-10	0.0520	6.3516	0.0010	0.5000	20	3.33E-14
0.999	0.01	0.25	0-100	6.0834	74.0234	0.9990	0.0100	43	8.88E-10
0.9		0.25	0-80	6.0834	70.7751	0.9000	0.0100	42	1.28E-11
0.75		0.10	0-80	6.0834	65.4705	0.7500	0.0100	40	3.58E-11
0.25		0.05	0-50	6.0834	41.3081	0.2500	0.0100	35	1.04E-13
0.1		0.10	0-40	6.0834	27.8108	0.1000	0.0100	16	2.45E-13
0.001		0.25	0-10	0.0400	6.3516	0.0010	0.0100	17	7.37E-13
1	0.999	0.25	0-10	6.0834	6.3506	1.0000	0.9990	3	7.28E-13
	0.9	0.25	0-10	6.0834	6.7007	1.0000	0.9000	7	4.31E-12
	0.75	0.25	0-10	6.0834	7.3557	1.0000	0.7500	9	1.74E-11
	0.25	0.25	0-20	6.0834	12.9613	1.0000	0.2500	24	1.03E-12
	0.1	0.25	0-30	6.0834	20.9571	1.0000	0.1000	32	3.74E-11
	0.001	0.25	0-400	6.0834	278.1078	1.0000	0.0010	46	2.43E-11
0.5	0.999	0.25	0-10	4.2654	6.3516	0.5000	0.9990	12	2.56E-13
	0.9	0.25	0-10	4.4904	6.3516	0.5000	0.9000	12	9.87E-13
	0.75	0.25	0-10	4.9005	6.3516	0.5000	0.7500	11	1.15E-12
	0.25	0.25	0-10	6.0834	9.3109	0.5000	0.2500	11	3.22E-13
	0.1	0.25	0-30	6.0834	15.1765	0.5000	0.1000	20	2.61E-12
	0.001	0.25	0-200	6.0834	195.8996	0.5000	0.0010	34	9.28E-13
0.01	0.999	0.10	0-10	0.4780	6.3516	0.0100	0.9990	27	5.45E-14
	0.9	0.10	0-10	0.4940	6.3516	0.0100	0.9000	26	1.21E-13
	0.75	0.10	0-10	0.5241	6.3516	0.0100	0.7500	24	1.67E-13
	0.25	0.10	0-10	0.6501	6.3516	0.0100	0.2500	17	3.09E-14
	0.1	0.10	0-10	0.6021	6.3516	0.0100	0.1000	16	1.70E-13
	0.001	0.10	0-10	5.4385	6.0856	0.0100	0.0010	19	7.94E-11

In Table 4-5, the 36 different damage combinations studied are listed along with the frequency range used in the updating and the maximum Δr used in each case. It was necessary to increase the frequency range in many of the cases where the density was reduced in order to capture the damaged PSD's peak. All of the 36 cases were first run with a Δr of 0.25 and in cases where convergence was not achieved, the maximum Δr was systematically decrease in sequential order to values of 0.1 and 0.05 until convergence was achieved using the respective maximum Δr listed in the table. In all of the cases with the limit Δr less than 0.25 adaptive stepsize control was automatically implemented to ensure convergence in the minimum possible number of iterations. The results for all cases were that the damage scale factors were identified exactly within the specified tolerance. The ability of the algorithm to accurately identify the combination of damage scale factors for all damage combinations further verifies the desired robustness of the method. The number of iterations taken to achieve convergence as well as the negligible parameter error are listed in Table 4-5 and the convergence rate shown in Figure 4-17.

The surface plot shown on the left of Figure 4-17 represents a curve fit of the data points tabulated in Table 4-5. The data points used to generate the curve fit are shown as red diamonds on the plot. To the right of the error surface is a top view contour plot where the colormap corresponds to the number of iterations. The expected trend in Figure 4-17 is that as the magnitude of either of the damage parameters increase the number of iterations to convergence also increases. There is one point which is a notable outlier occurring at $\delta_{EI} = 0.1$ and $\delta_{\rho} = 0.5$. Closer examination reveals that this point corresponds to the point at which the smallest value of Δr was used. In this particular case the frequency lines chosen corresponded to inflection points during the convergence routine. This result was coincidental and necessitated the use of a very small step to achieve convergence. Selection of different frequency lines would have also avoided this

anomaly however to minimize the number of variations being studied the frequency lines corresponding to the half magnitude point of the peaks of the PSD were used for all cases. A study of the variations caused by frequency line selection is presented in Chapter 5.

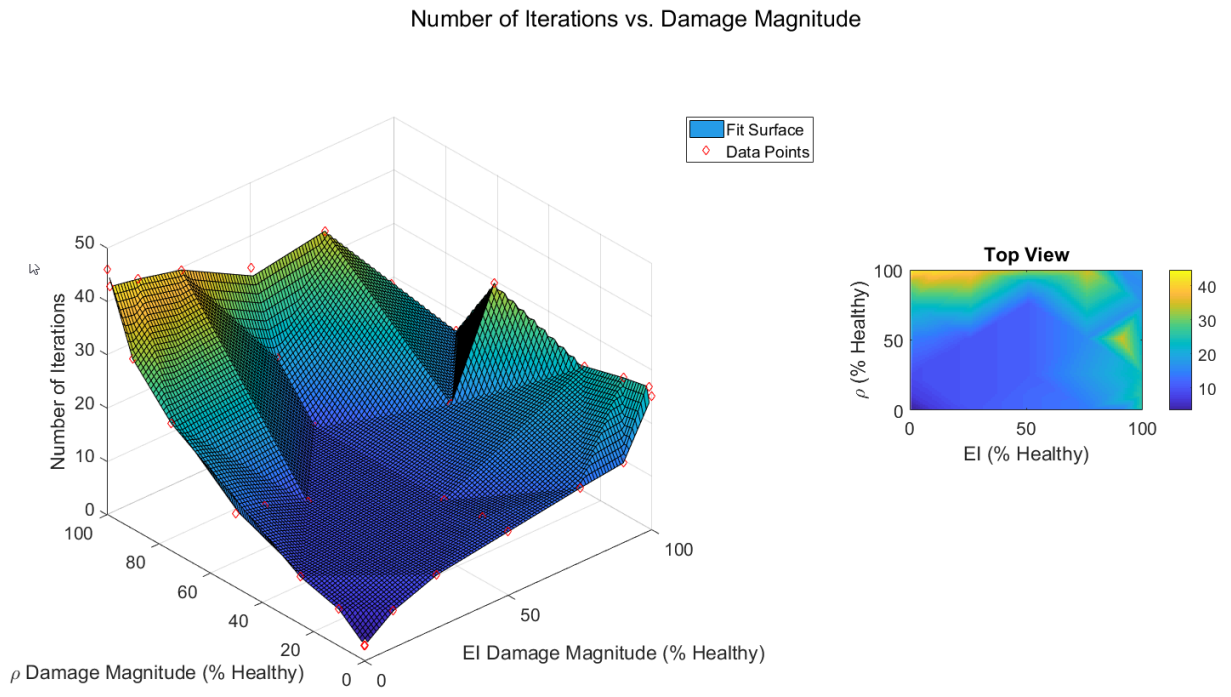

Figure 4-17: Number of iterations to convergence vs. damage magnitude for variations in bending stiffness and density.

A surprising result shown in Figure 4-17 is that the number of iterations required for convergence when both damage parameters are small (lots of damage) is less than when one parameter is large and one is small. This is contrary to the basic understanding that there is a correlation between the number of iterations and distance between healthy and damaged PSD. In the particular case where both parameters have a large amount of damage they converge more quickly because in general, when damage is present both parameters decrease uniformly during the initial steps and then "branch out" towards their respective parameter value. A plot showing the typical branching behavior is given in Figure 4-18. This branching often occurs in between the

two parameter values and hence one parameter must increase from the branching point while the other decreases. When both of the parameters are near one another it takes very few steps to achieve convergence from the branching point whereas when the parameters are well separated numerous iterations are needed to achieve convergence from the branching point.

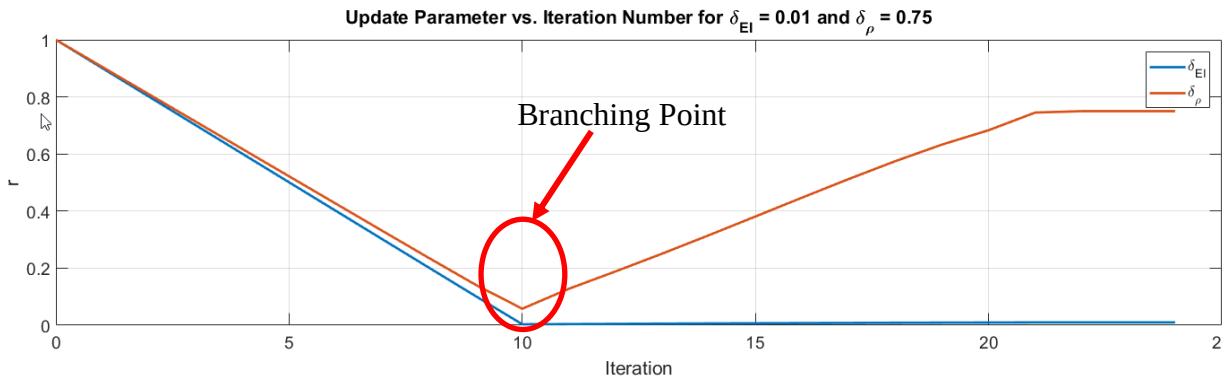

Figure 4-18: Update parameters as a function of iteration number showing the branching point at which the parameter values separate during the update routine.

In the multivariate damage cases presented, a set of cases were studied where either the density or stiffness was left at their undamaged values to allow for comparisons to the cases where the solution space was one-dimensional (only one variable, rather than two in the current case). In these cases, the damage scale factor was allowed to vary within the algorithm but its true value was left at the nominal, undamaged value. Using these test cases, it was shown that the algorithm performed the same or better in the multivariate case as it did in the single update parameter solution space. The caveat to these results was that in several cases the adaptive stepsize control was automatically activated whereas in the single variable case the control was not needed. A comparison between the single update parameter and dual parameter update cases are given in Figure 4-19.

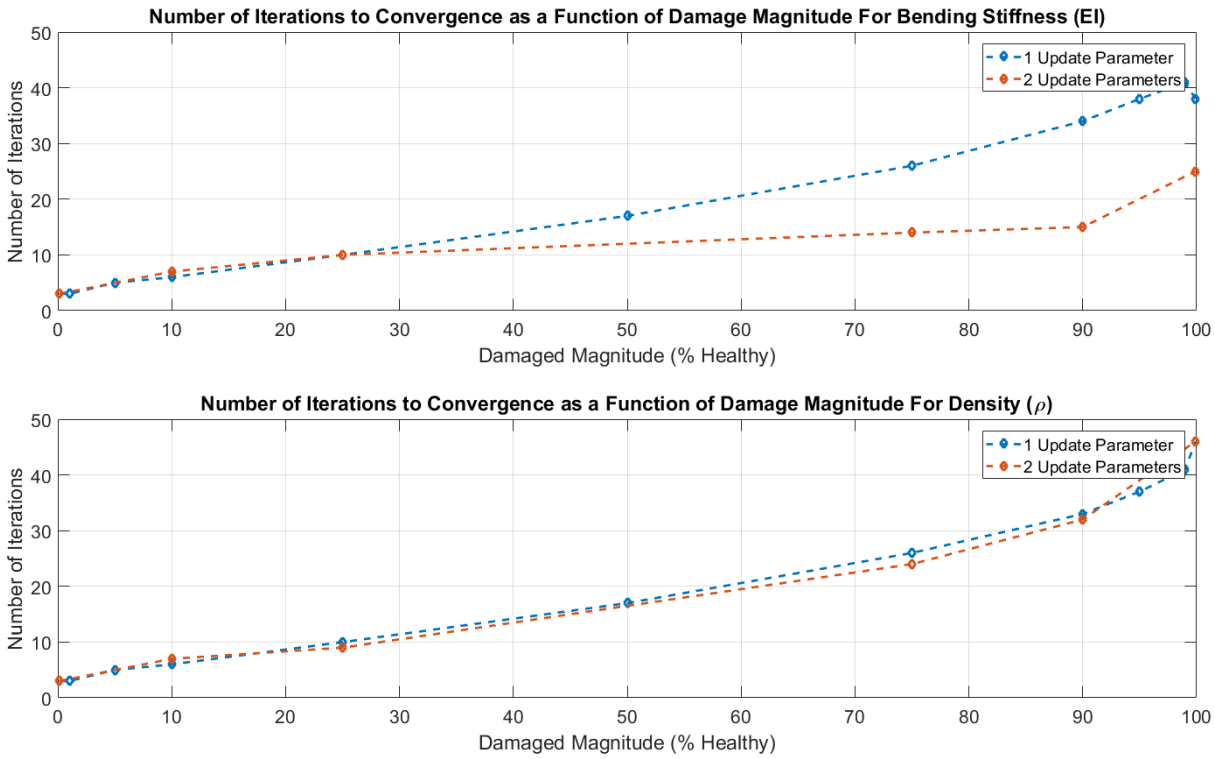

Figure 4-19: Comparison between number of iterations to convergence vs. damage magnitude for (upper) variations in bending stiffness using only one update parameters (δ_{EI}) and two update parameters $(\delta_{EI}, \delta_{\rho})$ and (lower) variations in density using only one update parameters (δ_{ρ}) and two update parameters $(\delta_{EI}, \delta_{\rho})$.

4.5 Selecting Frequency Lines

One of the input parameters which have the largest impact on the quality of the converged solution is the frequency lines used to start the iterations as well as their progression throughout the updating routine. To this end, a detailed review of best practices in selecting frequency lines is covered in the current section.

4.5.1 Frequency Line Selection Criteria

While for smaller problems, like those studied in the current section, it is possible to manually select a small number of frequency lines, for general large-scale problems it is desirable to incorporate mechanisms within the algorithm to automatically select all available frequency

lines which meet some predefined criteria. One such criteria is that frequency lines lying between the model and damaged PSD peaks for each mode should be avoided when possible. Figure 4-20 provides a non-dimensionalized schematic highlighting the optimal (Regions 1 and 3) and suboptimal (Region 2) candidate frequency line regions.

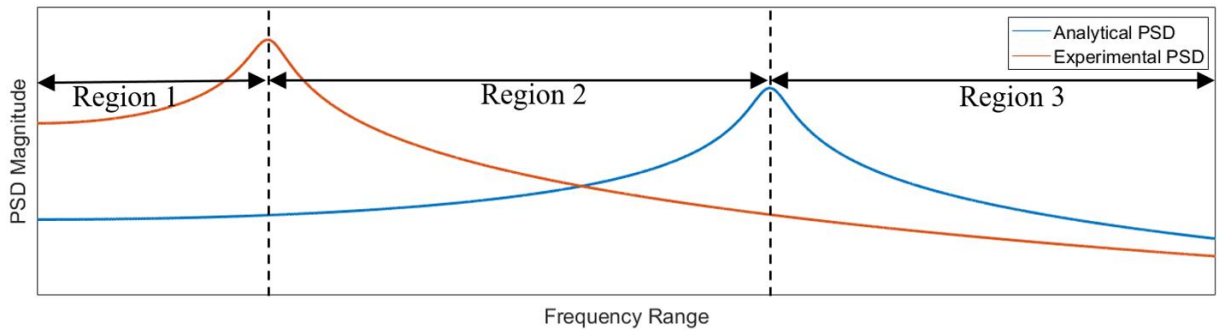

Figure 4-20: Optimal (regions 1 and 3) and sub-optimal (region 2) candidate frequency line selection ranges.

In the case of a single pair of selected frequency lines, as has been utilized thus far in this dissertation, selection of frequency lines in region two will cause convergence to an incorrect set of parameters, as discuss in Section 3.9. This occurs because at two frequency lines (one on the healthy and one on the damaged PSD) in region 2, the closest set of points in the solution space which minimizes the system error will be at the intersection of the two curves, rather than their overlap. As more frequency lines are added to the algorithm these effects diminish however under direct comparison, lines in regions 1 and 3 will always outperform lines in region 2 on the basis of accuracy and/or number of iterations to convergence. There are cases of large damage and closely coupled modes where selection of frequencies in region two are unavoidable. Additional lines from regions 1 and 3 will aid in convergence in these cases.

Once the available frequency line pool has been narrowed to lines in regions 1 and 3, whenever possible, additional constraints may be applied. When dealing with data contaminated with noise, frequency line selection filtering will be done via a coherence threshold. All values below a predefined coherence threshold will be ineligible for selection. Trial and error of frequency line selection criteria has also given merit to choosing pairs of frequencies where, in example, using a line at fifty percent of the peak magnitude on the model PSD, a corresponding line at fifty percent of the peak on the measured (damaged) PSD should also be chosen. This methodology of selecting frequency lines on the healthy and damaged PSD in pairs has been adapted throughout the dissertation.

4.5.2 Frequency Line Updating

The ability of the algorithm to update the frequency lines corresponding to the model PSD at each linearization point is one of the novel contributions of this research. While this adaptive frequency line selection is not necessary for relatively small damage cases (where the model and damaged PSD have an overlapping portion of regions 1 and/or 3) it is imperative for ensuring accurate convergence in a reasonable amount of iterations for larger damage cases. This becomes especially important when utilizing noisy data as the updated frequency lines produce sensitivities which are out of the measurement noise when traversing large gaps between the model and damaged PSD. To illustrate the utility of frequency line updating, the damage cases studied in Section 4.4.1 are repeated without the use of frequency line updating. In all cases the default limit Δr was set to be 0.25 and the frequency range was set to 0-10Hz as was done in Section 4.4.1. In the case of iterations without frequency line updating, the maximum Δr had to be systematically reduced using values of 0.25, 0.1, 0.05, 0.025 and 0.01 until convergence was reached or convergence was deemed not possible. Table 4-6 shows the damage cases studied, along with the

maximum (limit) Δr required to reach convergence as well as the converged system parameter, iterations, and error.

Table 4-6: Damaged system parameters, initial frequency lines, and converged solution parameters.

Damage Level (%)	δ_{EI}	Δr Limit	ω_1 (Hz)	ω_2 (Hz)	Converged Solution	Iterations	Error (%)
0.1	0.999	0.25	6.0834	6.3516	0.9990	3	6.67E-14
1	0.99	0.25	6.0518	6.3516	0.9900	3	6.73E-14
5	0.95	0.25	5.9254	6.3516	0.9500	6	1.64E-13
10	0.9	0.25	5.7670	6.3516	0.9000	6	1.74E-05
25*	0.75	0.25	5.2525	6.3516	0.7500	11	2.96E-14
50*	0.5	0.25	4.2592	6.3516	0.5000	19	1.11E-13
75*	0.25	0.25	2.9747	6.3516	0.2500	29	6.66E-14
90*	0.1	0.05	1.8298	6.3516	0.1000	41	1.39E-14
95*	0.05	0.025	1.2377	6.3516	0.0500	46	6.94E-14
99*	0.01	0.025	0.4368	6.3516	0.0100	52	1.04E-13
99.9*	0.001	0.01	0.0800	6.3516	0.0010	113	0.00E+00

* = Utilized adaptive step size control

Table 4-6 shows that without frequency line updating all of the damage scenarios correctly converged to their true solution. One of the key differences between these cases and the cases with frequency line updating is the Δr limit required to achieve convergence. On this simple single variable system without measurement noise, decreasing Δr is a suitable approach to ensure convergence with the penalty being a negligible increase in the number of iterations for all but the most severe of damage cases. Overlaying a plot of the number of iterations to convergence for the cases run with and without frequency line updating allows for ease of comparison and is shown in Figure 4-21.

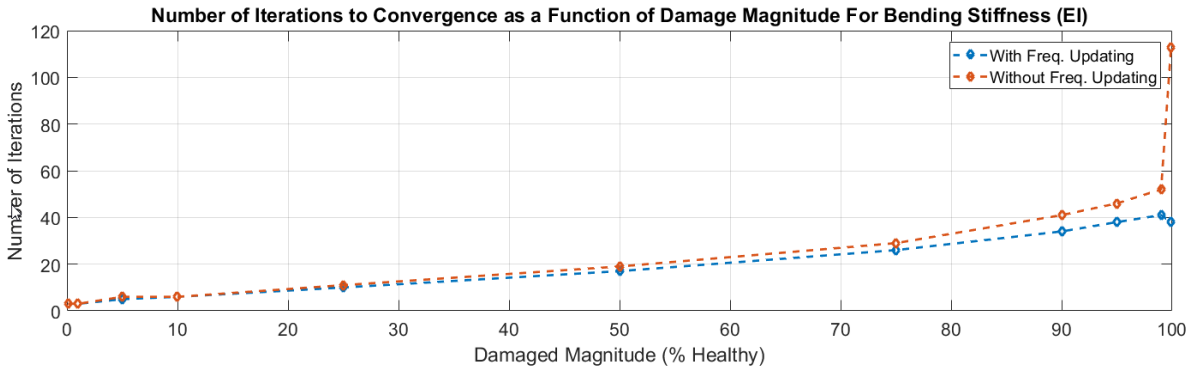

Figure 4-21: Comparisons between the number of iterations to convergence with and without frequency line updating.

When the solution space becomes more complex with the addition of numerous update parameters and measurement noise Δr limitations alone are no longer sufficient for ensuring proper convergence and the utility of frequency line updating increases.

4.5.3 Frequency Line Effectiveness as a Function of Peak Magnitude

In order to aid in the selection of frequency lines it is desirable to know the relative importance of each frequency line. The sensitivity of the update parameters is highly non-linear with respect to the frequency lines and as such careful consideration should be taken when selecting frequency lines. Typically, the coherence measurement will increase in the vicinity of the peaks, indicating peak regions are ideal candidates for updating. While this is true, it is also known that sensitivities on either side of the peak of the PSD typically are of opposite signs meaning that choosing sensitivities at or near the peak can lead to oscillations in the update parameters and hence more iterations and a higher likelihood of poor solution quality. Furthermore, it is equally important to incorporate a distribution of frequency points along the PSD in the updating routine to accurately capture the set of parameters that match the measurement PSD on a global sense, rather than in local regions near the peak. To this end, pairs of frequency

lines were selected corresponding to percentages of the peak amplitude for the model and measured PSD. These pairs were evaluated at amplitude ratios of 5%, 10%, 25%, 50%, 75%, 90%, 95% and 100% (frequency line taken as the peak value). The system used for these studies is the same system studied in Section 4.4.1 with a damage scale factor of $\delta_{EI} = 0.5$. The results of the analysis have been tabulated and are given in Table 4-7.

Table 4-7: Damaged system parameters, initial frequency lines, and converged solution parameters.

Magnitude Ratio ($\%_{pk}$)	Δr Limit	$\omega_{1,0}$ (Hz)	$\omega_{2,0}$ (Hz)	Converged Solution	Iterations	Error (%)
1	0.25	3.0933	7.5428	0.5000	8	2.11E-13
5	0.25	3.8174	6.7997	0.5000	8	1.60E-12
10	0.25	3.9974	6.6187	0.5000	12	1.11E-13
25	0.25	4.1664	6.4496	0.5000	15	2.22E-14
50	0.25	4.2592	6.3516	0.5000	19	1.11E-13
75	0.25	4.3194	6.2956	0.5000	15	1.55E-13
90	0.25	4.3524	6.2626	0.5000	12	4.44E-14
95	0.25	4.3664	6.2486	0.5000	9	8.88E-14
99	0.1	4.3834	6.2316	0.5000	11	0.00E+00
100*	0.25	4.3984	6.2203	--	100	4.98E+02

* = Solution does not converge

The same procedure was repeated for damage scenarios of 5%, 25%, 50%, 75% and 95% to represent the effects of various frequency lines at varying levels of damage. In many cases using higher magnitude ratios and/or having higher damage levels adaptive stepsize control was implemented and stepsize limits were adjusted ranging from the baseline of 0.25 to 0.05 to achieve convergence. The detailed tables of results related to these supplemental cases have been omitted and instead the resulting convergence rates have been summarized in Figure 4-22.

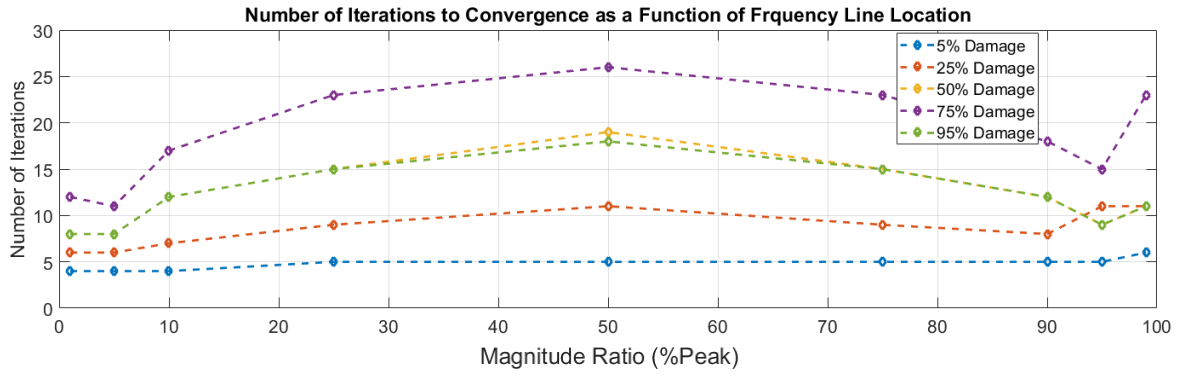

Figure 4-22: Plot of the number of iterations to convergence vs the magnitude ratio of the chosen frequency evaluation points.

It is clear from Figure 4-22 that frequency lines at the higher and lower ends of the spectrum produce convergence in fewer iterations. Although this faster convergence is desirable it does not come without consequence. Utilizing frequency lines which are located at a small percentage of the peak magnitude inherently have a lower SNR and lower coherence. Thus, in the presence of noise these lines will have to be used with caution. Likewise, frequency lines chosen at relatively large magnitude ratios must be chosen cautiously. As the frequency line approaches the peak value the rate of convergence decreases and appears to approach an infinite number of iterations as the frequency line ratio goes to one. Additionally, using higher magnitude ratios typically requires a smaller allowable step size as overshoots are not as robust to convergence. It is observed that frequency line ratios between 90%-95% produce convergence in the fewest number of iterations while also maximizing the likelihood of a high coherence measurement. As such, this ratio range is deemed to be ideal where values between 5% and 95% are suitable, pending the coherence filtering.

4.5.4 Effects of Increasing the Number of Frequency Lines

One of the key features of the current algorithm is the ability to add more frequency lines as the solution space becomes more complex. For these simple problems the addition of frequency lines does not significantly affect the outcome of the algorithm and thus a detailed discussed will be performed as it becomes relevant to the discussion in Chapter 5.

4.6 Effects of Noise

Up to this point the algorithm has been shown to be effective in identifying the correct parameters in a noise-free environment. While this is a very promising start, in practice there will certainly be measurement noise present on the measured strain PSD that will not be accounted for in the modeled response (with the exception of the noise covariance matrix weighting the objective function, as shown in equation (3-27)). To demonstrate the tolerance of the SHM algorithm to noise, three additional damage cases were studied, each incorporating varying levels of measurement noise.

The additive noise was introduced by transforming the strain PSD into the time domain using the inverse Fast Fourier Transform. Once in the time domain, a random, zero-mean, Gaussian noise was added such that the standard deviation of the noise was proportional to the standard deviation of the noise-free PSD [43, 98]. These noisy time domain signals were then transformed back into the frequency domain via the Fast Fourier Transform. For the i^{th} measurement at the n^{th} strain sensor location, the noisy signal was calculated as:

$$\breve{\varepsilon}_{n,i}(t) = \varepsilon_{n,i}(t) + \frac{\eta}{100}\sigma\left(\varepsilon_{n,i}(t)\right)N_{n,i}(t) \tag{4-16}$$

where $\breve{\varepsilon}_{n,i}$ is the noisy strain cross-correlation signal in the time domain, $\varepsilon_{n,i}$ is the original noise-free signal in the time domain, η the desired noise level, given as percent signal standard deviation, $\sigma(\varepsilon_{n,i})$ the standard deviation of the original signal and $N_{n,i}$ the generated random noise vector. For the current study, MATLAB was used to generate a Gaussian distribution which was uncorrelated both between sensor locations ("*n*") and measurement sets ("*i*"). A sample PSD of sensor two relative to sensor one, both before and after the addition of a twenty-five percent measurement noise (η = 25), is given in Figure 4-23.

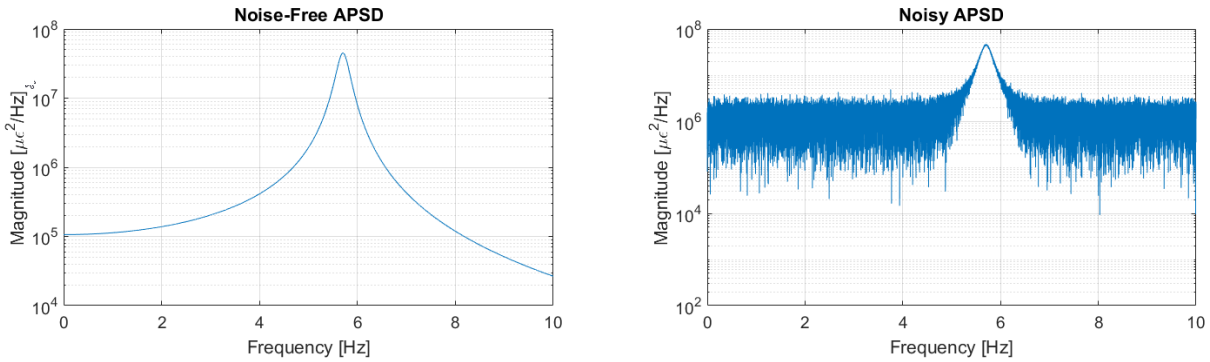

Figure 4-23: Noise free simulated measured response (left) and the same response with a noise level of twenty-five percent added (right) to the auto-PSD of strain location one.

The subroutine written to incorporate simulated measurement noise was developed to include the capability of computing multiple measurements sets. These multiple measurement sets were used to study the effects of spectral averaging and test the coherence-based frequency line selection method. The coherence-based frequency line selection method is an autonomous feature of the SHM algorithm which classifies and ranks potential frequency lines based on a number of factors, including coherence. For the current studies, spectral averaging was done using the standard linear averaging techniques and the coherence calculated using the ratio of cross and auto

power spectra [99]. An example of the resulting averaged PSD and coherence for the 25 percent noise, calculated with 10 averages, is given in Figure 4-24.

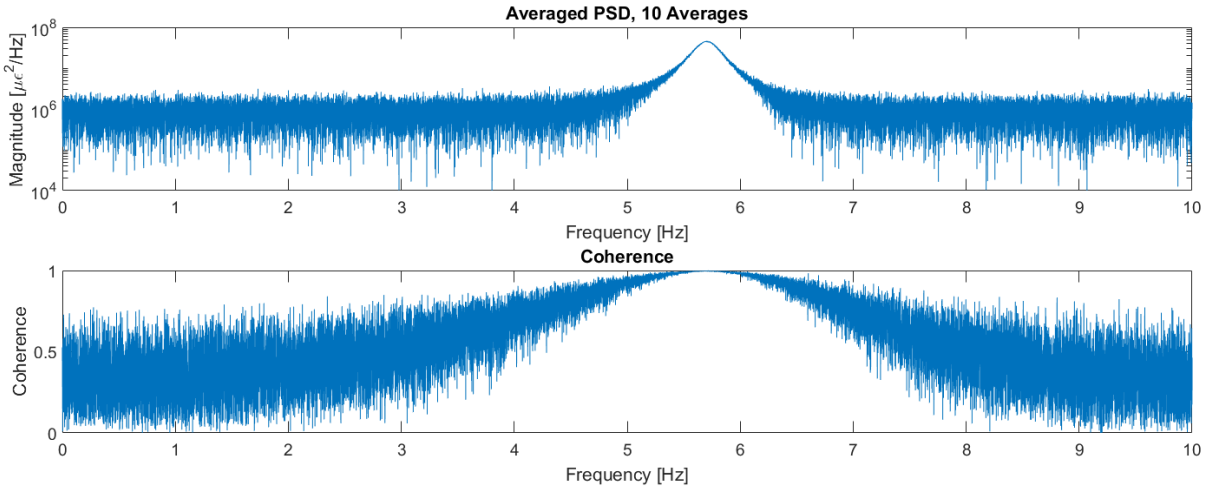

Figure 4-24: Simulated noisy PSD subjected to twenty-five percent measurement noise and the corresponding coherence for the PSD of strain location two relative to location one, calculated with 10 spectral averages.

The addition of the noise necessitated some changes to the input information for the SHM algorithm. The most notable change to the algorithm stems from the fact that the magnitude of the real and imaginary portions of the PSD vary by several orders of magnitude as shown in Figure 4-25. Figure 4-25 decomposed the noisy signal shown in Figure 4-23 into its real and imaginary components to demonstrate the relative magnitude between the two components. This discrepancy in magnitude means that a one percent noise, calculated relative to the magnitude PSD, affects the real and imaginary portions of the PSD differently. Once the one percent noise is added in the time domain, the signal is converted to the frequency domain. In the presence of the one percent noise, the real portion of the PSD experiences roughly one percent noise whereas the imaginary portion of the PSD response has an equal order of magnitude as the noise signal (approximately one-hundred percent noise).

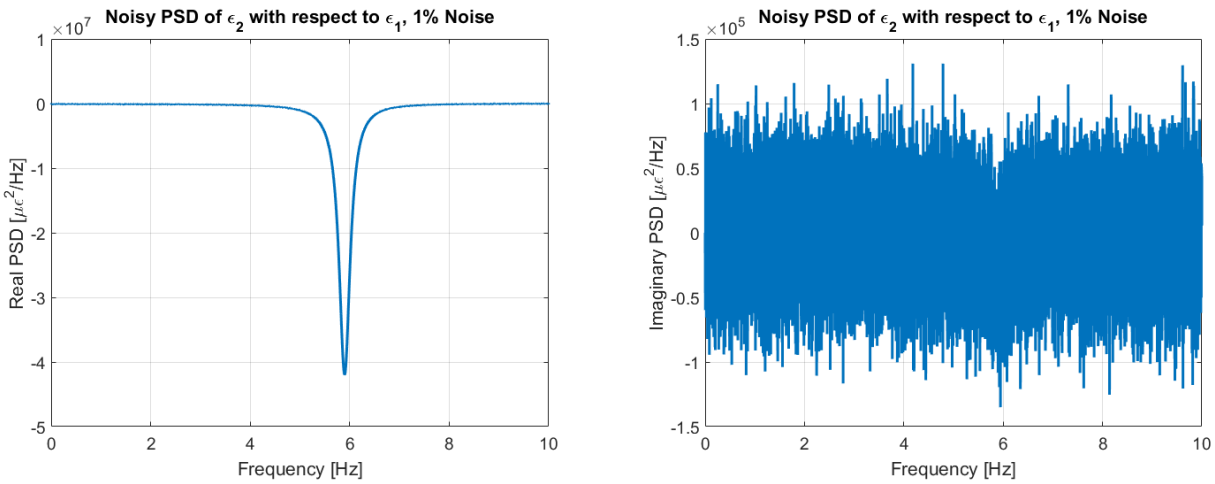

Figure 4-25: Simulated noisy PSD subjected to one percent measurement noise showing the difference in the impact the noise has on the real (left) and imaginary (right) portions of the PSD.

To give relevance to the noise levels and demonstrate the utility of the algorithm in the presence of noise, the batch-stacking process of the modeled and measured PSD was modified to use magnitude information, rather than real and imaginary components. Because the noise level was calculated relative to the PSD magnitude, the use of the magnitude PSD in the batch-stacking gives the current noise study the most relevance. In practice the real and imaginary portions of the signals would be used when they are nominally equal in signal-to-noise ratio (SNR). Whenever one signal dominates the other, as in the current case, it would be advantageous to use the dominate signal or the magnitude. While using the magnitude will always avoid these potentially large differences in SNR, in cases where the real and imaginary portions are similar in SNR using the real and imaginary portions give the maximum available information per frequency line. Maximizing the available information per frequency line becomes increasingly important in experimental work when limited high quality (high coherence) frequency lines may be available.

Three damage cases were studied with varying levels of noise to assess the algorithm's performance. To recover the loss of information associated with using magnitude only, an additional frequency line was chosen on each the model and measured PSD. These additional lines yielded a total of four frequency lines and thus effectively the same amount of information as the two frequency lines used in the noise-free cases previously presented. In all cases, a step-size limit factor of 0.25 was applied and the simulation run over a frequency range of 0 to 10 Hz. The three damage cases, each run for six noise cases, are presented in Table 4-8 with their respective results.

Table 4-8: Damage cases, noise levels, and converged system outputs for the eighteen noise test cases presented.

	Noise Level, η	δ_{EI} Converge	δ_{EI} % Error	δ_{ρ} Converge	δ_{ρ} % Error	Iterations
	0	0.9900	4.11E-10	0.9990	4.13E-10	4
Damage	0.1	0.9898	0.02	0.9988	0.0199	3
Case 1	1	0.9880	0.1996	0.9970	0.1994	4
	10	0.9828	0.7268	0.9916	0.7383	*
δ_{EI} = 0.99	25	0.9712	1.8964	0.9816	1.7382	*
δ_{ρ}= 0.999	50	0.9629	2.7354	0.9728	2.6222	*
	100	0.8027	18.9145	0.8127	18.6509	*
	0	0.9000	1.89E-13	1.0000	2.73E-12	7
Damage	0.1	0.9004	0.0424	1.0004	0.0445	8
Case 2	1	0.8990	0.1127	0.9989	0.1150	9
	10	0.8921	0.8730	0.9915	0.8528	9
δ_{EI} = 0.9	25	0.9026	0.2885	1.0033	0.3306	*
δ_{ρ}= 1	50	0.8707	3.2603	0.9683	3.1696	*
	100	1.0217	13.5194	1.1369	13.6911	*
	0	0.5000	3.35E-13	0.9000	3.21E-13	12
Damage	0.1	0.4999	0.0109	0.8999	0.0112	11
Case 3	1	0.5001	0.0141	0.9001	0.0157	*
	10	0.5022	0.4477	0.9041	0.4509	14
δ_{EI} = 0.5	25	0.4873	2.5347	0.8762	2.6471	*
$\delta\rho$=0.9	50	0.4954	0.9218	0.8933	0.7479	*
	100	0.4849	3.0294	0.8772	2.5292	*

* Convergence not achieved, parameters and error derived from minimum cost function value.

Damage case one represents a very small change in both parameters and provides perhaps the most realistic damage event. The second damage case is such that the stiffness has been reduced by ten percent and the density remains unchanged (although allowed to vary within the algorithm). The most severe damage case is presented in damage case three where the elemental stiffness has a fifty percent reduction with a corresponding ten percent reduction in density.

The results of all eighteen cases were that the algorithm performed well even under unrealistically large noise scenarios. In the presence of 100 percent noise the algorithm struggled to reliably identify the correct parameters, however it did yield a rough damage estimate. At realistic noise levels (one to ten percent) the algorithm repeatability identified the correct system parameters to an accuracy of less than one percent for all cases studied. The major drawback of the increased noise levels was the inability of the algorithm to converge in low SNR scenarios. While it is possible to relax the convergence criteria and achieve convergence, a penalty in terms of accuracy is incurred as a result. Rather than reduce the convergence tolerances, and in turn increase the error, it was decided to allow the algorithm to run for a maximum of thirty iterations. If the solution had not converged in thirty iterations, the damage scale factors were taken as the values of parameters which produced the minimum cost function value during the thirty iterations.

In all cases it was noted that the solution approached the true parameter values in roughly the same number of iterations as the corresponding noise-free cases. In the situations where noise was present on the signal, the parameters tend to oscillate about their true values, never satisfying the error requirement for convergence because of the noise present on the signal. The parameter values, as well as the error, cost function value, and change in parameters versus iteration number are shown in Figure 4-26 for damage case three with 25 percent additive noise. In Figure 4-26 it is observed that after nine iterations the solution has approached the true system parameters as the

error and cost function values are both approaching zero. As the iterations continue, the update parameter values oscillate about their true values until the iteration limit is reach.

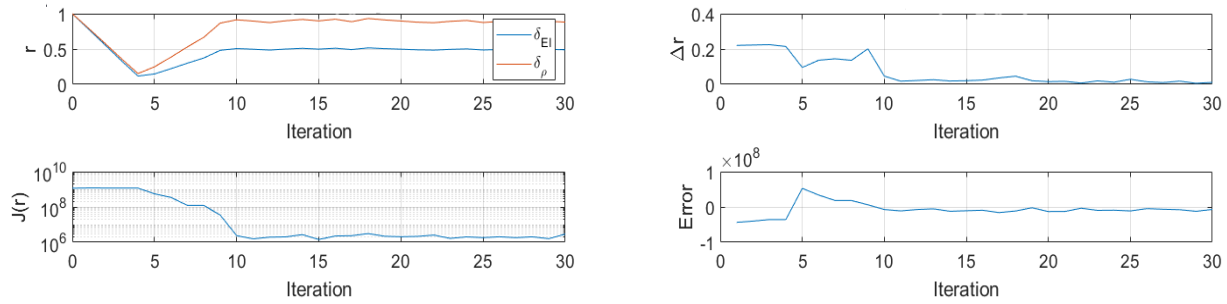

Figure 4-26: Plots of (clockwise from upper left) (1) the update parameter values, (2) norm of the change in parameters, (3) sum of the error vector and (4) cost function value as functions of iteration number.

Chapter 5: Analytical Validation of Full-Scale Test Article

The test article used for the validation of the work presented in this dissertation is a thin-wall rectangular carbon/epoxy beam. While the previous chapter utilized the basic geometry and properties of the beam, the analysis was restricted to a single Timoshenko beam element undergoing in-plane bending only. In the current chapter, the finite element model of the beam is expanded to allow for damage localization to be performed and provide a more realistic assessment of the algorithm's capabilities. Several damping models are considered and discussed with the intent of accurately modeling experimental data. Parametric studies are performed which capture the algorithm's performance in terms of computational time and memory as well as converged parameter error. The capabilities of the algorithm are also compared against contemporary SHM methodologies in the final section of the chapter.

5.1 Description of Expanded Analytical Problem

In the current chapter, the thin-walled composite beam model presented in Chapter 4 is refined. In order to capture the three-dimensional behavior of the beam, the Timoshenko beam FEM is expanded to include axial and torsion behavior so that there are six DOF per node. Additionally, a variable number of elements were used in the FEM definition. A generic representation of a "*n*" element beam is shown in Figure 5-1.

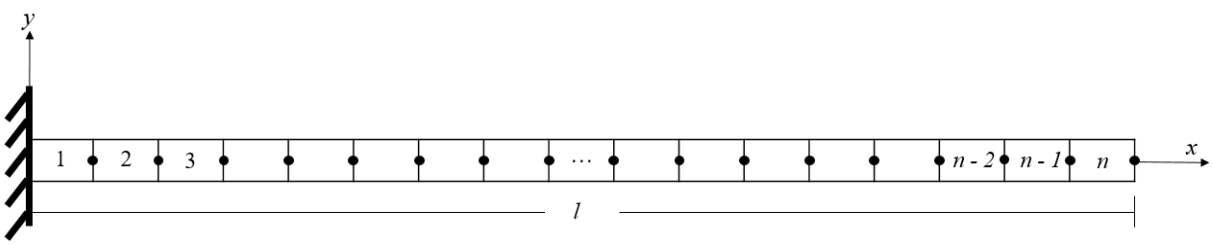

Figure 5-1: Thin-walled composite cantilever beam represented by "*n*" Timoshenko beam elements.

Looking at the "i^{th}" element, the nodal degrees of freedom of each of the n elements are given in Appendix A and repeated here for clarity as given in Figure 5-2.

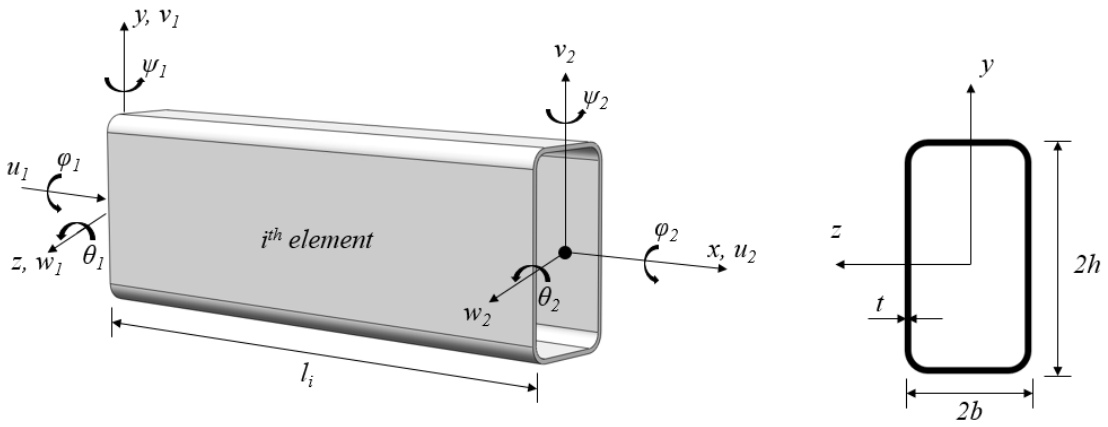

Figure 5-2: Degrees of freedom associated with the i^{th} element of the Timoshenko beam model of the thin walled composite beam.

The system matrices for the beam elements were developed using Timoshenko beam bending theory with decoupled axial and torsion behavior, as shown in Appendix A. For simplicity, it is assumed that the axial, bending, and torsion behavior are uncoupled so that the shear center is aligned with the beam's centroid. As was done in Chapter 4, a baseline problem description is established in this chapter and all subsequent comparisons are made to this baseline configuration. In order to adequately justify the selection of the baseline problem, the following subsections delve into the challenges and features associated with the current algorithm.

In anticipation of the build up to the experimental testbed, the baseline system properties have been chosen to match those of the experimental setup discussed in Chapter 7. The cross section of the beam is uniform and the section properties were calculated using the geometry given in Figure 5-2. The baseline parameters for the geometric and material properties of the beam,

modeled after an existing thin-walled carbon/epoxy beam, are given in Table 5-1. A detailed discussion of the development of the beam's properties is given in Chapter 7.

Table 5-1: Baseline system parameters.

l (in)	b (in)	h (in)	t (in)	A (in^2)	I_{zz} (in^4)	I_{yy} (in^4)	k_s	E (lb/in^2)	G (lb/in^2)	ρ ($lb\text{-}sec^2/in^4$)
92	0.5	1	0.04	0.243	0.134	0.483	0.65	4.42E+06	2.90E+06	1.20E-04

5.2 Selection of the Model Size

While it is the design of the framework to allow for SHM of full-scale aerospace structures utilizing finite element models with thousands, or even hundreds of thousands, of degrees of freedom, the current method is prohibitively computationally expensive using commercial analysis software (MATLAB) and a "typical" current desktop computer. The greatest expense comes in terms of inverting the dynamic stiffness matrix needed to generate the model PSD. The reader is reminded that the dynamic stiffness matrix, given in equation (3-9), contains the system matrices formulated in terms of the unknown system parameters being updated. As a result, the dynamic stiffness matrix is symbolic and hence computationally expensive to store and invert, in terms of required system memory. It is important to understand the relationship between computational cost and algorithm performance and as such a series of benchmark tests were conducted. All of the benchmarking presented in the current work were done on a Dell T3500 desktop computer, the specifications of which are given in Table 5-2 below, in conjunction with MATLAB 2017a.

Table 5-2: Specification of computer used for bench marking.

Operating System	*Build Date*	*Processor*	*Number of Cores*	*Clock Speed*	*RAM*	*Virtual Memory*
Windows 10 Pro	2013	Intel Xeon X5660	6	2.80GHz	24GB	105GB

The direct application of the algorithm requires the inversion of the symbolic dynamic stiffness matrix. By inverting the matrix symbolically, quick substitutions can be made for specific frequency domain and parameter values making this direct symbolic inversion desirable. The drawback however lies in the fact that symbolic inversion is extremely memory intensive as MATLAB must store large strings of symbolic characters rather than efficient double precision numbers. For the symbolic inversion studies, test cases were run varying the number of elements in the model and studying the relationship between the number of elements, the memory required for the inversion, and the time to symbolically invert the matrix.

Comparisons were made between the inversion of fully and sparsely populated dynamic stiffness matrices. In the current study (and in the case of most large-scale FE models) the system matrices are sparse and this property can be used to one's advantage in terms of storage and algebraic manipulations. It is important to note that this sparse form of the dynamic stiffness matrix is, in general, valid if the damping model has the same connectivity as the mass and stiffness matrices, or is proportional to the mass and stiffness matrix (Rayleigh damping). Using damping models such as extended Rayleigh, modal or generalized proportional damping can lead to a fully populated damping matrix and in turn a fully populated dynamic stiffness matrix. The impact of the choice of the damping matrix chosen will be extensively discussed in subsequent sections of this chapter.

In the current study, the sparse dynamic stiffness matrix was of block tridiagonal form and the methodology of Reuter and Hill [100] was implemented in MATLAB to perform symbolic inversion. Figure 5-3 provides a graphical summary of the amount of memory and time required to perform these symbolic inversions of the sparse dynamic stiffness matrices using the Reuter and

Hill approach versus the standard MATLAB inversion function (inv) on a fully populated dynamic stiffness matrix.

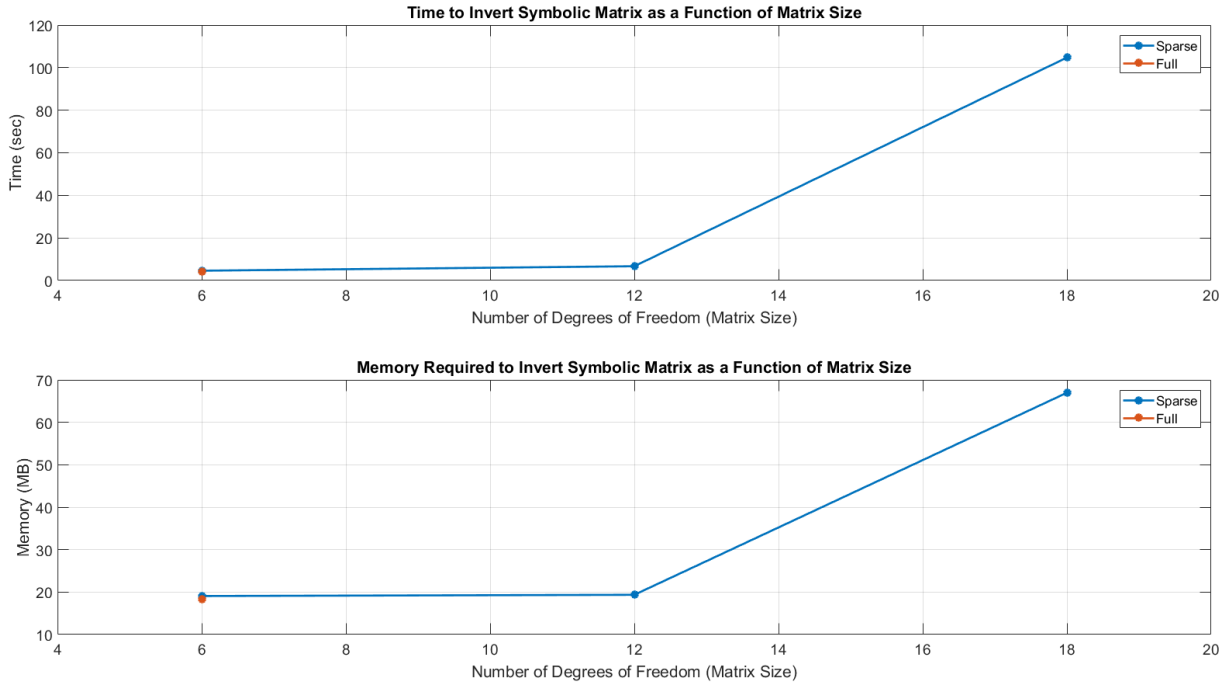

Figure 5-3: Time and memory required to invert a symbolic dynamic stiffness matrix for various model sizes.

In Figure 5-3 it is noted that the memory required to symbolically invert the fully populated matrix is only possible on a single cantilever beam element system (which corresponds to a 6x6 matrix). In the case of the single element the sparse and full matrices are indeed the same as indicted by the nearly overlapping blue and orange dots in Figure 5-3. Adding a second element doubles the number of DOF and in turn the size of the dynamic stiffness matrix to 12x12. On the current machine, this 12x12 symbolic inversion requires more memory than the approximately 130GB of RAM and virtual memory available to MATLAB. From the MATLAB website [101], the amount of memory required to perform symbolic inversion of a fully populated matrix can be approximated as:

$$\text{Memory Required} \cong 2.2x10^{N}\ Bytes \tag{5-1}$$

where N is the size of the square matrix being inverted. In the case of a 12x12 this would roughly correspond to 2.2 terabytes. Using this approximation, the largest matrix the current desktop could symbolically invert is a 10x10. Subsequent trial runs confirmed this to be the case.

Empirical studies performed on the block tridiagonal matrix formed using a Rayleigh damping model showed that only three elements (18x18 matrix) may be symbolically inverted before exhausting the available system memory. In both the full and sparse cases, this is a prohibitively small number of elements. While it is a certainty that computation power and memory availability will increase with time, the amount of time required to solve meaningful problems utilizing symbolic inverse of the dynamic stiffness matrix would be astronomical.

In order to circumvent the limiting number of elements able to be symbolically inverted, a workaround in the current algorithm was implemented. The workaround utilizes the fact that numerical inversion is orders of magnitude faster and less memory intensive than symbolic inversion. To this end, the dynamic stiffness matrix is formed symbolically as previously described and then converted to a MATLAB function. The advantage of a MATLAB function is that it allows rapid and efficient (from a memory standpoint) dynamic stiffness matrix evaluations. Once the MATLAB function is formed, the dynamic stiffness matrix is evaluated at the current parameter set repeatedly over the desired frequency domain prior to being inverted. This allows for numeric inversion of the dynamic stiffness matrix and in turn much larger problems to be solved. The studies previously performed using symbolic inversion were repeated using numeric inversion and their result presented in Figure 5-4.

While this numeric inversion does aid in the limitation of model size restrictions, it does not completely alleviate it. The major drawback is the requirement that the PSD model be numerically calculated and stored at each value of frequency relative to the analysis. When the frequency lines being utilized are fixed this can be a very small number and take up little memory however when frequency line updating is in use a large number of frequency lines must be calculated and used to update the current iteration's frequency line set. Furthermore, just as was the case for symbolic inversion, numeric inversion is much more efficient on sparse matrices stemming from the use of a Rayleigh damping model. More sophisticated damping models require fully populated matrices be stored and operated on and in turn limit the size of the problems which may be studied using current computing technologies.

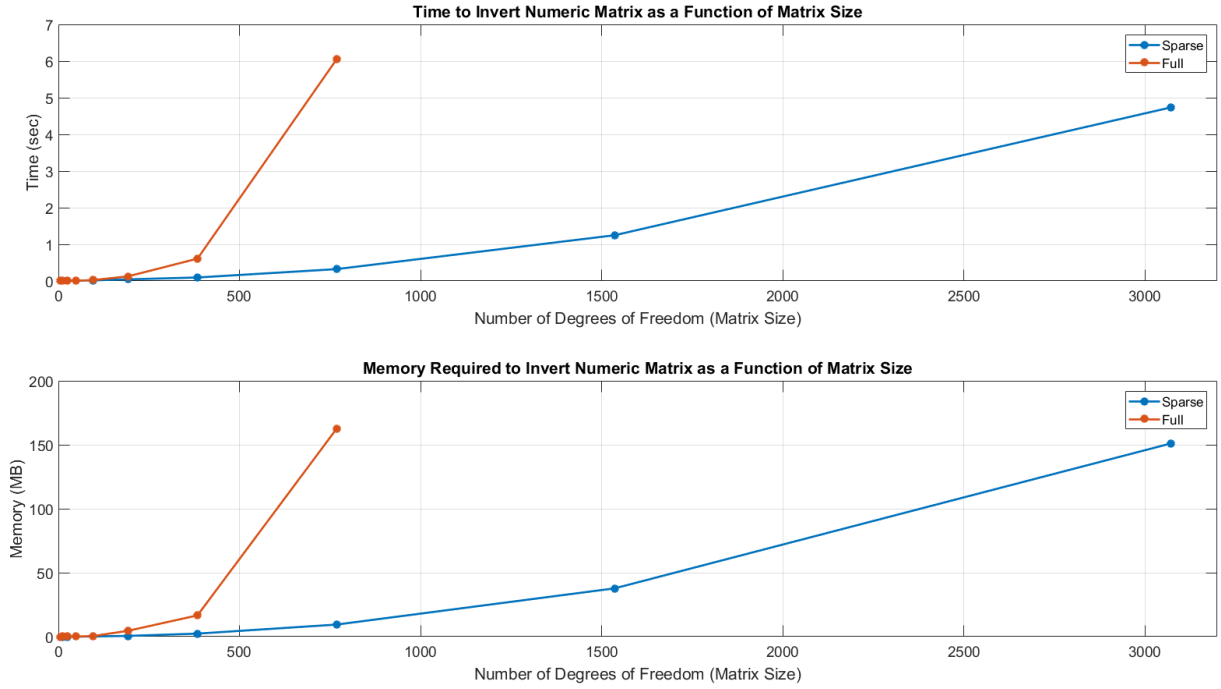

Figure 5-4: Time and memory required to invert a numeric dynamic stiffness matrix for various model sizes.

The numeric inversion of the dynamic stiffness matrices shown in Figure 5-4 was computed to provide an accurate comparison between the limiting factor of inverting the symbolic

and numeric dynamic stiffness matrix, however it does not provide the entire picture. In practice the inversion of the dynamic stiffness matrix is an intermediate step in the calculation of the model PSD, in accordance with equation (3-21). In order to provide a more accurate assessment of the capabilities of the algorithm on the current desktop computer, the analysis was repeated. This time the performance metric was the time and memory required to numerically calculate the model PSD for a given number of elements, over a given number of frequency lines. In this case, parallel processing was utilized on the looped calculation over the number of frequency lines being calculated. On the current system this translates to each of the six cores simultaneous computing a model PSD at a given frequency line. While this parallel processing speeds up the computation by roughly a factor of six, it also increases the dynamic memory used in the computation which is more difficult to reliably benchmark.

The total static memory required to store the model PSD is what is reported in Figure 5-5 and is independent of the use of parallel processing. It is known that the dynamic memory required to perform these calculations is higher than the static memory required to store the resulting PSD and as such these numbers are for comparison purposes only and cannot be directly extrapolated to find the maximum number of elements possible on the current system. Those limits were roughly established via trial and error, doubling the number of elements in the model until the computation was terminated due to insufficient system memory.

Due to the fact that a large number of variables are being explored in this chapter, the number of elements used in the analyzes has been restricted to 18. This provides a good compromise of modeling accuracy, computational speed, and theoretical complexity under which the algorithm is evaluated. Subsequent analysis has shown that increasing the number of elements in the model has little to no impact (aside from computational time) on the generated solution. The

major advantage of including additional elements is to refine the size of the damage region, which is limited to the size of the elements modeling the structure and in turn being represented as the damage parameters.

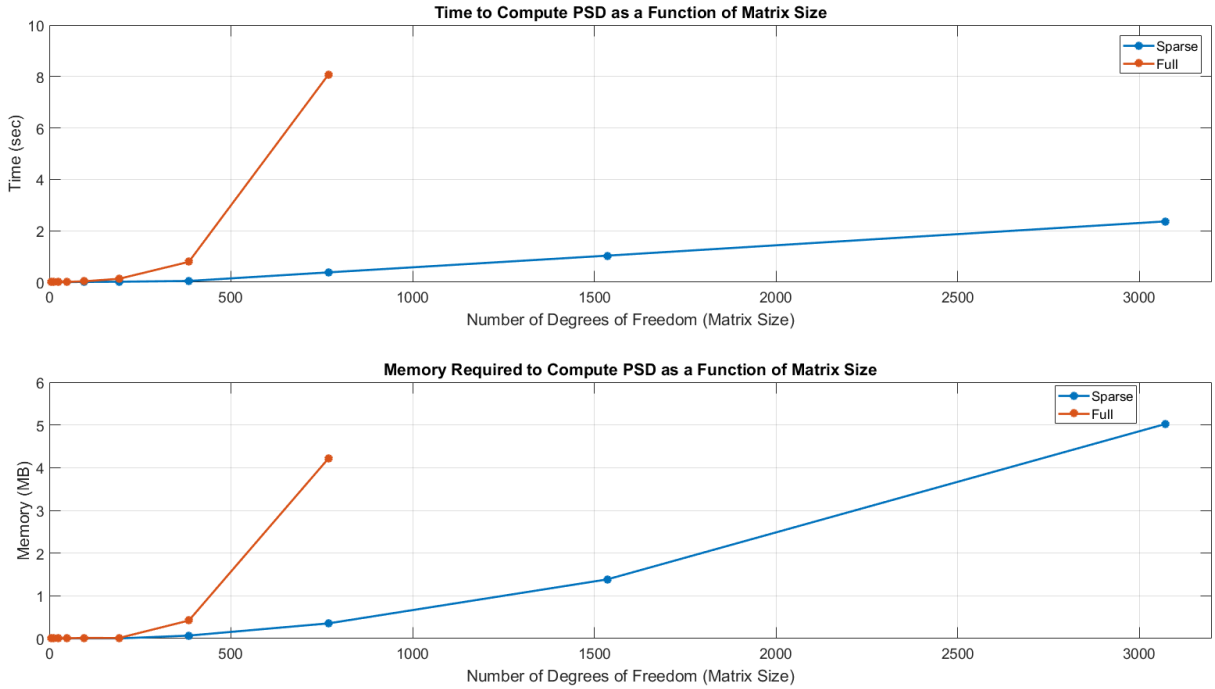

Figure 5-5: Time and memory required to calculate the model PSD as a function of model size.

As alluded to earlier, the amount of time it takes to generate the model PSD not only depends on the model size selected but also on the number of frequency lines used in the analysis. In order to provide a complete picture of the capabilities of the algorithm on the current desktop computer an additional analysis was done comparing the time and memory required to compute the model PSD for a system with 16 elements (96 DOF), 32 elements (192 DOF) and 64 elements (384 DOF) and varying numbers of frequency lines. Figure 5-6 provides the results of this study of varying number of frequency lines.

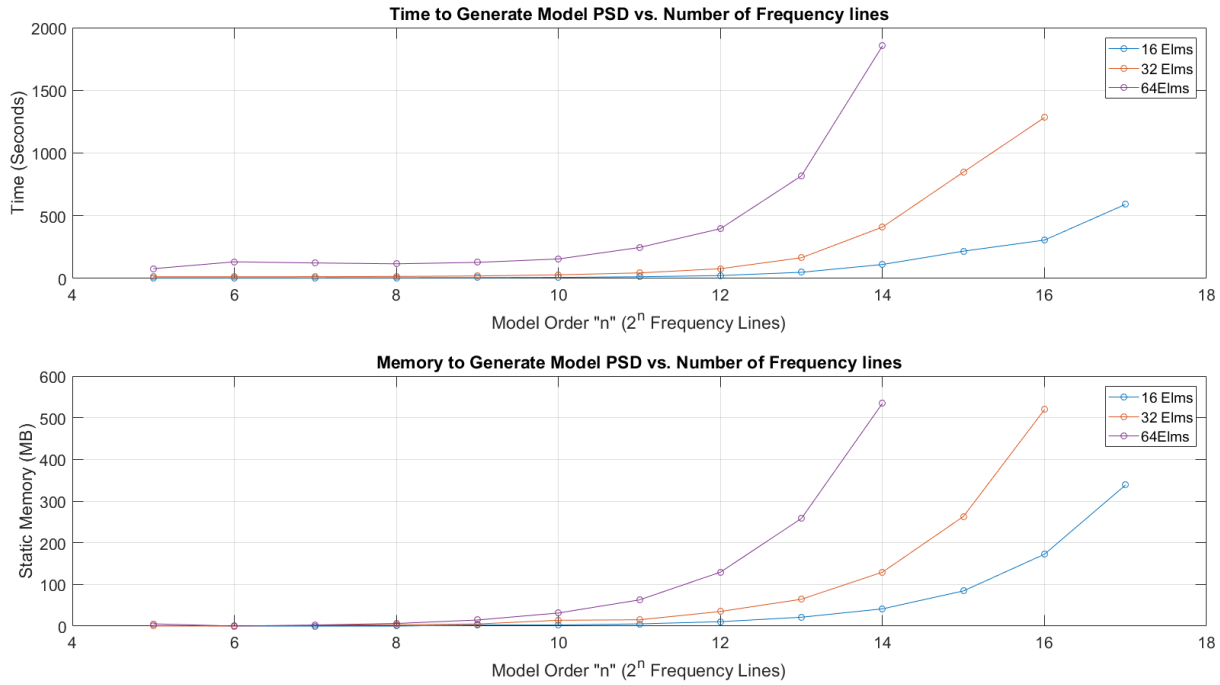

Figure 5-6: Time and memory required to calculate the model PSD as a function of number of frequency lines.

It is recommended that the model be computed with as few frequency lines as possible to maximize computational efficiency. In theory, best practice would be to compute the model PSD in only the regions where the coherence of the measured PSD is high. In practice, it is likely an evaluation of the model PSD across a broad frequency range will be necessary the first iteration of the algorithm to make informed choices of the frequency lines of interest. Subsequent iterations of the algorithm should allow for fewer and fewer model PSD calculations as the modeled and measured PSD begin to converge.

5.2.1 PSD Convergence Studies

Above and beyond the convergence of the modal parameters over the modes of interest, the FE model must contain enough elements to allow for convergence of the PSD themselves. This ensures that the model PSD, when coupled with the correct physical parameters, will accurately represent the experimental behavior of the structure over the frequency range of interest. One

feature of the strain-displacement transformation is the ability to evaluate the strain at any point within the element. This fact was utilized and the code was modified such that the strain response at any location along the beam's length could be simulated, regardless of the number of elements in the model. To this end, the strain auto-PSD was simulated at a location 10" from the root of the beam for varying model size. The PSD of the baseline problem for various model sizes at 10" from the root is given in Figure 5-7.

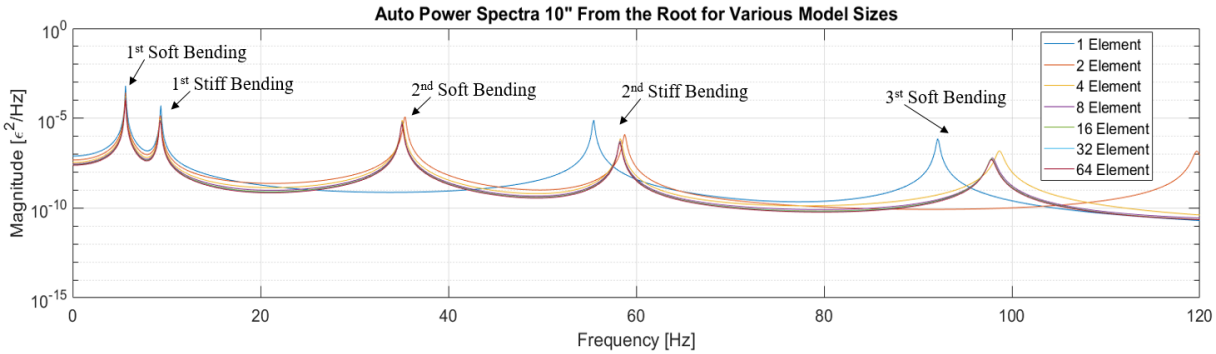

Figure 5-7: Auto-PSD of a simulated strain sensor 10" from the root for various model sizes.

For the current beam model, over the first five modes being studied, it was shown that models containing 16 or more elements produce virtually identical PSD as shown in Figure 5-7. Because of the large number of problems being studied in the current chapter, as well as the non-linear relationship between model size and computational time, an 18 element FEM has been defined as the baseline system. Incorporation of more elements does not affect the performance of the algorithm with two exceptions (1) computation time and (2) accuracy of the effective damage parameters for small damage events. The former of these exceptions has been addressed in this section and the latter will be discussed in detail in subsequent sections.

5.3 Damping Model Selection

The selection of the damping model is crucial to the operation of the algorithm from the standpoint of minimizing error. The algorithm functions based on the assumption that the model of the undamaged structure accurately represents the physical (measured) behavior prior to a damage event. This implies that the damping model needs to accurately reflect the damping in the structure to the extent that the model and measured PSD have minimal error in the regions of high coherence used in the model updating. As discussed in the previous section, it is advantageous for the maximum available model size and the computational speed of the algorithm to use the simplest (i.e. sparsest) damping model which accurately models the physical system's behavior.

To evaluate the accuracy of the PSD under differing damping models, a variety of proportional damping models were studied and their performance documented. The performance evaluation was based on the damping model's ability to recreate the damping ratios that were experimentally observed. The possible damping models explored in this section are Rayleigh, Extended Rayleigh, Modal and Caughey. The details of each of these damping models are given in Appendix B and omitted here.

In the current section, the quality of the proposed damping models is assessed by comparing the experimental damping constant (ζ) to those damping constants extracted from the model PSD, constructed using the identified modal parameters. Two methods were used to estimate the damping factors from the model PSD; curve fit of the PSD and state-space calculations. Curve fitting was done using a custom function written in MATLAB [102] based on MATLAB's "modalfit" function. The code loads the relevant model PSD and plots the stability diagram of the PSD peak of interest. From the stability diagram, a suitable model order is chosen for each mode which produces a stable model in both frequency and damping. Using the chosen

model order, a localized least-squares complex exponential fit was performed on each mode, fitting a set of complex damped sinusoids using Prony's method [103].

Figure 5-8 provides an example of the generated stability plot and curve fit for one of the damping models and modes of interest. The process is repeated, where in the case of the current model the modes are well separated and curve fit done independently. The method is also applicable for closely spaced modes in which case a global, rather than local, polynomial fitter must be used to resolve the closely spaced modes.

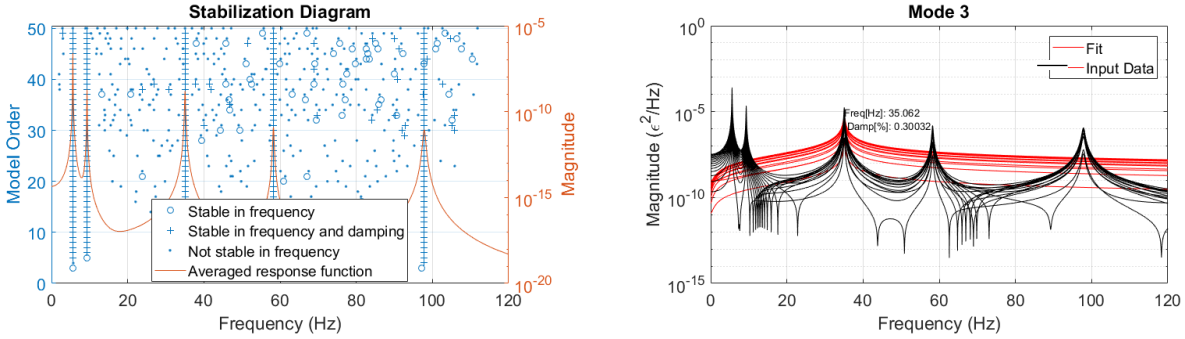

Figure 5-8: Stability diagram and curve fit CPS and modal parameters used to estimate damping ratio and damped natural frequencies.

With regards to modal parameter extraction using state-space modeling, standard modal identification techniques were used. The important results of state-space modeling of dynamics systems is given in the subsequent equations however for a thorough explanation the reader is referred to Rao's book on the topic [104]. In state-space form, the equations of motion given in equation (3-1) are written as:

$$\begin{bmatrix} [M] & [0] \\ [0] & [M] \end{bmatrix} \begin{Bmatrix} \{\dot{x}(t)\} \\ \{\ddot{x}(t)\} \end{Bmatrix} + \begin{bmatrix} [0] & -[M] \\ [K] & [C] \end{bmatrix} \begin{Bmatrix} \{x(t)\} \\ \{\dot{x}(t)\} \end{Bmatrix} = \begin{Bmatrix} \{0\} \\ \{f(t)\} \end{Bmatrix} \tag{5-2}$$

Assuming a harmonic, free-vibration response, the transient response may be written as:

$$\begin{Bmatrix} \{x(t)\} \\ \{\dot{x}(t)\} \end{Bmatrix} = \{\psi\} e^{\lambda t} \tag{5-3}$$

and the derivative of the response as:

$$\begin{Bmatrix} \{\dot{x}(t)\} \\ \{\ddot{x}(t)\} \end{Bmatrix} = \lambda \{\psi\} e^{\lambda t} \tag{5-4}$$

premultiplying (5-2) by $[M]^{-1}$ and substituting in (5-3) and (5-4) results in the state-space form of the equations of motion in the standard eigenvalue form:

$$\left[\begin{bmatrix} [0] & [I] \\ -[M]^{-1}[K] & -[M]^{-1}[C] \end{bmatrix} - \lambda \begin{bmatrix} [I] & [0] \\ [0] & [I] \end{bmatrix} \right] \{\psi\} = \begin{Bmatrix} \{0\} \\ \{0\} \end{Bmatrix} \tag{5-5}$$

The solution of the eigenvalue problem given in (5-5) yields a set of complex conjugate pairs of eigenvalues λ and eigenvectors $\{\psi\}$. For the current structure being modeled, the system will always be underdamped and hence have a damping ratio less than critical. In this case, the natural frequencies of the system are related to the real and imaginary portions of the eigenvalues by:

$$\omega_n = \sqrt{\lambda_{\mathrm{Re},n}^2 + \lambda_{\mathrm{Im},n}^2} \tag{5-6}$$

and the damping ratio also related to the eigenvalues and frequencies by:

$$\zeta_n = \frac{-\lambda_{\mathrm{Re},n}}{\omega_n}. \tag{5-7}$$

With the damping ratios and natural frequencies determined, the damped natural frequencies are given as:

$$\omega_{d,n} = \omega_n \sqrt{1-\zeta_n^2} \tag{5-8}$$

A MATLAB script was written which takes the system matrices as inputs and returns the damped natural frequency and damping ratios using equations (5-5) thru (5-8). The results of both the state-space and curve fitting analysis for each of the damping models considered are listed in Table 5-3 along with the experimental values used to generate the model damping matrix.

Table 5-3: Experimental and extracted modal parameters for the damping models under consideration.

		f_1 [Hz]	ζ_1 [Hz]	f_2 [Hz]	ζ_2 [Hz]	f_3 [Hz]	ζ_3 [Hz]	f_4 [Hz]	ζ_4 [Hz]	f_5 [Hz]	ζ_5 [Hz]
	Experimental	5.260	0.030	8.830	0.048	32.400	0.105	53.700	0.151	90.500	0.360
Modal	**Curve Fit**	5.610	0.031	9.320	0.045	35.100	0.105	58.300	0.151	97.800	0.360
Damping	**State Space**	5.607	0.031	9.324	0.045	35.062	0.105	58.257	0.151	97.833	0.378
Rayleigh	**Curve Fit**	5.610	0.043	9.320	0.045	35.100	0.117	58.300	0.250	97.900	0.635
Damping	**State Space**	5.607	0.043	9.324	0.046	35.062	0.116	58.257	0.249	97.833	0.629
Caughey	**Curve Fit**	5.610	0.021	9.330	0.024	35.100	0.059	58.200	0.067	97.799	0.214
Damping	**State Space**	5.607	0.021	9.324	0.023	35.062	0.057	58.257	0.074	97.833	0.203
Extended	**Curve Fit**	5.610	0.031	9.320	0.046	35.100	0.113	58.200	0.153	97.900	0.409
Rayleigh	**State Space**	5.607	0.031	9.324	0.046	35.062	0.113	58.257	0.173	97.833	0.421

In order to more easily visualize the accuracy of each of the proposed damping models, the frequencies and damping ratios were normalized by their experimental values and plotted versus mode number for the first five modes. Figure 5-9 shows these normalized damping values for each of the studied models.

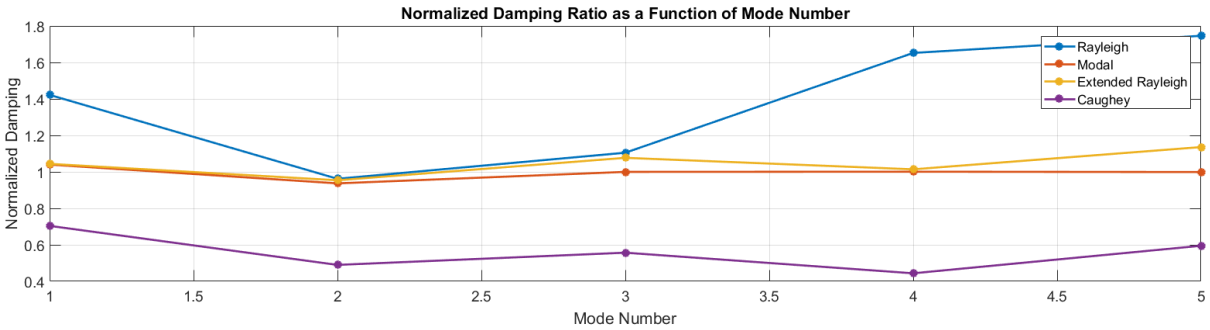

Figure 5-9: Normalized damping ratios for the first five modes.

In the case of the Rayleigh damping model, the values of the proportionality constants were determined by solving a system of equations using two modes as inputs. These two modes were chosen as modes 2 and 3 which is why the agreement between the experimental and the modeled damping values are so close for these modes. Away from these modes the extracted model damping values are on the correct order of magnitude but the Rayleigh damping struggles to correctly extrapolate damping across the modes not used in the initial calculation of the proportionality constants. Caughey damping also struggles to reproduce the experimental damping ratios largely due to the numerical error associated with the well separated modes chosen in the analysis. Selection of a cluster of low frequency modes tend to perform better with Caughey damping. Both modal damping and extended Rayleigh damping models do a good job of accurately reproducing the correct damping ratios with modal damping performing slightly better. As a result, modal damping has been chosen to be implemented throughout the remainder of this dissertation where possible. The impact that the damping model has on the form of the PSD is shown in Figure 5-10.

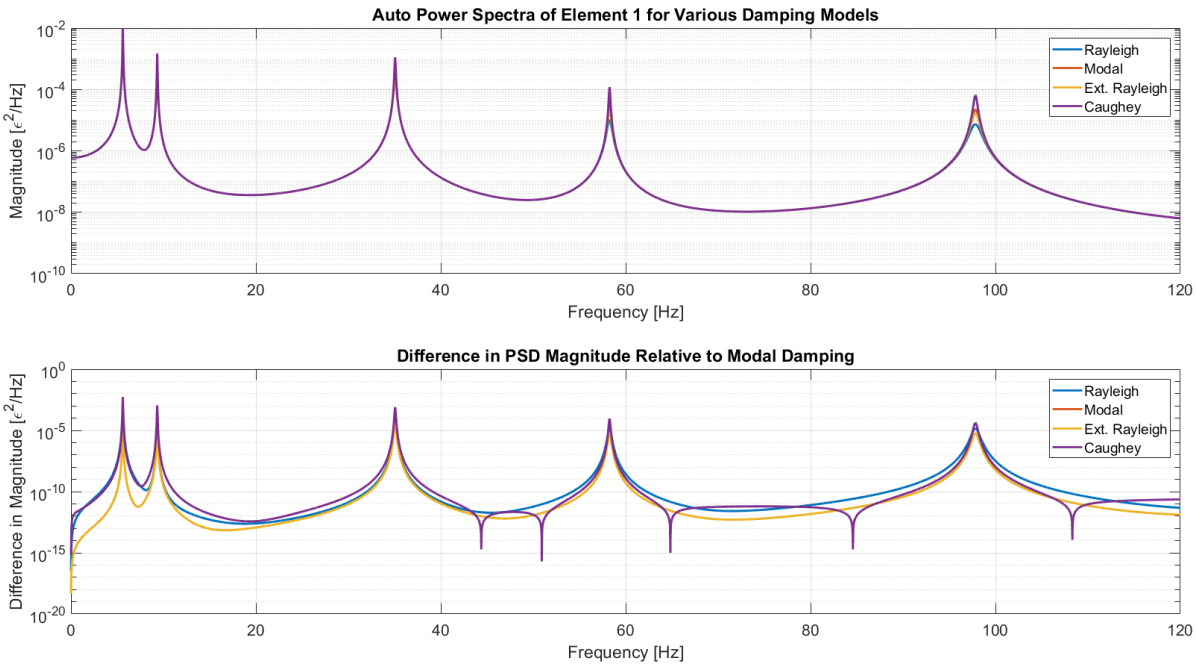

Figure 5-10: (Upper) Comparison between the model PSD generated with the damping models under consideration. (Lower) Difference in PSD magnitude of the generated models relative to the modal damping PSD.

From the upper plot in Figure 5-10, it is observed that the damping model chosen plays a very small role in the form of the PSD except near the PSD peaks. Thus, choosing frequency lines away from the peaks reduces the impact the damping models have on solution quality. The lower plot in Figure 5-10 shows the absolute value of the difference in the magnitude of the PSD computed using the modal damping model as a baseline.

The final aspect to consider in terms of the damping model is the convergence of the modal parameters generated by such a model. Since the modal damping model has been adopted for the remainder of this dissertation, the convergence of the predicted modal parameters as a function of model size was calculated and plotted in Figure 5-11 to verify the modal parameters returned from the developed model remain constant with model size for a reasonable number of elements.

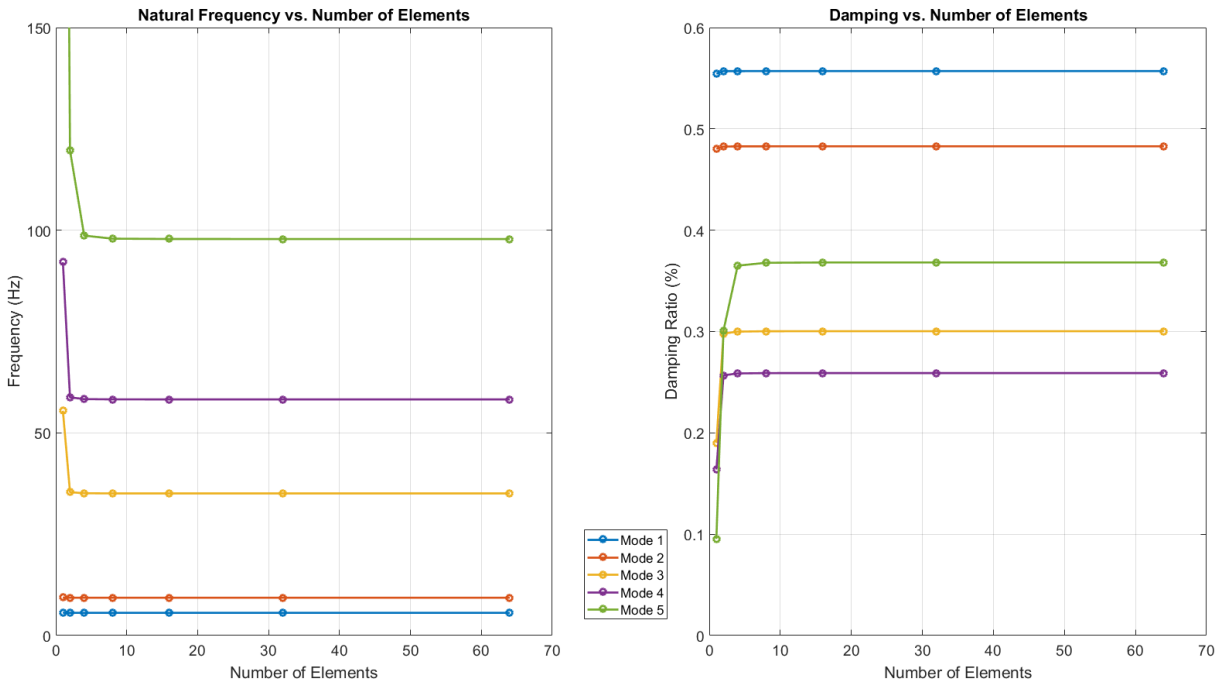

Figure 5-11: Modal parameters as a function of model size using modal damping.

5.4 Algorithmic Additions

As the solution space becomes more complex additional features must be incorporated into the algorithm to aid in efficient and stable convergence of the updating process. For the results presented in this chapter, three additional features were added to the algorithm's operation which ensure such behavior. Coherence based frequency line selection helps provide only the best available information as inputs to the algorithm. Parameter sensitivity screening ensures only parameters which contribute in a meaningful way to the parameter update are included in the update at each iteration. Element grouping and selective element inclusion help select elements such that the parameter sensitives will be large enough to be meaningful and exclude elements which have a low signal-to-noise ratio. The details of each of these additions are given in the following sections.

5.4.1 Coherence Based Frequency Line Selection

The inclusion of realistic noise on the measurement signal necessitates a change in the way frequency line selection should be carried out. Previously, frequency lines were chosen as ratios of the modal peak magnitudes, without regard for the quality of the measurements at these frequency locations. In measurement data sets there is inherent noise which impacts different frequency lines in different ways. Some lines, particularly those near resonance, will experience very little noise degradation whereas frequency lines at lower magnitudes often suffer from low SNR and hence may provide poor quality information to the algorithm. These low-quality frequency lines at best increase the covariance matrix, leading to larger errors in the converged solution, and at worst lead to incorrect solutions.

To combat the selection of frequency lines of low quality, an additional layer of filtering is done on the selected PSD lines. The average measured PSD (and in the case of the current chapter, simulated PSD measurements) sets are computed by iteratively implementing equation (5-9) for $i = 1$ to N, where N is the number of spectral averages desired:

$$\left[\tilde{S}(\omega)\right]_{Ave,i} = \frac{1}{i}\left[\tilde{S}(\omega)\right]_i + \left(1-\frac{1}{i}\right)\left[\tilde{S}(\omega)\right]_{Ave,i-1} \tag{5-9}$$

In addition to the average PSD computation, the enhance frequency line selection criteria depends upon the coherence of the averaged PSD. In order to apply such screening, the coherence of the measurement signal is calculated using the magnitude-squared coherence between the PSD of the k^{th} roving DOF and m^{th} reference DOF taken after N spectral averages is given as:

$$\gamma^2_{k,m}(\omega) = \frac{\left|\tilde{S}_{k,m}(\omega)\right|^2}{\tilde{S}_{k,k}(\omega)\tilde{S}_{m,m}(\omega)} \tag{5-10}$$

The enhanced frequency line selection criteria first computes the average PSD and coherence in accordance with equations (5-9) and (5-10). The candidate frequencies are then down selected such that only values between 10 percent and 95 percent of a given modal peak are considered. An additional layer of filtering identifies all frequency lines which have a coherence value greater than a predefined threshold. The set of frequency lines contained in the intersection between the percentage peak and coherence thresholding are identified as protentional lines for updating. From there the operator has a number of options as to selecting frequency lines, namely:

(1) Manually input desired frequencies.
(2) Select frequencies based on ratios of peak-magnitude. In this case the algorithm searches for the frequencies nearest the identified ratios which meet the coherence criteria.
(3) Select all lines which meet both the percentage peak and coherence selection criteria.

The interdependency between the choice of frequency lines and the performance of the algorithm is explored in detail in subsequent sections.

5.4.2 Parameter Sensitivity Screening

While it is the goal of the algorithm to be robust enough to identify any update parameter desired, in practice this objective is not always possible. In particular, the parameters of interest must impact the portion of the PSD which the sensors can monitor as well as provide adequate sensitivity to potential damage scenarios. The extent of which parameter sensitivity creates problems in the updating routine depends on the specific instrumentation, modeling scheme, and desired damage scale factors of the structure being studied. In the current development, Timoshenko beam elements are being used to model the response of a thin-walled carbon beam.

Since Timoshenko beam elements are being used in the model, beam section properties are the logical choice for the update parameters within the algorithm.

Eight beam section properties were identified as potential update parameters within the current demonstration. Specifically, these parameters are axial stiffness (EA), bending stiffness about y and z (EI_y and EI_z), shear area stiffness about y and z (GA_{sy} and GA_{sz}), torsional stiffness (GJ), mass per unit length (ρA), and mass times the polar moment of inertia (ρI_p). It is emphasized that these parameters can be chosen to best suit the modeling and structural configurations and meet the end objective of damage identification. The only limit on the desired update parameters is they must be included in the formulation of the dynamic stiffness matrix and/or strain-displacement transformation matrix. In the current work, it is assumed that the beam properties and cross section are such that the shear center is coincident with the centroid. Moreover, damage is such that the shear center remains aligned with the centroid.

Scaling of the sensitivities is one of the more challenging aspects in the current work. Sensitivities of the model PSD with respect to each update parameter are required in the updating scheme and are calculated using a second order central difference approach. Although each parameter is scaled such that its influence in the solution space is uniform, the sensitivities cannot be scaled in such a manner. Certain parameters inherently impact the formulation of the PSD more so than others and these discrepancies can manifest themselves as sensitivities differing by orders of magnitude.

Within the current routine, as with all sensitivity-based updating methods, parameters with sensitivities varying by orders of magnitudes tend to lead to a lack of robustness and often incorrect solutions. The largest reason behind these unstable solutions is the fact that a parameter which has

negligible impact on the model PSD, with respect to other update parameters within the solution space, can "wonder" wildly within the solution space having little to no impact on the error metric. To demonstrate the vast differences in parameter sensitivity between the identified eight potential update parameters, plots of each parameter's absolute sensitivity as a function of frequency are given in Figure 5-12 for the baseline 18 element FEM. The published sensitivities are calculated for the eight update parameters of the first element. Similar plots for the remaining elements can be generated however are omitted for brevity as they follow the same trends shown in Figure 5-12.

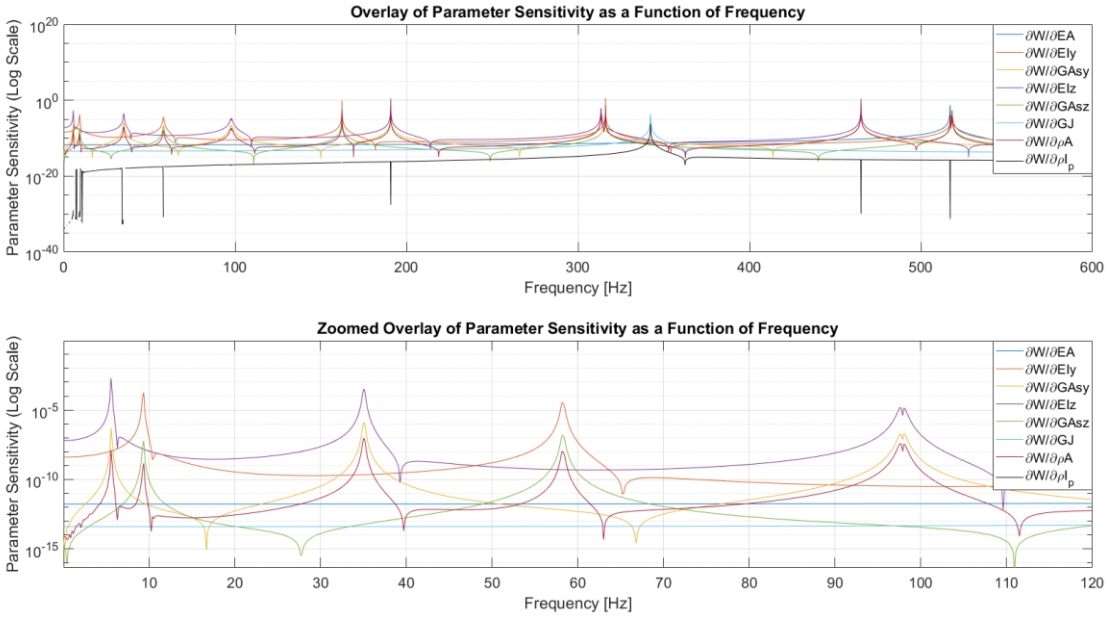

Figure 5-12: Beam section property update parameters' absolute sensitivities as a function of frequency. The lower plot shows a zoomed region for clarity.

As can be seen, the parameter sensitivities are highly non-linear and all of the update parameters have the greatest sensitivities in the regions of the PSD peaks. It is noted that with the current FEM the axial, bending, and torsion modes are decoupled such that the sensitivities of the update parameters have meaningful magnitudes only in the regions of their respective PSD peaks. The upper plot in Figure 5-12 is plotted from 0 to 600Hz to show the sensitivity of the parameters

related to the torsion and axial modes of the beam. In the lower plot, a zoomed region over the five modes being studied in the current analysis are shown. Perhaps the most important information to be taken from this plot is the orders of magnitude difference in sensitivities between update parameters. It is observed that bending in each plane is dominated by the bending stiffness with secondary sensitivities of the shear area and mass per unit length 4-8 decades lower than their bending stiffness counterparts.

The result of these orders of magnitude difference in sensitivities is that parameters with higher sensitivities move towards their true values whereas parameters with low sensitivities can wonder around the solution space with little impact on the objective function. The effects of the sensitivity scaling mismatch can be minimized by selecting more frequency lines at modes with lower sensitivities such that the sensitivity of each parameter is on the same order when summed over the chosen frequency lines. This approach works well for parameters such as axial or torsional stiffness but does not benefit parameters such as mass per unit length which influences the model PSD orders of magnitude lower than the stiffness parameters. Working with materials and structures with a higher density and/or cross sectional area would also help alleviate this shortcoming.

The amount of tolerance the algorithm has to parameter sensitivity scaling is inversely proportional to the complexity of the solution space. In other words, if only a few update parameters are desired, the algorithm has been shown to be robust to widely varying sensitivities (see the studies in Chapter 4). As the solution space becomes increasingly complex, through the addition of increased update elements and/or parameters per element, the algorithm becomes less accurate on parameters having relatively low sensitivity. As such, it is recommended that initial

iterations be performed using update parameters which have the sensitives, summed over the chosen frequency lines, within a couple orders of magnitude of one another.

The solutions given by the algorithm are approximate in nature as the identified parameters set will be modeling damage with the resolution of the element size within the model and/or the measurement set whereas the actually damage may be contained in a sub-region of the element. For the current discussion it is sufficient to note that the damage scale factors produced by the algorithm are effective parameters, inferring that the parameters capture changes in other parameters not being characterized (such as damage size or parameters not considered in the update space). As such, any damage scale factor omitted from the solution space because of low parameter sensitivity is captured in the effective parameters identified such that the model reliably predicts the behavior of the structure in the damaged state. Furthermore, once a damage region has been identified the solution space may be revised such that few update parameters are contained (fewer elements being updated as elements deemed undamaged may be fixed) in the solution space but include parameters of different orders of magnitude.

Looking back to the lower plot in Figure 5-12, over the chosen frequency range of 0Hz to 120Hz, no torsion or axial modes are present and as such the theoretical sensitivities of related parameters over the frequency range is zero. As such, these parameters (*EA, GJ, and* ρI_p) are excluded from the current analysis. Additionally, the parameters related to the shear correction factors (GA_{sy} and GA_{sz}) have a negligible impact on the PSD in comparison to their respective bending stiffness over the frequency range of interest and are also omitted from consideration. Inclusion of data from high frequency sensing systems could include the shear modes of the structure, in which case these terms would be dominant and hence included in the analysis. For the current work these shear terms do not contribute in a meaningful manner.

The more difficult of the parameters to address is the mass per unit length. Under the current development the density and area of the beam under study are very small in comparison to the stiffness and inertia parameters and hence test the limits of the algorithm. Robustness is however demonstrated by performing an initial update using the stiffness parameters to identify potential damaged elements before including the density parameter in a reduced solution space.

5.4.3 Strategic Selection of Update Elements/Element Grouping

In order to allow for reasonably sized problems to be accurately and efficiently solved it is desirable to condition the solution space by grouping elements by region. This reduces the number of parameters being optimized at once and in turn increases the computational efficiency. Once a potential damage region is identified, the region may be refined down to an element scale analysis. In the current analysis, the 18 element FEM is initially discretized into six groups as shown in Figure 5-13. The updated parameters will be assumed uniform across all elements in a given group during the update routine. Once a particular group (or groups) has been identified as containing a potential damage scenario, the element mesh density in that group can be iteratively increased until the damage is concentrated into a single element or a minimum number of elements.

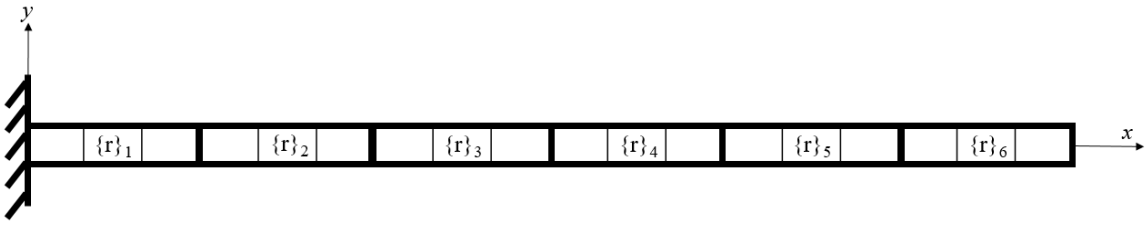

Figure 5-13: Schematic of element grouping whereas 18 elements are divided into 6 update parameter groups.

In addition to element grouping, careful selection of which elements to include within the groups is also recommended. Not all of the elements need to be included in the update groups if it

is known they do not contain damage, any potential damage has negligible impact on the parameters of interest, or the measurement quality in the region of those elements is substandard. In the current demonstration all of the elements are contained in the initial update grouping and only eliminated once the algorithm has deemed them to be free from damage. In practice, on large scale aircraft structures such as the main wings, elements near the tip or representing attached pods may be required for accurate FE representation but be inconsequential to the SHM results. In these cases, inclusion of such elements in the update parameter space would only hinder the algorithm's abilities. The grouping and element selection input to the algorithm provides a convenient way to maintain these elements in the model while eliminating them from the solutions space.

A final method for screening of updating parameters is by sensitivity. In the previous subsection the rational for the inclusion or exclusion of certain parameters from the update from the onset were discussed. In addition to this initial screening, during the update routine the sum of the sensitivity of each parameter over all chosen frequency lines is calculated. These summed sensitivities are then again summed over the elements in the update yielding a scalar sensitivity ranking for each update parameter at each iteration. An active parameter sensitivity filter is defined such that parameters which fall below the threshold at any iteration are temporarily held fixed and only included in the update at steps at which their sensitivity contribute in a meaningful way. An example of these summed sensitivities as a function of iteration step are shown in Figure 5-14 along with the defined threshold depicted as the black dashed line. In the example shown the threshold is set at two orders of magnitude lower than the maximum sensitivity. For the identified solution space size this was found to be a stable yet inclusive threshold and used throughout the chapter.

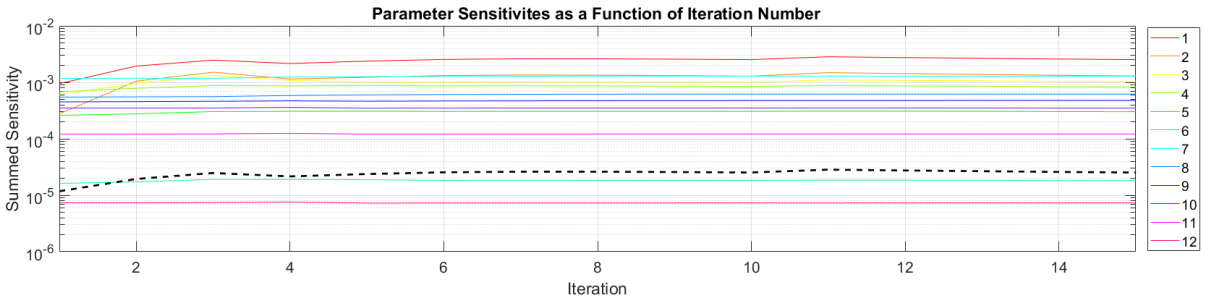

Figure 5-14: Progressive parameter sensitivity screening as a function of iteration for the twelve update parameters, denoted in the legend as 1 through 12. Parameters which fall below the threshold (denoted as the black dashed line) are held fixed for the current iteration.

5.5 Analytical Studies

In the current section a parametric study of the algorithm's performance to varying input conditions is tested and documented. The baseline system, as established above, is an 18 element FEM of a thin-walled carbon/epoxy beam. Initially, the 18 elements are divided into 6 update groups, each containing 3 elements, with bending stiffness in each plane used as the update parameters. As the possible regions containing the damage are eliminated, the element groups are reconstituted to eventually contain a single element and the mass per unit length included in the update. Measurement noise is simulated in the time domain as discussed in Chapter 4 and is assumed to be a realistic 0.5% for the baseline problem. Frequency lines have been selected by specifying the PSD peaks, and peak-magnitude ratio locations. Using the first five modes and two lines per mode (corresponding to 0.95 and 0.5 the magnitude of each modal peak) on each of the modeled and "measured" PSD, 20 lines were selected for the baseline problem using a coherence threshold of 0.99. For the analytical damage studies presented in this section it is assumed there is a single crack present in element 5 of the 18 element FE model, as shown in Figure 5-15. In the current example the damage parameters of the fifth element were selected to be δEI_z = 0.95 and δEI_y = 0.80 which simulate a crack in the element affecting the bending stiffness in both planes.

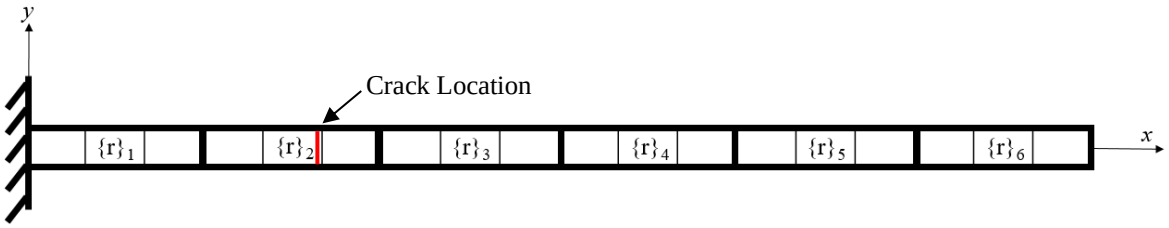

Figure 5-15: Schematic of the initial damage model configuration, showing the damaged element amount the initial element groupings.

The intricate details of the algorithm operation were the focus of Chapter 4 and are omitted throughout the parametric studies as to not be redundant, instead focusing on the results. For clarity however, since a number of new features are implemented in this chapter a brief overview is warranted. While the system currently being studied is simple enough the algorithm could operate directly on the update parameters associated with each of the elements, the purpose of the chapter is to demonstrate the capabilities and features of the algorithm, which include the element grouping and refinement features. As previously discussed, the grouping feature utilizes the same update parameters across a predefined number of elements to reduce the complexity of the solution space as well as bolster parameter sensitivity. The steps of the baseline problem are presented below, with the same process implemented for each of the parametric studies in the subsections to follow.

For the current demonstration, the 18 elements are initially grouped into six groups such that the update parameters associated with each set of three adjoining elements are assumed to be the same. The algorithm is run until convergence and the change of parameters within each group are quantitatively compared to their healthy values. The relative order of parameter change provides insight into which groups may contain elements which are damaged. After the initial update of the six update parameter groups the algorithm provides an indication of the suspected damage region(s). Figure 5-16 provides the update parameter values for each of the twelve

parameters for the baseline problem as a function of iteration for reference DOF two. The light blue and orange parameters shown in Figure 5-16 both correspond to group two and indicate potential damage contained within that group as all other parameters converge back to their healthy values.

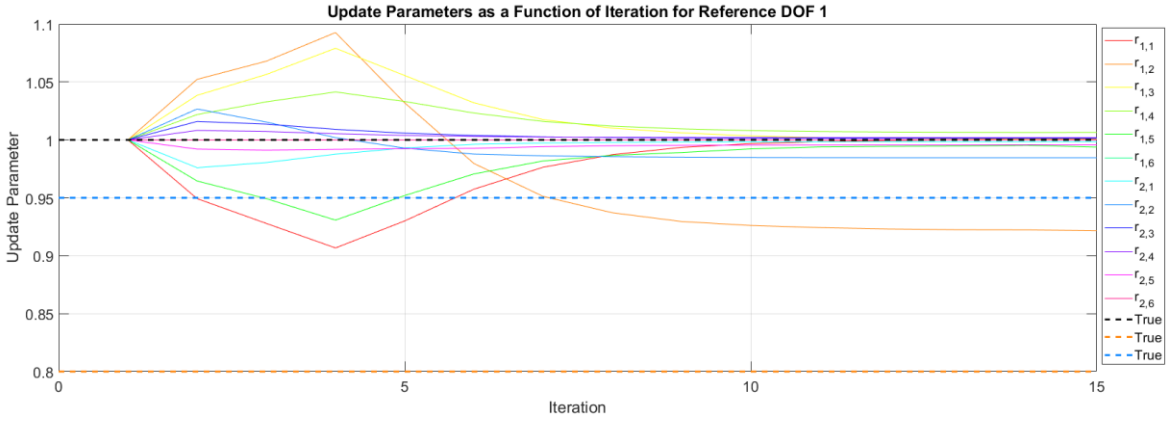

Figure 5-16: Update parameters for each of the six parameter groups during the initial update.

The algorithm is repeated using all of the available reference DOF to yield a set of update parameters for each reference DOF. In Figure 5-17 a waterfall plot of the twelve converged update parameters as a function of reference DOF are plotted along with their true values indicated by the dashed line. An important result can be seen in Figure 5-17, although the elements are grouped in terms of their update parameters, element five (which is in group two) shows clear signs of anomalies leading one to suspect damage may be present in this element, which in fact is the case in the current analysis. While this is useful information for the selection of the refined groupings for subsequent analysis runs, the changes of all of the parameters when using reference DOF 5 would be suspicious and as such the magnitudes of the damage unreliable. Examining the mean values of the parameters, averaged over all of the converged reference DOF leads to a more accurate estimate of the damage parameters under the framework of the current groupings.

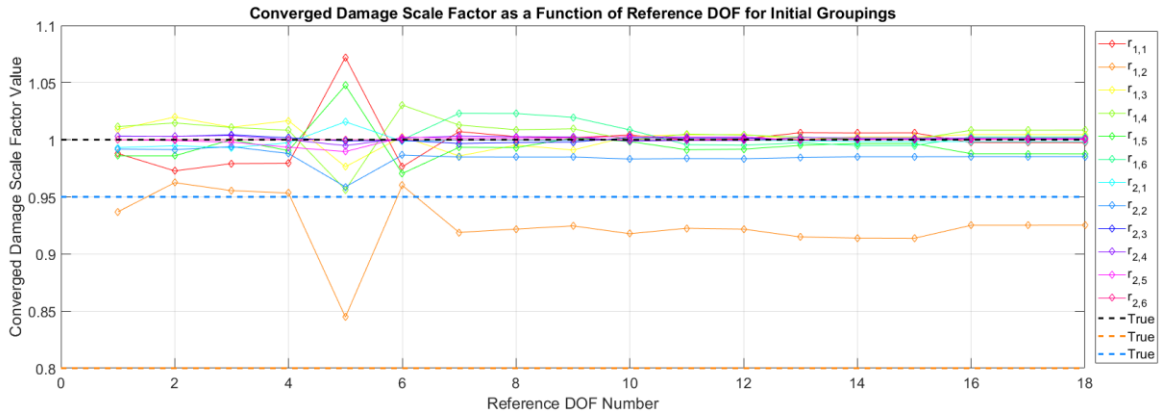

Figure 5-17: Plot of the twelve update parameters converged values as a function of reference DOF during the initial update.

The reader is reminded that since the elements are combined in groups and update parameters assigned to groups rather than individual elements the true damage parameters (indicted by the dashed lines on Figure 5-16 and Figure 5-17) are not in the solution space. The expected result is that the larger damage event is "smeared" over a larger area leading to an effective group damage scale factor which is lower than the true value. This is indeed the result of the initial algorithm run, as confirmed by Figure 5-18 which plots the mean parameter values for all 12 update parameters, averaged over the 18 reference DOF.

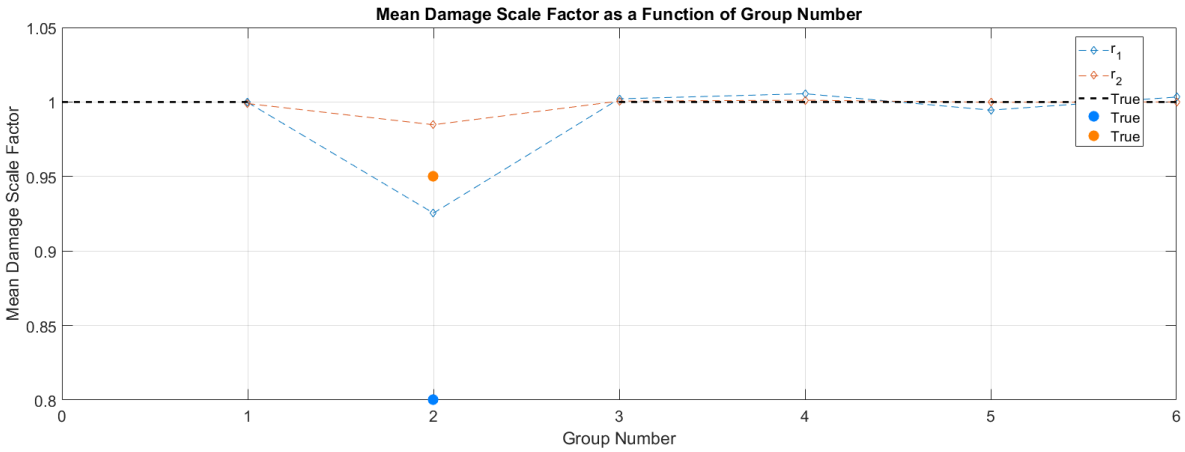

Figure 5-18: Plot of the mean update parameters values for each of the groups averaged over the 18 reference DOF.

Figure 5-18 reinforces the notion that group two likely contains an element that is damaged. Depending on the fidelity required, the solution with the damage smeared across the group may be used in further analysis or the group definitions refined and the damage scenario studied in greater detail. It is recommended at this point the groups are reconstituted to include potentially damaged elements and further study the potential damage scenario.

Before moving to the refined group study, it should be noted that the results of this smeared damage identification represented by the large element groups closely resemble the algorithm's operation in practice, in which the exact solution will likely not be contained within the solution space. In practice, the algorithm will need to identify the effective parameter set which produces a modeled structural response matching the measured response from a damage event that is unlikely to exactly match the model element size. As a result, the damage contained within an element will be "smeared" appearing as a smaller change in a particular parameter over the entire element rather than a large change of the parameter(s) in a highly localized region. In the current example the damage parameters of the fifth element were selected to be $\delta EI_z = 0.95$ and $\delta EI_y = 0.80$ which simulate a crack in the element affecting the bending stiffness in both planes. Since the group parameters are effective parameters acting over a broader range (three elements) one would expect that the converged parameter set for the grouped elements would be less than the true simulated damaged value of the element. This is in fact what happens as the algorithm correctly identifies the damage is in group two (elements four, five and six) however is of lower magnitude than the "true" damage value. In practice the parameter values in the damage regions are obtained by refining the element mesh in the potential damage groups.

For the current example, the mesh refinement transitioned from three elements per group to a single element per group so that the damage can be limited to a single element. In practice the

group size would begin with the groups containing a sufficiently large number of elements such that all of the parameters of interest which may have been subjected to a damage event are included. For large scale structures this might entail group sizes of dozens to hundreds of elements per group. Once a potential damage site has been identified those groups may be further and further refined in subsequent analysis runs to the point where the analyst has the desired level of damage resolution or the parameter groups of interest contain a single element. Thus, refining the resolution of the damage size is limited by the element size in the model. As a result, the damage localization will be as precise as the length scale of the elements used to model the damage region.

Utilizing the results of the initial update it is clear that the damage is contained in region two and as such the subsequent damage identification run ("Run 2") was comprised of three groups, containing elements four, five and six, respectively. The refined groups are shown in Figure 5-19.

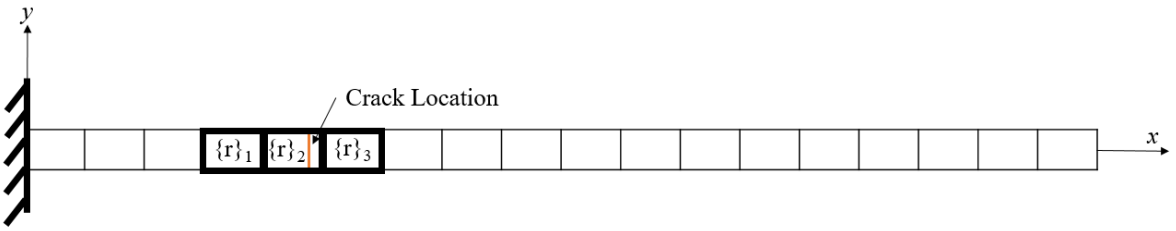

Figure 5-19: Schematic of element grouping for the secondary run where group two has been subdivided into three groups to increase the resolution of the damage detection.

The remaining 15 elements are included in the batch-stacking and update routine however their respective parameters are left unchanged reducing the solution space to six variables. Repeating the analysis for the baseline problem using these new grouping definitions, the algorithm is able to correctly identify the damage as being in element five and also providing the correct damage magnitude, which in the current example is known a priori and contained within

the solution space. The results presented in Figure 5-17 are updated to reflect the newly defined update groups and damage parameters and plotted in Figure 5-20.

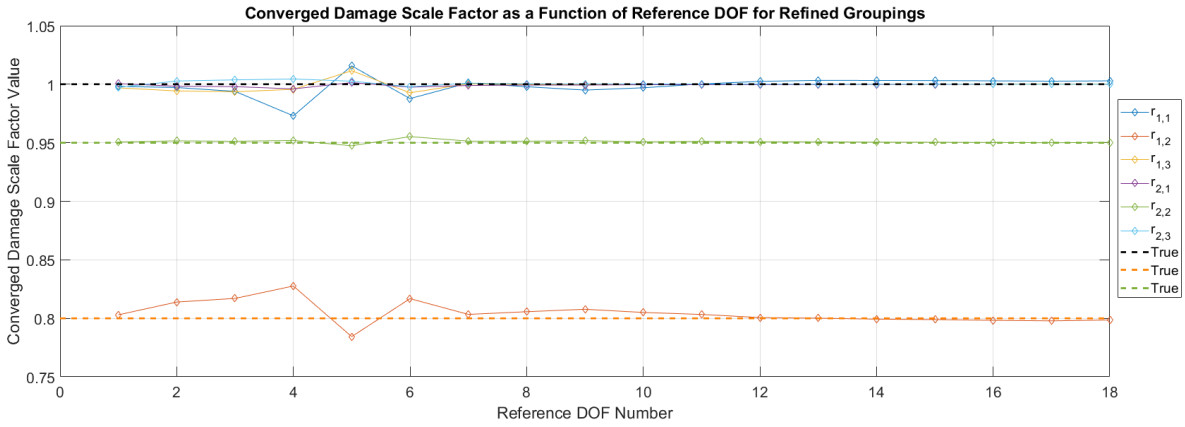

Figure 5-20: Plot of the six update parameters converged values as a function of reference DOF during the second update.

While it appears that the lower reference DOF lead to larger solution error, the reason for the errors is the fast convergence rate coupled with the current stopping error. Continuing the analysis for more iterations tends to produce lower errors as the step size near convergence is smaller. Again, the mean parameter value, averaged across all of the reference DOF is computed and used to represent the parameters' converged values, shown in Figure 5-21.

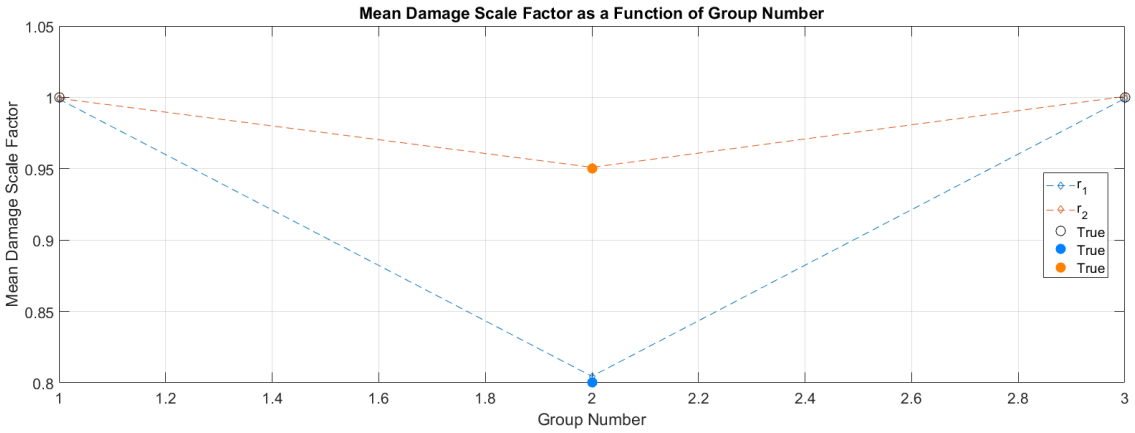

Figure 5-21: Plot of the mean update parameters values averaged over the 18 reference DOF.

As a final step, with the damaged element isolated, the mass per unit length is entered into the updating space and the analysis repeated ("Run 3"). The algorithm correctly identifies the mass parameter as well, as shown in Figure 5-22.

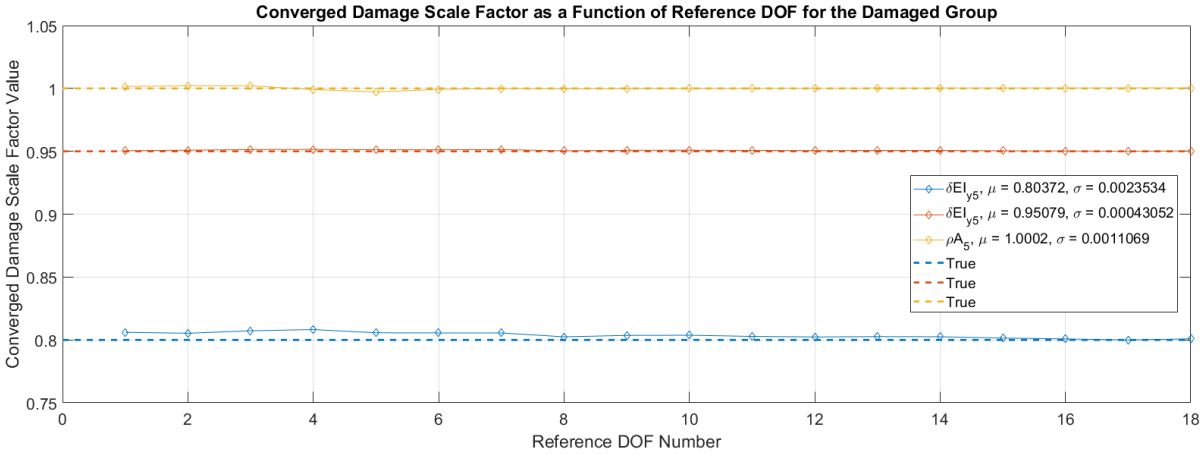

Figure 5-22: Plot of the three update parameters converged values as a function of reference DOF during the final update run. The mean (μ) and standard deviation (σ) of the parameters of all eighteen reference DOF are also given in the legend.

All of the steps required to refine the grouping may be automated within the algorithm by defining threshold values or manually implemented as being done presently. In the parametric studies presented in the subsequent sections the timing and iteration values are given as the mean time and iterations required for a single reference DOF, and the final results represented by their mean error on subsequent plots.

5.5.1 Varying Number of Analysis Lines

An important consideration in the implementation of the algorithm is the number of frequency lines one should use in the update. Too few frequency lines lead to solutions with large amounts of error. Analysis run with too many lines converge very slowly and may not converge in a reasonable amount of iterations. In Chapter 4 it was also shown that not all frequency lines contribute to the update equally, meaning that choosing 100 random lines will likely lead to a

worse solution than 100 carefully chosen lines. It is known from the studies of Chapter 4 that distributing the frequency lines over a number of PSD peaks as well as dispersing them on each peak lead to the most efficient use of the lines.

With this in mind, the ratios of peak amplitude were chosen for each of the cases studied and are listed in Table 5-4. In all cases, all five of the modal peaks in the 0-120Hz range being studied were used. Additionally, the lines were selected in pairs as discussed in Chapter 4. This implies that for an analysis case where, for example, 50 lines are desired, 5 frequency line ratios were chosen, yielding five lines per PSD peak for each of the "measured" and analytical responses, leading to 50 total lines.

Table 5-4: Update ratios used for parametric study on analysis lines.

Number of Analysis Lines	Update Ratio										
	0.95	0.9	0.8	0.75	0.7	0.6	0.5	0.4	0.3	0.2	0.1
4*	×	×	×	×	×	×	✓	×	×	×	×
10	×	×	×	×	×	×	✓	×	×	×	×
20	×	×	×	✓	×	×	✓	×	×	×	×
50	✓	×	×	✓	×	×	✓	×	✓	×	✓
100	✓	✓	✓	×	✓	✓	✓	✓	✓	✓	✓

* = Uses only modes 4 and 5

Three metrics have been defined on which the performance of the algorithm is evaluated by means of the parametric studies. Most important is the accuracy of the algorithm which was quantified as the mean error of the update parameters. Of secondary importance is the computational cost of the update, which was quantified as time to compute, and the number of iterations to compute. As previously mentioned, the algorithm was run for all 18 of the available reference DOF and as such the times and iterations listed are the mean values taken over all reference DOF which converged. The amount of time and number of iterations varied by

approximately an order of magnitude between the best and worst reference DOF. In practice, a subset of elements to use as references in the updating routine could be chosen, depending on each sensor's response quality and the desired statistics on the converged parameter sets, speeding up the calculation.

The most important metric in terms of characterizing the algorithm's performance is the accuracy of the converged parameters. Figure 5-23 shows the absolute value of the mean parameter error as a function of the number of analysis lines used. The error was averaged both over reference DOF and update parameter set. The "All Parameters" legend entry correspond to the mean of all the update parameters in the analysis whereas the "Healthy" and "Damaged" parameters are the means of the parameters that were unchanged and changed in the analysis, respectively. Runs 1 through 3 correspond to the initial analysis grouping (Run 1) as well as the refined groups and final analysis (Runs 2 and 3, respectively) previously discussed.

Initial observation of Run 1 in Figure 5-23 appears to be an error of approximately 10 percent for the Damaged Parameters set. This large error is merely an artifact of the "smearing" that was previously discussed in which a smaller damage feature is smeared over a large group region, resulting in higher damage scale factors for the damaged group than their true values. The accuracy of the parameters for the defined solution space is easily verified by looking at the distribution of the converged parameter set (mean and variance) which show high precision and a reliable result. Runs 2 and 3 contain the true parameter values within the solution space and therefore provide the low parameter error that would be expected. While negligible gains in accuracy can be obtained by increasing the number of frequency lines, as shown in Figure 5-23, increasing the number of lines increases the computational cost.

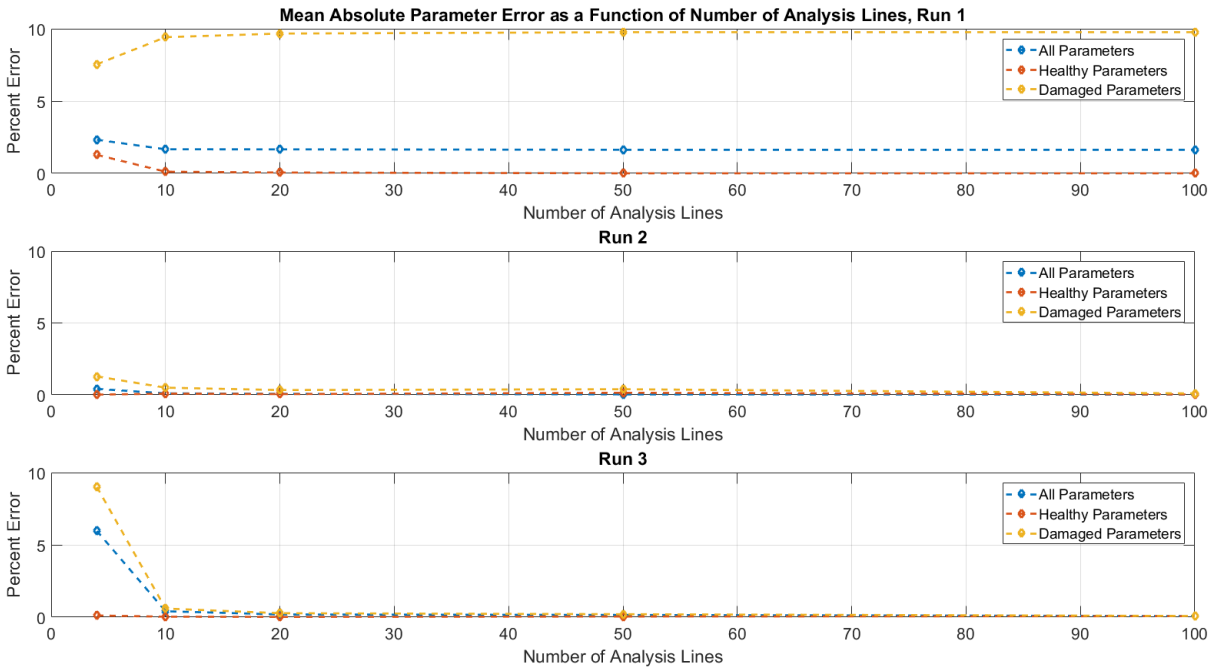

Figure 5-23: Mean parameter error as a function of the number of frequency lines.

The performance of the algorithm in terms of computational cost has been evaluated by looking at both the number of iterations to convergence as well as the time to convergence. The time is of course dependent on the system being used for the analysis and is the same as that previously described and specified in Table 5-2. Figure 5-24 provides the trend lines for the mean iterations to convergence as a function of the number of analysis lines for the three analysis runs. The general trends are the more variables in the solution space, the more iterations to reach convergence (each successive analysis run has fewer update parameters in the current example), as would be expected.

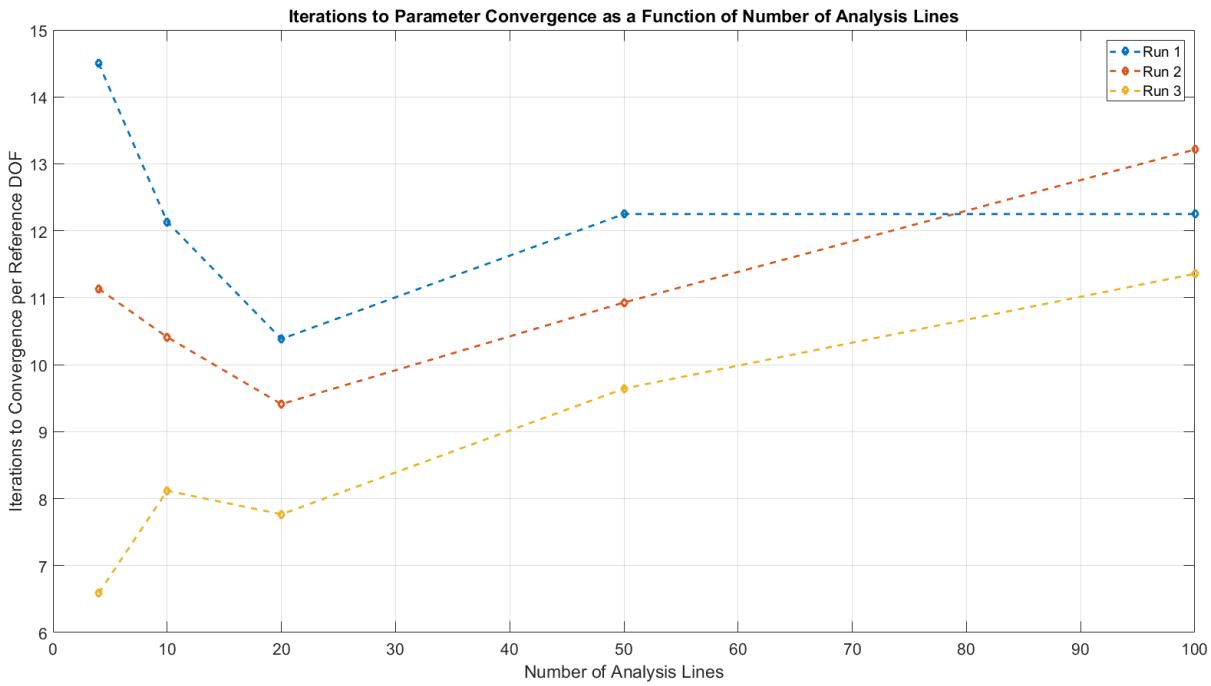

Figure 5-24: Number of iterations to convergence as a function of the number of frequency lines.

The outlier in Figure 5-24 is for Run 1 using 100 analysis lines. In the current demonstration the maximum number of iterations was set to 40. Any reference DOF which did not converge within the 40 iterations was removed from the mean. Using more frequency lines is known to cause slower convergence as is using reference DOF closer to the free end of the beam (lower signal-to-noise of the reference signal). In the case of Run 1, for 100 analysis lines, only four of the reference DOF converged within the 40 iterations, leading to an iteration mean which was skewed low due to the use of only the best reference DOF. The same trends are repeated in Figure 5-25 with respect to the time to convergence as a function of number of analysis lines. For the current analysis 20 frequency lines were identified as the optimal number, providing the best compromise of accuracy and speed. The same 20 lines were used in the baseline problem as well as all subsequent analysis performed in this parametric studies section.

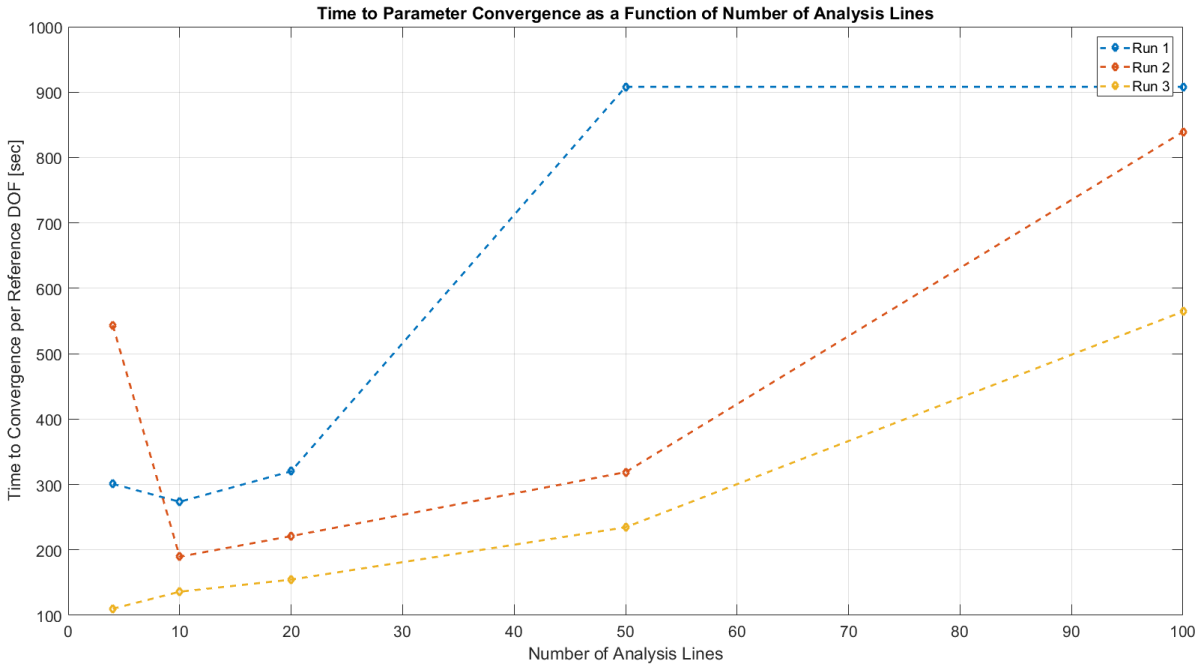

Figure 5-25: Time for convergence as a function of the number of frequency lines.

5.5.2 Varying Levels of Noise

For the baseline problem, the noise level present on the simulated measurement signal was chosen to be 0.5% to match noise levels observed in experimental testing with the fiber optic strain sensing system used in this dissertation. In order to evaluate the algorithm performance to varying levels of noise, Gaussian noise levels of 0.1%, 0.5%, 1%, 5% and 10% were added to the simulated measurements in accordance with equation (4-16). The same metrics were used to evaluate the algorithms performance, namely, mean parameter error, iterations to convergence, and time to convergence.

The absolute mean parameter error, averaged over all parameters and reference DOF are shown in Figure 5-26. In all three of the run cases, the error is relatively constant and, in some cases, even decreases with increased noise. While this result is counter intuitive, it is an artifact of the coherence-based frequency line screening. The analysis lines chosen must be of sufficiently

high quality as to meet the criteria of the coherence threshold. As a result, increasing the noise for moderate noise levels leads to a shift in the selected frequency lines, typically toward the peaks, but little to no change in the converged parameter accuracy. As the amount of noise is further increased, the amount of lines available over the selected baseline 0.99 coherence threshold decreases to the point which an analysis with the specified number of lines is not possible. In these cases, the operator would be required to decide whether to proceed with fewer frequency lines or reduce the coherence threshold to obtain the desired number of lines. There is certainly a trade-off between the number of frequency lines and the quality of each line so this decision would need to be made on a case-by-case basis.

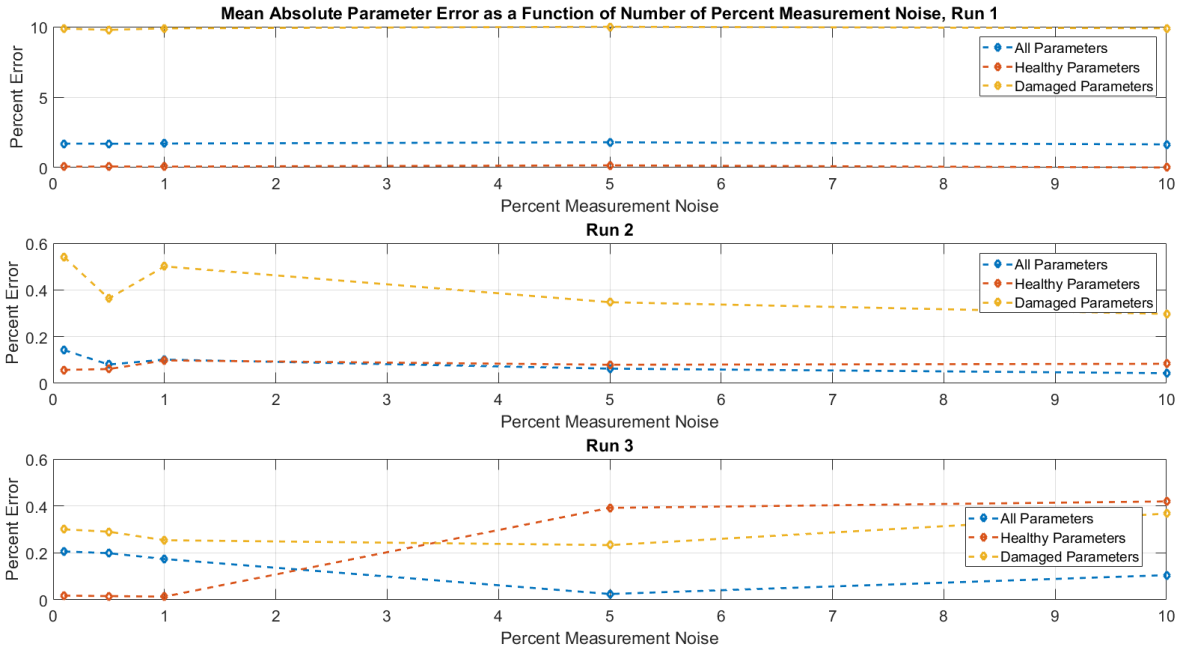

Figure 5-26: Mean parameter error as a function of measurement noise.

Even at the 10 percent noise level under the current demonstration the fourth and fifth modes have amplitudes which are within the defined noise signal. As a result, the algorithm has automatically shifted the lines associated with these peaks to the nearest peak(s) which contain

available frequency lines meeting the criteria. It is also important to note that an additional filter is in place such that each frequency line in the analysis set must be unique. In line with the mean parameter error, the number of iterations to convergence as a function of measurement noise is relatively constant over the chosen noise levels, as shown in Figure 5-27.

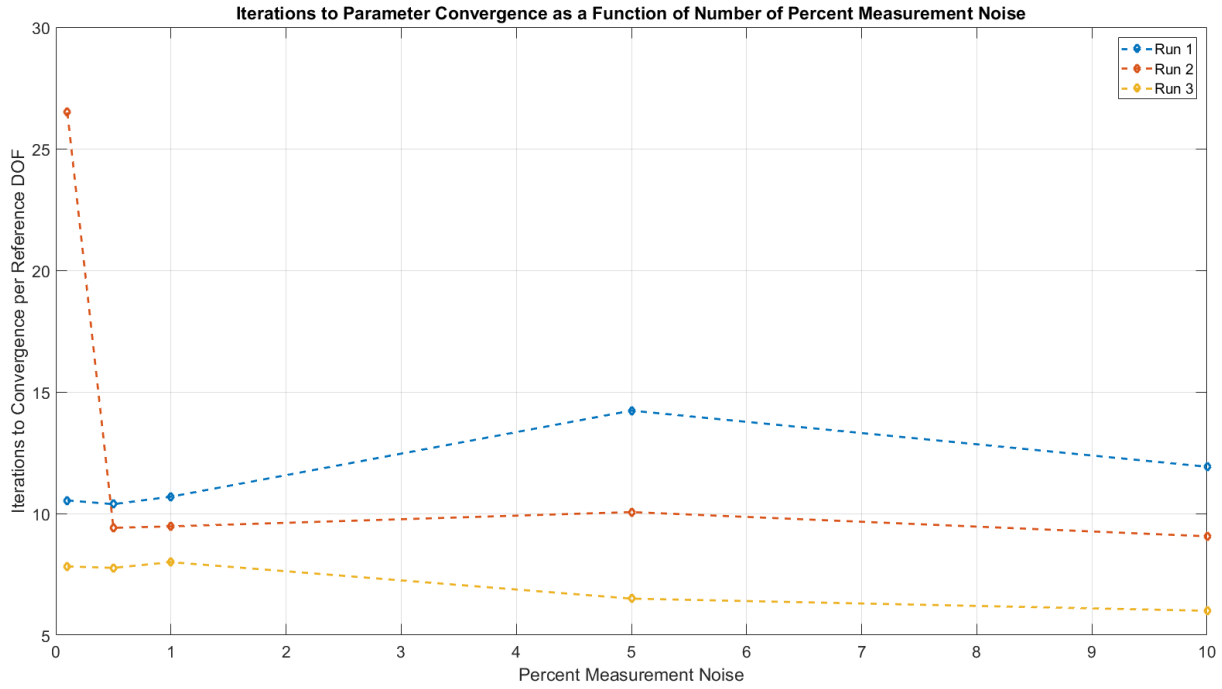

Figure 5-27: Number of iterations to convergence as a function of measurement noise.

The trend in time to convergence appears to have some dependency on the number of update parameters in the solution space. In Figure 5-28, the largest solution space shows an increase in the time to convergence as the noise increases. This is in contrast to the smallest parameter set case, shown by the yellow line, in which an increase in noise leads to faster convergence. The sample size is however small and no definitive conclusions can be made based solely on Figure 5-28. Instead, taking the totality of Figure 5-26 through Figure 5-28, it is clear that the performance of the algorithm is relatively unaffected by reasonable amounts of measurement noise, provided that there are enough frequency lines which satisfy the coherence

threshold. Once the coherence threshold is decreased, the relative noise has a larger impact as lower quality lines may be used in the analysis, allowing larger amounts of noise to induce error in the analysis.

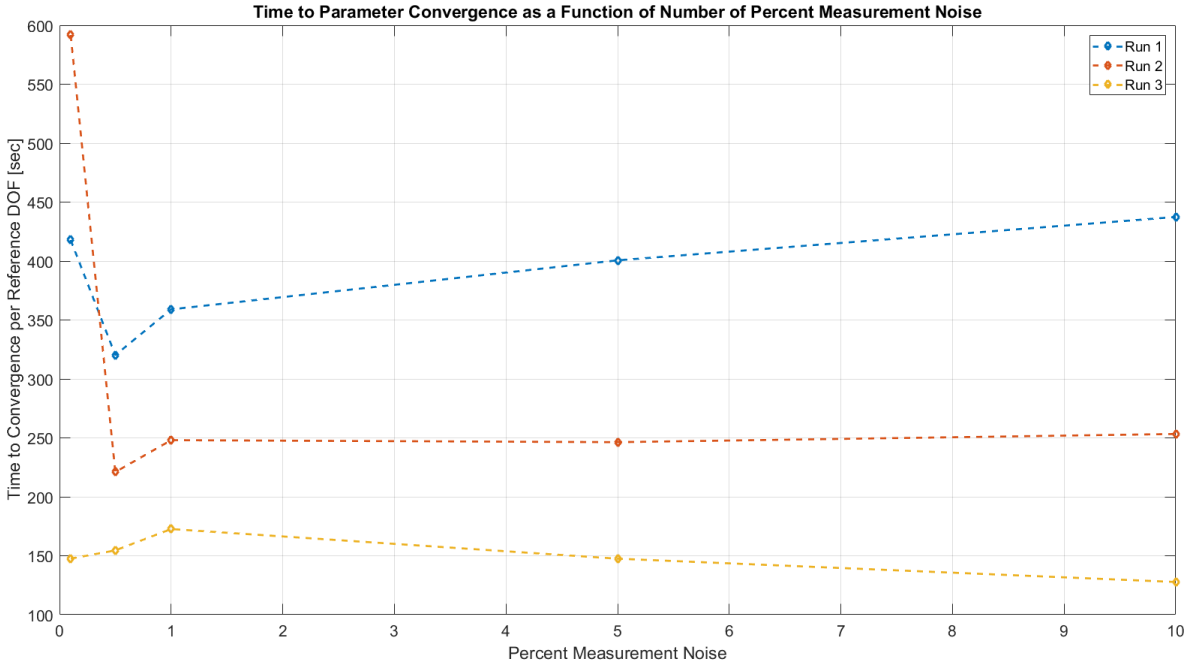

Figure 5-28: Time for convergence as a function of measurement noise.

5.5.3 Varying Coherence Threshold

In order to provide a more complete depiction of the effects of measurement noise on the algorithm performance, varying levels of coherence thresholds were studied. As previously mentioned, increasing the noise level for a fixed coherence threshold simply drives the analysis lines into region of high coherence and tends to have little to no impact on the performance. The caveat being when the noise is so large that there are not enough high-quality lines at which to take data. In light of this, the baseline system description will be varied slightly in current study, where 1% measurement noise (baseline problem is a more realistic 0.5% noise) will be used with

coherence thresholds of 0.99,0.95,0.9,0.80 and 0.7 to test the limits of the algorithm's noise tolerance.

The algorithm was again run for all available reference DOF. Only the reference DOF achieving convergence within 40 iterations for the specified stopping criteria were included in the averaged algorithm performance. The same three runs of the algorithm previously discussed were analyzed varying the number and size of the element groupings. The resulting mean parameter error as a function of the selected coherence threshold is given in Figure 5-29. The anticipated result of the analysis is that as the coherence threshold increases from 0.7 to 0.9, the error of the parameters decreases as a result of the use of higher quality information in the updating routine, as shown in Figure 5-29.

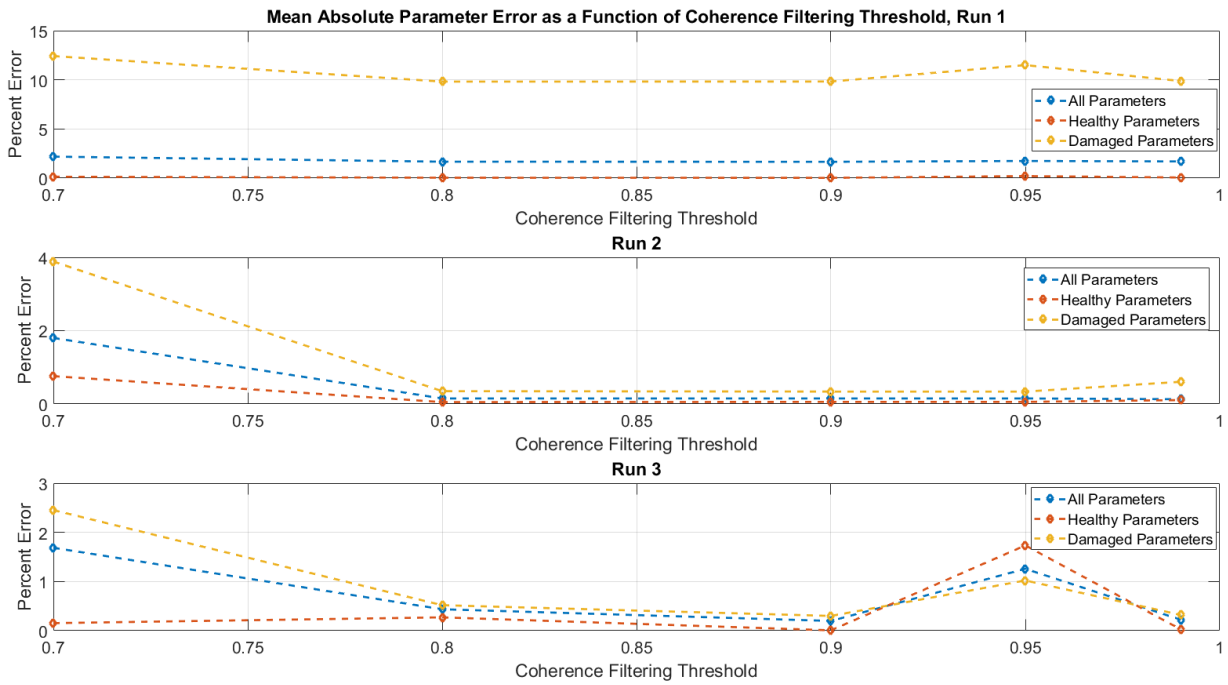

Figure 5-29: Mean parameter error as a function of coherence threshold.

An anomaly occurs at a coherence level of 0.95 as the parameter error slightly increases, especially for run case 3. The error computed for a given analysis run has previously been shown

to be dependent on the specific location and number of frequency lines chosen. It is possible that this anomaly occurs as a result of the 0.95 coherence threshold pushing the frequency lines into suboptimal locations, such as inflection points, as discussed in Chapter 4. Regardless of the cause of this slight increase in error at 0.95, the error values are still so low they are within one standard deviation of the mean parameter error. It is likely that a slightly different set of frequency line filtering criteria would lead to the mean behavior falling back to the anticipated trend however in the spirit of performing a parametric study with as little variation between test cases as possible no modifications have been made.

The number of iterations to convergence as well as the time to convergence were also plotted and are given in Figure 5-30 and Figure 5-31, respectively. Both of these speed performance metrics are relatively unaffected by the chosen coherence threshold and any variation is within the noise of the testing parameters. The lack of dependency on coherence threshold to convergence speed is likely caused by the fact that the stopping criteria is calculated as a function of the distribution of the PSD evaluated at the initial analysis line set. This means that as the noise in the system goes up, the variation of the PSD and in turn the allowable convergence error increases, leading to a solution with more allowable error in the same number of iterations.

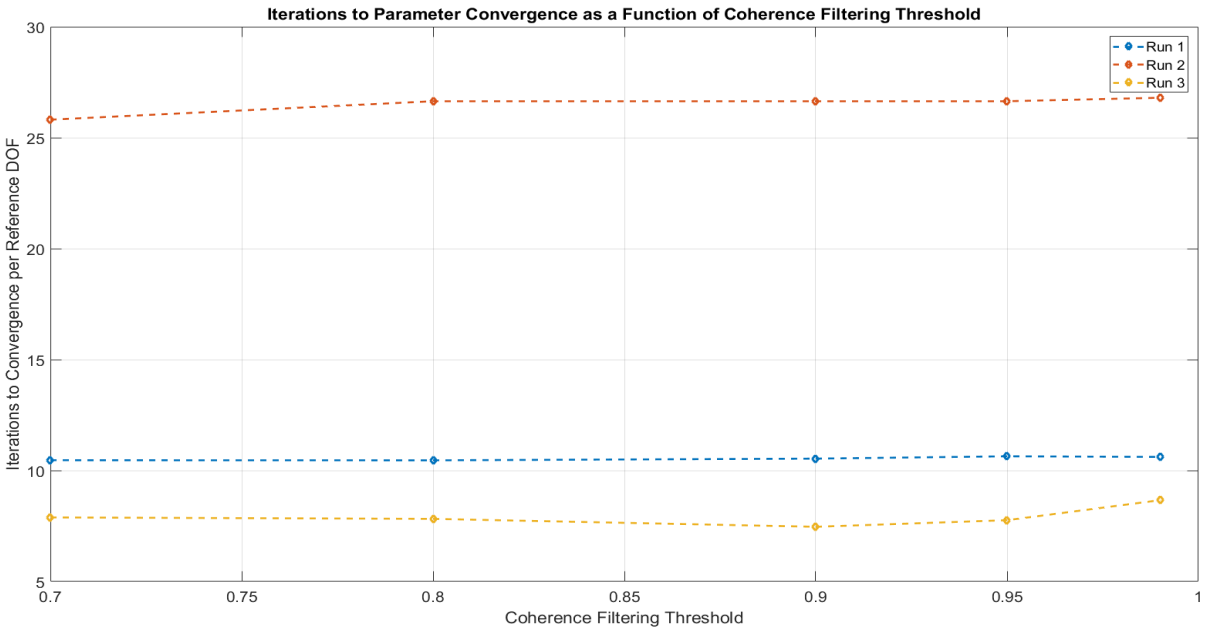

Figure 5-30: Number of iterations to convergence as a function of coherence threshold.

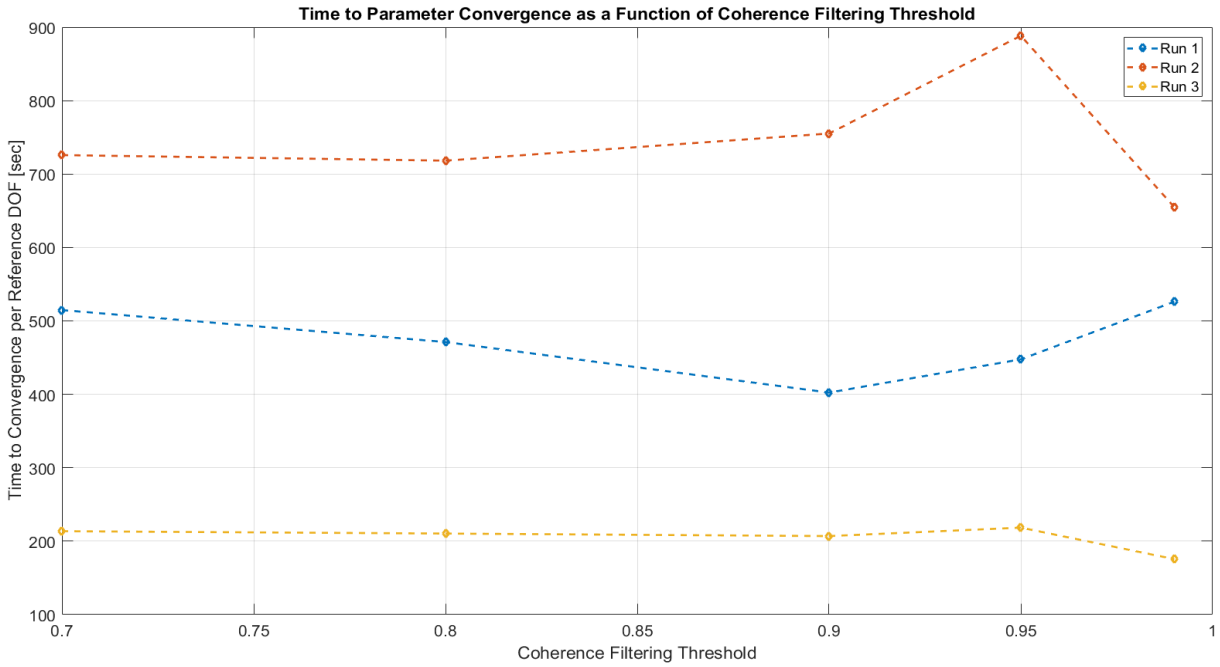

Figure 5-31: Time for convergence as a function of coherence threshold.

5.5.4 Varying Number of Update Parameters

While an informal study of the effects of varying number of update parameters has been given in the previous sections, using Runs 1 thru 3 as the variations, a formal parametric study is given here. The main reason for the formal study is that in the previous sections the number of update parameters is being varied largely through varying the number and size of the parameter update groups. In the current section these variables are eliminated from the analysis and each element is treated as its own group. This provides the most direct comparison of the algorithm performance as a function of number of update parameters.

In the current section the number of update parameters within the model are varied between 2 and 36 by representing groups as a single element to generate the correct number of update parameters in the solution space (i.e. 2 update parameters would be a single group of 1 element, 36 update parameters are 18 groups, each containing a single element). In the case of using a single element per group, no refinement is possible and as such a single run was done for each case where the element groups used were centered around the damage region (element 5). In practice the potential damage region is likely not known a priori and as such this is an artificial construct for the sake of the parametric study. The absolute mean parameter error as a function of number of parameter groups is given in Figure 5-32.

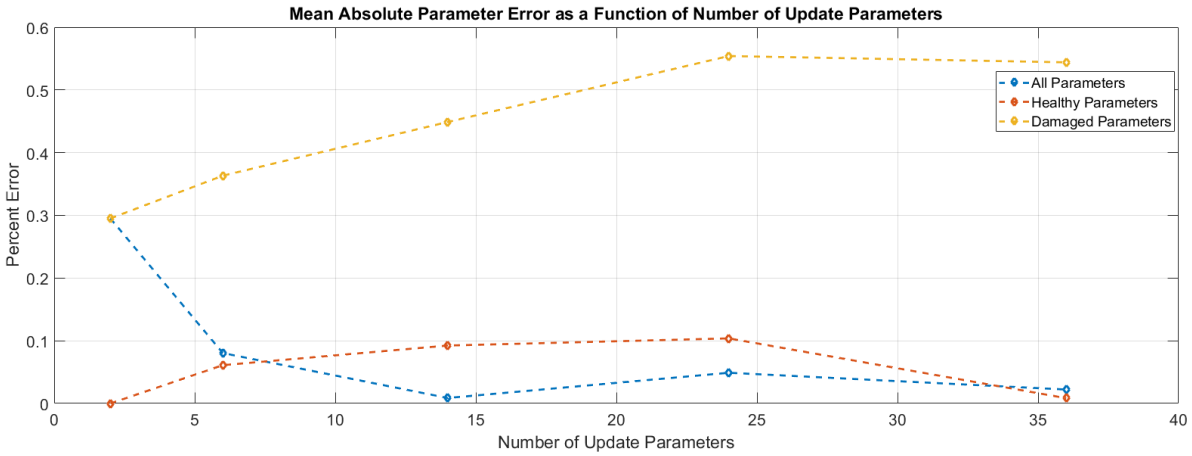

Figure 5-32: Mean parameter error as a function of number of update parameters.

The mean parameter error is relatively constant for all of the update parameters as shown in Figure 5-32. Larger errors in parameter value would be present if update parameters of various magnitude sensitivity were allowed in the solution space. With the use of the sensitivity-based screening previously discussed, the algorithm has been found to be robust to solution spaces in excess of 100 update parameters and possibly more. The current limiting factor in the number of update parameters is the variation of the relative magnitudes of the desired parameter sensitivities and the computational power of the processing machine. Increases in machine precision and computation power will aid in easing both of these restrictions and expand on the utility of the presented SHM methodology.

The major drawback of increasing the number of parameters, within the limitations of computational power and parameter sensitivity, is the computational time. Figure 5-33 shows the general trend in which the number of iterations to convergence is related to the number of update parameters in the solution space. In addition to an increase in number of iterations, there is also an increase in the time it takes to reach convergence, also plotted in Figure 5-33. This highlights another benefit of the grouping and mesh refinement scheme implemented throughout the

algorithm, allowing a minimal number of update parameters to be evaluated at once, leading to an efficient solution scheme capable of identifying damage down to the elemental level.

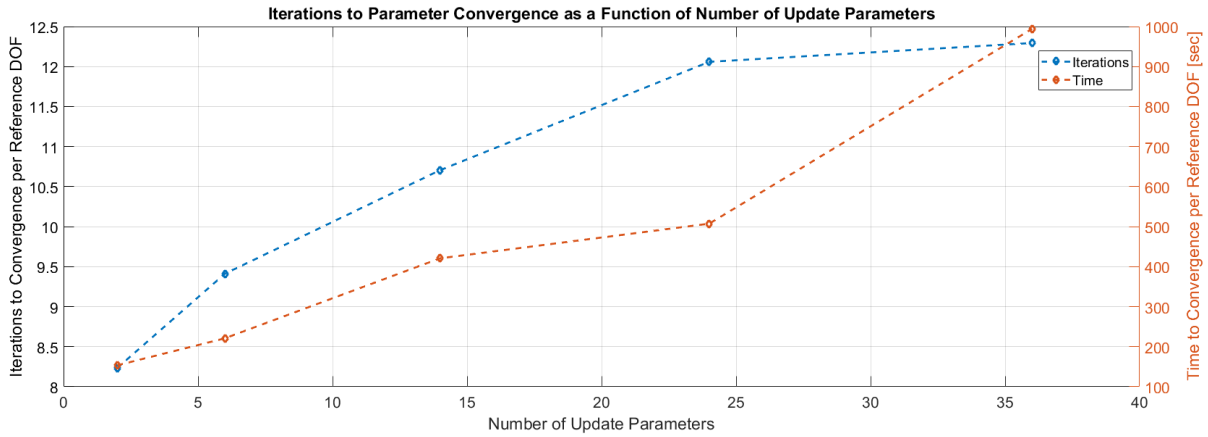

Figure 5-33: Average number of iterations and time to convergence as a function of number of update parameters.

5.6 Validation and Comparison with Alternative Methods

With the performance of the current SHM approach now well documented, it is important to characterize this performance relative to other SHM approaches. In 2015, Oliver [2] adapted a baseline problem on which parametric model updating based SHM methodologies may be compared. The system Oliver modified for this purpose was first proposed by Kabe [105]. Additionally, Oliver compiled the methods of several other researchers and compared it to his own approach using Kabe's modified baseline problem. The same baseline problem will be used in this dissertation as a means to establish a comparison between the current method and these alternative approaches complied by Oliver. The problem proposed by Kabe is a simple spring, mass system which models the behavior of a launch vehicle, as shown in Figure 5-34. Oliver expanded on the originally undamped problem by incorporating structural damping, denoted by the η_i values in the figure.

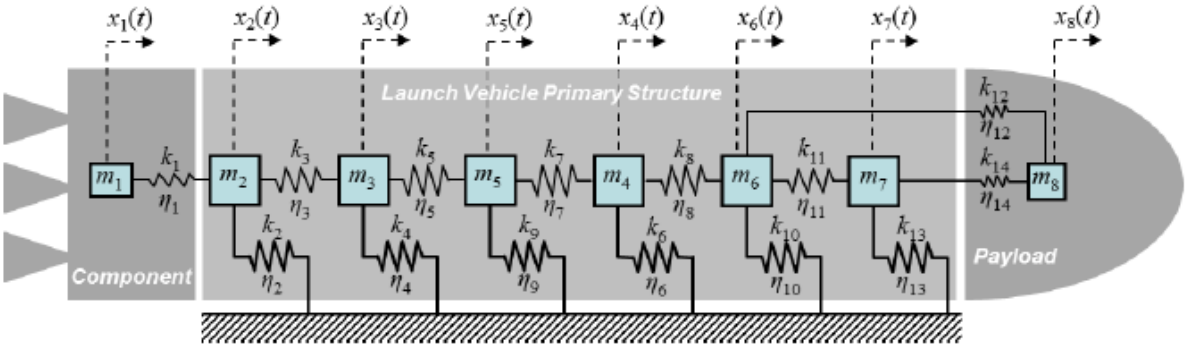

Figure 5-34: Baseline system used for comparisons between the current and alternative SHM approaches [2].

The system proposed by Kabe was adopted for the validation of the current algorithm because it is a relatively simple problem however incorporates a number of important SHM challenges including closely coupled modes caused by interconnecting structural systems and structural parameters varying orders of magnitude. In order to run such a problem, the algorithm was modified to utilize displacement, rather than strain, PSD which further shows the algorithm's versatility. This modification simply required the removal of the strain-displacement transformation matrix step from the formulation of the PSD and instead the displacement PSD were calculated, as given in equation (3-14).

A final modification was the incorporation of the complex stiffness matrix in the formation of the dynamic stiffness matrix. The inclusion of the complex stiffness matrix is necessary to model the structural damping parameters introduced into the problem by Oliver. The inclusion of complex stiffness was again a trivial change further demonstrating the utility of the current SHM methodology. The complex stiffness matrix can be written as:

$$\left[K^*\right] = [K] + j[K]_{\mathrm{Im}} \tag{5-11}$$

where the imaginary portion of the complex stiffness matrix stems from the structural damping terms. In the current example the structural damping is assumed to be proportional to the stiffness matrix such that the complex stiffness matrix is:

$$\left[K^*\right] = [K](1 + j\eta). \tag{5-12}$$

In the absence of viscous damping, the equation of motion given in equation (3-1) can be rewritten as:

$$[M(r)]\{\ddot{x}(t)\} + \left[K^*(r)\right]\{x(t)\} = \{f(t)\}. \tag{5-13}$$

Using the procedure discussed in Chapter 3, the displacement PSD of the modified Kabe system were calculated using the equation of motion given in equation (5-13). These displacement PSD were used as the model input for the SHM algorithm comparisons discussed in the current section. The details of the baseline and damaged systems studied are given in the following subsections.

5.6.1 Baseline System Description

The baseline, or undamaged, system parameters were taken from Kabe's original work [105] with the addition of the structural damping factors added by Oliver [2]. The parameters were chosen originally by Kabe to produce a complex set of FRF data on which to perform SHM which includes features such as closely coupled modes and parameters and sensitivities varying several orders of magnitude. The baseline parameters for the system given in Figure 5-34 are listed in Table 5-5.

Table 5-5: Baseline system parameters of the spring, mass, rocket model.

Mass Parameters	Stiffness Parameters		Damping Parameters	
$m_1 = 0.001$	$K_1 = 1.50$	$K_8 = 100$	$\eta_1 = 0.005$	$\eta_8 = 0.01$
$m_2 = 1$	$K_2 = 1000$	$K_9 = 900$	$\eta_2 = 0.50$	$\eta_9 = 0.002$
$m_3 = 1$	$K_3 = 10$	$K_{10} = 1000$	$\eta_3 = 0.01$	$\eta_{10} = 0.02$
$m_4 = 1$	$K_4 = 1000$	$K_{11} = 10$	$\eta_4 = 0.05$	$\eta_{11} = 0.005$
$m_5 = 1$	$K_5 = 100$	$K_{12} = 2$	$\eta_5 = 0.02$	$\eta_{12} = 0.002$
$m_6 = 1$	$K_6 = 900$	$K_{13} = 1000$	$\eta_6 = 0.002$	$\eta_{13} = 0.01$
$m_7 = 1$	$K_7 = 100$	$K_{14} = 1.5$	$\eta_7 = 0.01$	$\eta_{14} = 0.002$

To be consistent with the work previously done by Oliver, 4096 frequency lines were used to generate the PSD functions relative to DOF five used in the current SHM algorithm implementation. The baseline PSD for all DOF relative to x_5 are shown in a waterfall plot given in Figure 5-35.

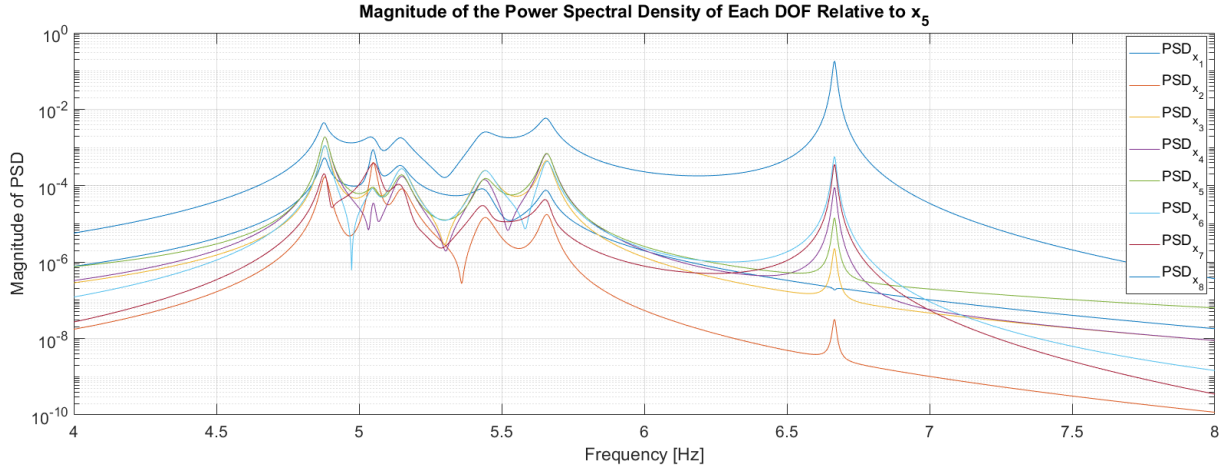

Figure 5-35: Waterfall plots of the PSD of each DOF relative to x_5.

As desired, the modes of the system are closely spaced and the damping so heavy some of the peaks are indistinguishable from one another. In particular, modes 2 and 3 both occur at 5.05Hz and appear as a single peak when looking at the PSD plots. Mode 7, which corresponds to vibration

of m_1, is decoupled from DOF 5 and hence does not contribute to the PSD shown in Figure 5-35. This highlights the advantage of utilizing all of the available reference DOF within the algorithm which ensures the maximum available information is included in each analysis and modes not well represented by a particular reference DOF are captured by others. Mode 8, occurring at 6.67Hz, corresponds to the vibration of m_8 and as such is also largely decoupled from the response of the other six DOF. The complexity of the system response presents a true test of not only the algorithm's robustness but also the automatic frequency line selection subroutine. Although unnecessary for the operation of the algorithm, for clarity, the eight natural frequencies and damping factors of the baseline system, obtained via solution of the complex eigenvalue problem, are given in Table 5-6 in the damaged system description section.

5.6.2 Damaged System Description

In order to evaluate the performance of the algorithm relative to the alternative methods, the same three damage cases used by Oliver [2] are also used in this dissertation. The three damage cases build on one another where the first damage case corresponds to a ten percent reduction of stiffness in spring eight, a main "structural member" spring. The second case adds a five percent damage to spring twelve, which corresponds to a secondary load path having a stiffness value two orders of magnitude less than spring eight. The last case incorporates a one percent increase in the mass of masses two, three, four, and five which could be used to simulate an event such as an increase in propellant weight relative to the baseline case in addition to the damage scenarios. The damage cases are shown graphically in Figure 5-36.

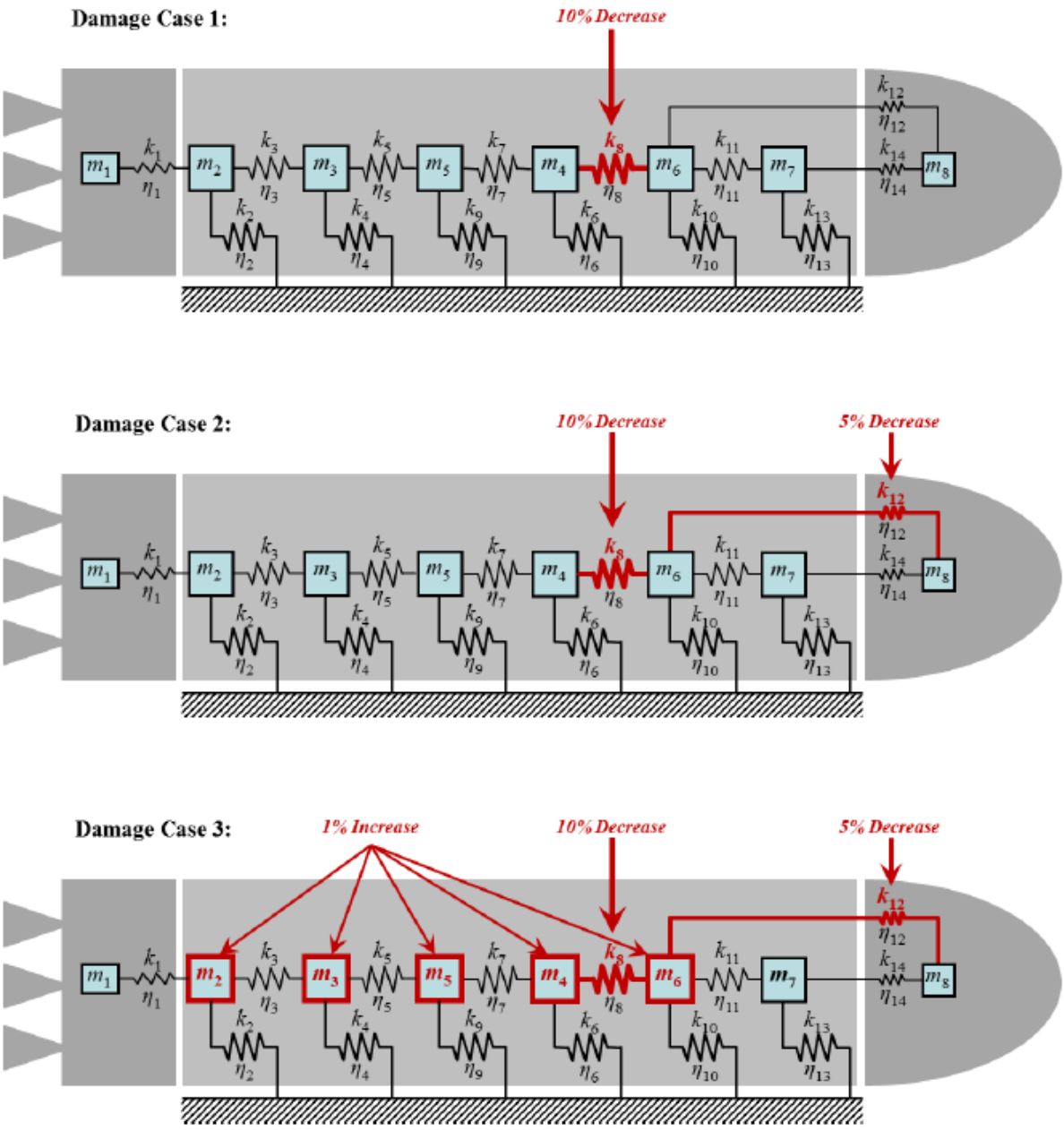

Figure 5-36: Three damaged cases used for algorithm performance comparisons [2].

The natural frequencies and damping ratios of the baseline and three damaged configuration cases have been tabulated for comparison and are given in Table 5-6. Also listed in the table are the relative changes in the frequencies and damping factors caused by each damage scenario.

Table 5-6: Modal parameters of the spring, mass, rocket model for the baseline and three damaged configurations.

		Mode							
		1	**2**	**3**	**4**	**5**	**6**	**7**	**8**
Baseline System	ω_n *(Hz)*	4.88	5.05	5.05	5.15	5.44	5.66	6.17	6.67
	ζ_n	0.0111	0.0489	0.0104	0.0247	0.0254	0.0124	0.0053	0.0021
Damage Case 1	ω_n *(Hz)*	4.88	5.05	5.05	5.15	5.42	5.64	6.17	6.67
	% Change	-0.034	0.000	-0.007	-0.022	-0.419	-0.354	0.000	-0.002
	ζ_n	0.0109	0.0489	0.0104	0.0245	0.0247	0.0134	0.0053	0.0021
	% Change	-1.72	0.007	0.222	-0.798	-2.68	8.58	0.000	-0.123
Damage Case 2	ω_n *(Hz)*	4.88	5.05	5.05	5.15	5.42	5.64	6.17	6.57
	% Change	-0.034	0.000	-0.013	-0.022	-0.42	-0.355	0.000	-1.436
	ζ_n	0.0109	0.0489	0.0104	0.0245	0.0247	0.0134	0.0053	0.0021
	% Change	-1.73	0.007	0.21	-0.804	-2.69	8.59	0.000	0.189
Damage Case 3	ω_n *(Hz)*	4.86	5.02	5.05	5.13	5.39	5.61	6.17	6.57
	% Change	-0.528	-0.492	-0.029	-0.504	-0.911	-0.849	-0.004	-1.438
	ζ_n	0.0109	0.0489	0.0107	0.0243	0.0247	0.0134	0.0053	0.0021
	% Change	-1.72	0.034	2.90	-1.90	-2.71	8.58	-0.296	0.036

The results of Table 5-6 confirm the previously discussed result that changes in frequency or damping alone are not a good indication of the presence of damage. The reader is reminded that computation of natural frequencies is not necessary for the operation of the algorithm and are instead computed for the sake of completeness in the analysis. For the current algorithm, the most important metric to determine whether damage identification is possible is the relative change in the PSD between the healthy and damaged systems. Since the algorithm relies on the residual error between the healthy and damaged system responses at discrete frequency lines, it is imperative to the operation that the damage has a discernable effect on the PSD response. To this end, an overlay plot of the baseline auto-PSD of x_5 as well as the auto-PSD of x_5 for each damage case is given in Figure 5-37.

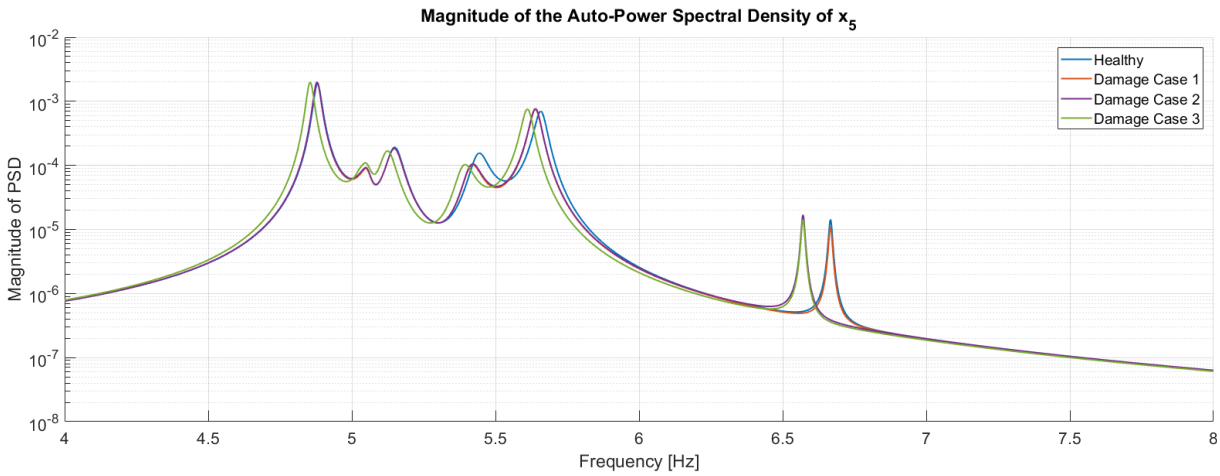

Figure 5-37: Overlay plot of the auto-power spectral density of x_5 for the healthy and damaged cases.

Figure 5-37 reveals the influence of the damage cases on each of the PSD peaks. Damage case one, indicated by the red line, shows very little deviation from the healthy PSD (blue line) for peaks one through four. Peaks six and eight however show large deviations from the healthy PSD, providing ample information for the SHM algorithm to operate. As the damage is increased by altering k_{12} in damage case two (purple line), peaks one and four start to show some deviation from their healthy states. The final damage case (green line) shows the largest shifts in the damaged PSD response due to the increase in mass at the selected DOF. The challenge for the algorithm in damage case three is to isolate the changes in the PSD that are caused by decreasing stiffness from those caused by increasing mass.

5.6.3 Current Algorithm Performance

Prior to comparisons between alternative approaches, a comprehensive study of the current algorithm was performed on the three damage cases. For each case, varying levels of measurement noise were added to the displacement PSD in accordance with the method given in section 4.6. In each case, the coherence-based frequency line selection subroutine was run to identify the best

frequency lines in the vicinity of 0.5 and 0.95 of each of the PSD peaks, yielding a total of 32 analysis lines. Each of the damage identification runs contained all 22 of the available update parameters (eight mass and fourteen stiffness parameters) in the form of the normalized damage scale factors utilized in the current approach. As before, a damage scale factor of 1 indicates no change in that particular parameter whereas a value of 0.5 would be a 50% reduction in that parameter's value. All of the algorithm settings remained unchanged from the previous sections in regards to stopping criteria, iteration step limit, and initial parameter uncertainty.

The noise levels studied in the current section range from realistic values of 0.1% and 1% to an extreme example of 10%. Overlaid plots of the magnitude of the auto-PSD of x_5 subjected to the three levels of noise studied in the current section is given in Figure 5-38.

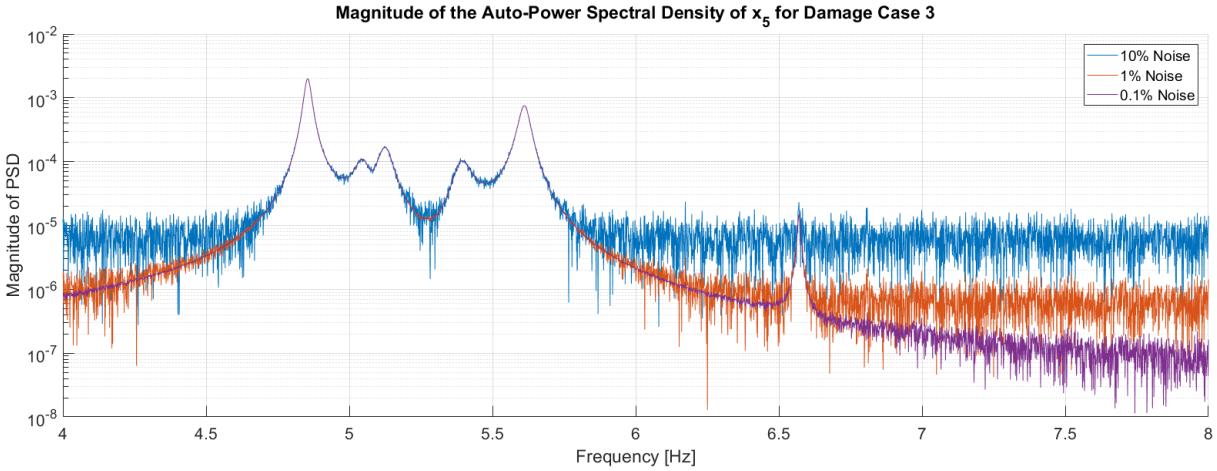

Figure 5-38: Overlay plot of the auto-power spectral density of x_5 for the three noise levels on damage case 3.

Nine total algorithm runs were performed covering each of the three damage cases at each of the three noise levels. Each of the analysis were performed using each of the eight available reference DOF and the results of the solutions that converged were averaged to yield the mean damage scale factor associated with each of the update parameters. The resulting 22 damage scale

factors are plotted with their converged value for each of the reference DOF which converged for damage case three with 0.1% noise in Figure 5-39.

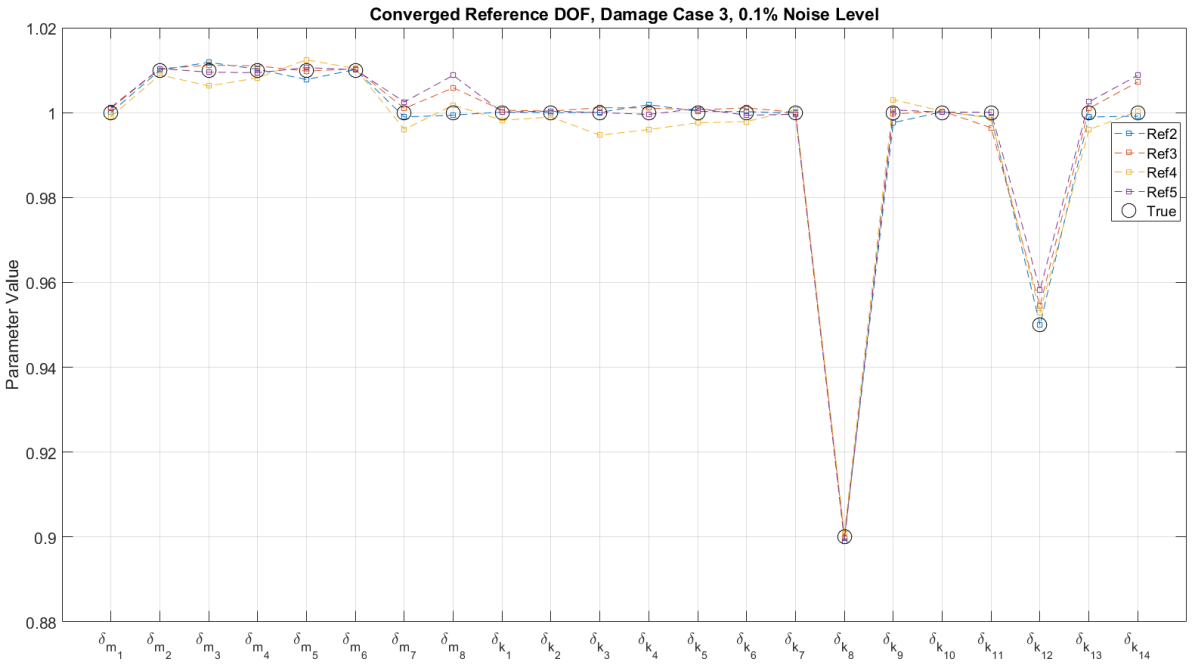

Figure 5-39: Converged damage scale factors for each of the 22 damage parameters plotted for each reference DOF which reached convergence as well as the true values for damage case 3, 0.1% noise.

Once the converged solution sets for each reference DOF were obtained, the mean and standard deviation of each parameter were calculated over the available converged reference DOF and reported as the solution values and variances, respectively. Using the data presented in Figure 5-39, the mean scale factor values and standard deviations for damage case three, 0.1% noise, are shown in Figure 5-40.

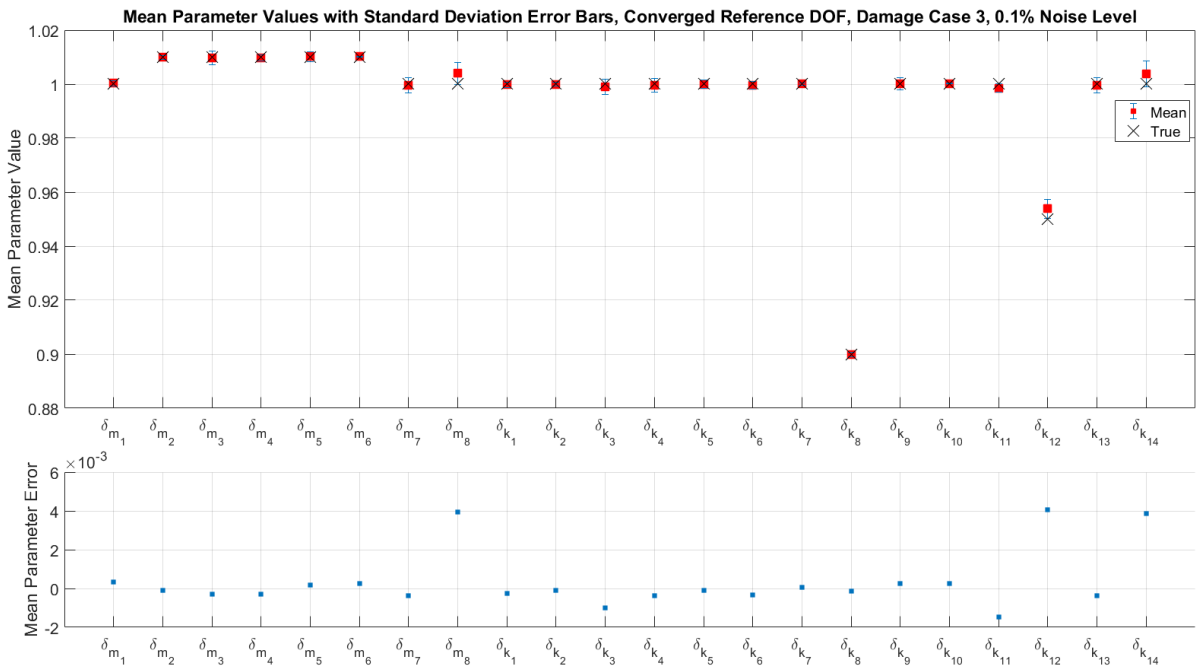

Figure 5-40: (Upper) Mean converged damage scale factors for each of the 22 damage parameters with error bars representing one standard deviation. (Lower) Mean parameter error.

The same calculation methodology was applied to all nine analysis runs and the mean parameter values were tabulated in Table 5-7. The trends in the data tabulated for the nine cases are that as the damage increases in complexity (moving from case one to case three) the solution error does not significantly increase. Increases in noise levels do however have a profound impact on the error of converged solution as shown in all three cases. Also important to note is that the average number of iterations to convergence increases with increasing levels of damage (or in this case complexity of damage, i.e. multiple parameter changes) and levels of noise. While the data is not reported for each individual reference DOF, for all of the nine cases, it is noteworthy that parameter errors as large as 8% were seen in some parameters for a single reference DOF with 10% noise. After averaging the data with all converged reference DOF however the maximum error was found to be 4.05%, demonstrating the utility of utilizing multiple reference DOF.

Table 5-7: Percent error of the mean damage scale factors for each of the nine damage cases run as well as the average number of iterations to convergence.

	Mean Damage Scale Factor Percent Error											
	True	Damage Case 1			True	Damage Case 2			True	Damage Case 3		
Parameter	Value	0.10%	1%	10%	Value	0.10%	1%	10%	Value	0.10%	1%	10%
εm_1	**0.001**	0.02	-0.24	0.95	**0.001**	0.06	-0.11	-0.79	**0.001**	0.03	-0.19	-1.18
εm_2	**1.000**	0.01	-0.09	1.72	**1.000**	0.02	0.06	1.74	**1.010**	-0.01	-0.12	1.03
εm_3	**1.000**	-0.02	0.16	-0.57	**1.000**	-0.03	0.23	1.97	**1.010**	-0.03	-0.47	-3.75
εm_4	**1.000**	0.07	0.32	3.54	**1.000**	-0.02	0.05	-1.59	**1.010**	-0.03	-0.09	1.00
εm_5	**1.000**	-0.05	-0.52	2.75	**1.000**	0.01	0.08	-3.72	**1.010**	0.02	0.03	0.08
εm_6	**1.000**	0.02	0.16	1.52	**1.000**	-0.01	0.52	-1.07	**1.010**	0.02	-0.04	1.26
εm_7	**1.000**	-0.02	-0.02	1.94	**1.000**	-0.02	-0.14	0.34	**1.000**	-0.04	-0.01	-1.02
εm_8	**0.002**	-0.03	-0.04	0.73	**0.002**	-0.12	0.07	-0.46	**0.002**	0.40	0.20	0.41
εk_1	**1.500**	0.02	-0.04	1.93	**1.500**	0.01	0.01	1.50	**1.500**	-0.02	-0.17	1.57
εk_2	**1000**	0.01	-0.08	1.73	**1000**	0.03	0.06	1.75	**1000**	-0.01	-0.12	1.03
εk_3	**10.00**	-0.21	-0.58	1.93	**10.00**	-0.17	-0.33	0.94	**10.00**	-0.10	-0.59	0.62
εk_4	**1000**	-0.03	0.19	-0.72	**1000**	-0.03	0.24	2.14	**1000**	-0.04	-0.49	-3.92
εk_5	**100.0**	0.03	-0.14	1.05	**100.0**	0.01	0.17	-2.69	**100.0**	-0.01	-0.17	-1.14
εk_6	**900.0**	0.08	0.38	3.83	**900.0**	-0.02	0.02	-1.56	**900.0**	-0.03	-0.09	1.07
εk_7	**100.0**	-0.03	-0.14	2.77	**100.0**	-0.07	-0.04	-2.04	**100.0**	0.01	-0.02	-0.17
εk_8	**90.00**	0.17	0.45	2.82	**90.00**	-0.01	0.37	0.97	**90.00**	-0.01	-0.14	0.72
εk_9	**900.0**	-0.05	-0.60	2.76	**900.0**	0.02	0.08	-4.05	**900.0**	0.03	0.07	0.18
εk_{10}	**1000**	0.02	0.15	1.37	**1000**	-0.01	0.55	-1.13	**1000**	0.03	-0.05	1.35
εk_{11}	**10.00**	-0.11	0.30	2.82	**10.00**	-0.05	0.42	1.44	**10.00**	-0.15	-0.26	-1.12
εk_{12}	**2.000**	-0.07	-0.12	1.37	**1.900**	-0.12	0.37	0.38	**1.900**	0.40	0.17	1.94
εk_{13}	**1000**	-0.02	-0.02	1.95	**1000**	-0.02	-0.15	0.33	**1000**	-0.04	-0.01	-1.02
εk_{14}	**1.500**	0.02	0.07	-0.13	**1.500**	-0.10	-0.30	-0.10	**1.500**	0.39	0.24	-1.54
Average Iterations	-	5	7.8	11.67	-	15.5	20	28.33	-	48.5	53	58.33

In theory, as the number of available reference DOF increases the mean parameter value will approach its true value minimizing this error. For the maximum error case in the current example, only three of the eight reference DOF yielded a converged solution, greatly diminishing the potential effects of averaging. In practice it is likely many more reference DOF would be available. It is also possible to tune the parameters of the algorithm specifically for each reference

DOF in turn increasing the convergence rate, although this may be cumbersome and was not done in this study.

Equally important to the mean parameter errors given in Table 5-7, the corresponding standard deviations complete the picture in terms of the confidence in the parameter estimation. Table 5-8 lists these standard deviations for all 22 parameters' scale factors for each of the nine test cases presented. Since these are standard deviations of the damage scale factors, normalized from 0 to 1 by definition, they can be thought of in terms of the percent parameter variation. In the current cases presented, the maximum standard deviation found was 0.06485 or 6.485% of that parameter. While this is rather large, it occurred in a worst-case scenario of 10% measurement noise and only three converged reference DOF, leading to the large deviation. In all but one case for the more realistic 0.1% and 1% noise studies these standard deviations were well below 1%. The exception to this was the stiffness scale factor associated with k_3 for damage case 1, 1% noise. In this case the standard deviation was 0.01337, still low enough to provide meaningful confidence in the identified parameter.

Table 5-8: Standard deviation of the damage scale factors for each of the nine damage cases run.

Damage Scale Factor Standard Deviations									
	Damage Case 1			Damage Case 2			Damage Case 3		
Parameter	0.10%	1%	10%	0.10%	1%	10%	0.10%	1%	10%
$\sigma_{\delta m1}$	0.0017	0.0073	0.0257	0.0016	0.0037	0.0402	0.0010	0.0058	0.0265
$\sigma_{\delta m2}$	0.0009	0.0068	0.0230	0.0012	0.0053	0.0167	0.0007	0.0057	0.0236
$\sigma_{\delta m3}$	0.0018	0.0079	0.0397	0.0024	0.0043	0.0261	0.0025	0.0066	0.0403
$\sigma_{\delta m4}$	0.0014	0.0056	0.0360	0.0011	0.0039	0.0185	0.0012	0.0044	0.0360
$\sigma_{\delta m5}$	0.0005	0.0072	0.0497	0.0011	0.0031	0.0234	0.0019	0.0066	0.0497
$\sigma_{\delta m6}$	0.0006	0.0067	0.0079	0.0005	0.0086	0.0388	0.0001	0.0066	0.0329
$\sigma_{\delta m7}$	0.0014	0.0070	0.0200	0.0018	0.0079	0.0301	0.0028	0.0041	0.0267
$\sigma_{\delta m8}$	0.0007	0.0026	0.0170	0.0013	0.0038	0.0402	0.0042	0.0059	0.0245
$\sigma_{\delta k1}$	0.0011	0.0078	0.0308	0.0013	0.0063	0.0191	0.0011	0.0079	0.0326
$\sigma_{\delta k2}$	0.0009	0.0068	0.0231	0.0012	0.0052	0.0168	0.0007	0.0055	0.0230
$\sigma_{\delta k3}$	0.0025	0.0134	0.0155	0.0026	0.0091	0.0263	0.0029	0.0154	0.0606
$\sigma_{\delta k4}$	0.0019	0.0085	0.0430	0.0024	0.0048	0.0272	0.0026	0.0069	0.0429
$\sigma_{\delta k5}$	0.0007	0.0057	0.0126	0.0009	0.0032	0.0253	0.0015	0.0024	0.0236
$\sigma_{\delta k6}$	0.0015	0.0063	0.0409	0.0013	0.0049	0.0194	0.0014	0.0049	0.0419
$\sigma_{\delta k7}$	0.0004	0.0044	0.0230	0.0003	0.0020	0.0118	0.0005	0.0026	0.0160
$\sigma_{\delta k8}$	0.0021	0.0019	0.0231	0.0009	0.0018	0.0218	0.0007	0.0025	0.0048
$\sigma_{\delta k9}$	0.0006	0.0082	0.0577	0.0014	0.0037	0.0228	0.0022	0.0077	0.0559
$\sigma_{\delta k10}$	0.0006	0.0070	0.0089	0.0005	0.0093	0.0396	0.0001	0.0070	0.0346
$\sigma_{\delta k11}$	0.0009	0.0061	0.0382	0.0012	0.0056	0.0649	0.0015	0.0034	0.0185
$\sigma_{\delta k12}$	0.0013	0.0092	0.0273	0.0022	0.0100	0.0325	0.0034	0.0096	0.0512
$\sigma_{\delta k13}$	0.0015	0.0071	0.0201	0.0018	0.0080	0.0299	0.0028	0.0041	0.0270
$\sigma_{\delta k14}$	0.0005	0.0074	0.0036	0.0004	0.0049	0.0236	0.0048	0.0059	0.0289

In keeping with the work done by Oliver, for the sake of comparison to other methods, the parameters were broken into three groups and the mean relative error for each group tabulated.

The three groups are: (1) healthy stiffness parameters, (2) damaged stiffness parameters and (3) mass parameters. The distinction between the healthy and damaged stiffness parameter sets is important to be able to classify potential false negative events (large damage parameter error, ε_{MRE}^{d}) and false positive events (large healthy parameter error, ε_{MRE}^{h}) [2]. The mass parameters have been included in the analysis so as to distinguish between changes in system mass and damage events. As such, the third error grouping is defined as the mean relative error of the mass parameters, ε_{MRE}^{m}. Each of these errors were calculated from the mean converged updated parameter errors listed in Table 5-7 such that:

$$\varepsilon_{MRE}^{d} = \frac{1}{N_r^d}\sum_{i=1}^{N_r^d}\left|\varepsilon k_i^d\right|, \tag{5-14}$$

$$\varepsilon_{MRE}^{h} = \frac{1}{N_r^h}\sum_{i=1}^{N_r^h}\left|\varepsilon k_i^h\right|, \tag{5-15}$$

$$\varepsilon_{MRE}^{m} = \frac{1}{N_r^m}\sum_{i=1}^{N_r^m}\left|\varepsilon m_i^m\right|, \tag{5-16}$$

where N_r^d is the number of damaged stiffness parameters and εk_i^d is the converged update parameter error of the i^{th} damaged stiffness parameter in equation (5-14). Likewise, the superscripts on *h* and *m* in equations (5-15) and (5-16) denote the healthy stiffness and mass parameters, respectively. The mean relative error for each of the three parameter groups is plotted as a function of noise level for damage cases one, two, and three in Figure 5-41, Figure 5-42, and Figure 5-43, respectively.

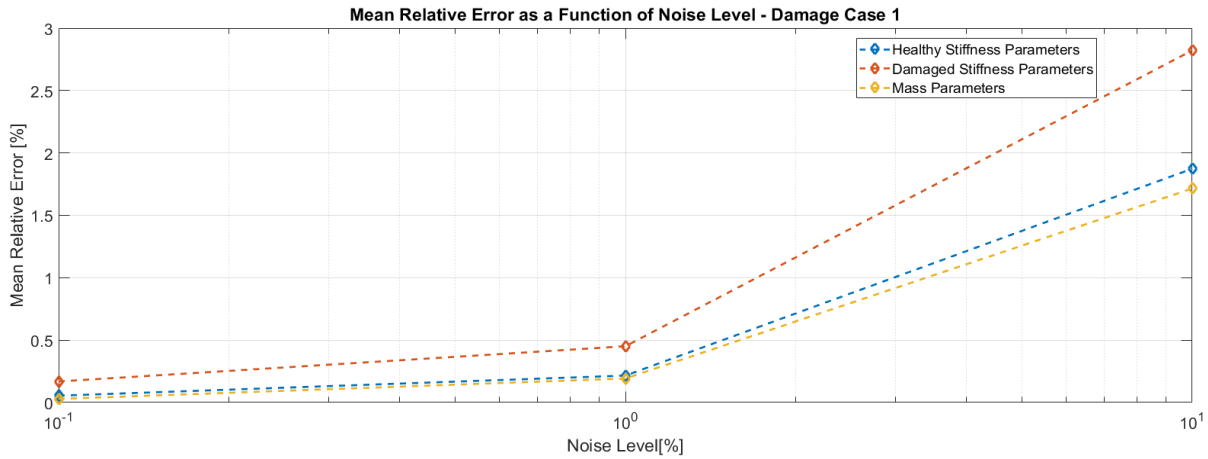

Figure 5-41: Mean parameter error as a function of noise level for damage case 1.

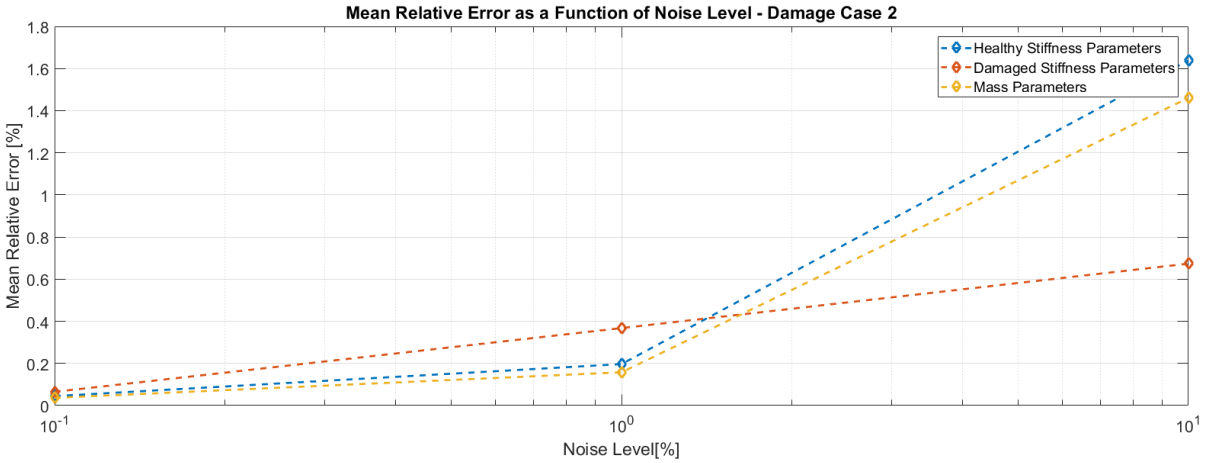

Figure 5-42: Mean parameter error as a function of noise level for damage case 2.

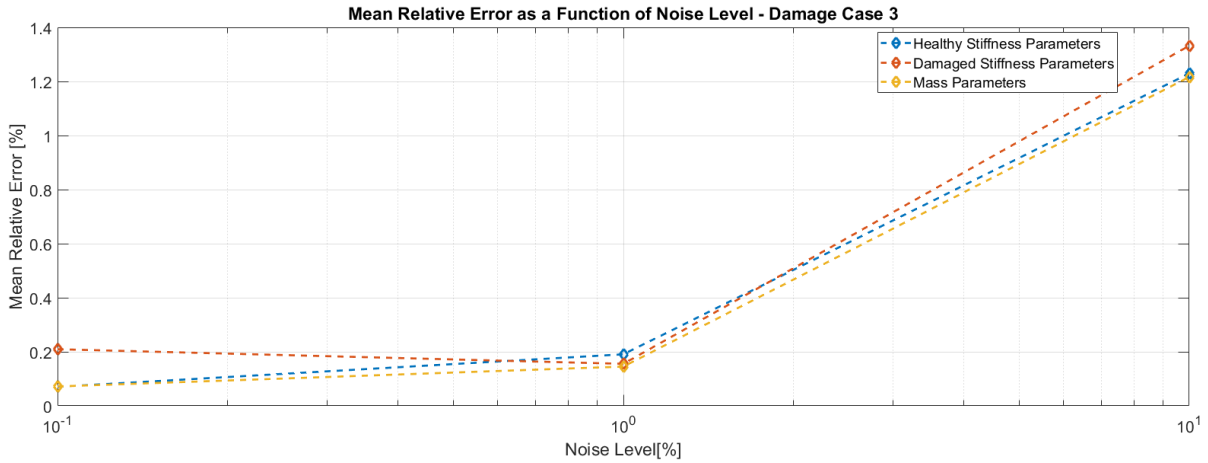

Figure 5-43: Mean parameter error as a function of noise level for damage case 3.

While the specific values of the mean relative parameter error vary on a case-by-case basis, the general trend of an increase in error with increasing noise levels is clearly visible. The mean relative parameter error was shown to be on the same order of magnitude for each parameter grouping and damage case, only largely varying across noise levels. This result suggests that the algorithm performance (as classified by parameter error) is driven by the measurement noise much more so than the parameter type or specific damage scenario.

5.6.4 Comparison of Performance Relative to Other Methods

In order to better evaluate the performance of the current SHM algorithm, four alternative approaches were applied to the same nine test cases and their performance benchmarked. The four alternative approaches considered are the methods of Oliver [2], Araujo dos Santos et al. [62], Zimmerman et al. [106] and Zang and Imregun [107]. Each of these algorithms are model updating based SHM techniques allowing for direct comparisons to be made. While the reader is referred to the respective papers for the details of each method, an overview of each is given below.

The algorithm developed by Oliver is a statistical model updating scheme which relies on minimizing the residual force vector using acceleration based FRF data. Oliver also builds upon the work of Tarantola and Valette [69], utilizing a Bayesian cost function to solve a generalized nonlinear least squares problem. Araujo dos Santos uses a method very similar to that of Oliver with a couple of major distinctions: (1) the FRF are formulated using mode shapes and natural frequencies, rather than direct computation, leading to the need to use mode shapes and frequencies spanning three times the frequency range of interest and (2) the solution of the residual force problem is done with a deterministic least-squares solution. Zimmerman et al. utilizes direct computation of the FRF (rather than derived from modal properties) to perform an FRF based updating using minimum rank perturbation theory (MRPT). Using MRPT, the Zimmerman

algorithm seeks to find the stiffness or mass change responsible for the difference between the modeled and measured FRF in a single step (rather than the iterative approaches of the other methods). Zang and Imregun use global shape and global amplitude correlation functions to perform a sensitivity based updating routine where these correlation functions are dependent on the modeled and measured FRF. Their approach also utilizes a deterministic least-squares approach to maximize the correlation between the two FRF using these correlation functions.

All of the results presented in the current sections, with the expection of those pertaining to the current method, were tabulated by Oliver [2] using the damage cases previously presented in this section. Since in the Zimmerman algorithm only changes in stiffness or mass are permissible, not both simultaneously, only stiffness parameter damage cases one and two are assessed in the initial comparisons. For the initial comparisons, the current algorithm was run again using the same parameters previously described in the absence of noise. The results of these damage identification runs for damage cases one and two are given in Table 5-9 and Table 5-10, respectively.

The results of the noise free studies on damage cases one and two are that all of the methods converge to negligible error. The current algorithm as well as the methods of Oliver and Dos Santos converged in two iterations. The Zimmerman approach is a single step and thus has no associated iterations and the Zang algorithm converges in an order of magnitude more iterations.

Table 5-9: Mean relative parameter error across alternative methods for damage case 1, no noise.

Mean Damage Scale Factor Relative Error - Damage Case 1					
Parameter	**Current Algorithm**	**Oliver**	**Dos Santos**	**Zimmerman et.al**	**Zang et al.**
εk_1	-1.39E-03	1.69E-09	-1.22E-09	0.00E+00	1.24E-04
εk_2	-1.12E-06	-1.38E-10	-3.33E-10	0.00E+00	2.65E-05
εk_3	-1.09E-04	2.94E-10	-1.01E-09	0.00E+00	5.25E-04
εk_4	-1.31E-06	-3.27E-10	1.07E-10	0.00E+00	-3.90E-06
εk_5	1.61E-04	3.14E-09	-8.19E-10	0.00E+00	2.91E-05
εk_6	-1.68E-05	2.03E-10	-6.27E-11	3.99E-10	8.01E-06
εk_7	2.18E-04	-1.13E-09	-6.59E-11	-3.60E-09	1.88E-05
εk_8	-5.43E-05	3.78E-10	1.22E-09	-1.11E-05	4.40E-05
εk_9	3.30E-05	1.32E-10	8.25E-11	4.00E-10	-1.11E-05
εk_{10}	-1.20E-05	1.00E-11	-6.25E-11	-5.65E-11	-2.81E-06
εk_{11}	3.29E-04	7.37E-09	8.58E-10	5.70E-09	3.61E-05
εk_{12}	5.62E-04	6.55E-08	5.81E-09	4.71E-11	5.46E-05
εk_{13}	-1.90E-06	-1.14E-10	-6.27E-11	-5.70E-11	1.87E-07
εk_{14}	-8.82E-04	-3.70E-08	-2.38E-09	-2.09E-11	-7.70E-05
ε^d_{MRE}	-5.43E-05	3.78E-10	1.22E-09	1.11E-05	4.40E-05
ε^h_{MRE}	2.86E-04	9.00E-09	9.90E-10	7.91E-10	7.05E-05
Iterations	2	2	2	N/A	13

Refinement of the stopping criteria is known to reduce the converged error of the current method but were left fixed to maintain uniformity throughout the dissertation. This increase in accuracy does come at the cost of computational speed and the parameters used in the dissertation were chosen to provide the best compromise between accuracy and speed. Furthermore, the level of errors for all of the methods in the noise-free studies are so small they are all essentially zero for all practical considerations.

Table 5-10: Mean relative parameter error across alternative methods for damage case 2, no noise.

Mean Damage Scale Factor Relative Error - Damage Case 2					
Parameter	**Current Algorithm**	**Oliver**	**Dos Santos**	**Zimmerman et.al**	**Zang et al.**
εk_1	-1.39E-03	-6.00E-11	7.64E-10	0.00E+00	-3.01E-04
εk_2	-1.09E-06	-4.79E-10	-4.90E-11	0.00E+00	-8.36E-07
εk_3	-1.12E-04	6.92E-10	1.40E-09	-1.90E-14	-8.48E-04
εk_4	-6.25E-07	-1.11E-10	5.33E-11	0.00E+00	1.07E-05
εk_5	1.55E-04	-6.41E-09	6.04E-10	-1.61E-14	9.42E-06
εk_6	-1.69E-05	-3.36E-10	-1.70E-10	-2.27E-05	-7.95E-07
εk_7	2.15E-04	6.01E-09	-5.53E-10	-1.78E-10	-3.97E-06
εk_8	-1.66E-05	-6.37E-11	4.46E-10	3.56E-04	1.80E-05
εk_9	3.22E-05	2.55E-10	1.45E-10	1.98E-11	-1.08E-06
εk_{10}	-1.18E-05	-5.91E-10	-1.84E-11	5.11E-06	-3.04E-07
εk_{11}	3.11E-04	-1.22E-08	-1.45E-09	4.42E-09	4.15E-05
εk_{12}	5.22E-04	-2.81E-08	-2.77E-09	8.06E-03	-8.72E-06
εk_{13}	-1.88E-06	1.53E-10	5.60E-11	5.11E-06	-1.81E-06
εk_{14}	-8.18E-04	1.06E-08	6.45E-10	-3.41E-03	5.87E-06
ε^d_{MRE}	2.69E-04	1.41E-08	1.61E-09	4.21E-03	1.34E-05
ε^h_{MRE}	2.99E-04	3.73E-09	5.04E-10	5.27E-04	9.47E-05
Iterations	2	2	2	N/A	21

A more realistic assessment of the performance of the algorithms is under the present of measurement noise. To this end, the same analysis procedure was repeated on damage cases one and two using the three levels of simulated measurement noise, 0.1%, 1% and 10%. The details of each individual parameter error have been omitted and instead the mean relative error of the healthy and damaged parameter groups for damage cases one and two are plotted in Figure 5-44.

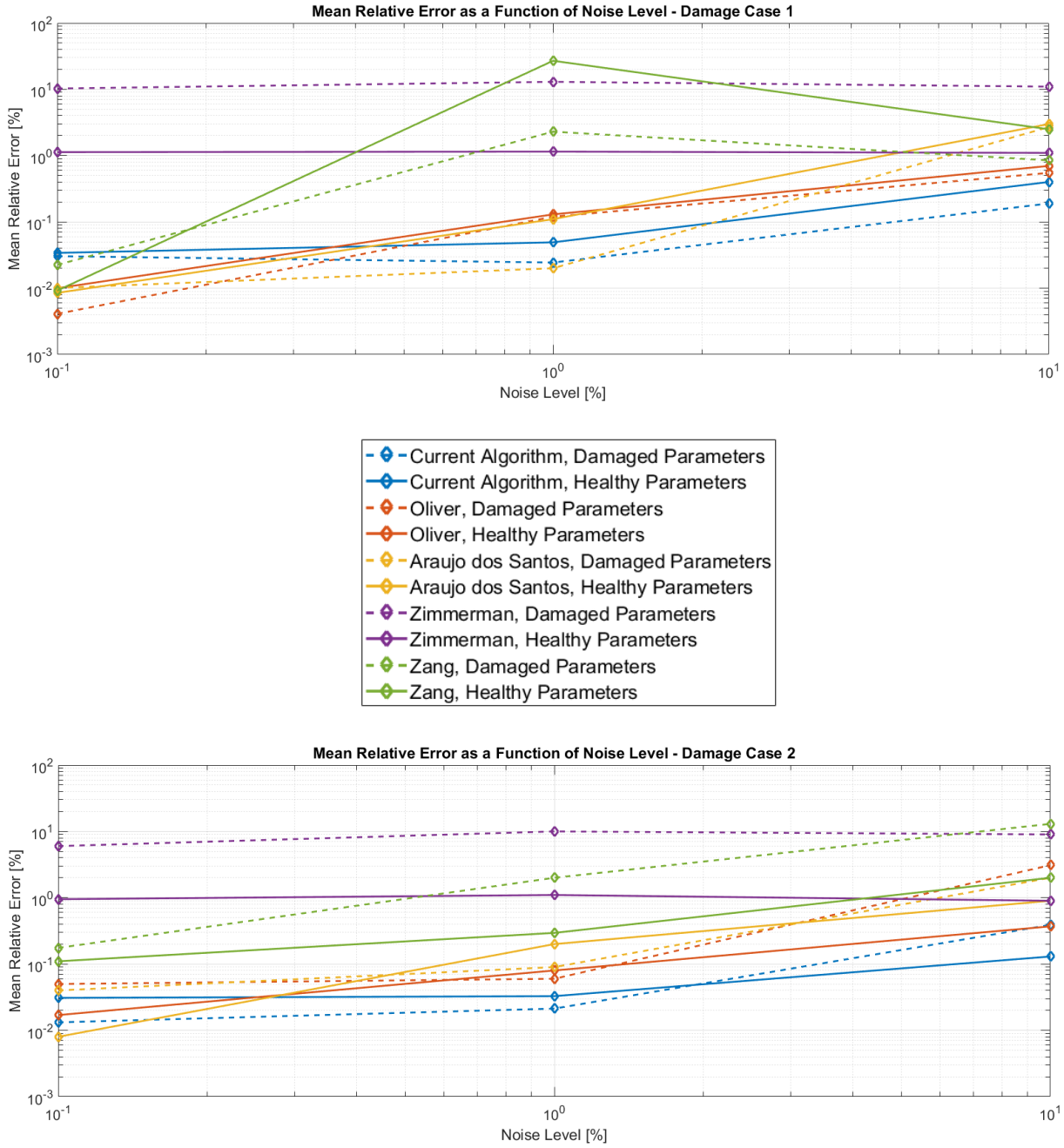

Figure 5-44: Mean parameter error as a function of noise level for damage cases 1 (upper plot) and 2 (lower plot).

Analysis of the plots in Figure 5-44 shows that the method of Zimmerman does not reach a meaningful solution in the presence of noise, with mean relative errors on the order of 100% or more. The method of Zang is able to accurately determine the parameter sets of interest for relatively low measurement noise but again struggles with the higher noise cases. It was noted by

Oliver that the method proposed by Zang does not converge for any of the noise cases after 100 iterations. It was also noted that although the Zang algorithm does at times produce meaningful solutions the behavior is not stable with measurement noise. The current algorithm most closely matches the performance of the methods proposed by Oliver and Araujo dos Santos, with all three algorithms converging in a similar number of iterations and mean relative error values.

The top three performing algorithms, the current and that of Oliver and Araujo dos Santos, were further compared using damage case three. The three algorithms were again run for 0.1%, 1% and 10% noise and the mean relative error calculated. For the damage case three runs, the mass parameters were incorporated into the solution space, bringing the total number of updated parameters to 22. All other algorithm settings were left unchanged from the previous runs. The results for each of the three algorithms applied to damage case three for the three chosen noise levels are shown in Figure 5-45 in terms of the percentage mean relative error.

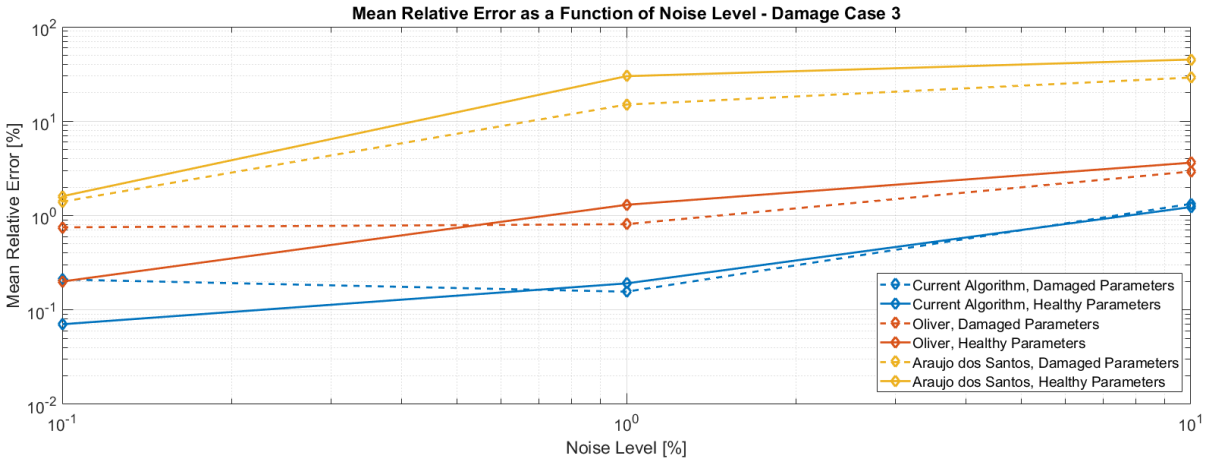

Figure 5-45: Mean parameter error as a function of noise level for damage case 3.

The results of the analysis show that the current algorithm outperformed the other two methods in terms of mean relative error for damage case three as well. Oliver's approach performed very well, even under the extreme 10% noise case, and was within a couple percent of

the current method. On a case by case basis, the current method only performs marginally better than Oliver's method for a given reference DOF. The gains in the current method become clearer as more reference DOF are used. This of course comes at the penalty of increased computational time as the computations relative to each reference DOF are performed serially. In principle, each of these computations could happen in parallel provided enough computational resources were available. The method of Araujo dos Santos performed well for the case of 0.1% noise however as the noise level increased the error became unacceptably large. It is believed that that inclusion of the mass parameters in the solution space causes the deterministic least squares to perform poorly under the larger solution space and range of parameter sensitivities.

Chapter 6: Validation of and Advancements in Fiber Optic Strain Sensing

One of the underpinnings of the dissertation thus far is the requirement that high density strain data be available to the algorithm for use in computing the strain PSD used as the damage feature. There are many methods available for dynamic strain sensing ranging from conventional foil gauges to digital image correlation and various types of fiber optic sensors. The current work focuses on the most practical sensor type which allow for in-flight, high density measurements. To this end, both wavelength division multiplexed (WDM) and optical frequency domain reflectometry (OFDR) optical fiber strain sensors were considered and compared.

The subsequent sections discuss the state-of-the-art of each of the sensor types at the onset of the current research as well as the latest advancements in dynamic strain sensing related to this research. These advancements were made through a collaboration with researchers at NASA Armstrong Flight Research Center (AFRC). All fiber optic dynamic strain measurements were recorded using AFRC developed equipment and sampling software. All experimental studies were performed at either AFRC or the University of California San Diego.

6.1 Traditional OFDR and WDM Techniques

At the onset of the research, it was desirable to perform an assessment of the current state-of-the-art of fiber optic strain sensing systems. As a result, in 2015, using a test article on loan from AFRC, the performance of both ODFR and WDM sensing systems were compared to the performance of accelerometers and a scanning laser vibrometer (SLV). The test article used for the comparisons was an aluminum plate that was previously instrumented with both WDM and OFDR sensors nearly collocated along its length.

The chosen test article was 0.195 inches thick, 12 inches wide, 37.75 inches in length, and made 6061-T6 aluminum. A 1.75 inch section of the plate was clamped yielding a cantilever configuration with an effective plate length of 36 inches. Six rectangular sections of the plate were removed such that the plate had discontinuous cross section properties, with response properties similar to a sub-scale wing box with internal spars and ribs. A dimensioned drawing of the plate is shown in Figure 6-1 along with the locations of the accelerometers, optical frequency domain reflectometry (OFDR) sensing fibers, and wavelength division multiplexing (WDM) sensing fibers.

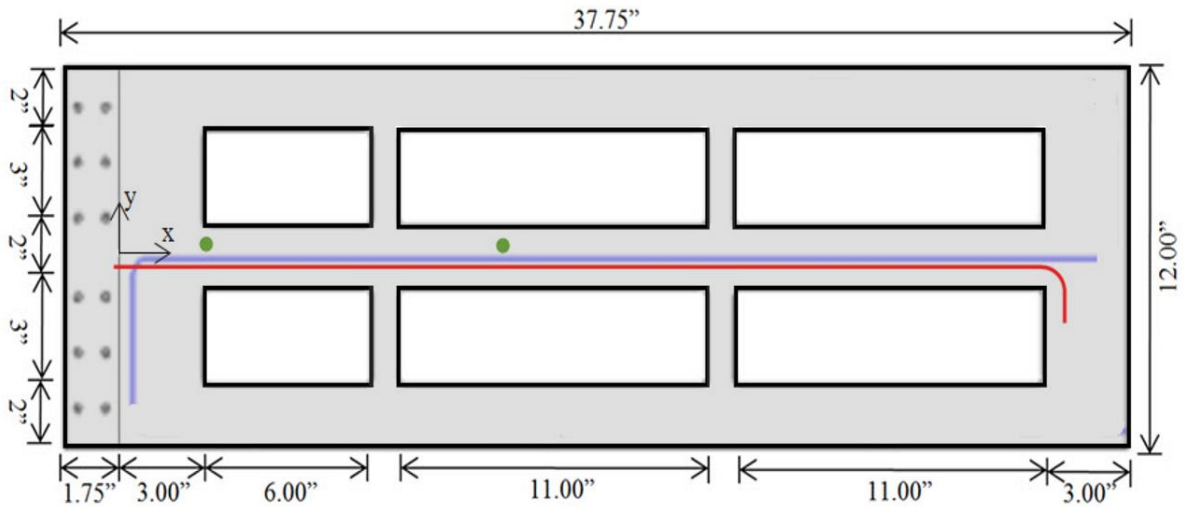

Figure 6-1: Schematic of the aluminum plate showing the existing 6 cutouts, OFDR optical fiber (blue), WDM optical fiber (red), and accelerometer (green) locations.

The aluminum plate’s dynamic response was recorded with four sensor types for the purposes of the current study (accelerometers, laser vibrometer, WDM optical sensors and OFDR optical sensors). Additionally, a piezoelectric PCB force transducer (model 208C02) was used for all force measurements in the current study. To minimize the mass loading on the plate, only two piezoelectric PCB teardrop accelerometers (model 352C22/NC) were used, as indicted by the

green dots in Figure 6-1. In order to produce a high-fidelity modal model of the plate, a Polytec PSV-500 SLV was used with 144 target locations. The SLV and accelerometers were used to develop baselines of the plate's response for comparisons with the fiber optic systems. The two types of optical fiber strain sensors evaluated were both based on fiber Bragg grated sensor technologies; (1) continuously grated FBGS Draw Tower Gratings fibers interrogated every 0.125 inch along the fiber length and multiplexed using an OFDR scheme and (2) 0.59 inch fiber Bragg grated sensors with 0.5 inch between adjacent sensor gratings manufactured by Technica SA and multiplexed using a WDM scheme. The test article and collocated sensors are shown in Figure 6-2 below.

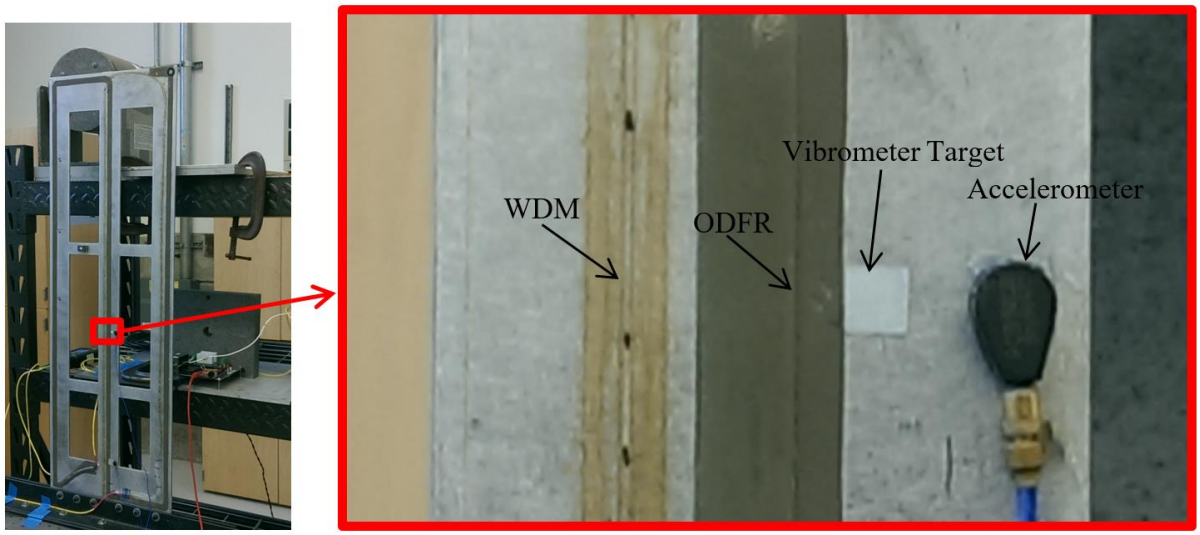

Figure 6-2: (Left) Cantilever aluminum plate as tested. (Right) Zoomed view of the sensors studied. Note that the optical fiber sensors are under sealant and the sensors themselves are the thin lines.

Each of the two distributed fiber optic sensor arrays tested required a unique interrogation system. The OFDR system tested in these initial studies was capable of sampling up to 60Hz. For the studies presented herein, the OFDR system was set to sample at a nominal value of 51Hz as this was the optimum trade-off between sampling rate and noise level. While the relatively low

maximum sampling rate is problematic for practical applications at the present time, the limitations are in computational power and mechanical actuation speed (of the armature for the sweeping laser). It is believed in the coming years these restrictions will be resolved and the low-cost approach will gain in popularity. The OFDR sensors have a spatial resolution that is tunable down to 1/8 inch spacing on a 40 foot run of fibers. The ability to adjust the sensor spacing and thus the number of sensors makes the approach tailorable to many applications over a range of length scales. Furthermore, one yard of the sensing fiber (up to 160 sensors) is on the order of $100, approximately one-third the cost of a single WDM sensor. An example of the interferogram returned for all of the sensors on a single OFDR fiber is shown in Figure 6-3.

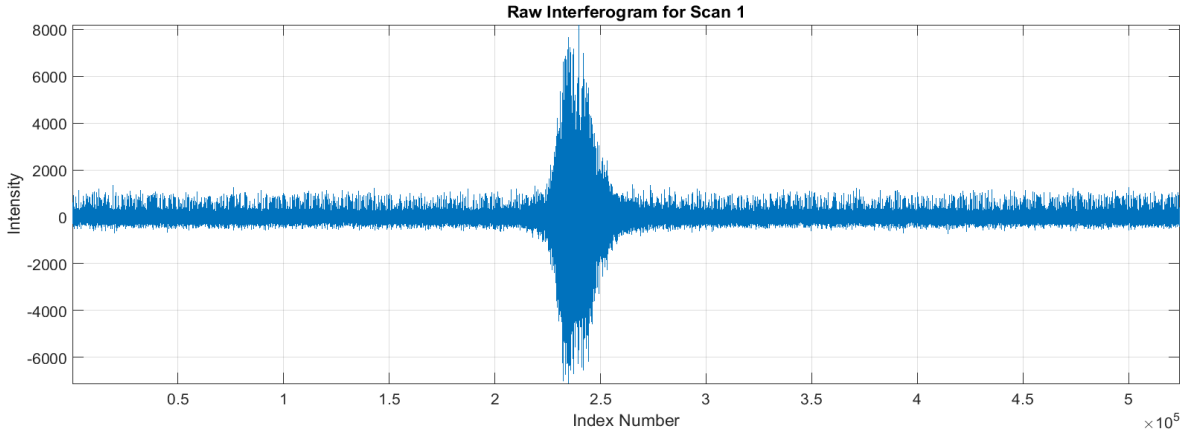

Figure 6-3: Raw interferogram of the OFDR system. All of the sensors are bundled around a central wavelength (x-axis) necessitating the use of the OFDR technique to recover an individual sensor response.

In the case of the WDM system, each sensor on a common fiber has a unique central wavelength. These wavelengths are application specific as they must have enough separation between central wavelengths such that under the maximum strain the reflected wavelengths of the sensors cannot overlap (as the fiber/structure is strained the wavelength of reflected light for each grating shifts; this shift must be less than the predefined wavelength range for that particular

sensor). A broadband laser source is used to interrogate the WDM fiber and a spectrometer is used to measure the returning light. Since each Bragg grating along the fiber has a unique wavelength range, the change in wavelength can be directly correlated to a sensor/location and transformed to strain. An example of a raw interferogram from the WDM system for eight sensors is shown in Figure 6-4 [108].

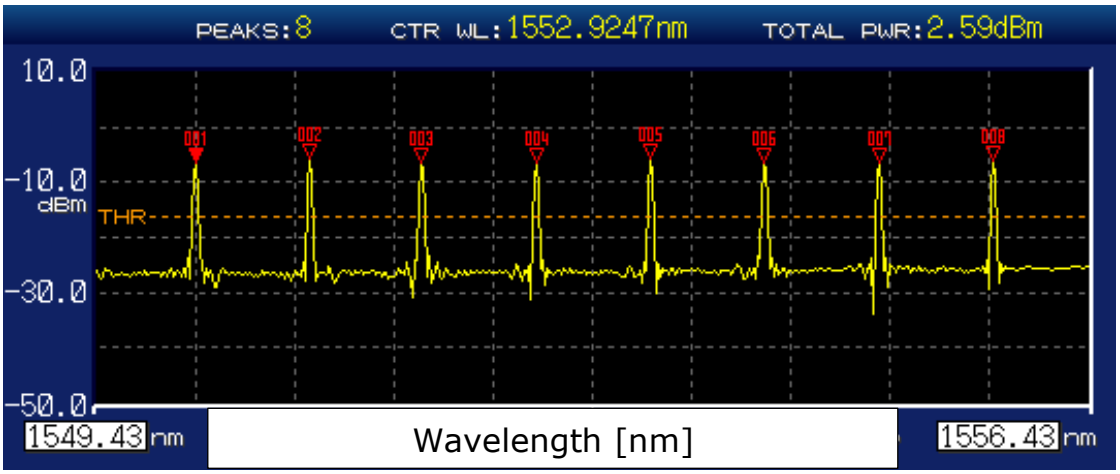

Figure 6-4: Raw interferogram of the WDM system. Since each sensor is written at a unique wavelength the individual sensors are easily deciphered [107].

The direct processing technique used in WDM sensing allows sampling rates up to the hundred kilo-Hertz range with the system tested sampling at 5 kHz. The major drawbacks of the WDM method is the cost of the sensors, the number of sensors that can be utilized on a single fiber, and the strain range which the fiber is limited to (the wider the strain range the wider wavelength band each sensor requires and thus the fewer number of sensors on a fiber). The customization of the central wavelength for each sensor on a fiber leads to prohibited high cost with a single sensor costing on the order of $300 and the fiber used in this study, having 36 sensors each spaced roughly 1 inch apart, costing on the order of $5000. Since fiber Bragg grated sensors are one-time use, these high costs make the WDM sensors undesirable if the OFDR sensors'

sampling rate is adequate for a particular application. For the current study 159 OFDR and 36 WDM sensors were utilized, each on a single respective fiber.

6.2 Modal Excitation Studies

The ability of each sensor type to accurately create a PSD representation of the structure is related to the excitation technique used to excite the structure. In order to determine the ideal excitation technique, a series of tests were performed which utilized either a modal shaker or modal hammer as the excitation source. To facilitate the development of the optical sensors, an automated impact hammer was developed to allow for repeatable broad spectrum (impulse) excitations [91]. The automated impact hammer was developed to yield repeatable excitation (as with the shaker) without mass loading or artificially stiffening of the structure. A summary of the excitation tests performed and the strengths and weaknesses of each test are given in the following sections.

6.2.1 Electrodynamic Shaker

Since it was desirable to obtain the PSD over a relatively wide frequency band, random excitation using a modal shaker was utilized in this study. Many amplitudes, periods, and bandwidth were tested before settling on the "optimal" excitation for this particular test setup. The chosen signal was a burst random signal with frequency content from 0-200Hz and having a 16 second period. The duration of the burst was set from five to fifty-five percent of the period in order to ensure proper time for decay of the vibrations. The excitation signal was generated by the PSV-500's native signal generator, feed through a LDS PA25E amplifier, and ultimately a MB Dynamics Modal 50 shaker. The input force from the shaker was measured by a PCB 208C02 force transducer which was mechanically fastened to the end of the shaker's stinger and glued to the plate surface with cyanoacrylate adhesive as shown in Figure 6-5.

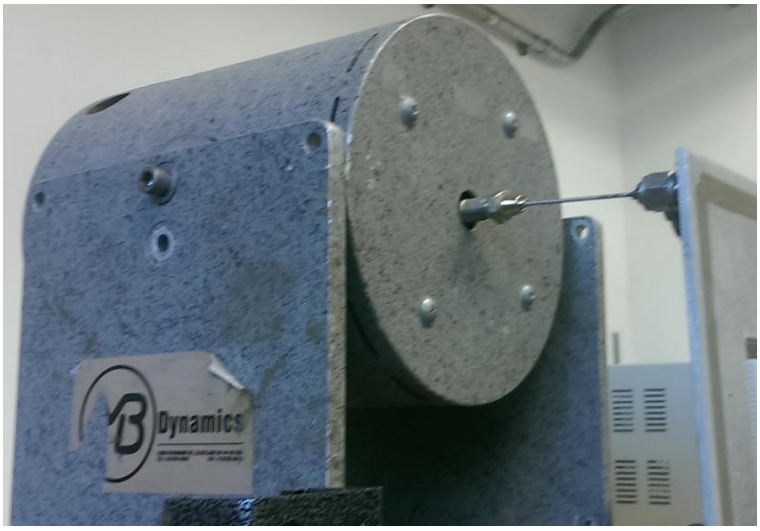

Figure 6-5: Electrodynamic shaker used in the excitation studies shown attached to the corner of the cantilever plate.

The shaker was found to do exceptionally well at building the modal models of the structure which were constructed by curve fitting the frequency response functions (FRF) and thus was best suited to be used with the vibrometer and the accelerometers. One drawback of the fiber optic interrogation systems being tested was that it did not incorporate the ability to interface with conventional data acquisition systems (the optical interrogator was designed to analyze light sources whereas traditionally DAQ use electrical signals). While this is an advantage in a sense that the optical systems are immune from electromagnetic interference, it also makes syncing the data between the two systems nontrivial. A consequence of not having the optical data synced with the traditional data acquisition hardware was that obtaining an input force time history correlated to the strain time histories was not feasible. Attempts were made to resample the force signal and manually time sync the data however this provided mixed results and was deemed not reliable enough to proceed. The inability of the fiber optic systems, as currently constituted, to capture the input force data necessitated the use of the PSD in order to build the modal models from the strain data (a main feature of the developed SHM system). A consequence of using the PSD was that

unaccounted for stiffness of the attached stinger caused the modal model to shift by a notable amount. It is important to mention that input force measurement capabilities could be added to the fiber optic sensing systems. Since the focus of the current dissertation was on in-situ SHM techniques, no efforts were made to adapt the system to allow for input force measurements.

Utilizing a correlated finite element model, it was found that having the attached force transducer, stinger, and shaker unaccounted for when calculating the PSD was the equivalent of adding a linear spring of stiffness 100lb/in at the force transducer-plate interface. As a result of the effects the added mass and stiffness of the shaker had on derived modal models when using the PSD, it was determined that an electrodynamic shaker would not be a suitable excitation technique for the optical strain sensors. The shaker was however used for the SLV measurements as the repeatability of the input force was more practical considering there had to be over 10,000 excitation cycles as the laser scanned through 100 points, doing 100 averages at each point, for each plate configuration.

6.2.2 Manual Impact Hammer

Modal hammers are typically used in roving tests where a (usually) small number of sensors are placed on the structure and then the structure is excited at a large number of points. In this case the FRF can be computed between each sensor and impact location. Due to reciprocity, this is equivalent to have a large number of sensors and impacting at a small number of points. With the use of fiber optics, the number of sensors that can be simultaneously acquired is near limitless making the use of the roving impact technique unnecessary. The impact hammer does however have the distinct advantage of allowing the input force to be imparted without the device under test incur any mass loading or artificial stiffening.

For the current study a Kistler Type 9722A500 modal hammer and corresponding load cell was utilized, as shown in Figure 6-6, with its impact tips. There were seven different tips that were tested at various force levels and locations in order to obtain the optimal impact setup. It was found that the small metal impact tip provided the most uniform auto-power spectrum over the frequency range of interest. It was also determined through the course of this testing that the ideal location for impact was approximately 1/3 of the way up the plate from the fixed end and along one edge. This location provided the best comprised between the excitation of each sensor type and had a moderate damping period allowing for repeated tests with minimal delay between impacts.

Figure 6-6: Manual impact hammer with various stiffness tips used in the current study.

While the impact hammer was shown to provide ample input across the frequency range of interest it was also determined that multiple samples were desirable to allow for averaging. In order to maximize the benefit of averaging of the PSD, it was important that all impacts be in the same location, and direction, as well as having roughly the same magnitude. It was found that manually impacting the plate lead to misalignments of consecutive impacts which reduced the

coherence between the input and response signals and as such decreased the effectiveness of the averaging.

6.2.3 Automated Impact Hammer

In order to overcome the limitations of both the shaker and manual impact hammer it was desirable to combine the best features of each into a new unit that would provide suitable excitation for this study. As a result, an automated impact hammer was developed which allowed for consistent, repeatable excitation (as with the shaker) but without mass loading or artificially stiffening the structure (as with the impact hammer). The hammer was constructed using a DC solenoid, steady state relay, and a microcontroller as shown in Figure 6-7.

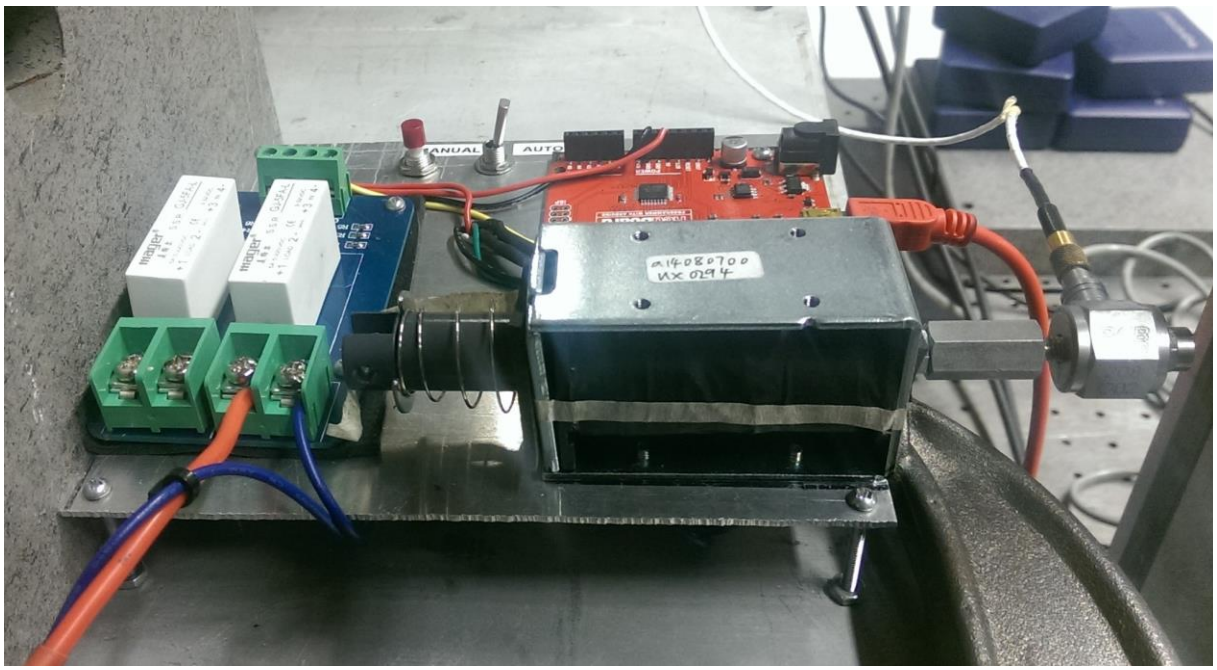

Figure 6-7: Automated impact hammer developed to provide repeatable broad-spectrum excitation for the current studies.

The same PCB 208C02 transducer used for the shaker testing was affixed to the end of the solenoid armature and the optimal metal impact tip fastened to the impacting end of the force

transducer. Tests were done to determine the optimal offset distance of the impactor relative to the plate and adjustments were made in the travel of the solenoid armature. The result was a repeatable impact that nearly identically replicated the ideal impact case from the manual impact hammer. In Figure 6-8 a single impact from the manual hammer is compared to a single impact from the auto-hammer, purposely offset in time to allow for ease of comparison.

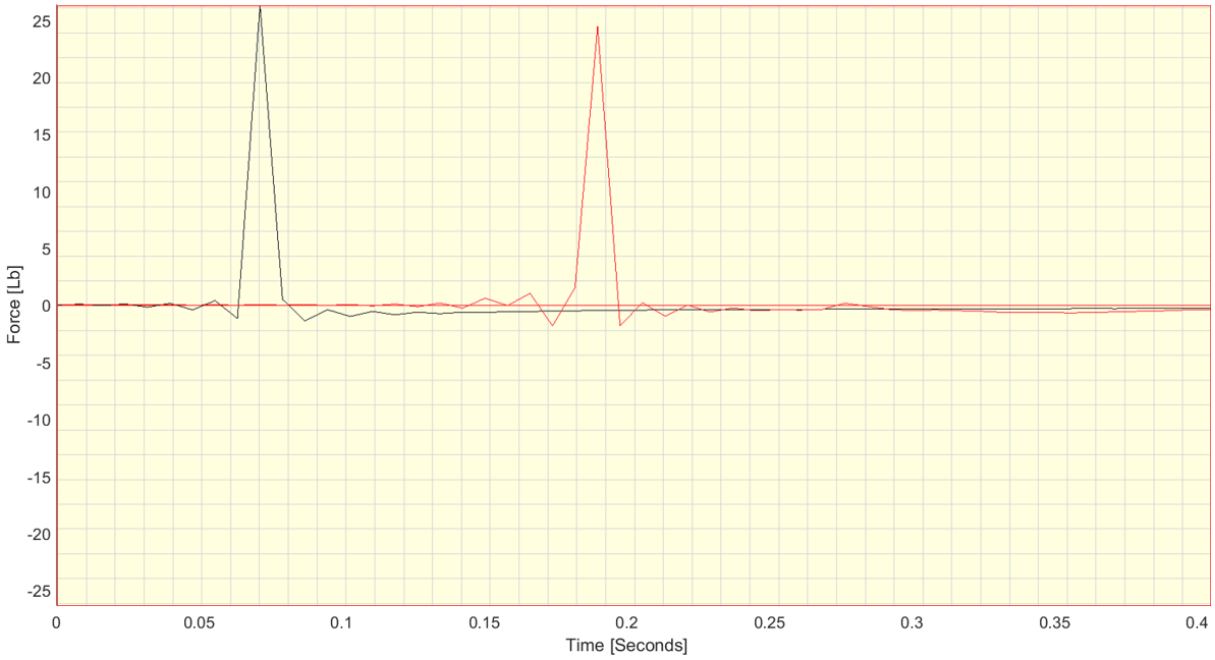

Figure 6-8: Comparison between the force time history of a manual hammer strike (black) and hammer strike of the automated system(red).

6.3 Frequency Domain Modeling

The current approach relies on developing accurate frequency domain models of the structure from which the SHM algorithm may draw its input information. In the current section these frequency domain models were developed and compared amongst sensor types. In order to obtain the required information, the time histories of each of the signals were sampled and transformed via Fourier analysis into the frequency domain. In the accelerometer studies, the input force and response were measured and the FRF and PSD were calculated. For the optic sensors,

the input force was not sampled by the data acquisition systems and only the PSD were calculated. In addition to developing the response spectrum, the frequency domain models were curve fit using ME'Scope software and the modal properties (natural frequency, damping, and mode shapes) were extracted. The following is a summary of the frequency domain responses and modal parameters developed from each sensor type.

6.3.1 Accelerometers

Using the acquired acceleration and force information from the Dactron Focus system the accelerance frequency domain response of the structure was obtained. The frequency range of interest for all accelerometer studies was restricted to 0-200Hz, containing the first ten modes of the cantilever plate. Figure 6-9 provides the FRF and PSD obtained from the accelerometers and force transducer. The FRF is shown as the response of accelerometer two with respect to the input force. The PSD is given as the response of accelerometer two relative to accelerometer one.

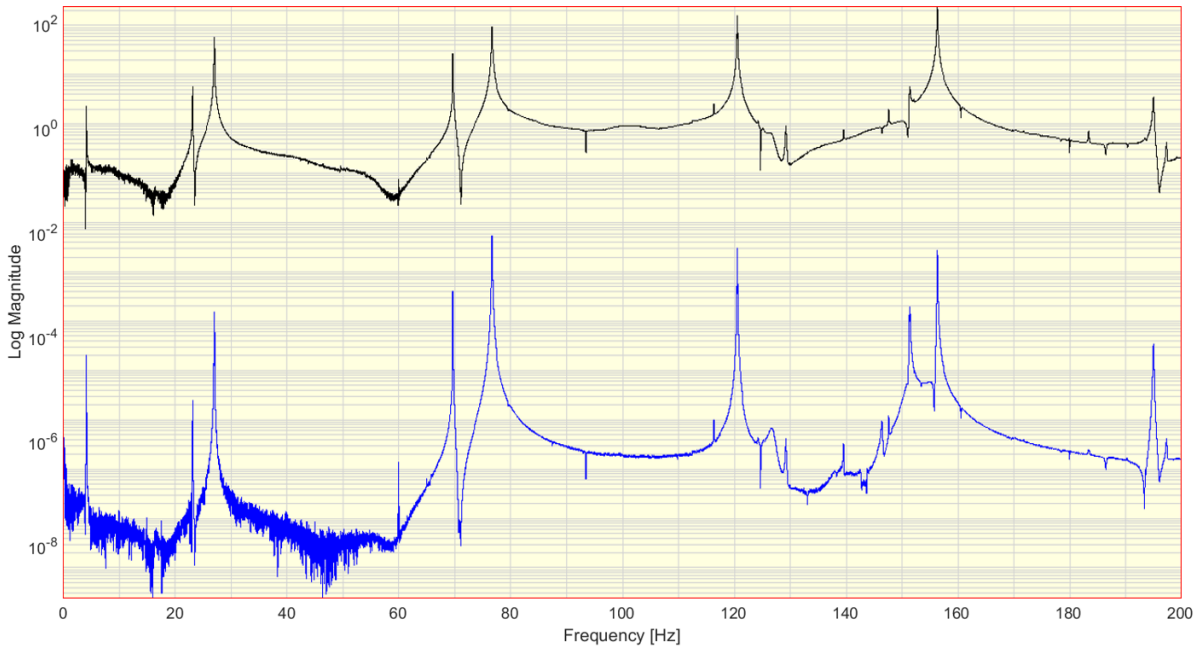

Figure 6-9: FRF (black) and PSD (blue) of the cantilever plate subjected to impulse excitation via the automated hammer.

Comparing the FRF with the PSD, it is clear that the PSD is able to accurately capture all of the out-of-plane modes of the plate under 200Hz, as is the FRF. The downside of the PSD is that it does incur more noise, especially at lower frequencies where the imperfections of the input force are accounted for in the FRF. Further efforts to minimize input force noise, and conduct complex averaging, would likely reduce or eliminate this low frequency noise.

6.3.2 Scanning Laser Vibrometer

The Polytec PSV-500 SLV was used to characterize the full field vibration response of the plate which aided in the validation of the optical fibers and finite element model. Utilizing the flash on a digital camera, the locations of the 144 points scanned the by SLV via the 1/8" square reflective tape targets adhered to the plate are shown in Figure 6-10.

Figure 6-10: Locations of the 144 vibrometer scan points utilized in the characterization of the plate's vibration response. The red dot is the visual pointing laser at the measurement location when the image was taken.

The SLV system does an excellent job of computing the FRF at each point as it scans through the points one by one. This allows the FRF of each point to be captured and then stitched together to yield the high-resolution mode shapes of the structure. The downside of this approach

is that only one point can be measured at a time making calculation of the sensor to sensor PSD impractical. As a result, only the FRF was calculated for each point of interest using the vibrometer. The plot of the FRF for all 144 vibrometer scan points is given in Figure 6-11 below.

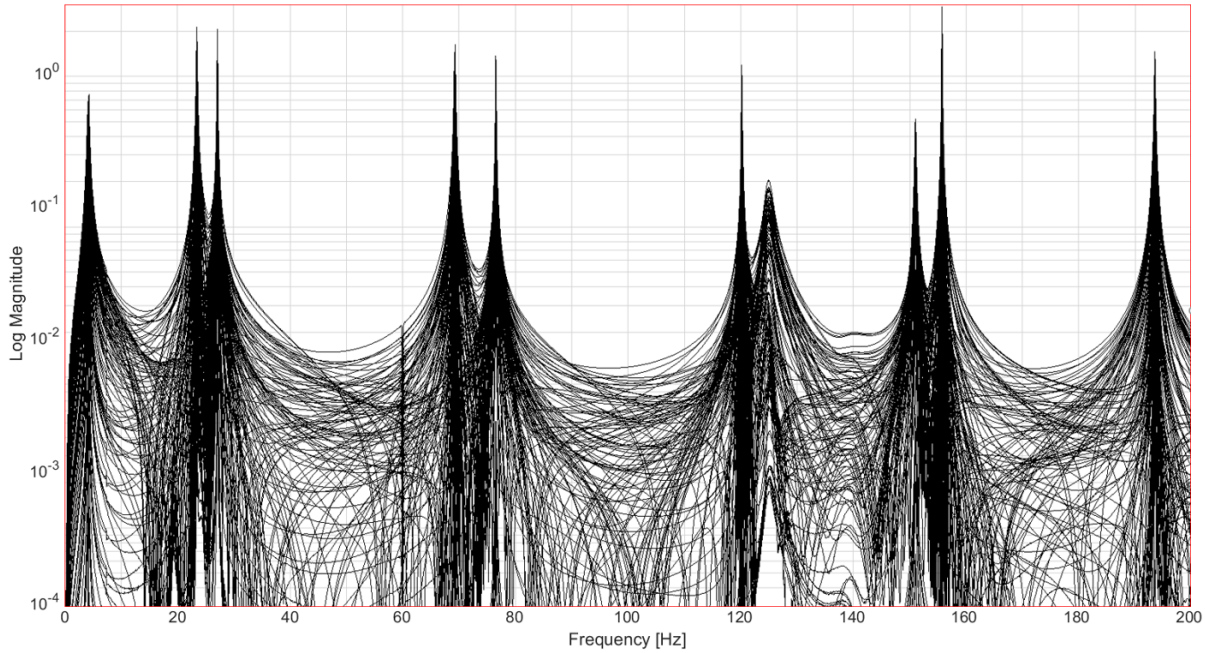

Figure 6-11: Overlay of the FRF measurements from the scanning laser vibrometer.

By examination of Figure 6-11, it is clear that the shaker's burst random excitation, coupled with 100 complex averages, maintains a very high coherence across the interrogated spectrum and yields a very clean FRF for all of the scan points. The FRF were curve fit to extract the modal parameter of which the natural frequencies are listed in Table 6-1 at the end of the section.

6.3.3 Optical Frequency Domain Reflectometry (OFDR) Fiber Optic Strain Sensors

In the current research, two different types of fiber-optic sensors for dynamic strain measurements were considered; WDM and OFDR technologies. The OFDR results presented in the current section were the state-of-the-art in real time sensing circa 2015. Section 6.4 discusses

the advancements in OFDR sensing as a result of the current work, the results of which are used in the experimental demonstration in Chapter 7.

The OFDR system as originally tested was designed largely with static strain measurements in mind. Applications of the system to dynamic measurements were shown to produce noise levels on the order of 20 microstrain as well as low sample rates and non-periodic sampling [91]. While it was understood at the onset that advancements to OFDR sensing would be required to meet the SHM objectives of dynamic strain sensing required for the current work, it was important to test the system to establish a baseline of the performance. It is believed as the technology improves the sampling rate restriction will be addressed and the low cost, high strain range, and high spatial resolution of these sensors will make them the best suited for instrumenting full-scale aerospace structures.

For the current study, the aluminum plate previously discussed was excited using the automated impact hammer. Ten impulse response strain time histories were collected using the OFDR fiber for each of the 159 sensor locations. Since the OFDR system had difficulties with maintaining a uniform sampling rate, the data was nominally sampled at 51Hz and then resampled at 51Hz in the time domain using a uniformly spaced time vector and cubic spline interpolation. The time history of the original and resampled signal for OFDR sensor 59 (sensor 59 is the OFDR sensor collocated with the tip-most accelerometer in Figure 6-2) is shown in Figure 6-12.

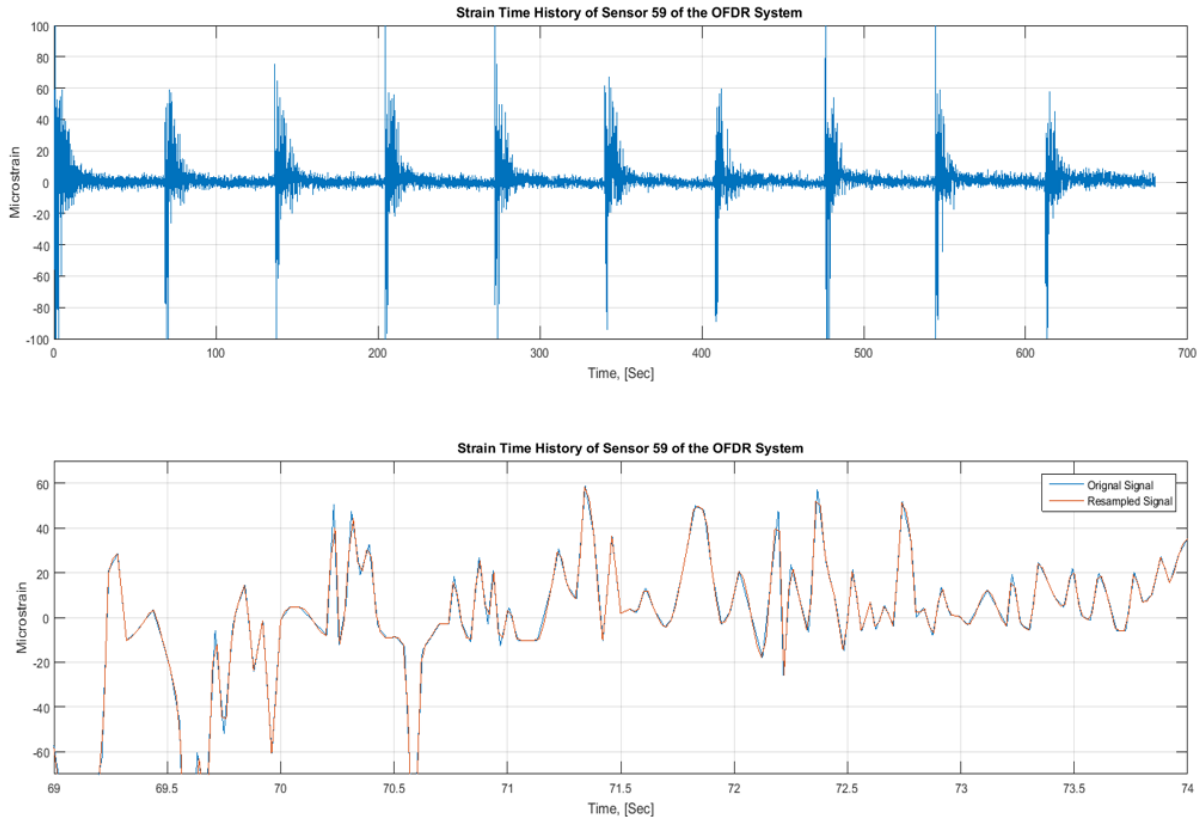

Figure 6-12: (Upper)Time history of OFDR sensor 59. (Lower) Time history of OFDR sensor 59 as sampled (blue) and after uniform resampling (red).

This resampled data was used to compute the PSD for the plate using 10 complex averages. For the current test the frequency domain response was limited to a 25.5Hz bandwidth, as shown in Figure 6-13. The curve fit modal parameters obtained from this OFDR PSD are given in Table 6-1 at the end of the section.

The pair of sensors shown in Figure 6-13 were taken to match the locations of the accelerometer pair being compared and should not be assumed to be an optimal sensor pair. It is noted that the OFDR sensors were able to properly identify the first two natural frequencies of the system which were the only two within its frequency range. It is believed that the third peak shown at 24.4 Hz in Figure 6-13 is actually mode 5, nominally at 74.5 Hz, "folding over" as no anti-alias filter was applied during sampling or resampling. The spectrum shown in Figure 6-13 is more

noisy than desirable for operation of the current SHM algorithm. Section 6.4 covers the advancements made in dynamic strain sensing using OFDR technology related to the current work.

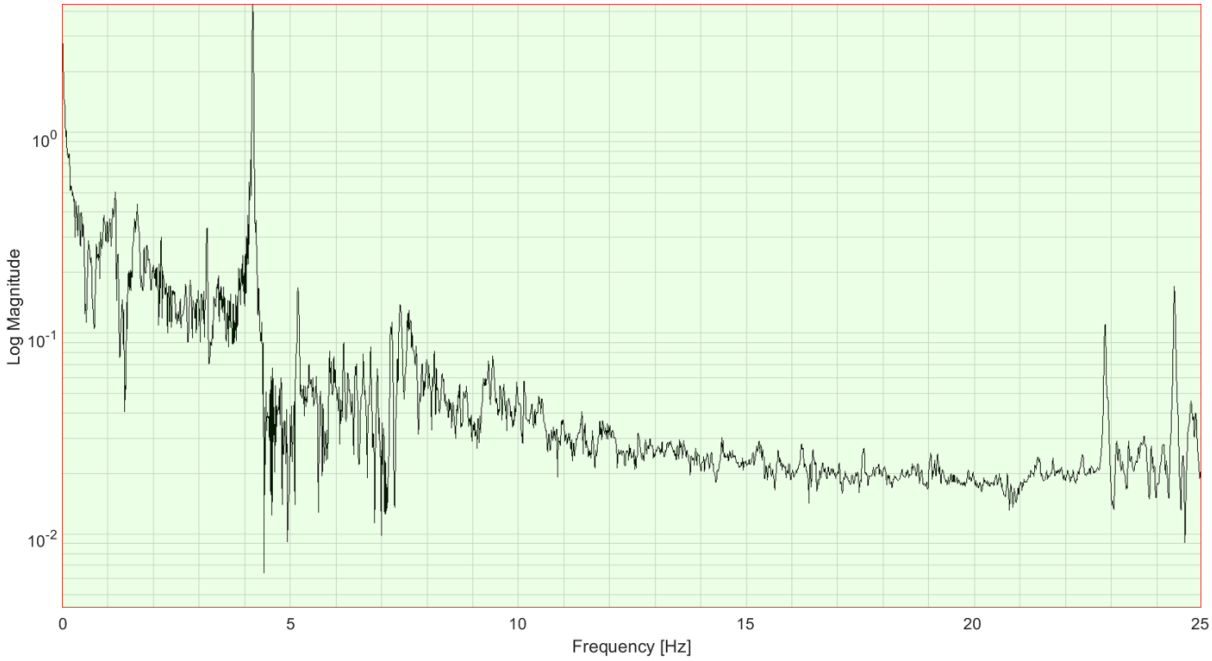

Figure 6-13: PSD between sensors 23 and 59, chosen to match the locations of the two accelerometers.

6.3.4 Wavelength Division Multiplexed (WDM) Fiber Optic Strain Sensors

WDM based sensors are the optical strain sensors typically employed for dynamic and acoustic measurements. While they are well suited for dynamic measurements, the high sensor cost and restrictive sensor number makes them sub-optimal for the proposed SHM methodology. Nonetheless, WDM sensors were tested to benchmark the current state of dynamic optical strain sensing. The WDM sensors tested, with their corresponding laser source and spectrometer, were able to sample data at rates up to 5 kHz and as such have a dynamic range similar to that of the vibrometer and/or accelerometers. The time history for 10 samples of the plate's impact response as measured by the WDM system is shown in Figure 6-14 for sensor 22 (sensor 22 is the sensor called out in Figure 6-2).

Figure 6-14: Strain time history of WDM sensor 22 for 10 samples excited by the auto-impact hammer.

Although the frequency range of interest for the current study was 0-200 Hz, the data was sampled at 5 kHz as the sampling speed was found to have no effect on the noise levels. The input force was not available to be sampled with the WDM system and as such the PSD was used to represent the frequency domain behavior of the plate. The PSD of WDM sensor 22, relative to sensor 33 (these are the sensor's that correspond to accelerometer two and accelerometer one locations, respectively), is shown in Figure 6-15.

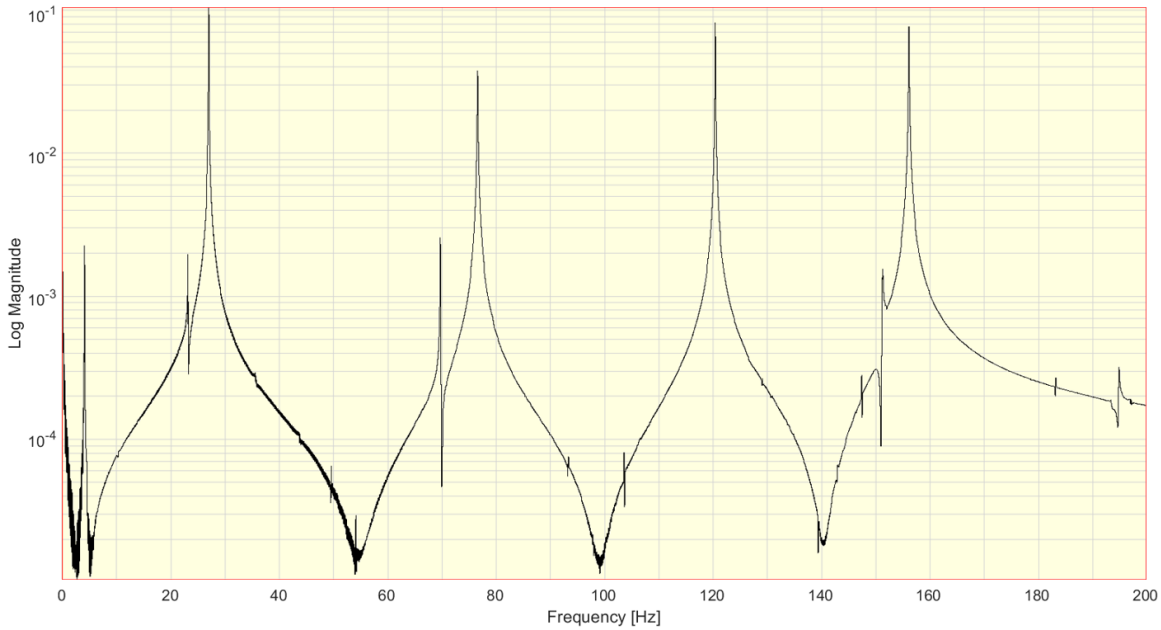

Figure 6-15: Power spectral density of WDM sensor 22 relative to sensor 33.

After curve fitting the PSD, the natural frequencies of the plate, as measured by the WDM sensors, were extracted and are given in Table 6-1 along with the other sensor types.

Table 6-1: Comparison of the natural frequencies of the plate measured by each respective system as evaluated in 2015.

	Natural Frequencies (Hz)				
Mode	**Accelerometer**	**Vibrometer**	**OFDR**	**WDM**	**Description**
1	4.19	4.19	4.18	4.17	1st Transverse Bending
2	23.3	23.3	22.9	23.2	1st Torsion
3	27.1	27.1	--	27.1	2nd Transverse Bending
4	69.8	69.8	--	69.8	2nd Torsion
5	76.8	76.8	--	76.7	3rd Transverse Bending
6	121	121	--	121	1st Chord-wise Bending
7	125	125	--	--	3rd Torsion
8	152	152	--	151	4th Transverse Bending
9	157	157	--	156	1st Chord-wise/2nd Transverse Bending

6.4 Advancements in OFDR Technology

The previous section demonstrated the ability of fiber optic strain sensors to monitor structural dynamics (WDM sensors) but also identified areas for improvement in OFDR sensing. While WDM sensors would have been the straightforward choice for monitoring of structural dynamics via fiber optic sensors, the limited number of sensors per fiber are a major drawback of the system and in turn future applications of the current SHM approach. OFDR sensors on the other hand, while currently limited in dynamic sensing range, provide tremendous upside for large scale sensing applications. The limitations associated with OFDR fibers are technology based (laser sweeping speed and computer processing speed being the two major limitations) whereas the limitations associated with WDM sensors, as they relate to large scale structures, are fundamental to the sensor operation.

NASA AFRC are world leaders in developing OFDR sensor technologies and were fundamental in advancing the state of OFDR dynamic sensing from the 2015 levels to present. Working with the fiber optic sensing group at NASA AFRC, a custom OFDR sensing system was developed for use in collecting dynamic strain data. The system was comprised of a swept tunable laser, consumer-based microprocessor and commercially available interferometer. The system is propriety to NASA and as such the details are omitted from the current dissertation. Instead a summary of the advancements made in processing of OFDR optical information is presented.

Previous data processing schemes related to OFDR sensors were focused on quasi-static applications where real-time strain values over relatively long periods of time took precedence over the accuracy of each individual measurement. In order to achieve real-time processing on a large number of sensors (hundreds to thousands of sensor locations per interrogator) sample rates were typically on the order of 20Hz and sensor locations assumed to fixed within the spatial dimension associated with the inverse FFT of the returning wavelength spectrum (more on this shortly). It is with this in mind that the following comparisons are made between the processing that was being performed with an aim of quasi-static testing and the desired dynamic measurements required for the current SHM system and presented here.

6.4.1 Raw Interferogram Data Extraction

The current work, and monitoring structural dynamics as a whole, is dependent on the accuracy of each individual sensor location at each individual sample in time. To achieve this accuracy, the method in which the raw optical data is converted to strain was redeveloped. In the case of the current OFDR data processing, the requirement for real-time data was removed, allowing for more computationally intensive processing of the data to achieve the best possible strain results. This post-processing of the data is not a hindrance to the current approach as

processing can still be done on-board an aircraft in flight and as computational speeds increase may be done in real-time. The process by which the high accuracy data is computed from the raw optical information is given below.

The raw optical information from the Bragg grated fiber optic sensors is first collected via the proprietary NASA AFRC FOSS system in the form of an interferogram. Figure 6-16 provides an example of such an interferogram, giving the intensity of the returning light on the vertical axis and the index number in the measurement array on the horizontal. The information in this interferogram is for a single point in time meaning if the fiber is being sampled at 100Hz the system would be generating 100 of these unique interferograms each second. Examination of the horizontal axis of the interferogram yields each of these interferograms are 524,288 points long. The amount of data being generated by the OFDR sensing system and the processing required to recover the individual strain measurements are major factors in the amount of computational resources required to process the data.

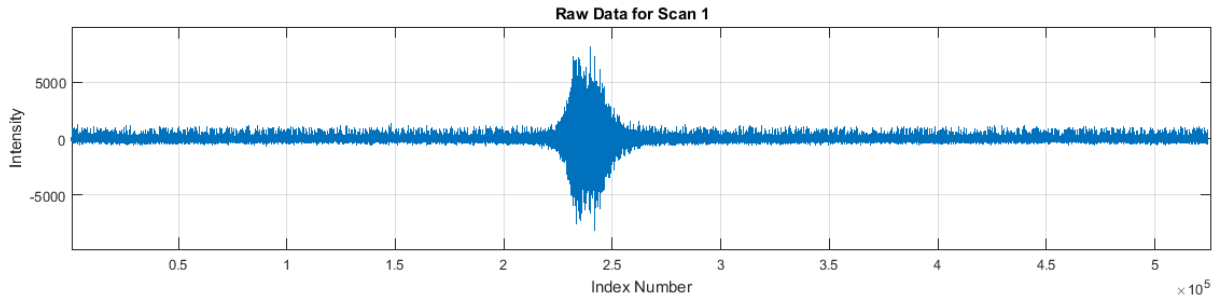

Figure 6-16: Interferogram of the raw optical data with the intensity of the signal on the vertical axis and the array index on the horizontal axis. This horizontal axis can be mapped to wavelength as will be done in subsequent steps.

The first step in the processing of the OFDR information is computing a fast Fourier transform (FFT) on the sampled interferogram. This step allows the reflected light from each sensor (having the same central wavelength, as seen by the "ball" of light in Figure 6-16) to be

separated into individual components. In order to get the desired strain resolution, it is important to sample the signal for a sufficient amount of time to obtain a large sample size in the interferogram (in the presented case 524,288 points per sample). This large sample size in the wavelength domain is one of the primary users of computational power. Computing the FFT of a 524,288-point sample at a rate of 100Hz is difficult for all but the most powerful of modern computers and is just one step of the data condensation routine. The magnitude of the FFT of the interferogram given in Figure 6-16 is presented in Figure 6-17.

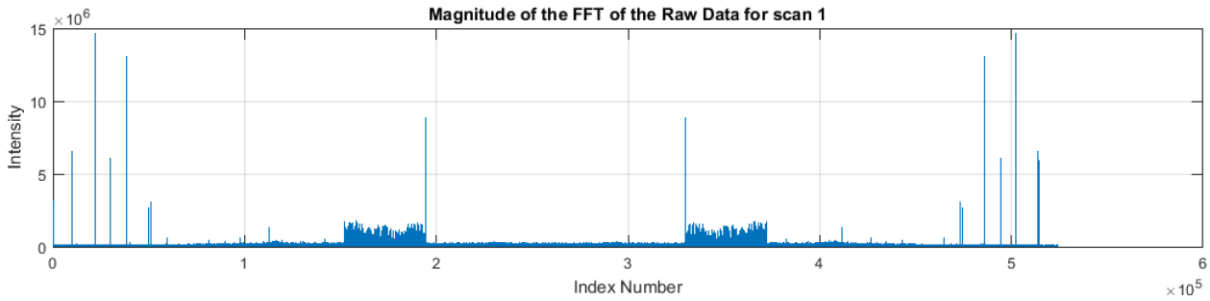

Figure 6-17: FFT of the interferogram of the raw optical data with the intensity of the signal on the vertical axis and the array index on the horizontal axis.

The computation of the FFT yields a complex signal, mirrored about the central index. In the current discussion the right half of the information (from data point 320,000 to the end of the array) is used to separate out individual sensors. Once a sensor has been located it is recombined with its conjugate pair using the symmetry relative to the central index. The cluster of data shown between indices 300,000 and 400,000 are the "top hats" associated with each individual sensor location. The next step of the data condensation process requires the individual sensor associated with each top hat be identified and separated out of the global array.

An example of such top hat identification is shown in Figure 6-18. The upper right plot shows the single sided spectrum extracted from Figure 6-17 where the red line is a cursor showing where in the sensor region the top hat extraction routine is currently operating. The plot in the

lower right is a zoomed view showing the same red cursor as well as a predefined top hat threshold given as the yellow horizontal line in the figure. Lastly, the plot on the left of Figure 6-18 is the extracted top hat. Ultimately the developed top hat extraction algorithm systemically goes through the data, extracting the information associated with each top hat as well as the indices within the array this information is stored at. It is important to note that these locations are transient due to Doppler effects in the fiber and as such this localization routine must be repeated for every time sample.

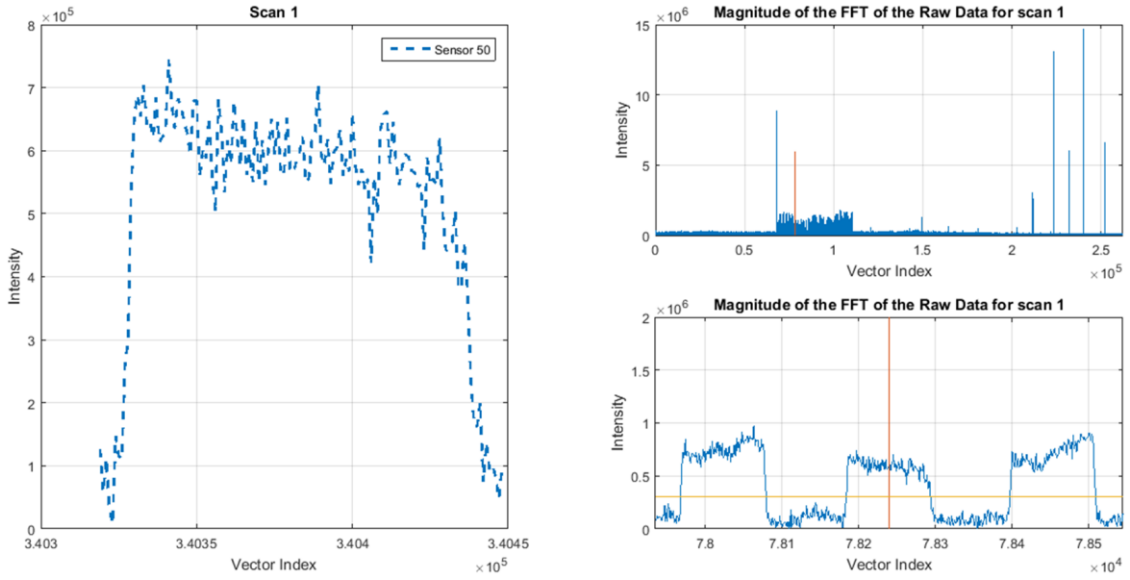

Figure 6-18: Developed GUI for checking the accuracy of the developed "top hat" extracting routine.

Once the top hat associated with each sensor has been identified the top hats are recombined with their complex conjugate pairs, an example of which is shown in Figure 6-19. The upper right plot in Figure 6-19 is the same as that in Figure 6-18 and is there to allow for visualization of where in the top hat extraction process the routine is operating. The lower right plot shows the extracted top hat combined with its complex conjugate pair. Note that the top hats have been zero padded both before, between, and after the complex pair to be 2048 points in length.

The amount of padding impacts the resolution and quality of the final strain value and has received much attention in obtaining accurate strain values. It is desirable for the total number of points to be an integer power of two for speed considerations when computing the inverse FFT (iFFT). In the current work, a 2048-point spectrum was found to be the best compromise of speed and accuracy.

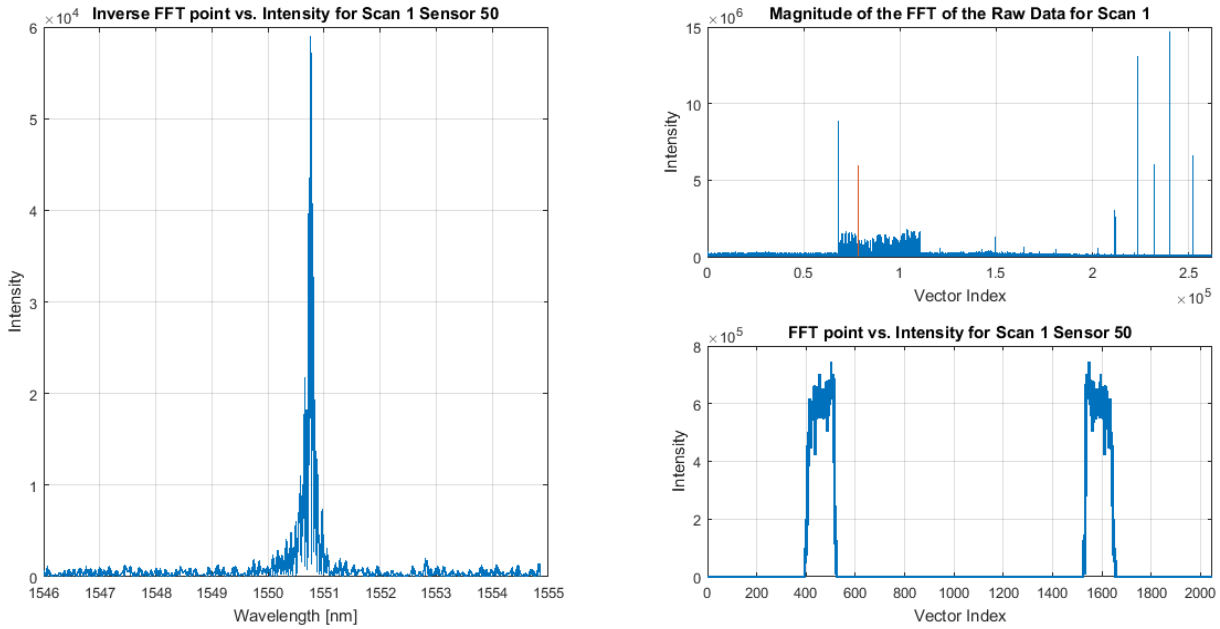

Figure 6-19: Developed GUI for checking the accuracy of the developed "top hat" combining routine.

The iFFT of the padded complex top hat pair is then computed and converted from the vector index to wavelength domain. The result of this iFFT process is given in the left plot of Figure 6-19. This plot represents the intensity of returning light of a single sensor (50 in this case) as a function of wavelength over which the tunable laser swept for the measurement. Similarly to the conversion from change in resistance to strain utilized in electrical strain gauges, the change in wavelength in fiber optic gauges is converted to strain via the formula:

$$\varepsilon_i = \frac{\Delta\lambda_i}{\lambda_{i,0}} GF \tag{6-1}$$

where $\Delta\lambda_i$ is the change in wavelength of the i^{th} sensor, $\lambda_{i,0}$ is the reference wavelength of the i^{th} sensor (typically the wavelength under zero strain) and *GF* is the gauge factor, a property of the optical fiber.

With the intensity versus wavelength for each sensor at each measurement in time known, the above formula necessitates that a single wavelength be approximated for each sensor at each time scan. Much of the work related to this research was devoted to determining the best method for estimating this single wavelength and as such it is the topic of the following subsection.

6.4.2 Wavelength Extraction and Strain Computation

Once the plot of intensity versus wavelength for each sensor at each point in time has been computed (as shown in Figure 6-19) the corresponding wavelength must be estimated from the distribution. While the tendency would be to use the peak value, as customary in most real-time systems, this has been shown to lead to unacceptable errors when monitoring structural dynamics. Typical real-time systems used to monitor quasi-static load cases overcome this error via temporal averaging. The scan rate of the current generation of swept lasers is the limiting factor in the sample rate of OFDR sensors and as such temporal averaging would further restrict the current approximately 150Hz upper sample rate bound (this bound is given as an approximate value since it depends on a number of factors, many of which are outside the scope of this dissertation).

Rather than rely on averaging, in the current work a number of approaches to estimating the wavelength were proposed and tested. The strain values from each of the methods were compared to three foil gauges which were interrogated using a custom data acquisition system

built and certified by AFRC. Figure 6-20 repeats the same plot shown on the left-hand side of Figure 6-19 and also contains additional information related to the types of wavelength estimations employed. The previous state-of-the-art in OFDR sensing was to use the center of mass (COM) of the overall signal to estimate the central wavelength. While this approach works quite well when the peak is near the central wavelength, it struggles when the peak has shifted to the extreme right or left of the wavelength range as the longer tail always skews the COM calculation towards the central wavelength in the domain.

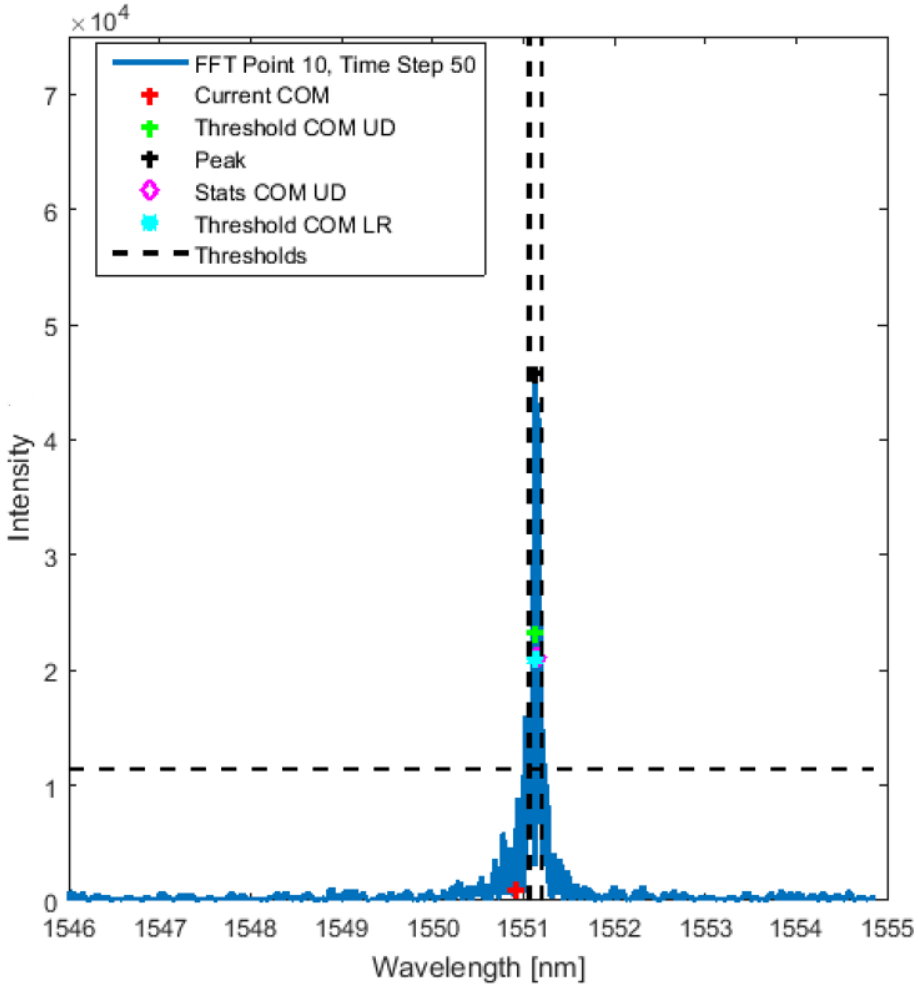

Figure 6-20: Single sensor wavelength versus intensity plot showing the estimated wavelength for each of the estimation techniques under consideration.

In an attempt to improve the COM calculations several wavelength estimation methods were tested. Most of the methods involved thresholding the signal such that only values within a specific horizontal threshold (Left-Right or LR threshold as shown in the plot) and/or vertical threshold (Up-Down or UD threshold as shown in the plot) of the peak intensity are used in the COM calculation. The "Stats COM UD" point referenced in Figure 6-20 plots a histogram to find trends in the data and assign the vertical threshold to contain all the data within the 95% confidence interval. While the results of this statistical approach were an improvement over the peak and COM computations, the extra computational expense was found to not be warranted when compared to using standard threshold values (the choice of these threshold values is discussed later in this section).

Figure 6-20 shows markers corresponding to the five wavelength extraction techniques investigated in relation to the research contained in this dissertation. While many of the methods yielded a very similar wavelength for the particular sensor and time measurement displayed, on more ambiguous sensors, or temporal measurements under higher noise levels, the difference between methods is more pronounced. One fault clearly shown in Figure 6-20 is that the traditional COM calculation, shown as the red "+" sign, under predicts the wavelength relative to all other methods leading to an error in the derived strain value.

In order to determine which wavelength estimation method was more precise, a static tip load was applied to an instrumented AFRC optical sensor validation testbed. The testbed, shown in Figure 6-21, was a cantilever aluminum plate containing an OFDR optical fiber and a series of foil gauges. Three of the foil gauges were oriented axially and nearly coincident with the axial portion of the optical strain sensing fiber. As such, these three foil gauges were used to assess the accuracy and precision of the developed OFDR processing technique.

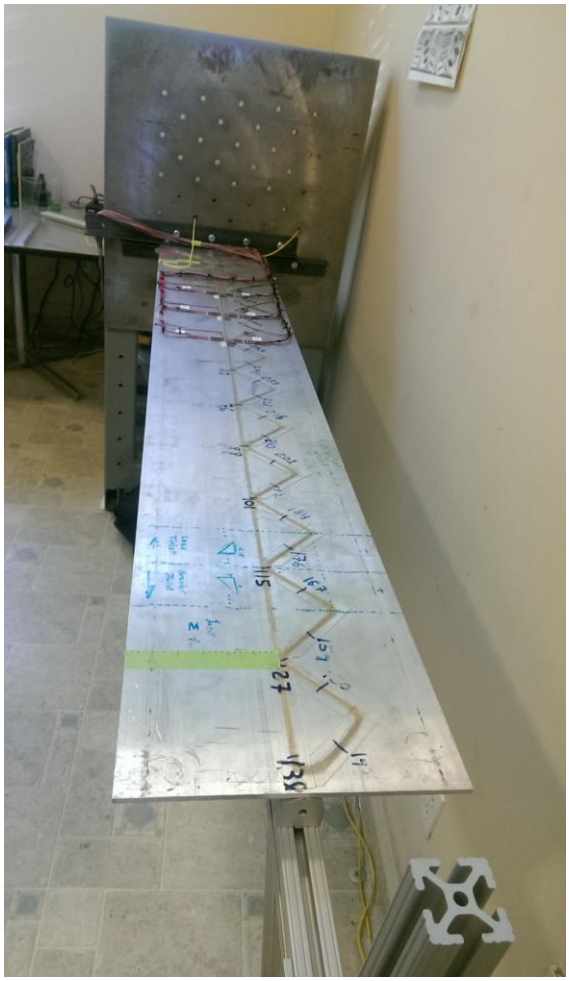

Figure 6-21: Aluminum plate used in the OFDR advancement studies. The wire bundles shown near the root are conventional (foil) strain gauges collocated with the axial optical strain sensing fiber.

Figure 6-22 provides the axial strain distribution along the centerline of the 72 inch long plate. Since a tip loaded cantilever plate produces a well-defined linear varying strain distribution along the span, the coefficient of determination (R^2) was used to evaluate the linearity of the strain distributions obtained. Values of R^2 close to one are indicators of a linear strain distribution and thus high spatial precision of strain measurements.

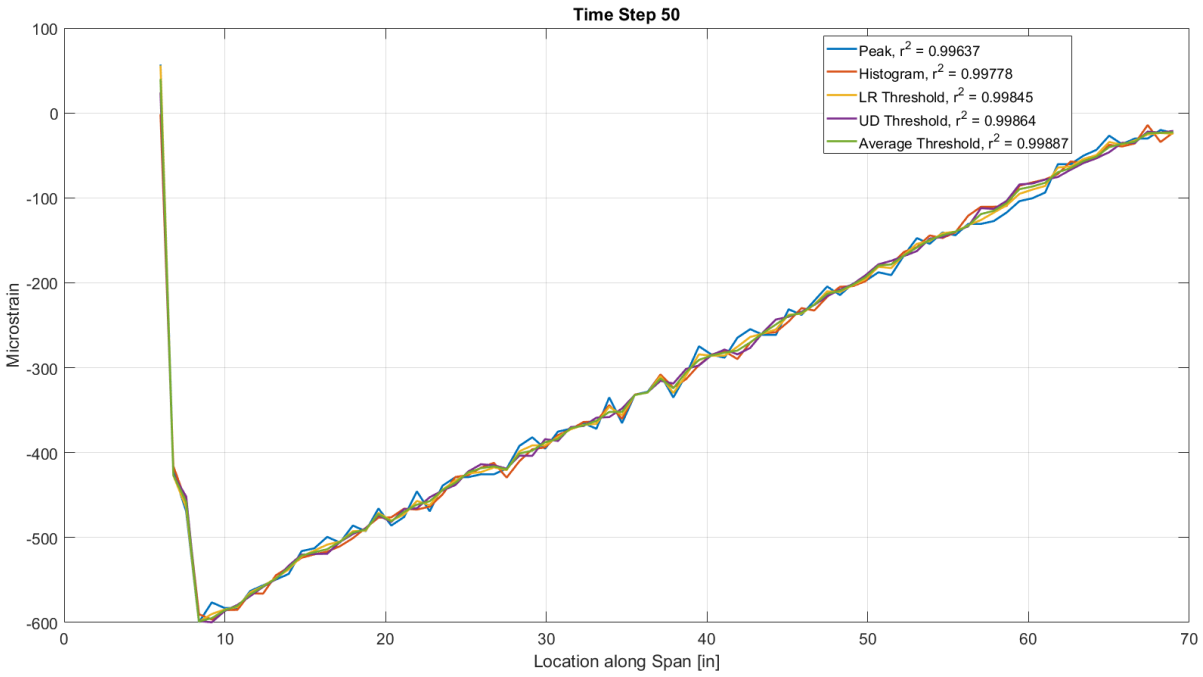

Figure 6-22: Strain distribution generated by each of the studied wavelength estimators along with their coefficients of determination.

The next step was to optimize the threshold values used in the wavelength estimation in order to obtain the maximum possible precision. Using the R^2 values to represent precision, a range of values were considered for both the LR and UD thresholds. The range of values considered are shown in Figure 6-23 along with the optimal value shown as a red line in each plot. This process was repeated with several data sets and the optimized values found to be constant. It is believed that for a given hardware setup these optimal values are universally applicable and only need to be updated if a change in the optical network hardware is made. For the optical network used in the remainder of this dissertation the horizontal threshold was set to be 3.5% of the wavelength domain and the vertical threshold 55% of the peak intensity, their respective optimal values.

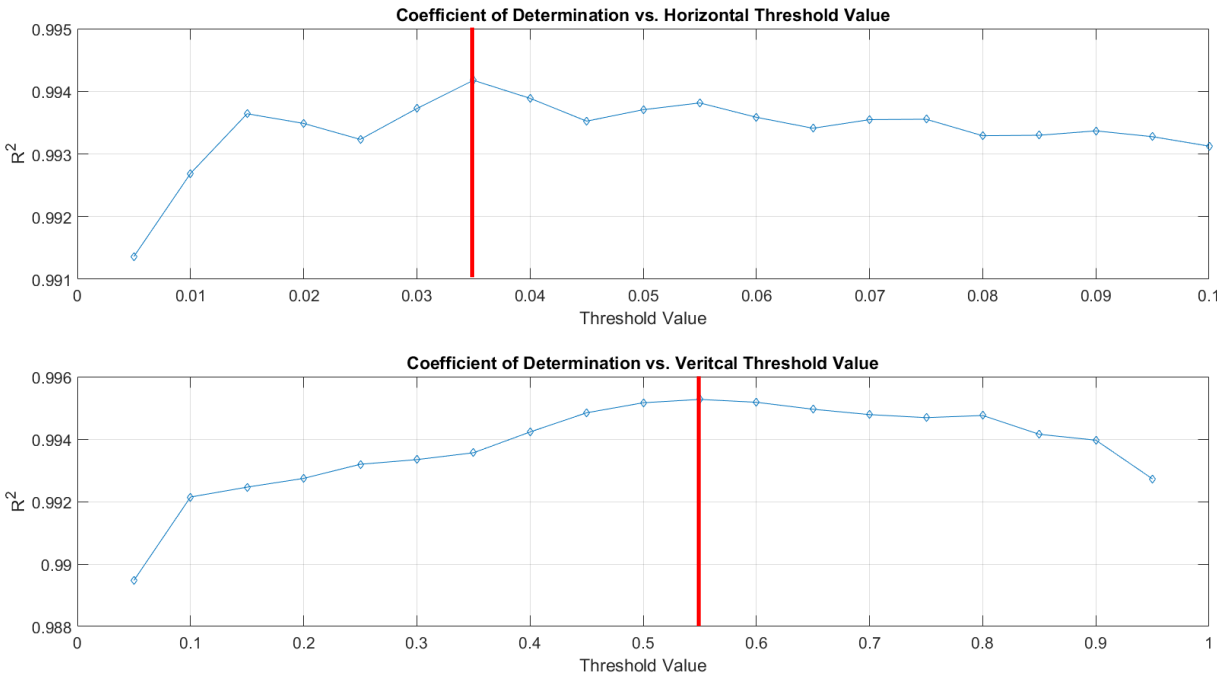

Figure 6-23: Coefficient of determination versus threshold sizes.

The final metric to be considered in the development of the improved OFDR processing scheme is the accuracy of the derived measurements. In order to evaluate the accuracy, three foil gauges were collocated along the fiber optic sensor mounted to the aluminum plate. A static tip load was placed on the cantilever plate and the strain values from each system calculated. Figure 6-24 provides a plot of the distributed strain values obtained by the fiber optic system with the three foil gauges overlaid at their respective locations. The maximum error between the measurements was found to be less than 5 microstrain, within the noise levels of the two systems.

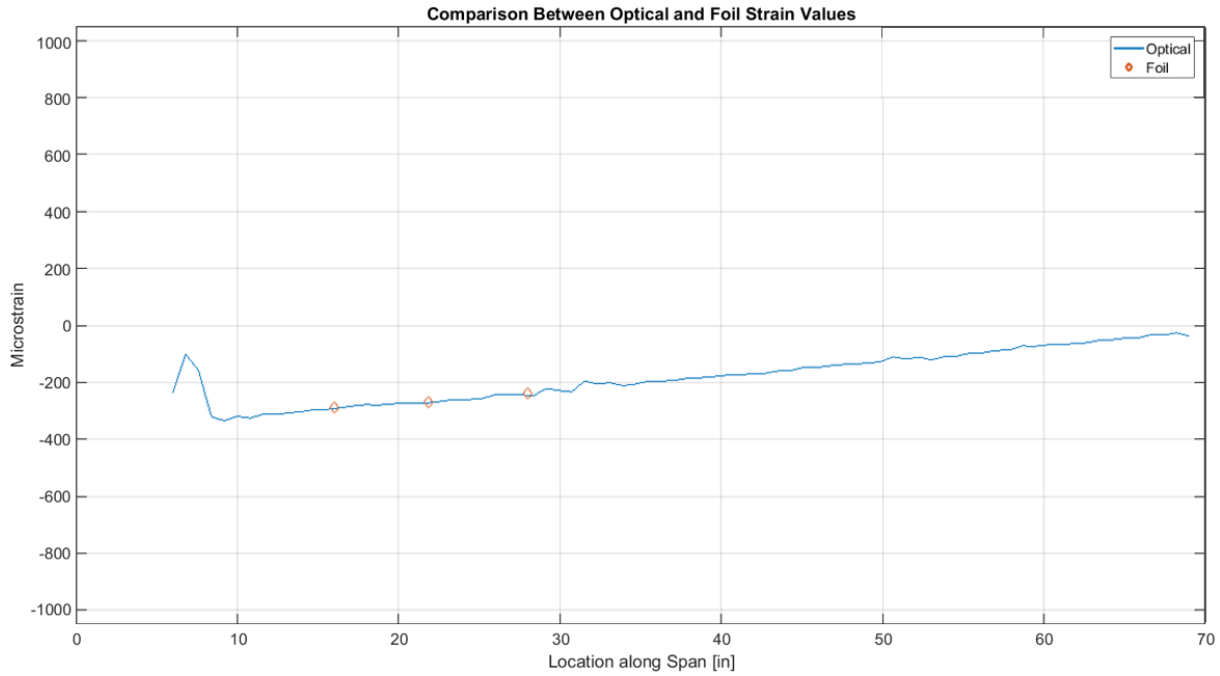

Figure 6-24: Comparison between the OFDR optical fiber and foil strain gauges for a tip load acting on the cantilever aluminum plate.

While the static tip loads placed on the plate provided a convenient method by which the precision and accuracy of the current state-of-the-art OFDR processing technique were evaluated, the ultimate objective was to monitor the transient strain levels caused by structural vibrations. To this end, the plate was subjected to an impulse excitation and the strain time history of each sensor along the optical fiber computed. Figure 6-25 provides the strain time history for two of the sensing locations along the optical fiber due to a single impulse excitation. When the sampled signals plotted in Figure 6-25 are qualitatively compared to those in Figure 6-12 the advancements made in dynamic OFDR sensing are apparent.

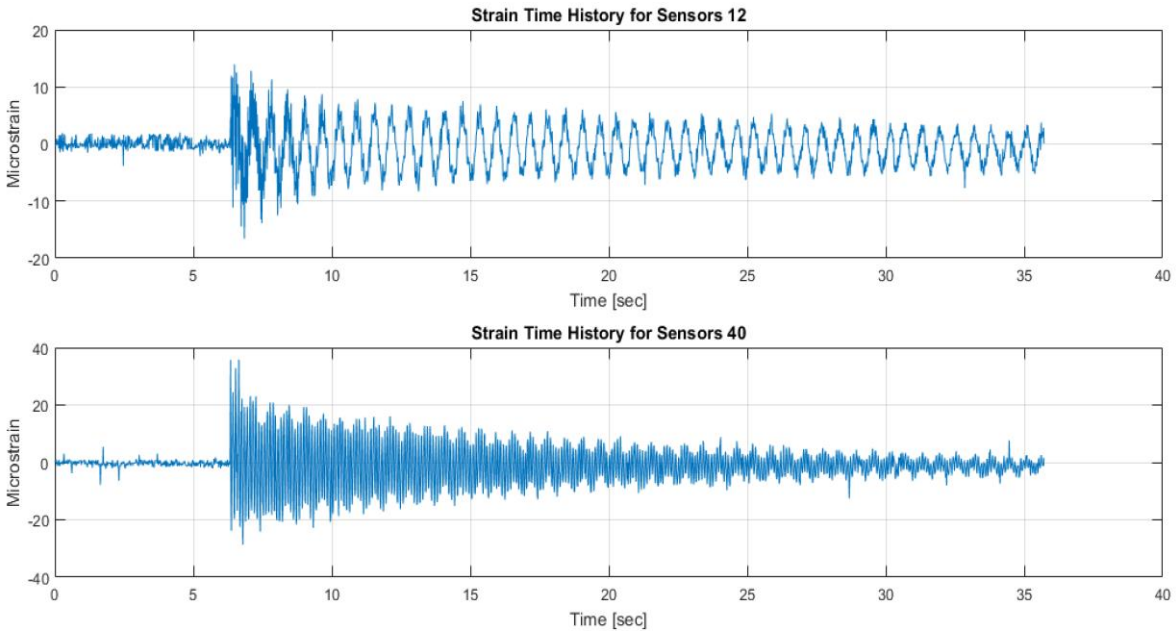

Figure 6-25: Strain time histories of an impulse excitation on the aluminum plate processed using the developed OFDR processing technique.

While the data presented in Figure 6-12 and Figure 6-25 were taken at different times, and on different test articles (both were cantilever aluminum plate with similar geometries), their impulse responses do provide a useful means by which the advancements in dynamic strain sensing via OFDR technologies may be qualitatively viewed. In the upper plot of Figure 6-26 one of the impulse response cycles given in Figure 6-12 has been isolated to represent the state-of-the-art in OFDR impulse response circa 2015 (prior to the advancements presented in this chapter). Likewise, one of the impulse response shown in Figure 6-25 was repeated in Figure 6-26 for the sake of comparison. Comparing the resulting strain time histories, it is clear the advancements in OFDR sensing produce an impulse response one would expect, i.e. a maximum response at the time of impact and undergoing an exponential decay towards its steady state response, and in turn the capability to accurately monitor dynamic strain.

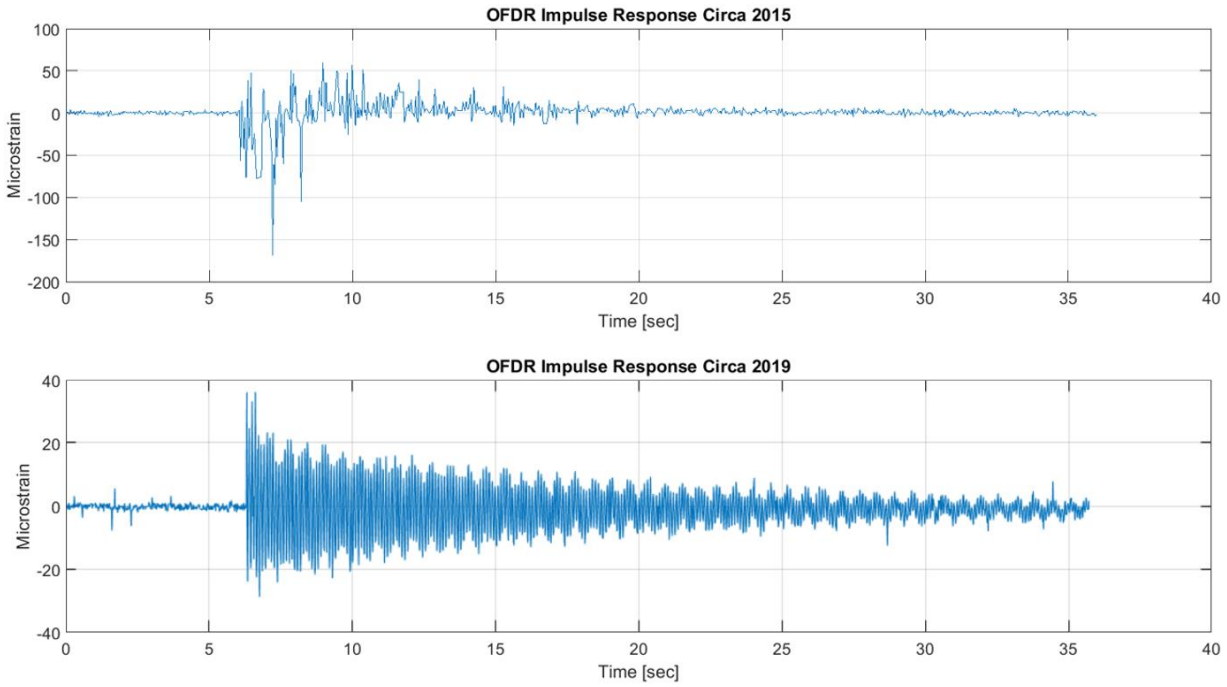

Figure 6-26: Strain time histories of an impulse excitation qualitatively showing the advancements in OFDR dynamic strain sensing.

In addition to the sampling rate increasing from 51Hz to 130Hz, the noise level decreased by a factor of 5 while simultaneously increasing the accuracy and precision of the measurement. As a result of these advancements, it is practical to use OFDR based strain sensors to monitor structural vibrations and in turn be used as input information into the proposed SHM algorithm. The following chapter details the experimental work that has been performed to date with the SHM algorithm utilizing the developed OFDR system and processing techniques outlined in the current chapter.

Chapter 7: Experimental Studies and Demonstration

In order to demonstrate the practical utility of the current SHM methodology experimental damage detection studies were performed. An experimental testbed was first developed for use in testing SHM algorithms. A series of tests were conducted on the testbed as a means to characterize the baseline response of the testbed as well as correlate an undamaged FEM. The follow sections discuss the development, correlation, and validation of the experimental testbed and corresponding FEM. The chapter is concluded by performing a series of experimental damage studies on the developed testbed. These damage studies serve to validate both the practicality of the developed SHM algorithm as well as the analytical work performed.

7.1 Experimental Testbed Development

The experimental testbed developed is a cantilever beam supplemented with airfoil masses to mimic the dynamic response of the main wing spar in an aircraft wing. The wing spar testbed is composed of: (1) a thin-wall carbon/epoxy beam with a near rectangular cross section, (2) a distributed fiber optic strain sensor network, and (3) three airfoil masses. The experimental testbed is shown in Figure 7-1 and a detailed description of each of the components of the testbed given in the following subsections.

7.1.1 Carbon/Epoxy Thin Walled Composite Beam

The wing spar selected was a commercially available, thin-wall, advanced composite beam. The beam is 98-inches in length with a near rectangular cross section having nominal dimensions of 2 inches by 1 inch, as shown in Figure 7-2.

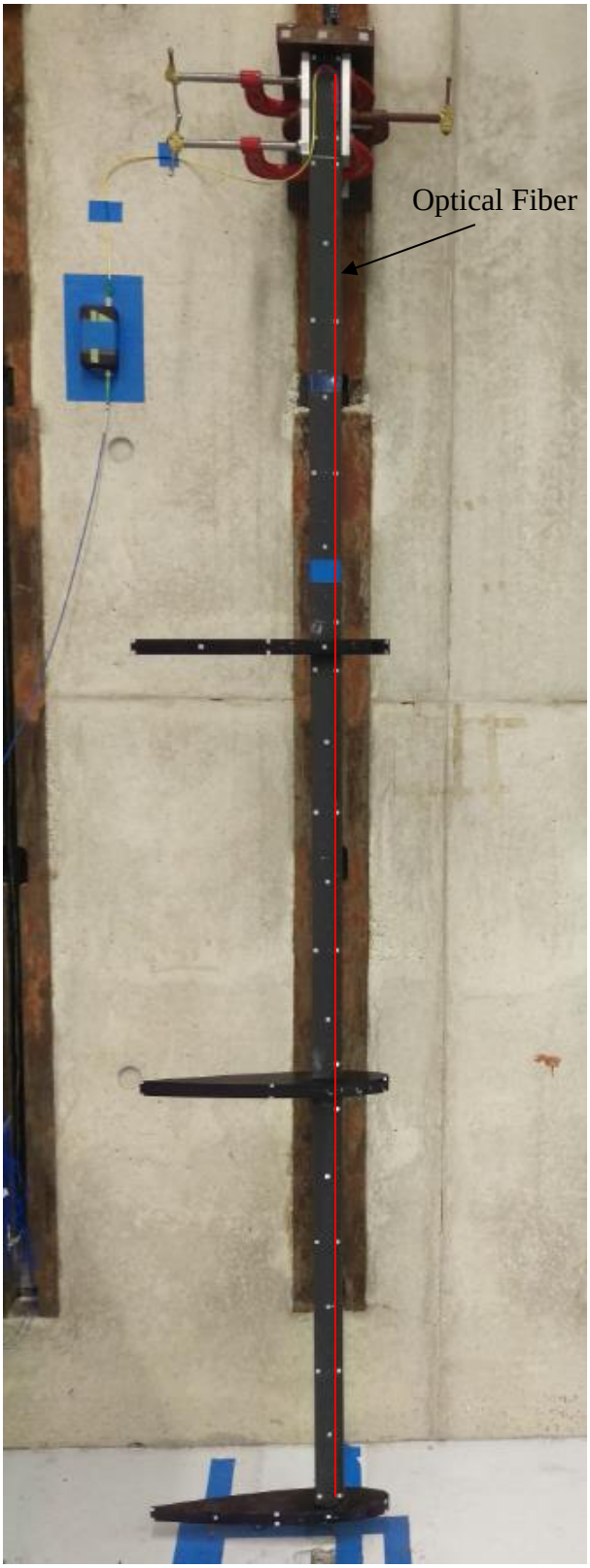

Figure 7-1: Experimental testbed as tested (the red line showing the fiber location is computer generated for clarity).

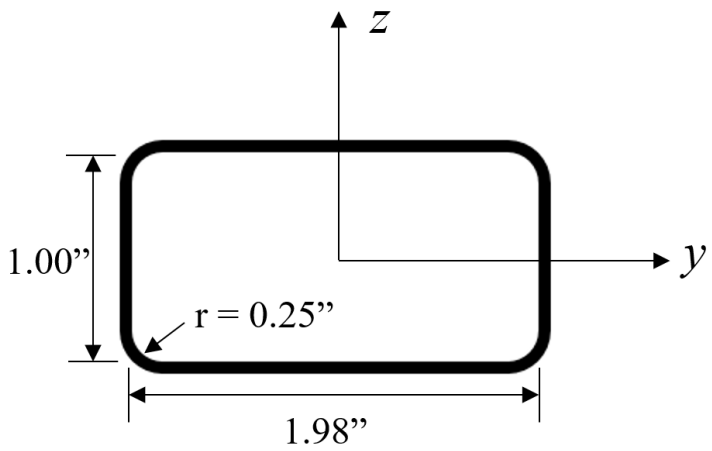

Figure 7-2: Thin-walled composite beam’s cross section profile and dimensions.

The beam was fabricated from three plies of intermediate modulus carbon/epoxy prepreg materials that were wrapped on a mandrel having cross section dimensions of 1.98 inch by 1.00 inch. The inner and outer plies are plain weave material orientated at 45 degrees with respect to the x-axis. The mid-layer is a uni-directional material where all the fibers are coincident with the beam’s length. A micrograph (50x) examination of the complete cross section was performed to study the manufacturing quality of the beam. The micrographs revealed there are significant overlaps of the materials as the plies were wrapped on the mandrels. Out-of-autoclave methods were used to cure the beam which lead to good compaction in the four corners (overall corner laminate thickness is 0.032-0.035 inch), but the short and long rectangular sides have varying wall thicknesses from 0.0385 to 0.0515 inch as a result of excessive resin (poor compaction) and/or ply overwraps. Figure 7-3 provides micrograph examples of a corner radius with good compaction (a), a long (horizontal) side with over-wrapped unidirectional plies (b), and a short (vertical) side (c), respectively. The micrographs clearly revealed individual plies, resin rich areas, ply overlaps, and fabrication voids (black spots).

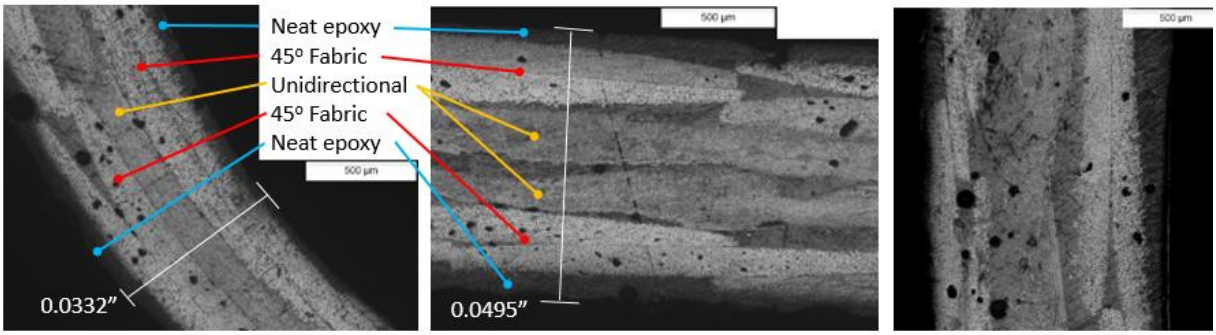

(a) **(b)** **(c)**

Figure 7-3: Micrograph examination of the beam's rectangular cross section for: (a) corner, (b) long side, and (c) short side.

A dimensional check of a fully compacted corner using the optical microscope revealed an overall wall thickness of 0.0332 inch (verified with Vernier caliper) that is composed of an outer neat epoxy layer of 0.004 inch, followed by an outer 45-degree fabric of 0.010 inch, a middle unidirectional layer of 0.0067 inch, an inner 45-degree fabric of 0.010 inch, and an innermost neat epoxy layer of 0.0025 inch. The material properties of the beam were experimentally approximated through a series of correlation studies (see Section 7.2) where both the woven and unidirectional plies were assumed to be made of the same material having the transversely isotropic properties given in Table 7-1.

Table 7-1: Transversely isotropic material properties of the composite beam obtained via model correlation.

Property	Units	Unidirectional	Woven Fabric
E_{11}	Msi	13.354	1.805
E_{22}	Msi	0.940	1.805
E_{33}	Msi	0.940	0.940
G_{12}	Msi	0.627	1.505
G_{13}	Msi	0.627	0.627
G_{23}	Msi	0.339	0.627
ν_{12}	--	0.255	0.439
ν_{13}	--	0.255	0.255
ν_{23}	--	0.386	0.255
ρ	lb/in^3	0.0464	0.0464
t	inch	0.0092	0.0184

7.1.2 Distributed Fiber Optic Strain Sensor Network

The composite wing spar was monitored using Bragg-grated fiber optical strain sensors manufactured by FBGS Draw Tower Gratings. The optical fibers had a nominal diameter of 0.005 inch and a linear weight of 0.00102 pound per foot. On one of the long sides of the rectangular cross section, the optical fiber was run straight along the beam's length, offset from the neutral axis in both planes as shown in Figure 7-4. By offsetting the fiber from the neutral axis of both planes the dynamic bending response of the beam in both planes was monitored using the single fiber. The optical fiber was attached to the outer surface using a 0.1875 inch wide coat of Micro-Measurements M-Bond AE-10 two-part strain gauge adhesive.

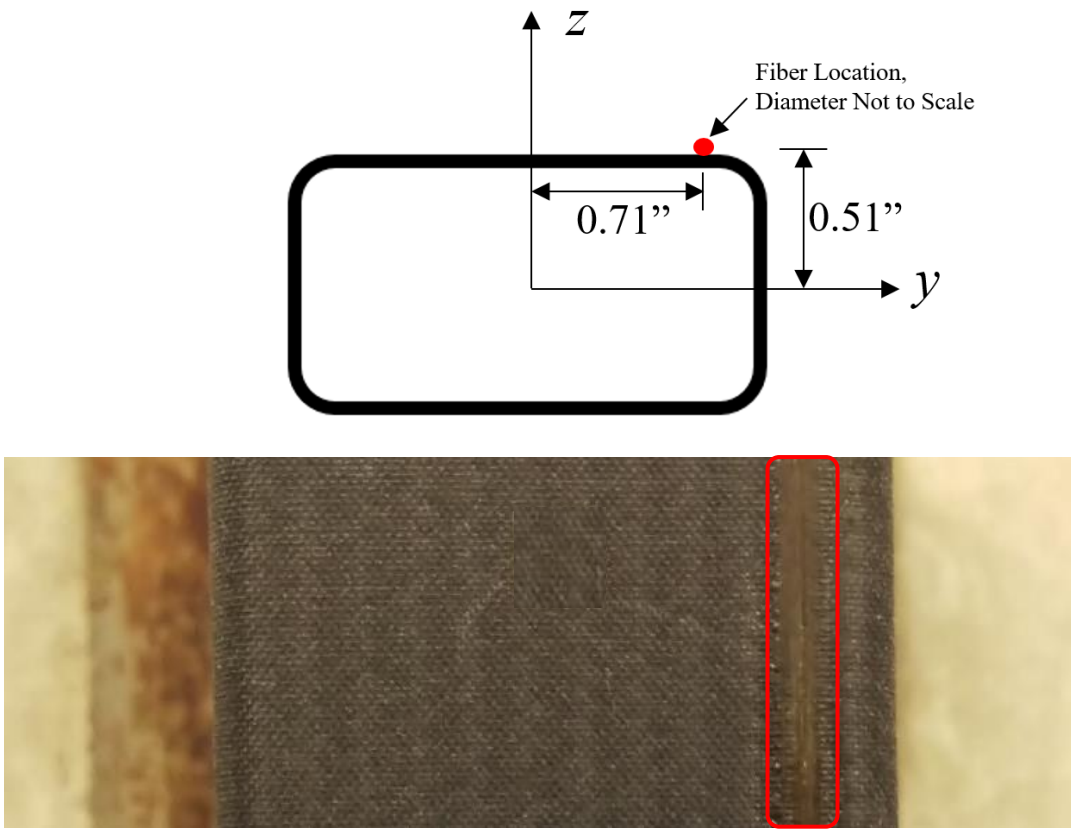

Figure 7-4: (Upper) Schematic of the optical fiber location relative to beam’s cross section. (Lower) Segment of the beam showing the optical fiber under strain gauge adhesive, as instrumented.

The Bragg-grated fiber optic strain sensors chosen for the testbed had a grating spacing of 0.157 inch (4mm) on center and a grating length of 0.0787 inch (2mm). The grating length is equivalent to the gauge length in conventional foil strain gauges as the strain value given at any sensor location is the average axial strain in this 0.0787 inch region. The 0.157 inch spaced gratings began at 4.82 inches from the beam’s root and spanned the beam’s length, providing up to 59-point measurement locations. The optical fiber was coupled to a fiber optic strain sensing (FOSS) system developed by the NASA AFRC. The details of the system are proprietary to NASA and hence omitted from the dissertation except to say a laser source and interferometer were utilized to interrogate the sensors and actively monitor their response using optical frequency domain

reflectometry (OFDR). The data collected by the FOSS system was processed using the developed advancements, as discussed in Chapter 6 of the dissertation.

7.1.3 Airfoil Masses

Three airfoil shaped masses were attached to the carbon/epoxy spar to bring the primary wing spar bending and torsion natural frequencies into a realistic wing natural frequency range (<30 Hz). These masses also introduced the coupled wing bending-twisting modes that are inherent in aircraft wings due to the offset of the line of wing mass centers with the line of shear centers. Each mass was waterjet from of A36 structural steel with a NACA-0016 profile having a chord of 17 inches and a depth of 1 inch. Each resulting mass had a nominal weight of 8.32 pounds. The properties of each of the three masses are listed in Table 7-2. A dimensioned CAD model as well as one of the as-built masses are shown in Figure 7-5 along with their coordinate axes definition.

Table 7-2: Properties of the airfoil masses given with respect to the quarter chord.

Weight (lb)	Chord (in)	Thickness (in)	y_{cg} (in)	I_{xx} (lb-in^2)	I_{yy} (lb-in^2)	I_{zz} (lb-in^2)
8.32	17	1	-3.115	141.24	4.46	138.45

The carbon/epoxy beam's centroid was centered at the airfoil quarter-chord. The centroid location for each airfoil cross section was calculated as 7.365 inches from the leading edge and thus the mass centroids are 3.115 inches rearward from the spar centroid. This offset introduced torsion coupling in the soft (flapping) bending vibration modes and conversely introduced soft (flapping) bending into the torsion modes. Since the airfoil section is symmetric, no coupling was introduced to the stiff (lead-lag) bending modes. The masses were mounted to the composite beam at 36", 65.75" and 97.5", from the beam's root to the center of the mass. The inclusion of airfoil masses reduced the modes of the structure such that the first six bending vibration modes were less

than 25 Hz. This includes the first three bending modes in the soft-plane (bending about the y-axis, out-of-plane, or flapping) and first three bending modes in the stiff-plane (bending about the z-axis, in-plane, or lead-lag).

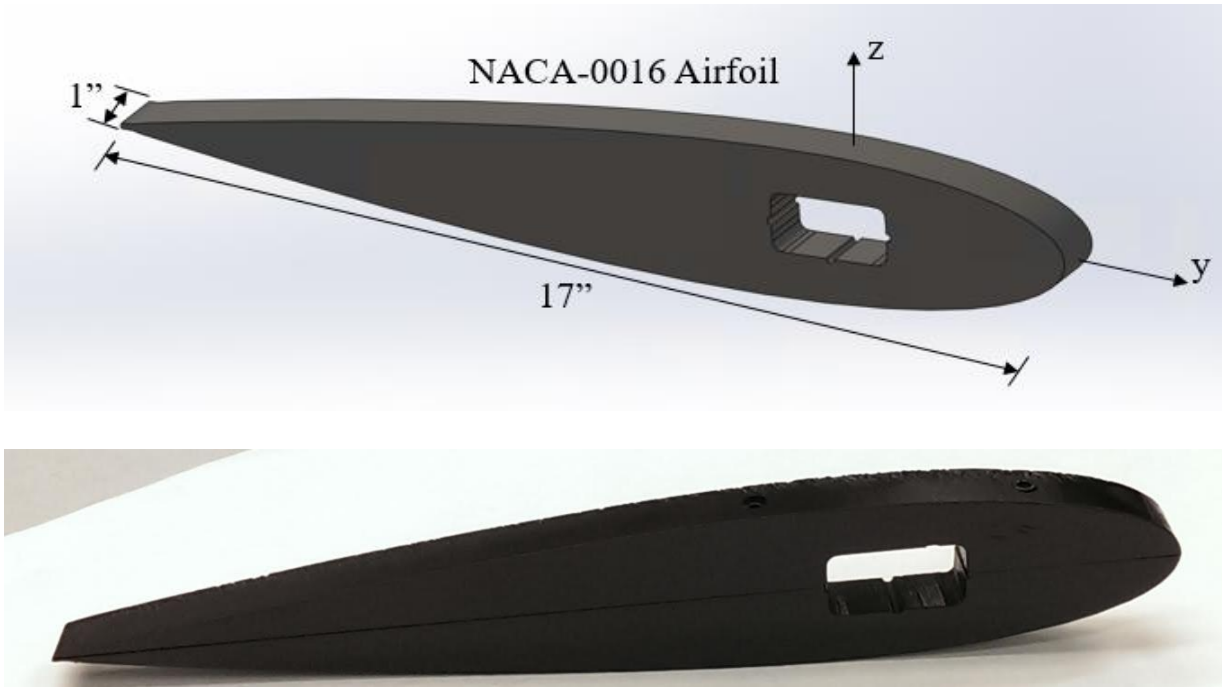

Figure 7-5: (Upper) CAD model of the airfoil mass. (Lower) Airfoil mass as constructed.

7.2 Correlation Studies on the Thin-Walled Composite Beam

A detailed FEM of the thin-wall beam was developed using FEMAP which included allowances for the variable carbon/epoxy wall thickness as well as the beam root attachment and strong-wall. In practice, the beam was mounted to the strong-wall using an aluminum slug which matched the beam’s interior dimensions and spanned the first six inches of the beam’s root. Aluminum plates were then placed on two sides of the beam and three c-clamps used to hold the beam in the fixture (the plates and clamps are visible in Figure 7-1).

Prior to the addition of the airfoil masses, both static and dynamic model correlation studies were done which allowed for a correlation of the FEM model on the bare composite beam.

Once the correlated model was developed, the model response of the beam with and without the airfoil masses was documented for future use. The FEMAP rendering of the NASTRAN beam model is shown in Figure 7-6.

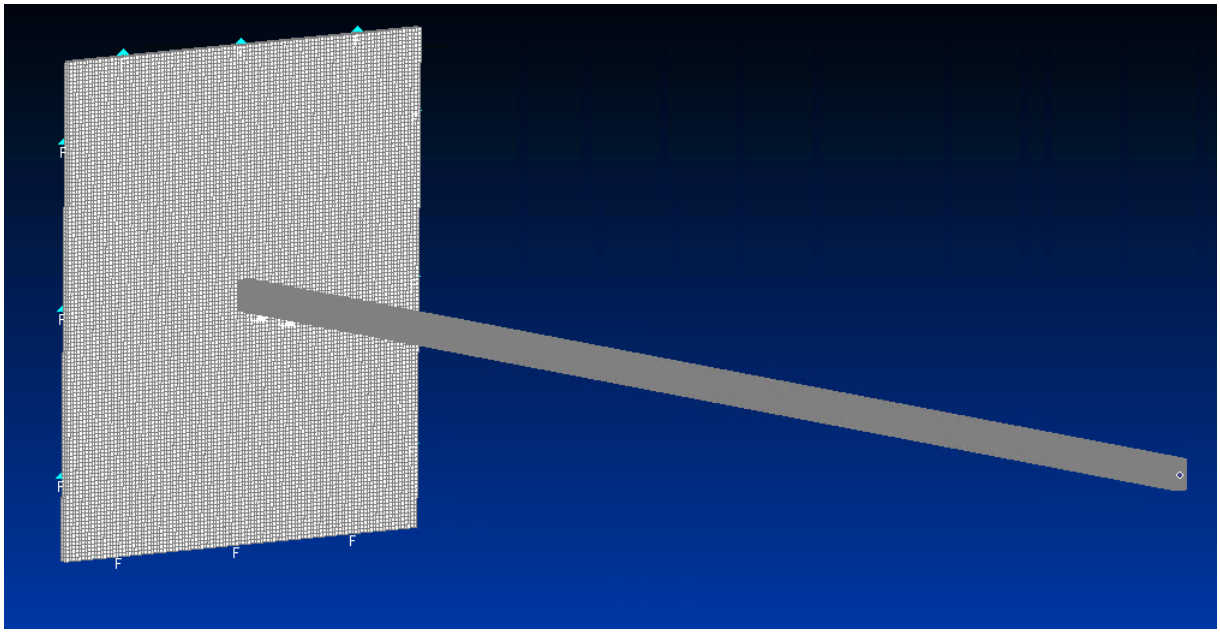

Figure 7-6: FEMAP rendering of the Nastran model of the bare beam, mounting fixture, and strong wall.

7.2.1 Static Correlation Studies

After the fiber optics were attached to the composite beam, the resulting beam was cantilevered to a strong wall using a specially fabricated root attachment that essentially fixed the first 6 inches of the spar. Static load cases were first employed to correlate the material properties of the beam and validate the optical fiber distributed strain measurements. The static testing involved placing either 5.5lb or 10.25lb shot bags on either the beam's tip, mid span, or both locations simultaneously. Each of the shot bags were equipped with a one inch wide nylon strap which was looped over the beam in order to apply the load, as shown in Figure 7-7.

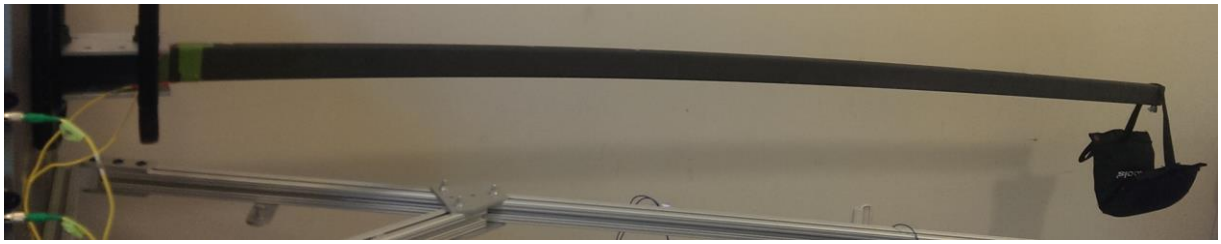

Figure 7-7: Tip loaded cantilever beam during static load testing.

During the initial static correlation studies, the FOSS system was interrogating the optical strain sensors throughout the loading/unloading process. Figure 7-8 provides a plot of the strain distribution due to a 10.25lb tip load on the composite beam as measured by fiber optic system. The plot also contains the finite element analysis (FEA) predictions of the strain distribution under the same load case using the correlated properties obtained via static and dynamic correlation (given in Table 7-4). In addition to the measured strain response, the beam's static displacement was measured and found to be within 0.2% for the tested cases.

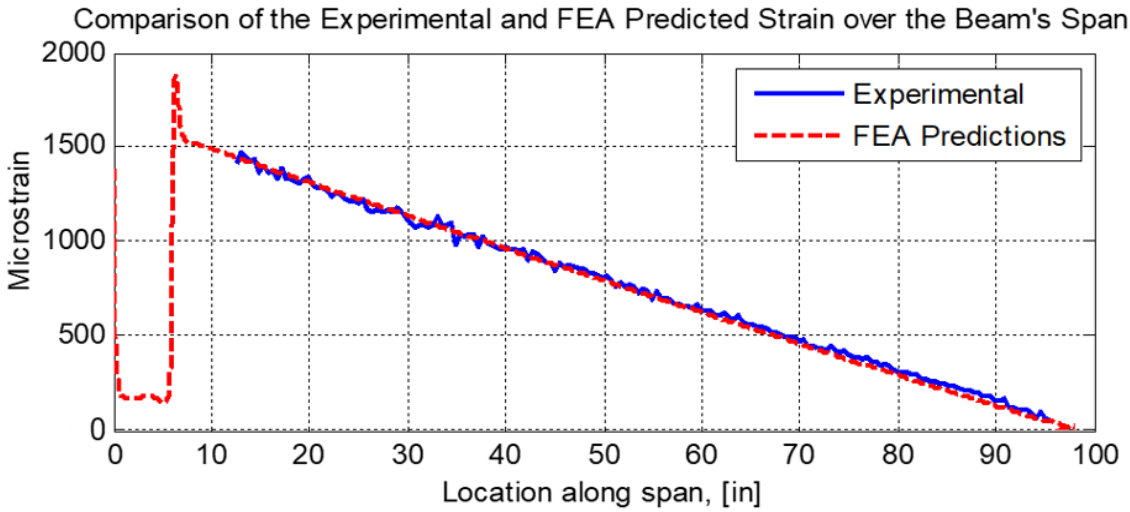

Figure 7-8: Measured and simulated strain responses for the beam under a 10.25lb tip load.

7.2.2 Dynamic Correlation Studies

In addition to the static correlation studies of the bare cantilever beam, a series of vibration tests were performed. The modal testing involved attaching six PCB micro-dot accelerometers at locations of 0.5”, 20”, 28”, 45”, 62” and 70” relative to the beam’s tip and a PCB force transducer at the tip, as shown in Figure 7-9.

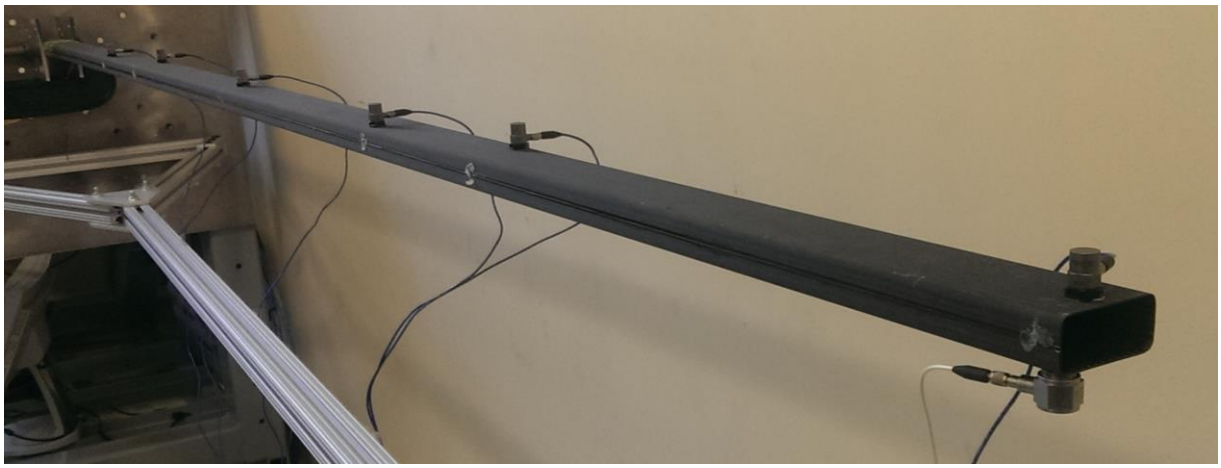

Figure 7-9: Modal testing configuration for initial model correlation studies.

Next, a series of tests were performed with either an impact force (hits at 2” and 24” from the free end), or a modal shaker performing a sine sweep from 0-500 Hz. While the fiber optic sensors were installed during the correlation studies, the limited frequency range available from the sensors made it desirable to supplement the information using accelerometers. The first six analytical bending natural frequencies from the FEM of the beam are compared to the experimentally measured results in Table 7-3, where the results are within 4.25% after the model was adjusted to include the weights of the accelerometers.

Table 7-3*:* Natural frequencies of the composite beam extracted from modal testing and NASTRAN simulations.

	Natural Frequencies (Hz)			
Mode	**Experimental**	**Analytical**	**Error (%)**	**Description**
1	4.688	4.714	0.555	1st Soft-Plane Bending
2	7.585	7.746	2.123	1st Stiff-Plane Bending
3	29.432	29.476	0.149	2nd Soft-Plane Bending
4	48.047	48.155	0.225	2nd Stiff-Plane Bending
5	81.256	79.588	-2.053	3rd Soft-Plane Bending
6	133.002	127.360	-4.242	3rd Stiff-Plane Bending

The set of equivalent transversely isotropic material properties that were identified which allowed for simultaneous correlation of both the static and dynamic responses, as well as an accurate density value, are given in Table 7-4.

Table 7-4*:* Transversely isotropic material properties of the composite beam obtained via model correlation.

E_{11} (Msi)	E_{22} (Msi)	G_{12} (Msi)	G_{13} (Msi)	G_{23} (Msi)	ν_{12}	ρ (lb/in^3)
13.354	0.94	0.627	0.627	0.339	0.255	0.0464

7.3 Incorporation of the Airfoil Masses within the Structural Model

The addition of the airfoil masses within the structural model was relatively straight forward. This straightforward implementation was in large part because the material properties of A36 steel are well documented and the geometry of the airfoil masses known exactly. The following subsections detail the incorporation of the airfoil masses within the NASTRAN model and the experimental validation of the composite beam test article with airfoil masses. These FEM, and their relevant data sets, are later used to validate the MATLAB FEM used to generate the model PSD.

7.3.1 Extension of the Model to Include Airfoil Masses

Prior to incorporating the airfoil masses into the developed MATLAB FEM, the NASTRAN model was updated to include the airfoil masses at their selected locations and study the effects the masses have on the beam's dynamic response. The masses were selected to be at locations 36", 67.75", and 97.5" from the beam's root. These locations were chosen to produce the most realistic bending mode shapes over the first three modes in each plane. Through finite element studies it was shown that lumping the mass at a single location did lower the frequencies of the system however after the primary mode the mode shapes begin to take the form of a fixed-pinned structure, rather than the desired fixed-free cantilever condition. The updated model containing the three airfoil masses is shown in Figure 7-10.

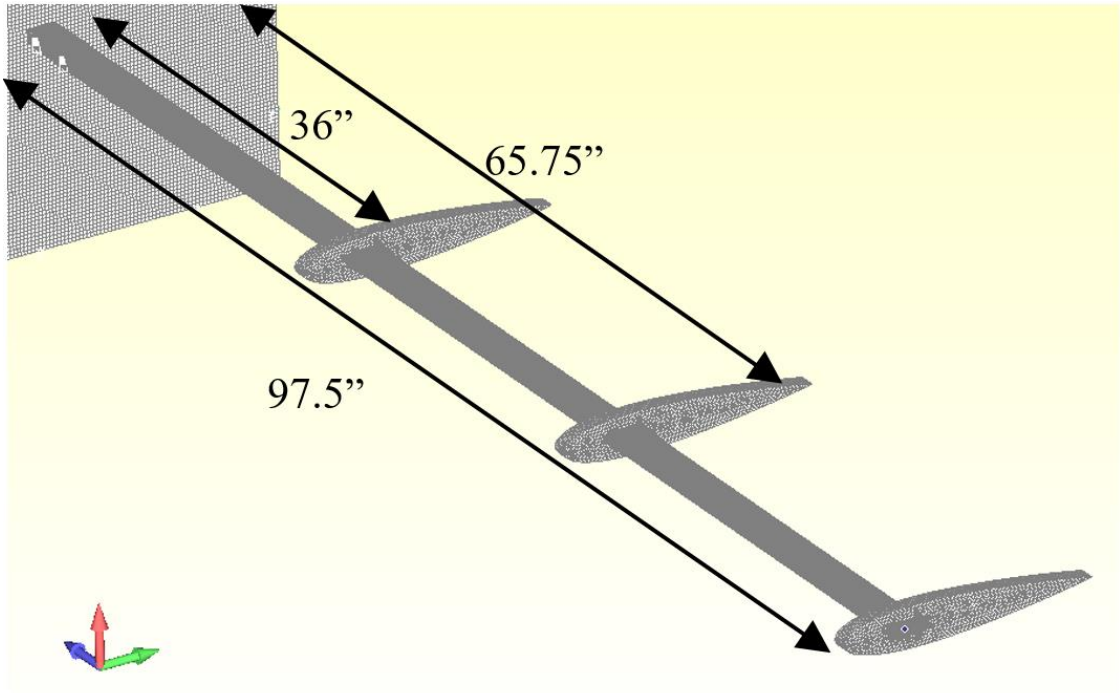

Figure 7-10: Testbed finite element model showing wing spar and three added airfoil masses.

The normal mode shapes and natural frequencies of the undamped finite element system were calculated by NX Nastran and are given for the first six modes of the system in Figure 7-11 and Table 7-5. Note that the inclusion of the airfoil masses lowered the first torsional frequency to within the first 6 modes via the offset of the airfoils' center of mass with the beam's center of mass. The FEM comprised of shell and solid elements (for the beam and masses, respectively) was used not only for correlation to the measurement data, but also for validation of the Timoshenko beam element model being used in the current work.

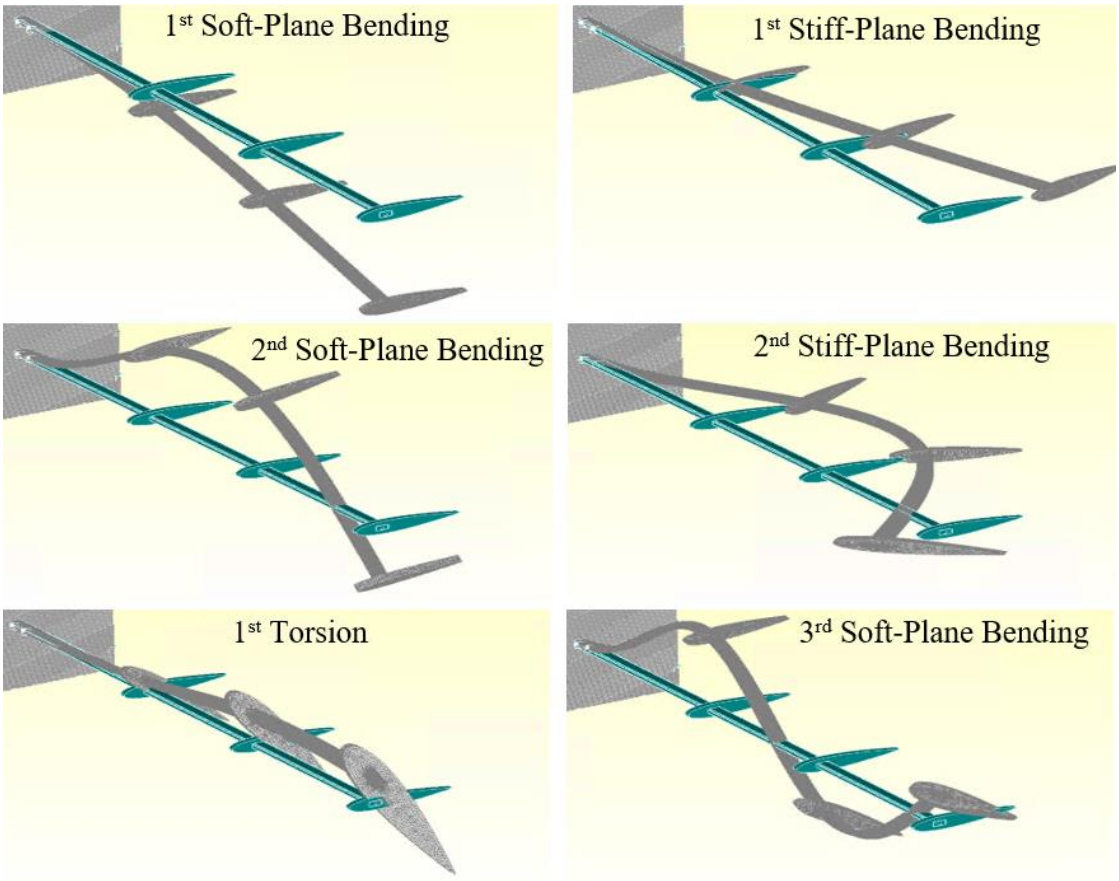

Figure 7-11: Mode shapes of the wing spar testbed computed via normal modal analysis in NASTRAN.

In addition to the NASTRAN shell/solid model previously presented, a beam model was prepared in NASTRAN using the equivalent laminate properties of the beam (calculated from the

transversely isotropic properties given in Table 7-4) and lumped mass elements attached to the nodes adjacent to the actual airfoil mass locations. The centroids of the airfoil masses were offset from the beam nodes to accurately represent the inertial contributions of the masses. The product of inertia terms corresponding to the offset airfoil masses were found to have negligible effect on the six bending modes used in the current analysis and as such were neglected. Lastly, the MATLAB FEM being used in this dissertation was modified to incorporate the effects of the airfoil masses. The results for the first eight modes using the three different FE approaches are presented in Table 7-5.

Table 7-5: Natural frequencies of the wing spar testbed extracted from normal modal analysis via NX NASTRAN and MATLAB.

Mode	Natural Frequencies (Hz)			Description
	NASTRAN Shell FEA	NASTRAN Beam FEA	MATLAB Beam FEA	
1	0.903	0.888	0.888	1st Soft-Plane Bending
2	1.488	1.469	1.470	1st Stiff-Plane Bending
3	5.853	5.777	5.778	2nd Soft-Plane Bending
4	9.437	9.249	9.249	2nd Stiff-Plane Bending
5	13.148	10.161	10.159	1st Torsion
6	16.461	15.484	15.484	3rd Soft-Plane Bending
7	26.336	24.520	24.520	3rd Stiff-Plane Bending
8	37.264	28.484	28.467	2nd Torsion

7.3.2 Experimental Model Validation via Scanning Laser Vibrometry

As a means to validate the developed FEM, measured dynamic response obtained by the fiber optic sensors, and provide a full-field assessment of the beam's dynamics, a Polytec PSV-400 SLV was used to monitor the beam's vibration response. The vibrometer used in the current study is a one-dimensional system meaning that deformation in only one plane at a time may be captured. As a result, two scans were required to capture the data in both the soft-bending and stiff-

bending planes. To fully capture the data, 52 vibrometer targets were affixed to the beam on the short face and 64 targets on the tall face, including targets on the airfoil masses and fixturing. The targets were made of 3M reflective tape and measure 1/8 inch square. The necessity of the targets (or lack thereof) was discussed in detail in a 2017 paper by Kosmatka, Martins, and Pineda [109]. In the current work the targets were included to yield the highest quality data as well as ensure repeatable results by fixing the measurement points with the reflective tape. The three images in Figure 7-12 show the setup of the vibrometer for the tall face (left), short face (right), and a zoomed view of some of the targets associated with the center section of the beam (center).

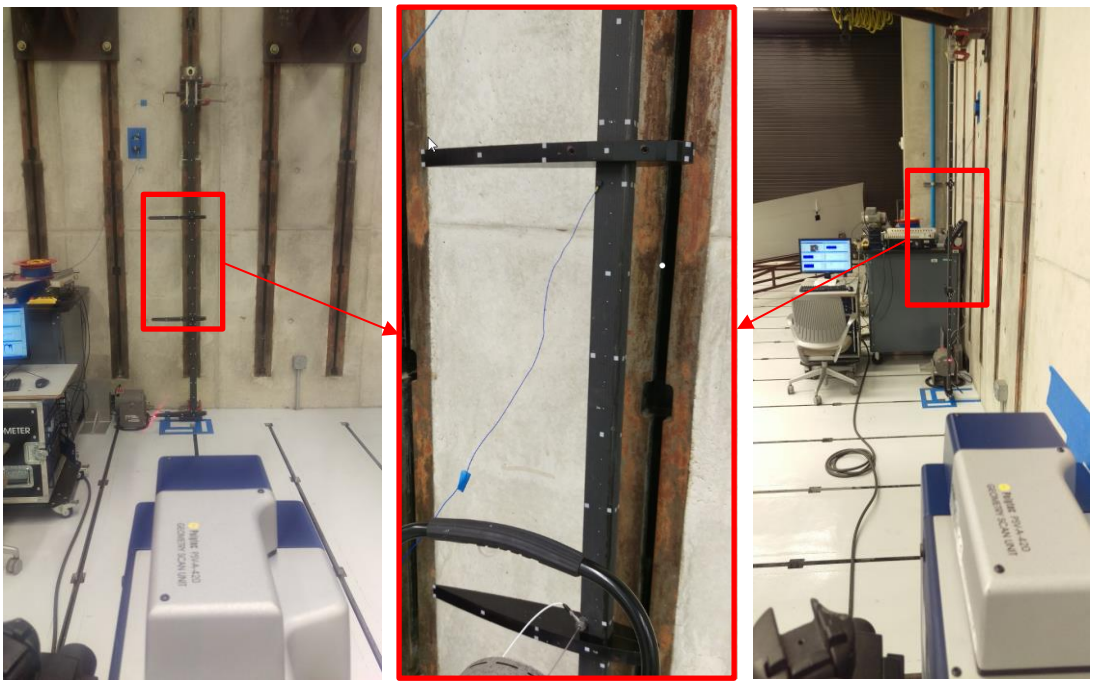

Figure 7-12: Scanning laser vibrometer setup for the (left) soft plane, (center) zoomed target region, (right) stiff plane.

Combining the results of the scans in both the soft and stiff planes yields the experimental frequencies and operational shapes of the beam obtained by the vibrometer in the velocity domain. The FRF data generated by the Polytec vibrometer was uploaded to ME'Scope where the data was

curve fit to yield the experimental modal parameters. One of the advantages of the high spatial resolution afforded by the vibrometer is the ability to clearly animate the experimental mode shapes. The vibrometer collected mode shapes for the first six modes of the wing spar testbed are given in Figure 7-13 along with their corresponding frequencies.

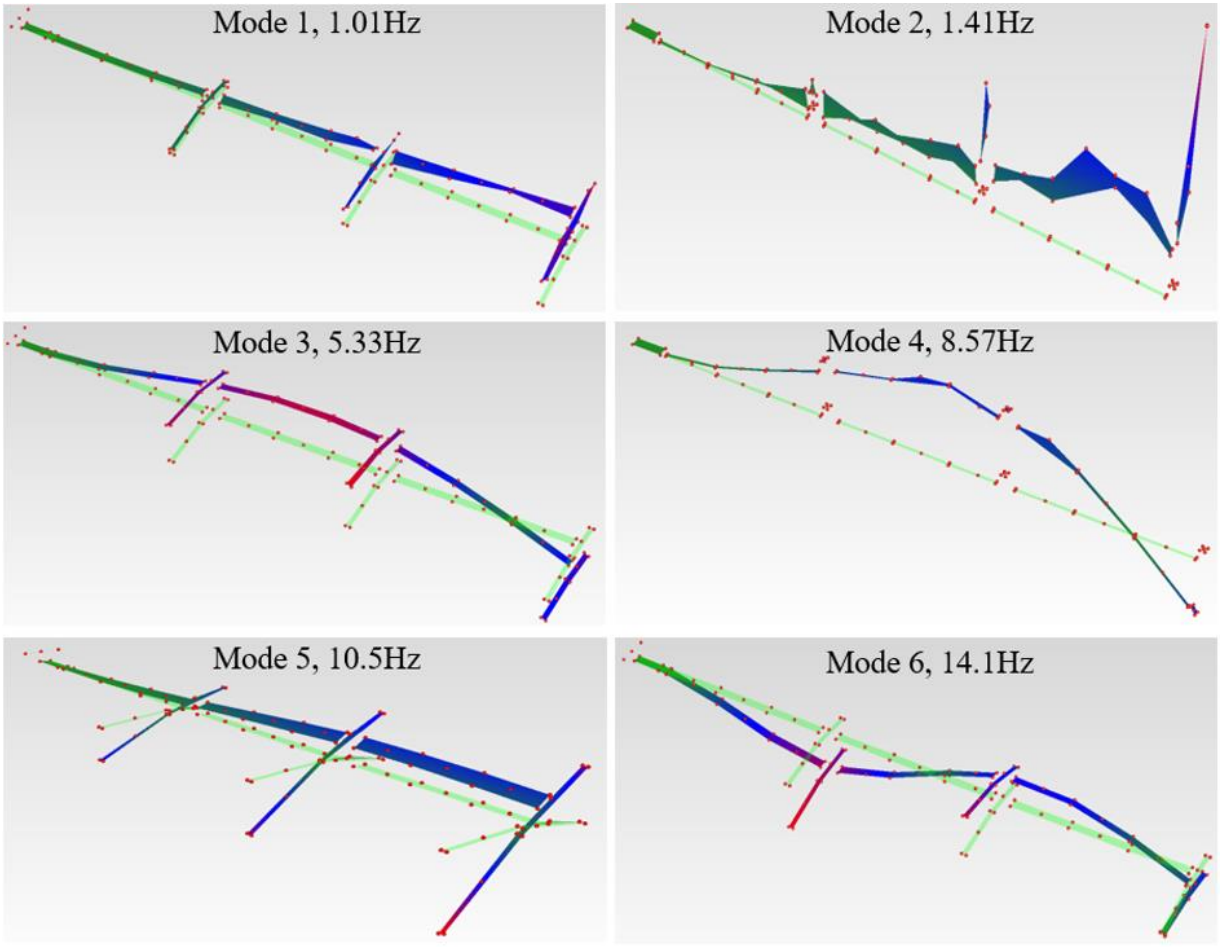

Figure 7-13: Extracted experimental mode shapes obtained via the scanning laser vibrometer (See Table 7-6 for description of modes).

The first two modes measured by the vibrometer, first bending in each plane, contained variations in the FRF response for each of the measured DOF, making curve fitting difficult. These variations in the FRF are likely caused by poor low frequency excitation and lead to more uncertainty in the estimated modal parameters. For the first bending mode in each plane this

uncertainty is represented by the non-smooth mode shapes shown in the first row of Figure 7-13, particularly noticeable in mode two. Further analysis reveals that the modal phase colinearity (MPC) value for modes one and two are the only modes with values less than 0.99 instead having values of 0.867 and 0.712, respectively. This suggests either poor excitation energy, or heavy damping (i.e. highly complex modes) associated with these modes.

In addition to the SLV, the FOSS system was also used to collect vibration data, allowing the frequencies and mode shape obtained by the FOSS system to be compared to those of the vibrometer. Although the FOSS system as currently configured is capable of sampling up to 130Hz, the system was set to sample at 50Hz (25Hz Nyquist frequency) to provide the highest level of accuracy in measuring the first six bending modes of the testbed. As a result, the second torsional frequency of the testbed was outside the detectable range of the OFDR system. Table 7-6 provides the experimentally determined frequencies, obtained by curve fitting the FRF and PSD data, as measured by the vibrometer and FOSS systems.

Table 7-6*:* Natural frequencies of the wing spar testbed experimentally determined via scanning laser vibrometry and FOSS.

	Natural Frequencies (Hz)		
Mode	**Vibrometer**	**Fiber Optics**	**Description**
1	1.01	0.90	1st Soft-Plane Bending
2	1.41	1.41	1st Stiff-Plane Bending
3	5.33	5.31	2nd Soft-Plane Bending
4	8.57	8.55	2nd Stiff-Plane Bending
5	10.50	10.43	1st Torsion
6	14.10	14.05	3rd Soft-Plane Bending
7	23.00	22.95	3rd Stiff-Plane Bending
8	29.40	--	2nd Torsion
Frequency Resolution	0.078Hz	0.033Hz	

The results of the initial experimental validation between the vibrometer and fiber optic strain sensing system show excellent agreement in the natural frequencies of the system, with each of the first seven modes having equal values within the frequency resolution of the two systems. Note that although the fiber optic sensors were able to detect the first torsion mode, the modal peak was very low in magnitude, resulting from the low sensitivity of the axial fiber optic sensors to the torsional strain. The second torsion mode was not detectable with the fiber optic system. The mode shapes extracted from the 59-fiber optic sensors are shown in Figure 7-14.

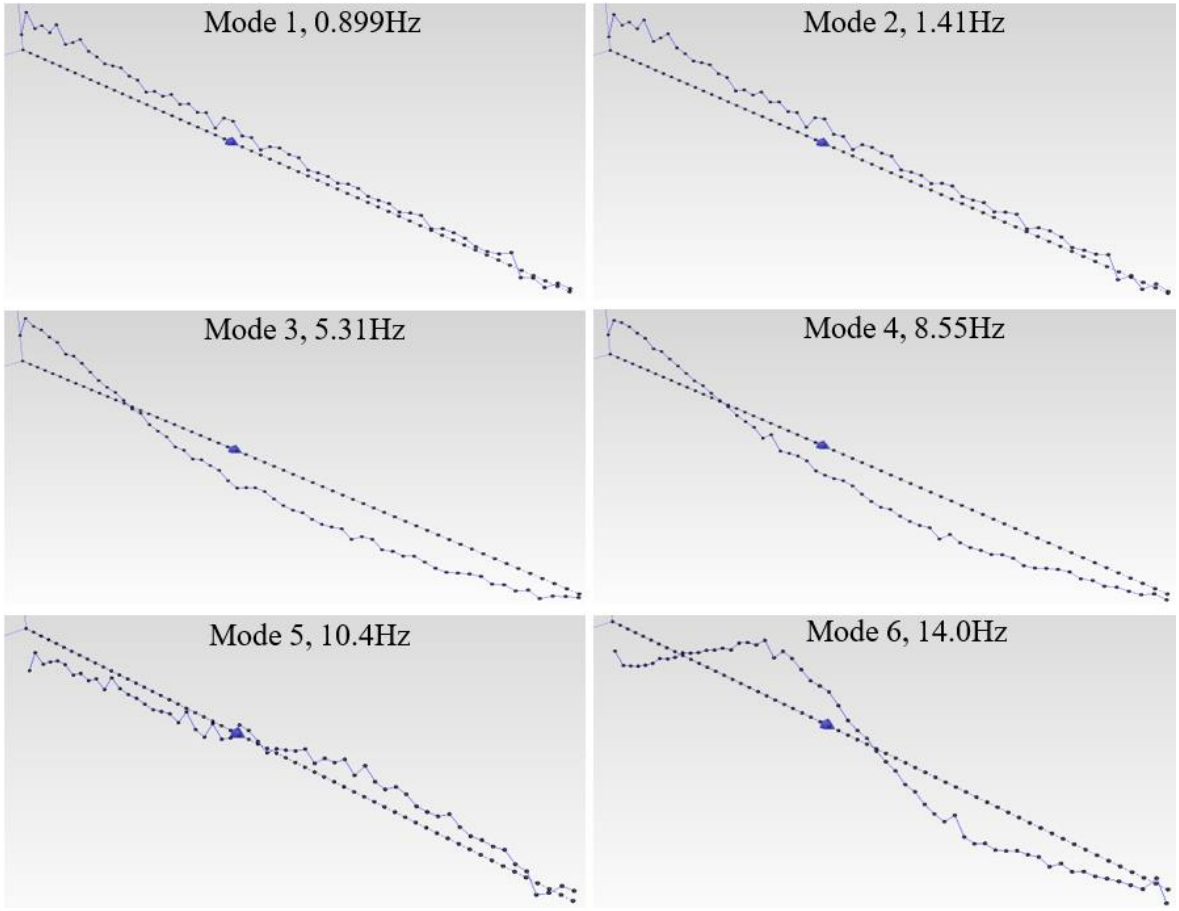

Figure 7-14: Extracted experimental strain mode shapes obtained via the fiber optic sensing system (See Table 7-6 for description of modes).

It is important to note that the mode shapes obtained from the FOSS system are strain mode shapes and as such one would not expect a direct correlation to the velocity mode shapes of the SLV. Additionally, it is noted that the fiber optic strain gauges on the current test article are aligned axially in a single run along the beam's length. These axial gauges are the reason for the single linear set of mode shapes shown in Figure 7-14. While this does cause a lack of resolution in the mode shapes in comparison to those of the vibrometer, an advantage of the fiber optics is the ability to capture all of these modes simultaneously whereas the vibrometer had to move positions and repeat thousands of excitations to provide essentially the same information as the FOSS system using just a handful of excitation cycles. The reader is further reminded that the modes shapes of the structure are inconsequential to the operation of the algorithm and merely shown for documentation and comparison sake. The important information required as the fundamental input for the algorithm are the strain PSD.

7.4 Experimental Implementation

In order to validate the analytical work previously presented, an experimental study was performed using the composite wing spar testbed. In the current section the undamaged testbed is evaluated and the experimentally derived PSD is used to refine the MATLAB FEM previously developed through an initial algorithm run. Damage is then inflicted to the beam to simulate a crack and an impact which are completely unknown to the algorithm. The vibration tests are repeated in the damaged configurations, from which the PSD are calculated and used to experimentally demonstrate and validate the SHM algorithm.

7.4.1 Experimental Testing Setup

The experimental testing was carried out using the AFRC FOSS system as the interrogation unit for the fiber optic sensors. Figure 7-15 shows the wing spar testbed as tested.

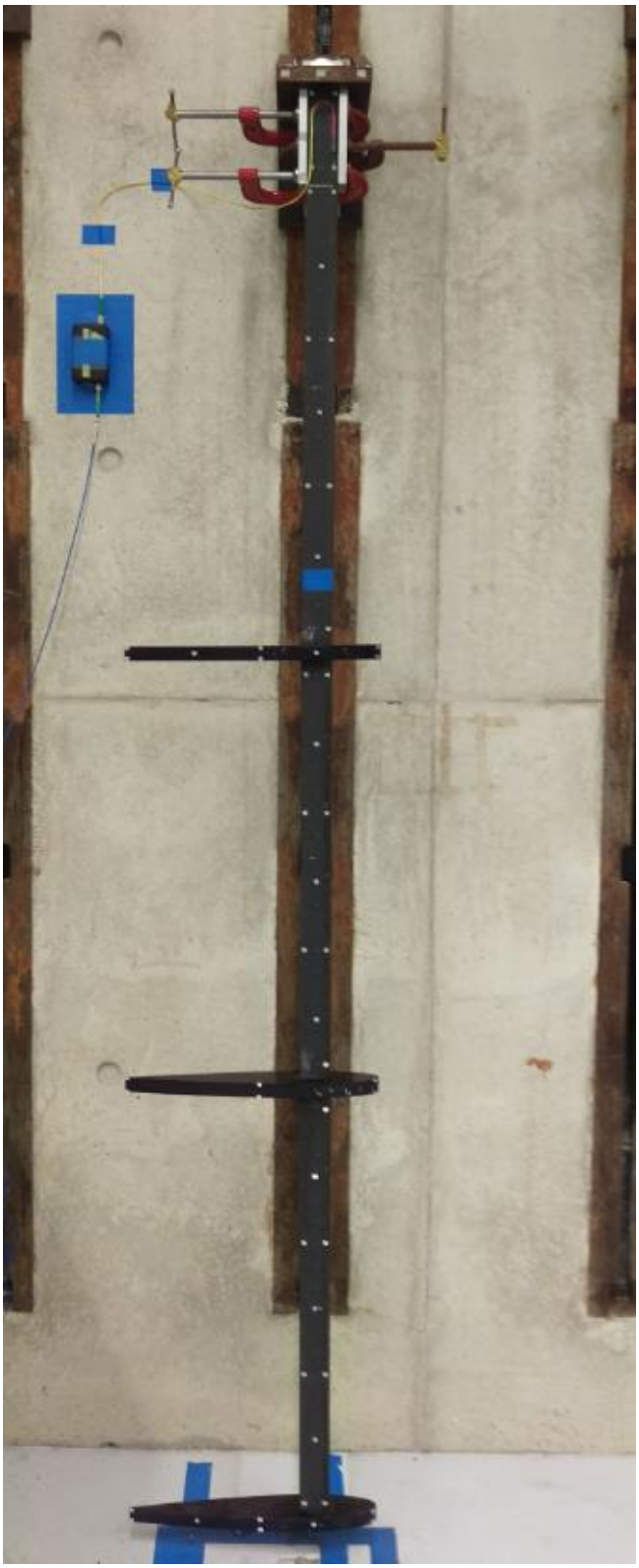

Figure 7-15: Test setup for the experimental implementation.

The testbed was excited via impact on the upper airfoil mass (closest to the clamped end) providing the requisite broad-spectrum excitation. The airfoil mass was impacted using an industrial hammer at an angle relative to the leading edge such that modes in both planes of the beam were excited. Five excitation cycles were repeated for each of the undamaged and damaged states to allow for complex averaging of the PSD. The response of the testbed was monitored using the 59 fiber optic strain sensors on a single fiber in conjugation with the ODFR based interrogation and processing scheme discussed in Chapter 6. The strain time history of each of the sensors along the beam's length are plotted in three-dimensional space in Figure 7-16 with the plot looking down the sensor location axis.

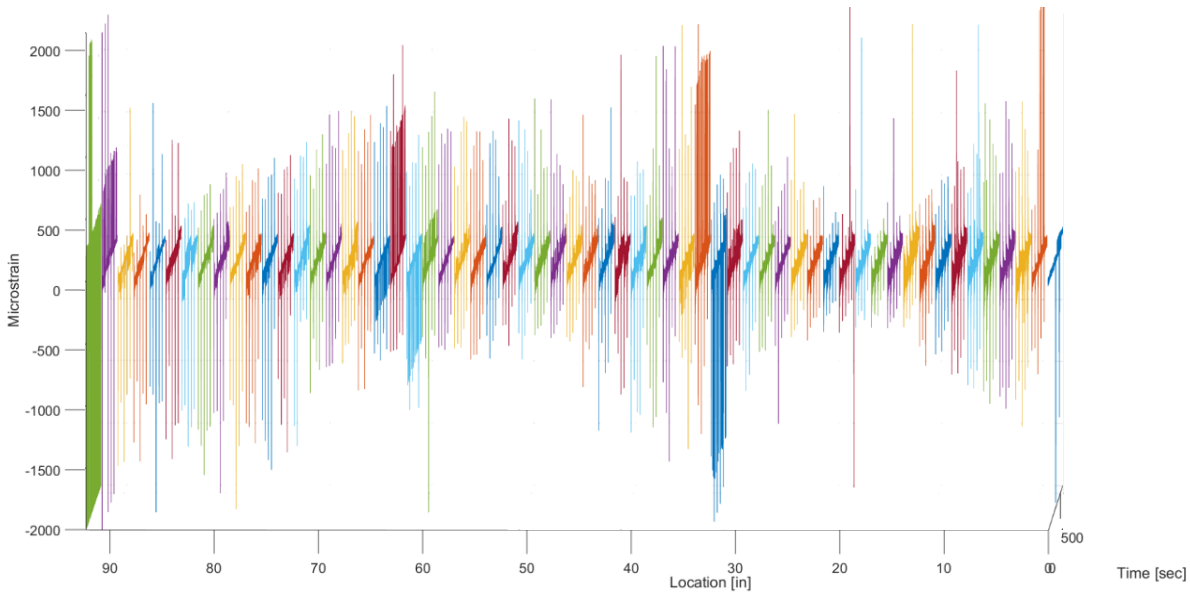

Figure 7-16: Strain time histories of each of the strain sensors for the five impact excitations.

The plot in Figure 7-16 shows the relative magnitude of the response of each of the sensors along the span for each of the impacts. Note the coordinates of the beam are ranging from 92 inches (the free end) to zero inches (the fixed end), where the first six inches of the beam contain the mounting fixture and are assumed to be fixed (and hence not shown). The remaining plots in this

chapter are done in a consistent manner where the effective length of the beam is 92 inches and the clamped six-inch root is neglected. At the locations surrounding 30 inches, 60 inches, and 92 inches the localized strain effects of the airfoil masses on the strain time histories are clearly visible in Figure 7-16. Another important conclusion from Figure 7-16 is the fact that there was a good distribution of strain energy throughout the overwhelming majority of the beam's length. This is important to ensure quality data was available from most, if not all, of the available sensors. In order to better visualize the strain time histories, the response of sensor five was extracted from the three-dimensional plot and is given in Figure 7-17.

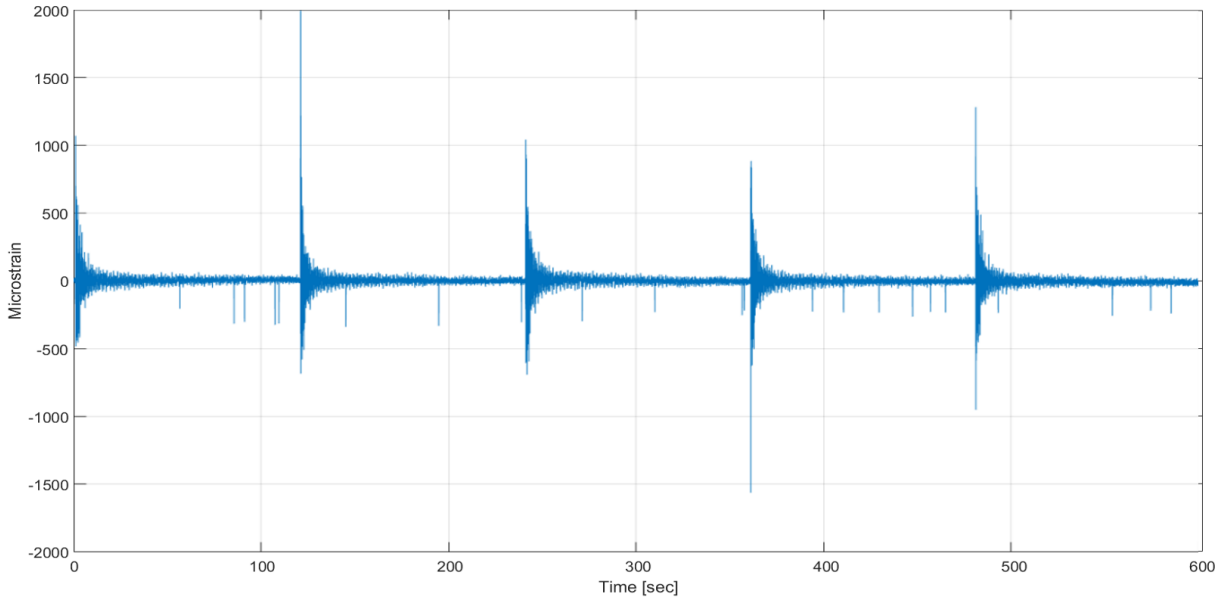

Figure 7-17: Strain time history of strain sensor five over each of the five impact excitations.

In Figure 7-17 it is observed that each of the five impulse responses shown are relatively uniform in magnitude. There were some variations in the initial response which is believe to be caused by an optical effect occurring in the fiber stemming from the impulse. It is also known that there was a "tick" in the microprocessor controlling data being moved across the serial bus from the interferometer to the analog-to-digital converter. These ticks manifest themselves as spurious

spikes in the strain data seen throughout the time histories of Figure 7-17. These ticks are not inherent to the technology and would likely be resolved by changing hardware. Furthermore, these spikes shown in the data presented in Figure 7-16 and Figure 7-17 tend to cancel out when taking multiple averages, as is the standard in computation of the PSD, and do not affect the operation of the algorithm.

Once the strain time histories were obtained using the methods of Chapter 6, the PSD of each sensor was calculated relative to each of the identified quality reference DOF. Substandard reference DOF would be those such as the last sensor on the fiber. The tip most sensor was exposed to very low strain levels being near the tip of the cantilever beam and also suffers from reflection problems related to termination of the optical fiber. Using sensor five as the reference DOF, the magnitude of the PSD for each of the 59 sensors was calculated, using five spectral averages in the complex domain, and are plotted in Figure 7-18.

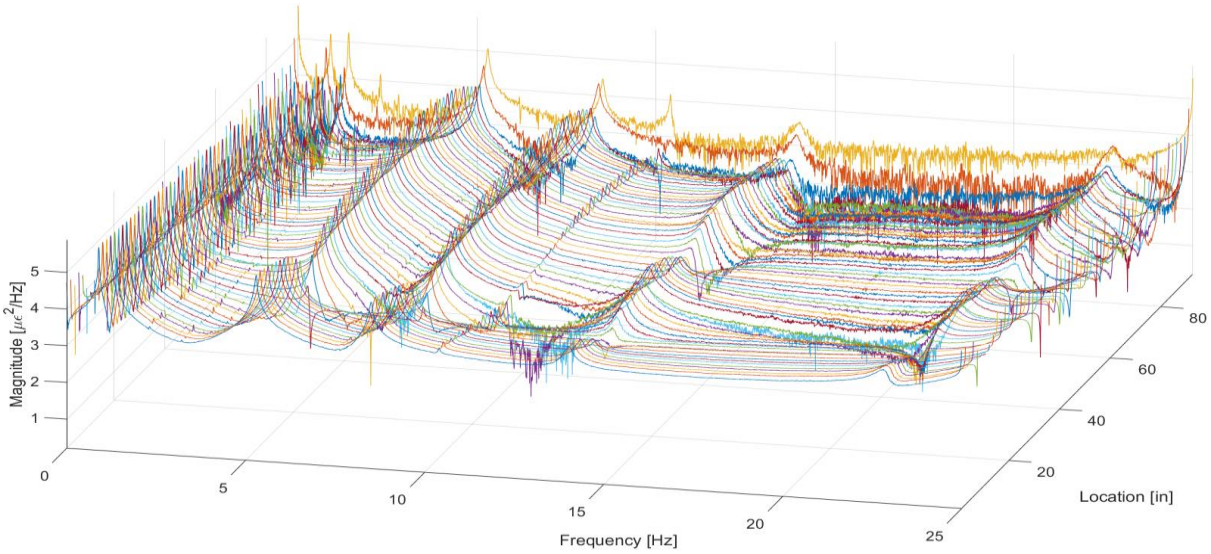

Figure 7-18: PSD of each of the 59 strain sensors as a function of frequency and location. In the current plot sensor five is the reference sensors.

It is observed that the PSD of the tip most two sensors have higher responses than the neighboring sensors. This increased response is believed to be a combination of two effects, the first being the localized strain associated with the tip airfoil mass. Secondarily, at the end of the fiber is a crude termination inflicted to end the transmission of light. This termination tends to produce localized reflections in the data impacting the sensors nearest the end of the optical fiber. Under the current algorithm, sensors not performing to acceptable standards can be excluded from the batch stacking so as to not corrupt the updating. To provide a more clear representation of a quality measurement used for the algorithm's input, the PSD of sensor two relative to sensor five was isolated from the three-dimensional plot and is shown below in Figure 7-19. In addition to the magnitude of the PSD, the coherence between the signals and the real and imaginary components of the PSD are also plotted.

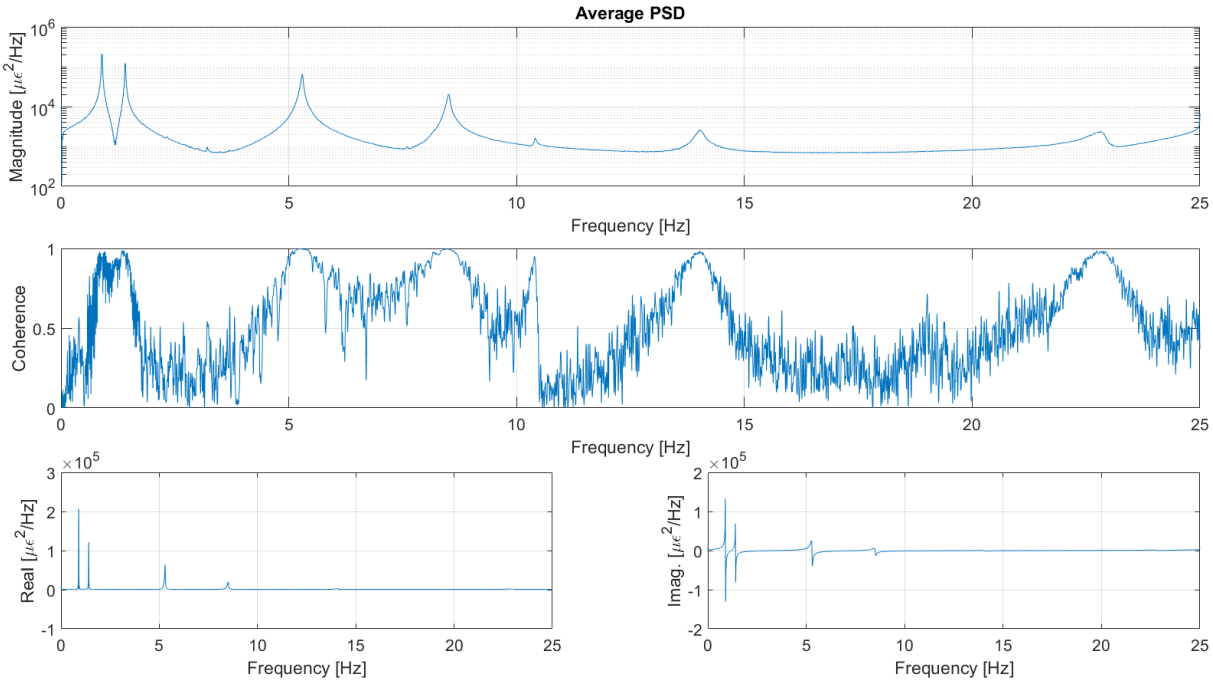

Figure 7-19: PSD of sensor two relative to sensor five, averaged over the five impacts in the complex domain. The upper plot shows the magnitude of the PSD whereas the middle plot gives the coherence between the two signals and the lower the real and imaginary portions of the PSD.

The PSD given in Figure 7-19 along with the corresponding coherence are an example of the fundamental inputs to the SHM algorithm. With the healthy beam's experimental PSD determined, a refined healthy FEM correlation was performed. The process for further correlating the healthy model as well as the methods used to study the damaged beam are discussed in the following sections.

7.4.2 PSD Model Correlation of the Baseline (Undamaged) System

In keeping with the analytical work done in Chapter 5, as well as allowing for computations to be completed in a reasonable amount of time, the experimental work was limited to discretizing the beam into 18 elements. This entails down selecting the optical sensors used in the analysis to match nodes of the Timoshenko beam model allowing for direct comparison between the modeled and measured PSD. The most straightforward means to perform the discretization was to place a node collocated with each of the three airfoil masses and use six elements in each of the regions between masses. The locations of the experimental strain measurements as well as the nodes chosen to define the eighteen elements in the beam's FEM are given in Figure 7-20. As a result of this down selection of measurement points, the subsequently referenced strain locations, and corresponding PSD, will be renumbered from those previously referenced for all 59 strain sensors. For example, reference to sensor one henceforward will correspond to the location along the beam's length approximately 6 inches from the clamped boundary, sensor two 12 inches and so forth. Each of the 18 red asterisks in Figure 7-20 correspond to both a sensor location and FEM node in all subsequent analysis and discussion.

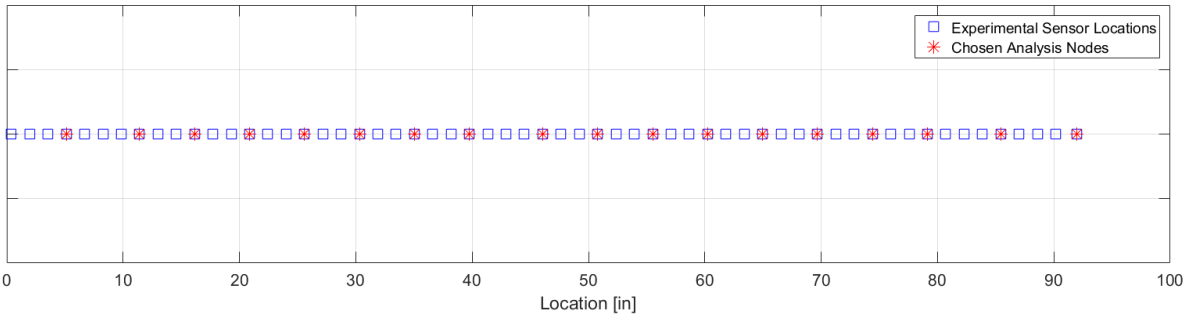

Figure 7-20: Locations of the experimental strain sensors overlaid with the chosen node/sensor locations defining the analysis elements.

While the model had been previously correlated to match both the static and dynamic performance of the beam it was important to provide a final correlation and determine the beam properties of each individual element. During the initial correlation it was assumed that all of the properties of the beam were uniform in all elements and the modeled response was matched to the natural frequencies and static strains of the beam. In the refined correlation efforts, the healthy strain PSD was used to tune the model such that the individual element properties varied. This variation of properties along the beam's span is caused by manufacturing imperfections and yields the best possible match between the undamaged model and measured PSD responses.

Since manufacturing imperfections and variations will certainly be part of not only each individual beam but also differing beams which are nominally identical, this final correlation is a natural step in the algorithm deployment strategy. In order to perform the refined correlation of the model, the SHM algorithm was run using the previously developed healthy beam model and measured PSD data sets as inputs. The PSD of the modeled and measured healthy beam responses for the auto-PSD of sensor one and cross-PSD of sensor two relative to one are shown in Figure 7-21, prior to PSD based correlation.

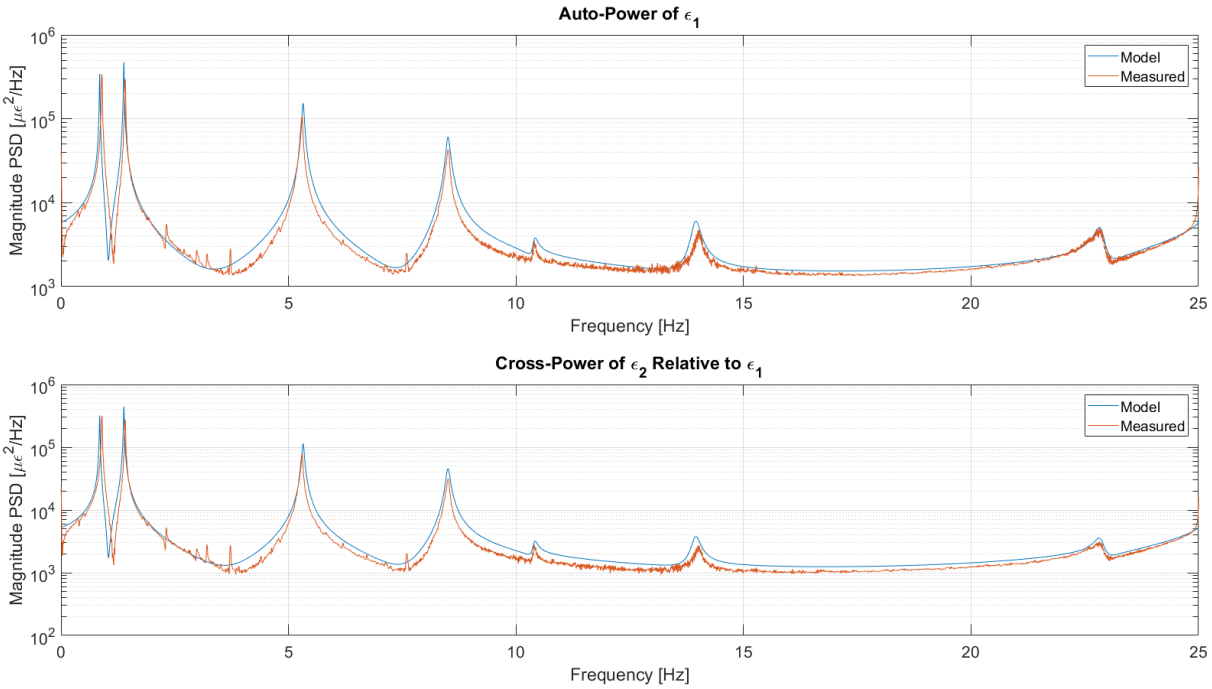

Figure 7-21: Overlay of the modeled and measured healthy PSD responses prior to PSD based model correlation.

In Figure 7-21 it is seen that there is generally good agreement between the modeled and measured responses. The reader is reminded however that the resolution of detectable damage is limited by the irreducible model error and as such it is important to perform this advanced correlation. The algorithm was utilized to correlate the analytical model to the experimental data obtained on the baseline (undamaged) beam by allowing variation of the beam's bending stiffness in each plane on an element-by-element basis. The SHM algorithm was run until convergence yielding a set of update scale factors for each of the possible 36 update parameters (bending stiffness, *EI*, in each of the two planes for each of the eighteen elements in accordance with the work presented in Chapter 5).

The resulting update scale factors for each of the eighteen elements are plotted in Figure 7-22. The reader is reminded that an update parameter value of one corresponds to an exact match

to the properties given in Table 5-1 whereas any value differing from one must be multiplied by the baseline property to obtain the engineering parameter of interest.

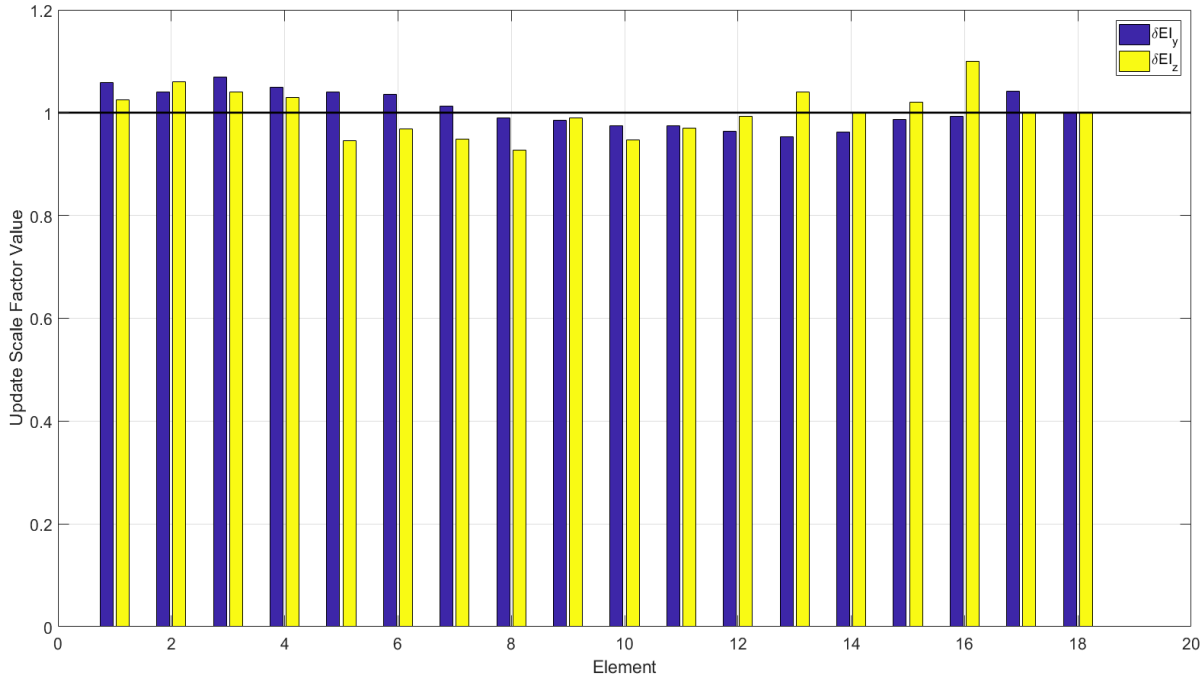

Figure 7-22: Bar plot of update parameter scale factors showing the converged baseline scale factors for each of the 36 update parameters.

Correlation of the original undamaged model via the algorithm lead to a unique set of properties for each element in the model as shown in Figure 7-22. All of the converged undamaged scale factors were found to be within seven percent of the baseline model providing further confidence in the baseline model as well as the correlated parameter set. Seven percent variation is well within the reasonable margin which would be expected based on the inherent material and manufacturing deviations discussed in previous sections and noted by the micrographs in Figure 7-3. Using the properties given in Figure 7-22, the FEM of the beam was generated in MATLAB and a comparison between the modeled and measured response of the healthy beam is shown post-correlation in Figure 7-23.

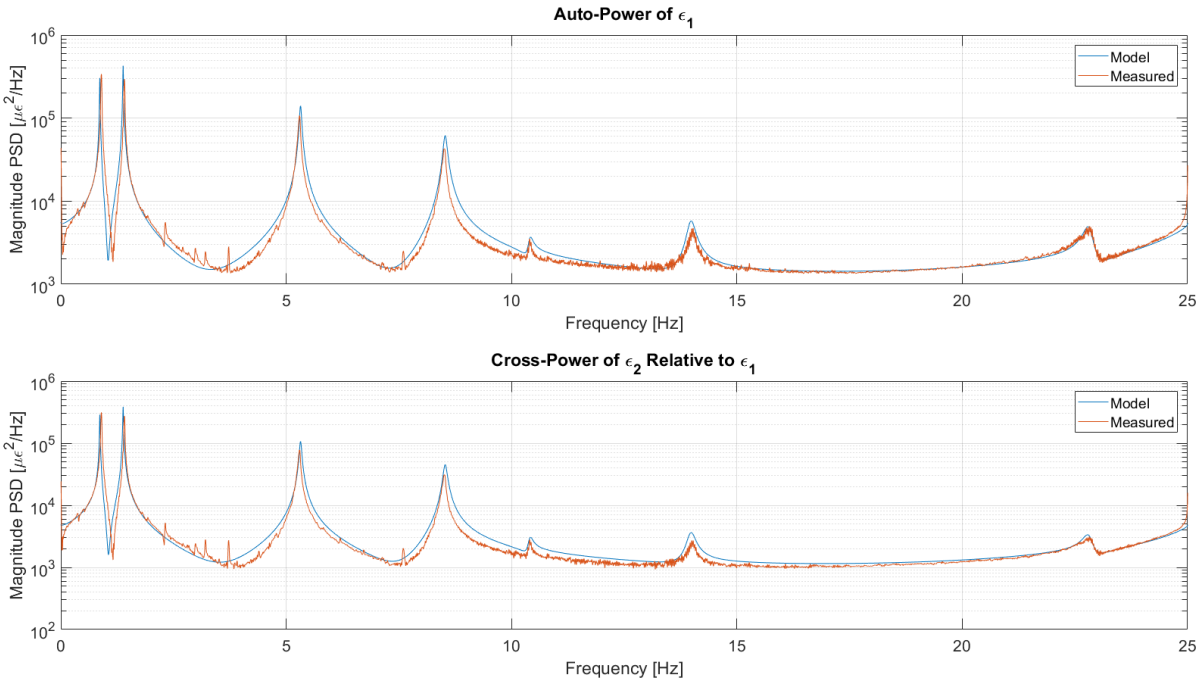

Figure 7-23: Correlated model PSD response of the healthy beam (blue) overlaid with the experimental data (red). The correlation was done using the information from reference DOF one.

The inclusion of the model updating step using the undamaged system measurements has increased the quality of the undamaged model. This step is recommended for each structure being monitored, even if nominally identical, as the typical variations from structure to structure will limit the severity of damage the algorithm is capable of detecting. In order to further refine the correlated baseline (healthy) model, the analysis was rerun using the PSD associated with using DOF two through 17 as reference DOF. The inclusion of this step both ensures the converged parameter set obtained using reference DOF one was universally valid, but also provides a statistical quantification of the parameters and a further refinement of the model. Sensor 18 is located at the end of the optical fiber which caused it to suffer from degraded sensing due to termination of the fiber. As a result, sensor 18 was not utilized as a reference sensor for the duration of the experimental work presented in this dissertation.

For the remaining 16 quality reference sensors, the analysis was repeated using each as the reference DOF. The result was a set of 17 of each of the update scale factors allowing for the mean, standard deviation, and ultimately 95% confidence interval of each of the 36 parameters to be calculated. The update scale factors presented in Figure 7-22 were supplemented with the information from the analysis results of the remaining reference DOF. The resulting mean update scale factor values and their associated 95% confidence intervals are presented in Figure 7-24 below. It is important to note that the update factors given in Figure 7-24 have been multiplied by the reference factors given in Figure 7-22 to yield the true update scale factors which correlate the baseline model.

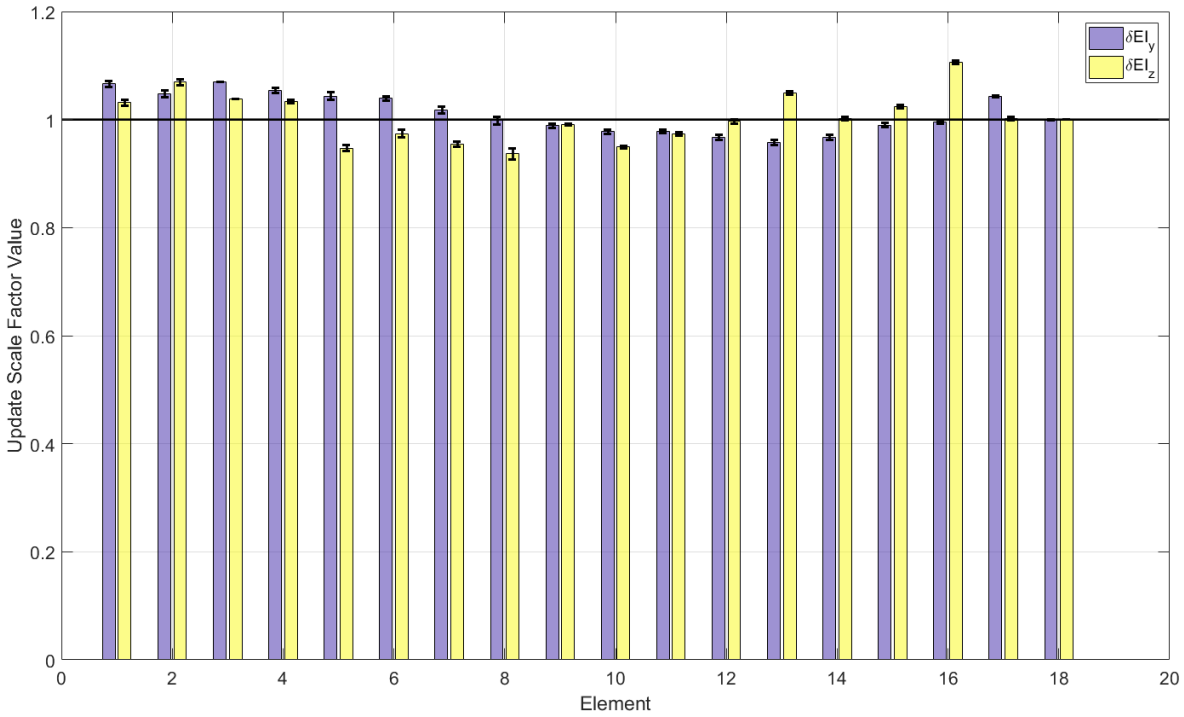

Figure 7-24: Bar plot of the mean update parameter scale factors showing the converged baseline scale factors for each of the 36 update parameters as well as their 95% confidence intervals.

The use of the increased number of references DOF provided a level of assurance in the converged system parameters and in turn the developed baseline model. The engineering

parameters associated with the mean update scale factors are given in Table 7-7 at the end of the chapter and are used as the baseline (healthy) values henceforth. The updated model associated with the mean scale factor values can be seen in Figure 7-25. Comparing Figure 7-23 with Figure 7-25 it is observed that incorporation of information from all of the available reference DOF, represented by the mean set of update scale factors, lead to a decrease in the modeling error. Incorporation of a large number of reference DOF to build a statistical basis for the update scale factors is a novel contribution of the current method.

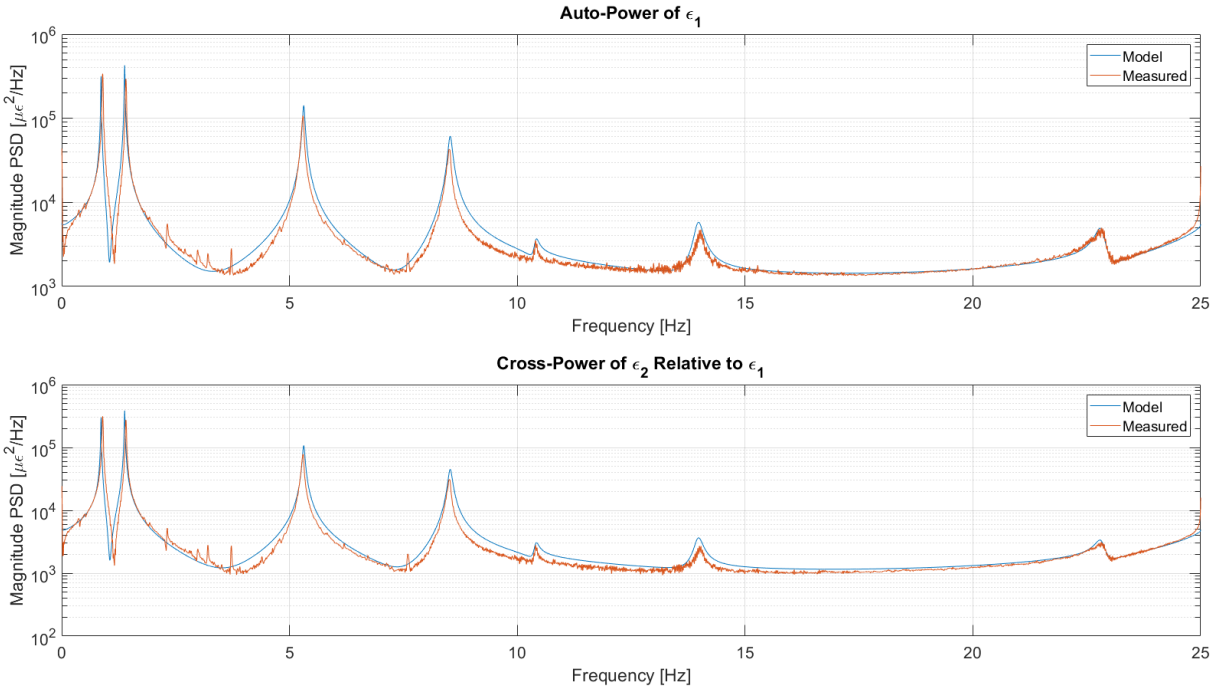

Figure 7-25: Refined correlated model PSD response of the healthy beam (blue) obtained via the mean scale factor values overlaid with the experimental data (red). The correlation was done using the information from all 17 quality reference DOF.

7.4.3 Damaged System Description

In order to test the algorithm's ability to detect damage of varying levels three damage cases were studied. The first damage case was designed to simulate a crack acting in a single spanwise location around the corners of the beam. The second damage location was chosen at

another spanwise location and was designed to simulate a large delamination to the composite beam. The third damage scenario studied was a combination of cases one and two. Figure 7-26 provides an image of the beam with the relative locations of damage cases one and two.

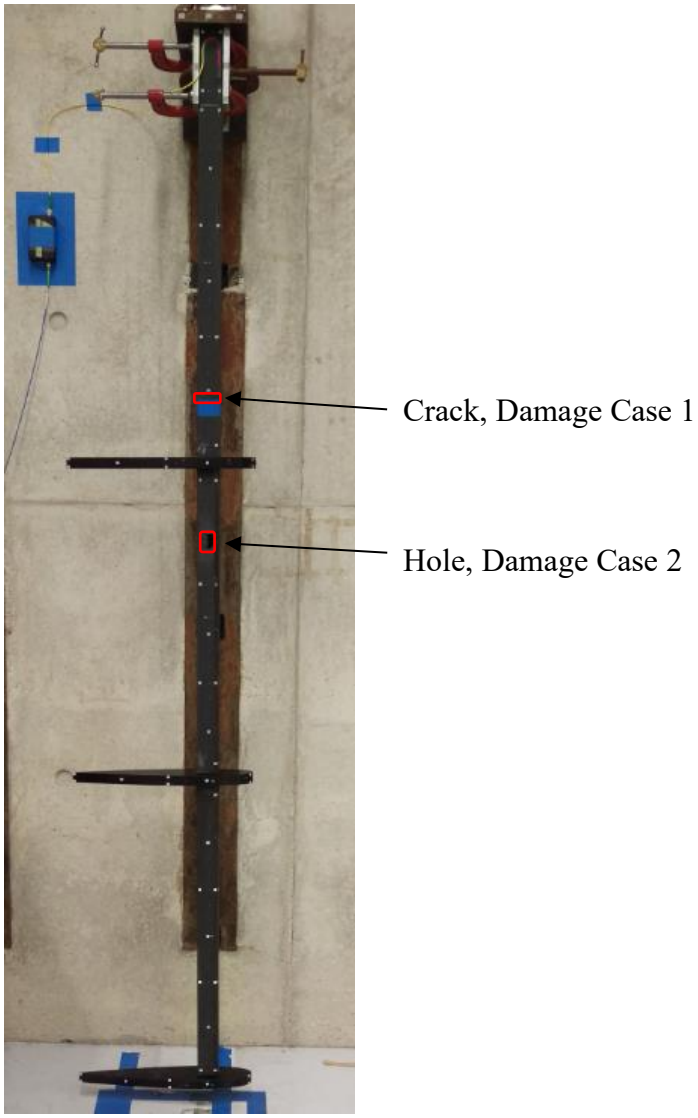

Figure 7-26: Relative locations of damage case 1 and damage case 2.

Damage case one was inflicted by cutting away a pair of corner sections on the beam using a razor saw at a location 25 inches away from the clamped end of the beam. The cuts were done on opposite corners of the beam, in effect removing an L-shaped portion of material on two

corners, leaving an L-shaped portion of material on the other two. For the two corners having material removed, the material comprising the radii of two corners of the beam as well as ½ the length of each side was cut. Figure 7-27 provides a schematic view of damage case one as well as images of the cuts on the beam as tested.

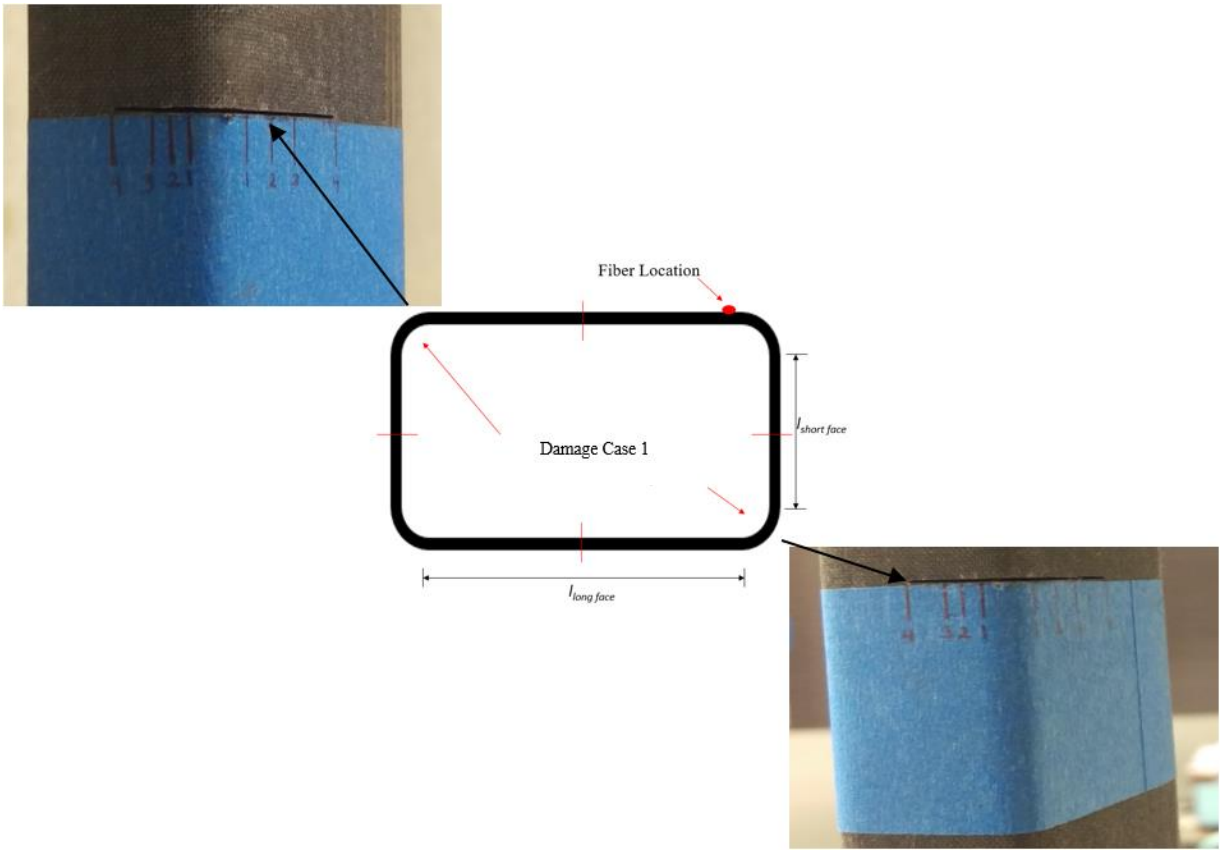

Figure 7-27: (Center) Schematic representation of the cuts corresponding to damage case one. (Top and Bottom) Actual cuts in the beam as tested for damage case one.

Damage case one was chosen to validate the algorithm on realistic sized damage that would be difficult to detect with visual inspection on large scale structures. Through a series of finite element studies, it was found that using beam elements to model small damage features required modal information outside the range of the current OFDR sensing technology. As the scanning

speed of the OFDR systems increase, and higher frequency spectrum information becomes available, the level of damage capable of being detected will decrease.

Damage case two was a pair of holes designed to simulate delamination acting over the long face of the beam, between a pair of adjacent strain sensors, centered 37.5 inches away from the clamped end of the beam. Although the hole clearly causes a reduction in mass, in addition to the reduction in stiffness a delamination would cause, from a system modal response perspective the change in mass is negligible largely due to the added airfoil masses. The holes representing damage case two are elliptical in shape to avoid stress concentrations and are symmetric (through both wide faces) to avoid an unsymmetrical response. Each hole, as shown in Figure 7-28, is 1.5 inches long and 1 inch wide.

Figure 7-28: Holes cut into the beam to simulate a catastrophic delamination 37.5 inches from the beam's fixed end, as studied in damage case two.

At each level of damage, a set of impulse excitations were performed to generate the damaged measurement PSD sets required for the SHM algorithm. For the strain data sets, the upper airfoil mass was struck with an industrial hammer to excite the testbed. The optical strain response was monitored for one-minute periods for each excitation cycle where five excitations were performed at each damage level to allow for complex averaging of the response spectra. Using the PSD, it was important that averaging was done to account not only for possible changes in structural behavior but also for unaccounted for changes in input force. In the current investigation using a manual industrial hammer provided such variation in the input force. In flight excitation conditions it would be advantageous to take hundreds of averages to account for all the possible variations. Figure 7-29 provides a comparison between the measured undamaged PSD and the resulting PSD for damage cases one and two over the frequency range of interest (0-25Hz).

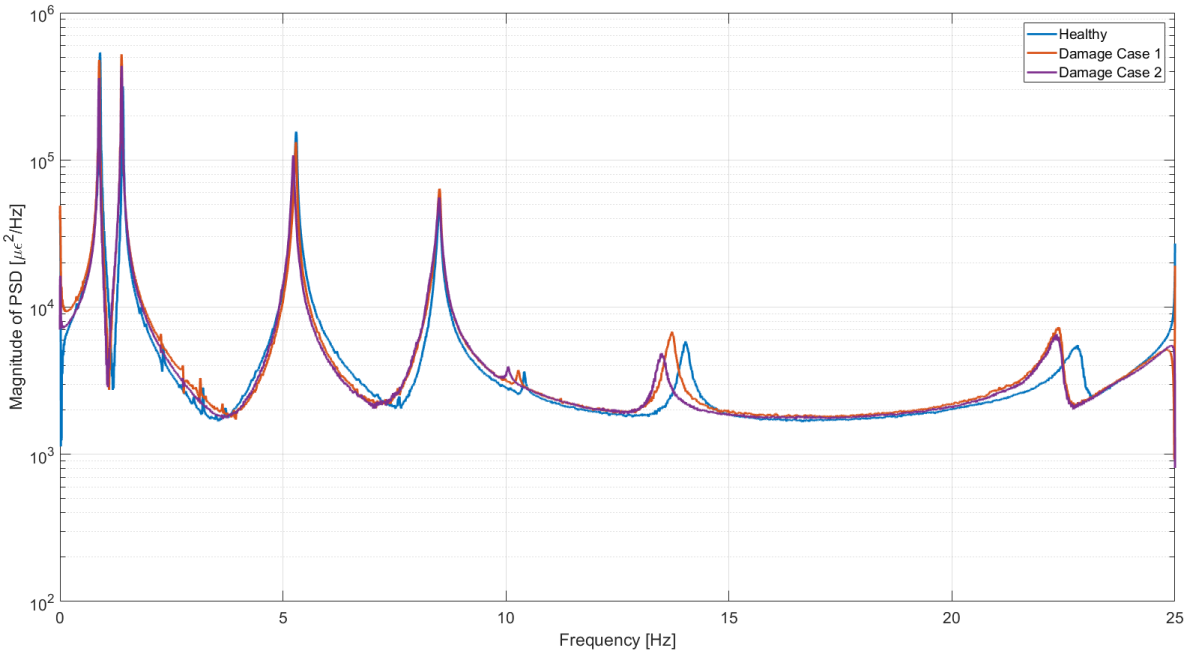

Figure 7-29: Comparison of the measured strain PSD for the undamaged (Healthy) and each of the damage cases.

For damage case one, the damage was found to primarily impact the portion of the PSD corresponding to the third bending mode in each plane, as shown in Figure 7-29. Damage case two however only slightly shifted the second bending mode in the soft-bending plane in addition to further shifting the third mode in the soft-bending plane from the damage case one levels. Note that damage case two also significantly altered the first torsion mode of the beam however the low sensitivity of the axial fiber to torsional (shear) strain made updating of the torsion properties unobtainable. Incorporation of supplemental strain information in multiple directions at a single point (i.e. an optical strain rosette) would provide ample sensitivity to torsional strain for such updating to be performed. The following subsections discuss the details of the damage identification performed on damage cases one and two.

7.4.4 Experimental Damage Identification – Damage Case One

Using the measured strain PSD of the damaged testbed, in conjunction with the correlated model PSD, damage identification was performed using the developed SHM algorithm. This identification served to both experimentally validate the developed method and support the conclusions reached during analytical implementation. The first step in implementation of the algorithm was to identify the frequency lines of interest on which the algorithm optimized the update scale factors. The damage was found to primarily impact the PSD in the vicinity of the third bending mode in each plane with minor effects on the PSD surrounding the second mode. As such, it was desirable to concentrate the update frequency lines about these regions of the PSD. Furthermore, the decreased magnitude of the response of the third bending modes made it such that an increased number of lines were used to increase the sensitivity in these regions, maximizing the distribution of information available to the algorithm.

Using the correlated model PSD previously developed, in conjunction with the coherence, and PSD of the damaged measurements, 44 frequency lines were identified to use in the damage identification. The initial frequency line set as well as the correlated undamaged model PSD and damaged measurement PSD are given in Figure 7-30. Using the PSD information at these lines as the fundamental input information for the algorithm to operate on, updating was performed on the 18 elements, containing 36 update scale factors.

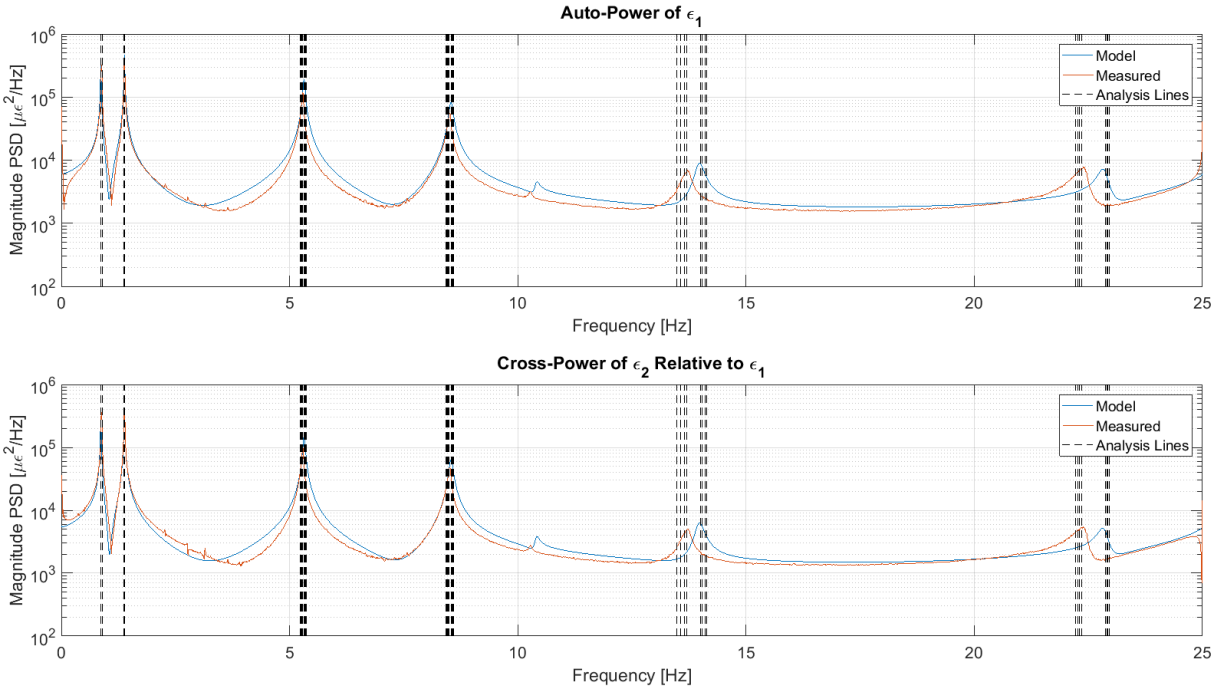

Figure 7-30: Comparison of the strain PSD for the correlated model PSD and damage case one PSD as well as the frequency lines chosen for the analysis.

Through trial and error, it was found that using a maximum step size of 0.025 produced the most stable solution however at the cost of a large number of iterations. The SHM updating routine converged to the final solution in 263 iterations. Figure 7-31 provides the update scale factors returned by the analysis in the form of a bar chart. The model of the beam above the chart in Figure 7-31 provides a reminder to the reader of the layout of the 18 element beam model, containing the

boundary condition at the root as well as the locations of the damage in the beam and the airfoil masses. The reader is further reminded that the updating scheme yields a set of normalized update scale factors which must be multiplied by the correlated model parameters to provide the engineering parameters of the beam. As such, a horizontal black line is included in the figure to represent the baseline damage scale factors at their initial values of one.

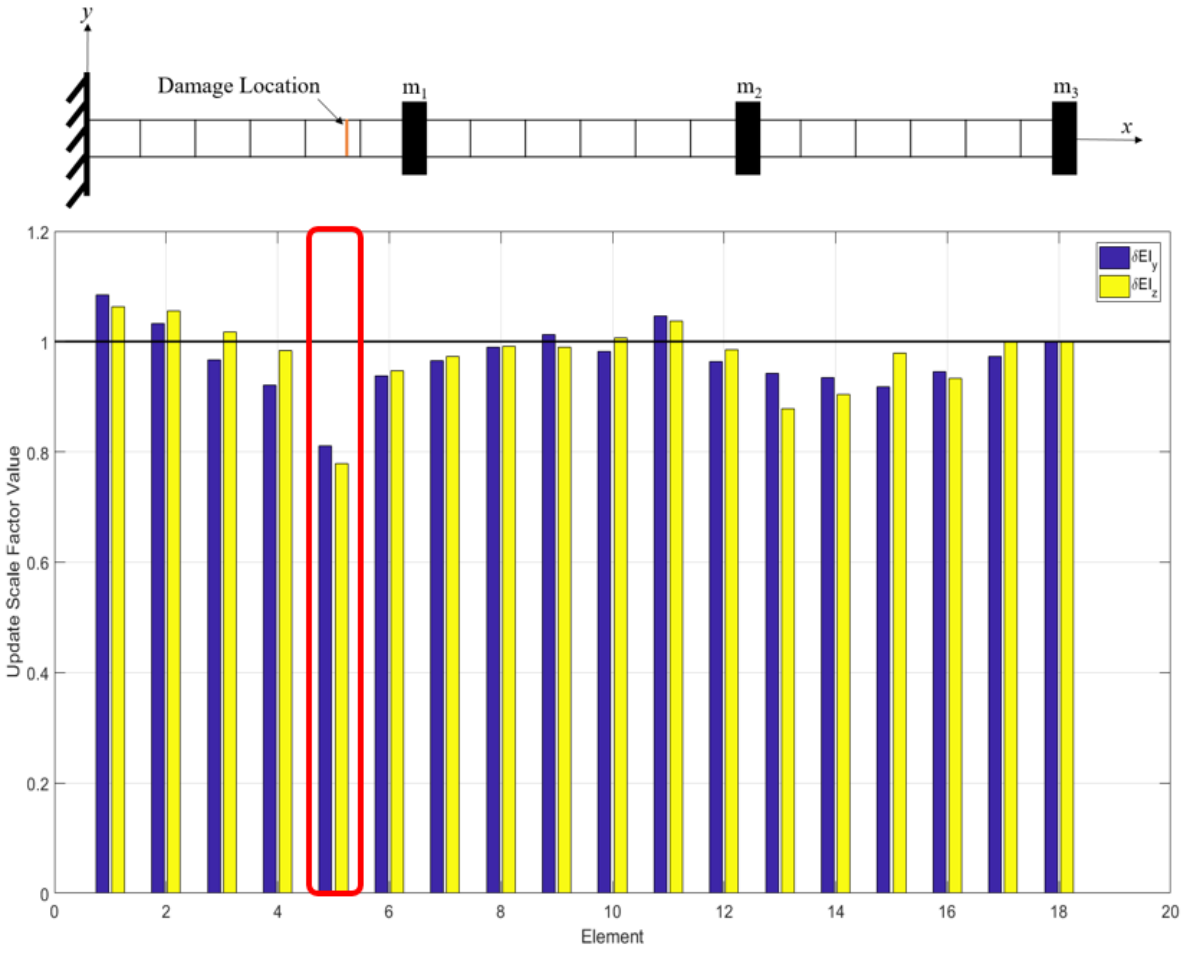

Figure 7-31: Bar plot of update parameter scale factors showing the converged damage scale factors of damage case one for each of the 36 update parameters.

Using the converged damage scale factors from reference DOF one, the updated correlated model was computed and compared to the measured damaged PSD to verify the quality of the

solution. A plot of the updated modeled and measured PSD of the damaged system is given in Figure 7-32. Visually it is apparent the solution scale factors identified by the algorithm yielded a PSD which closely matched the PSD of the measured response. While the algorithm result suggests damage was present in element five, using only a single reference DOF does not allow for any statistical assessment of the solution quality. In order to provide such an assessment, each of the remaining DOF were used as reference DOF to obtain a set of update parameters and provide a statistical estimation of the range of update parameter values.

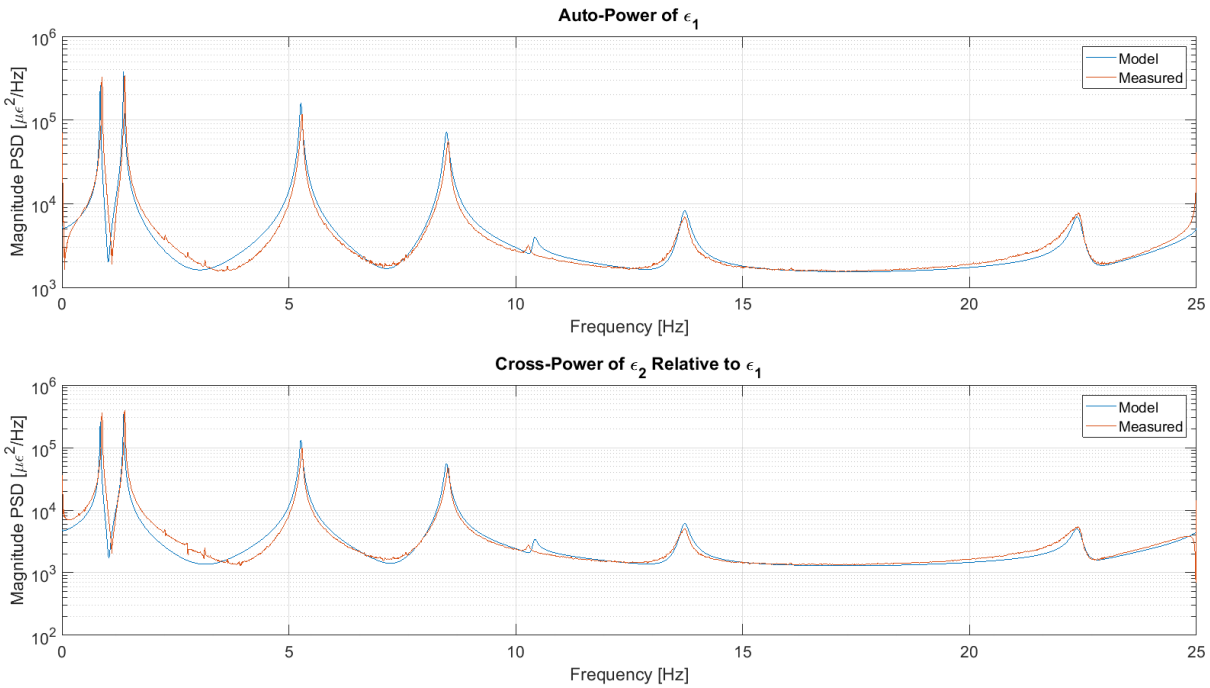

Figure 7-32: Updated model PSD response of damage case one (blue) overlaid with the experimental data from damage case one (red).

Starting from the converged update scale factors given in Figure 7-31, the analysis was repeated using each of the remaining DOF as the reference. In each case, the algorithm was allowed to run for a maximum of 50 iterations. Fifty iterations was chosen as the maximum to increase computational efficiency as it was empirically noted that reference DOF that produced a converged

solution tended to do so within 25 iterations. In the event that a particular reference DOF did not obtain convergence within the 50 iterations the iteration which yielded the lowest value of the cost function was used to represent the associated damage scale factors for that reference DOF. The analysis was run using 44 analysis lines, where the frequency lines associated with the measurement set was the same as those presented in Figure 7-30 and the lines corresponding to the model were updated to reflect the same relative amplitude to the respective PSD peaks as those given in Figure 7-30, shifted in frequency to account for the updated model produced by the initial update.

Once a set of damage scale factors was determined for each of the reference DOF, the mean and standard deviation of each of the 36 parameters were calculated (each parameter had 17 possible values from each of the reference DOF update runs which were averaged to produce the mean update scale factor value). Assuming a normal distribution of each of the update scale factors, the 95% confidence intervals of each of the update scale factors were calculated. Using the confidence interval associated with each parameter it is possible to make statistical conclusions as to whether or not a given element may contain damage. As such, using multiple reference DOF aids in reducing false positive detection events under the developed method.

The bar chart presented in Figure 7-31 was updated in Figure 7-33 to represent the mean value for each of the 36 update scale factors. Also shown in Figure 7-33 are the 95% confidence intervals associated with each of the parameters. The difference in the converged model PSD shown after the initial parameter update, as shown in Figure 7-32, is visually indistinguishable when repeated using the refined parameter estimates given in Figure 7-33 and as such has been omitted. Repeating the analysis over all 17 quality reference DOF provides assurance that the

original parameter estimates represent a minimum cost function value, as shown by the small 95% confidence intervals presented in Figure 7-33.

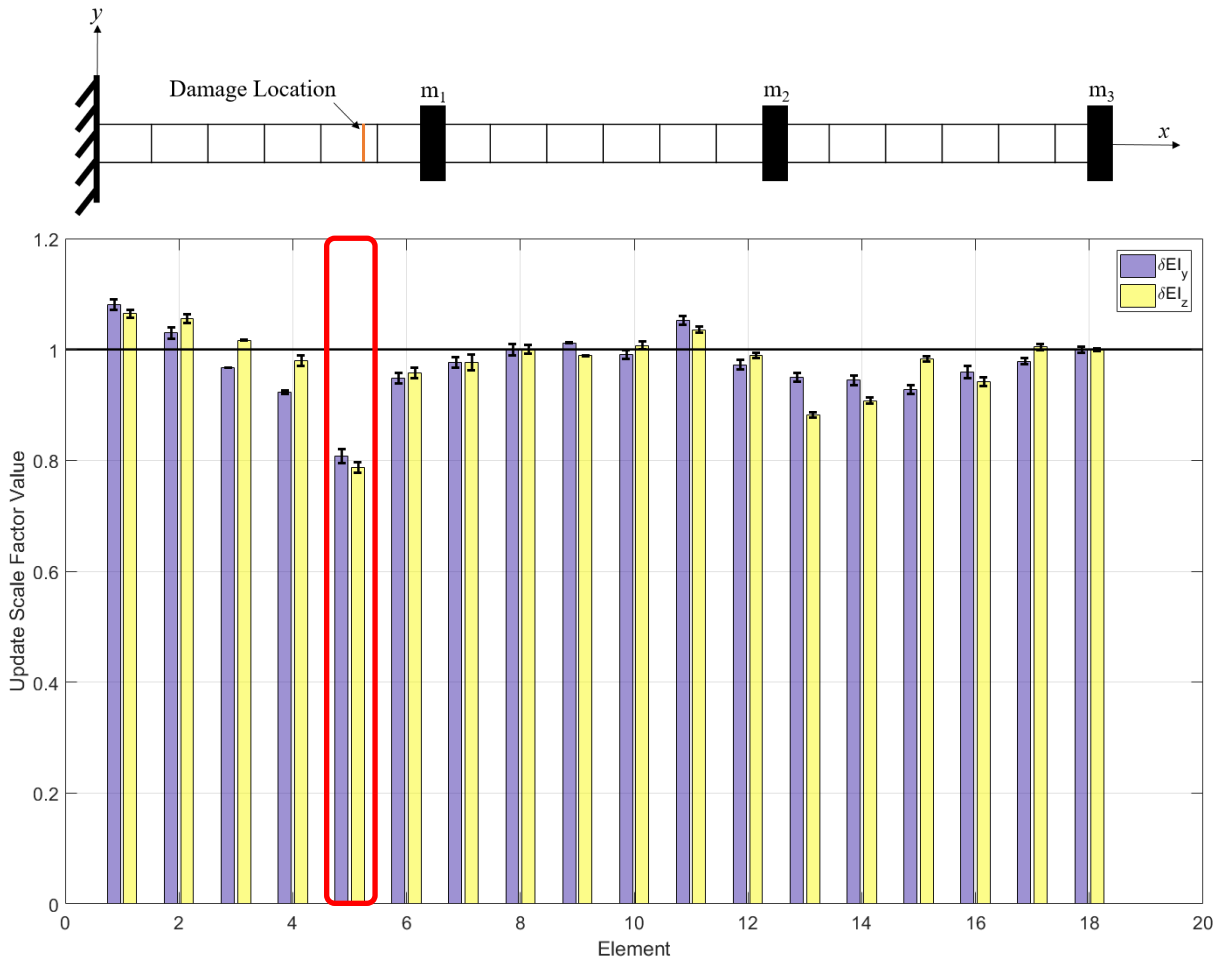

Figure 7-33: Bar plot of mean update parameter scale factors and 95% confidence interval for each of the 36 update scale factors.

In order to examine the correlation between the updated model PSD and the damaged system measurement, the modeled and measured PSD of all 18 sensors relative to sensor one were plotted in a three-dimensional plot given in Figure 7-34. Examination of Figure 7-34 reveals an important function of the SHM algorithm; the converged update parameter set yields a global model of the structure which is accurate across all DOF. Thus, the parameter set identified by the

algorithm can be used to generate a correlated finite element model which ultimately allows for advanced damage studies and prognosis to be performed.

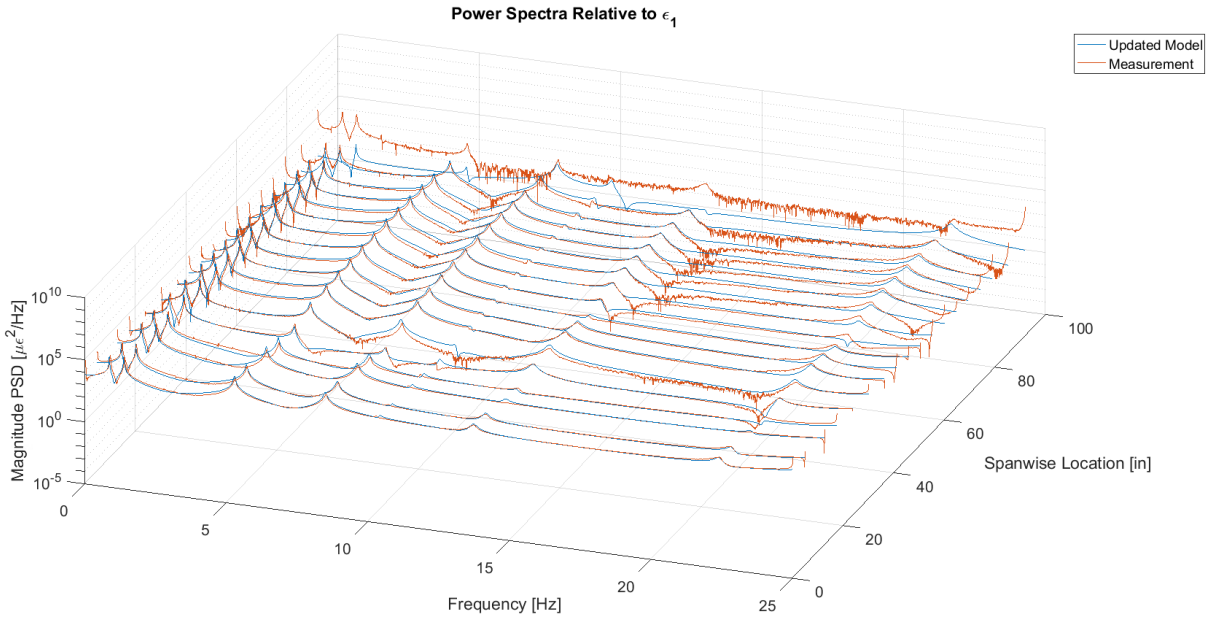

Figure 7-34: Correlated model PSD response of damage case one (blue) overlaid with the experimental data (red) across all 18 DOF for damage case one.

Returning to the results shown in Figure 7-33, the SHM algorithm output provided an indication of the presence of damage in element five but also the possibility of false-positive detection events, particularly in elements 4, 13, 14 and 16. While it is ultimately the responsibility of the analyst to determine an allowable threshold for false-positive events, the current results would make it difficult to distinguish between a single damage event in element five and a multiple damage location scenario. In the event of the single damage location, the presence of the lower stiffness values in the undamaged elements tends to underestimate the severity of damage in the damaged element. In order to differentiate between the case of multiple damage locations or a single damage location, the analysis was repeated with a decreased number of update parameters to increase the precision of the estimated update scale factors.

In the current study, any element containing a parameter which was reduced by more than five percent in the initial analysis was used for a refined damage study. This corresponds to elements 4, 5, 6, 13, 14, 15, and 16 being included in the refined analysis. Starting with the data presented in Figure 7-30, the analysis was repeated using the 14 update scale factors associated with the aforementioned seven elements, holding all other factors to their baseline converged values as given in Figure 7-24. Once again, sensor one was used as the reference DOF for the initial correlation. Once the initial correlation was performed those scale factors were used as the initial values for the subsequent 16 correlation runs. Averaging the update scale factors for the 17 reference DOF, a refined update parameter set was calculated as shown in Figure 7-35.

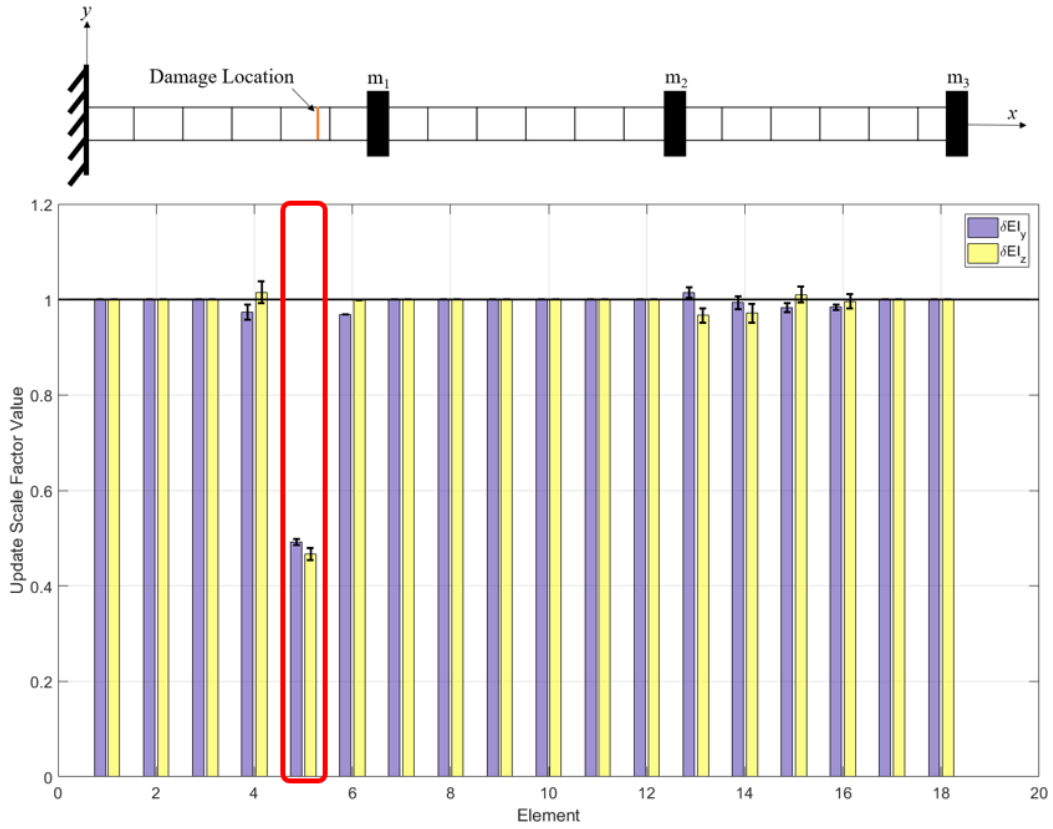

Figure 7-35: Bar plot of mean update parameter scale factors and 95% confidence intervals for each of the 14 update scale factors used in the refined estimate of damage case one. Note that although all 18 elements are shown, only the 7 shown with the confidence intervals were allowed to vary in the updating run.

Clearly the smaller update parameter set yielded a more accurate solution to the single damage location known to exist in element five. While a more refined estimate of the damage location and severity is desirable, in the practical case where information is not known beforehand great care must be taken to not ignore the possibility of smaller damage features present in multiple elements. Whether or not a refined damage estimate is calculated, the algorithm has shown the ability to detect the presence of the simulated crack and identify the location of highest likelihood in the initial updating. In-situ knowledge of the most likely location of a structural flaw would be of great value to operators and inspectors alike and a large step in the direction towards the desired condition-based maintenance.

With the algorithm's ability to experimentally detect the presence and location of damage demonstrated the question becomes how accurate of an estimate of the type and severity of the damage was produced under the current experimental setup. These questions are more difficult to answer however as analytically assessing the level of damage inflicted in the composite beam as a result of the cuts, expressed in terms of the bending stiffness in each plane alone, is not a straightforward task. The complex micromechanics associated with damage behavior in a composite beam are an area of research in and of itself. Inclusion of such features are beyond the scope of the current work and in particular the equivalent laminate material properties used to demonstrate the algorithm's capabilities.

As OFDR interrogation technologies continue to advance the frequency range capable of being sensed, and increased computational power allow for more sophisticated models, it is likely these micromechanics based damage models will be incorporated in the SHM model updating routine. Furthermore, it is envisioned a multi-scale FEM will be incorporated in which initial damage detection and localization may occur using a course model, such as demonstrated here.

Once a region of interest has been identified, a more refined model of the region may be implemented to get the best possible estimate of the type and severity of the damage to be used in prognosis.

Using the current beam model and state-of-the-art OFDR sensing system it was important to benchmark the performance of the algorithm relative to the resolution of damage being studied. In order to provide the best estimate of the effective update scale factors which characterize a single damage event in element five, an additional set of runs were conducted under which only the parameters associated with element five were allowed to vary. Starting with the same information given in Figure 7-30, an analysis was run using each of sensors one through 17 as the reference DOF yielding 17 independent estimates of the scale factors associated with the bending stiffness in each plane of element five. The resulting mean scale factors from the analysis are presented in Figure 7-36 along with the previous estimates obtained with the eighteen and seven element analyses. The scale factors obtained using a single update element (two parameters) are the best estimates of the true damage scale factors associated with the single damage event under consideration.

Comparing the damage scale factors calculated using a single damage element reflecting the true location of the damage to the estimates returned for the initial implementation yielded an error of 89.2 percent in the estimate of the damage scale factor associated with bending stiffness about the y-axis and 100.9 percent in the estimate of the damage scale factor associated with bending stiffness about the z-axis. As the solution space was reduced, the converged update scale factors approached their estimated true values (as given by the black dashed lines in Figure 7-36). Using the refined parameters associated with the seven-element update case these errors were reduced to 15.4 and 19.0 percent, respectively.

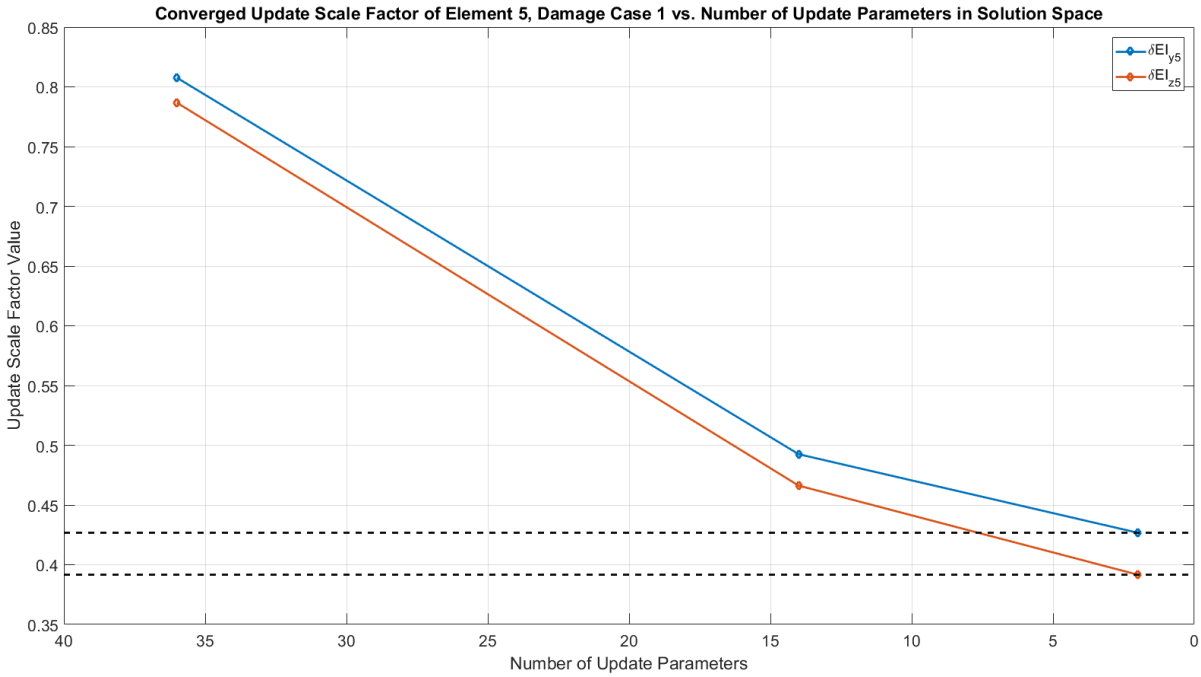

Figure 7-36: Plot of mean update parameter scale factors for each of the bending stiffness scale factors associated with element five for the 18, 7 and 1 update element case. The black dashed lines correspond to the estimated true damaged parameter values.

These parameter errors are largely attributed to irreducible model error caused by both the reduced frequency range (limited PSD range) and also the simplicity of the equivalent laminate properties used to model the beam's behavior. Additionally, all of the damage caused by the crack is forced to manifest itself into converged update scale factors in the form of changes in bending stiffness. In reality, the damage case being studied is far more complex and would require a more detailed model to capture these complexities. Further complicating the analysis are the large masses which were necessary to mimic the dynamic response of flexible aerospace structures (such as wings) and also bring a suitable number of modes into the sensing range of the current state of OFDR interrogators. The presence of the masses dominated the dynamic response of the beam, providing a true test of the algorithm's ability to extract the correct material properties.

7.4.5 Experimental Damage Identification – Damage Case Two

The goal of the algorithm is to continually monitor the structure and update the baseline model whenever a damage event occurs. To this end, damage case one can be thought of as a single damage event which was detected, quantified, and the model updated accordingly. If the operator continues to utilize the structure under observation it is possible additional damage events may occur, in this case damage case two. Using the converged damage case one model PSD as the new baseline, the damage identification process was repeated using the measurements associated with damage case two. The correlated baseline model PSD is thus plotted in Figure 7-37 along with the damage case two measurement set and 44 frequency lines chosen for the analysis.

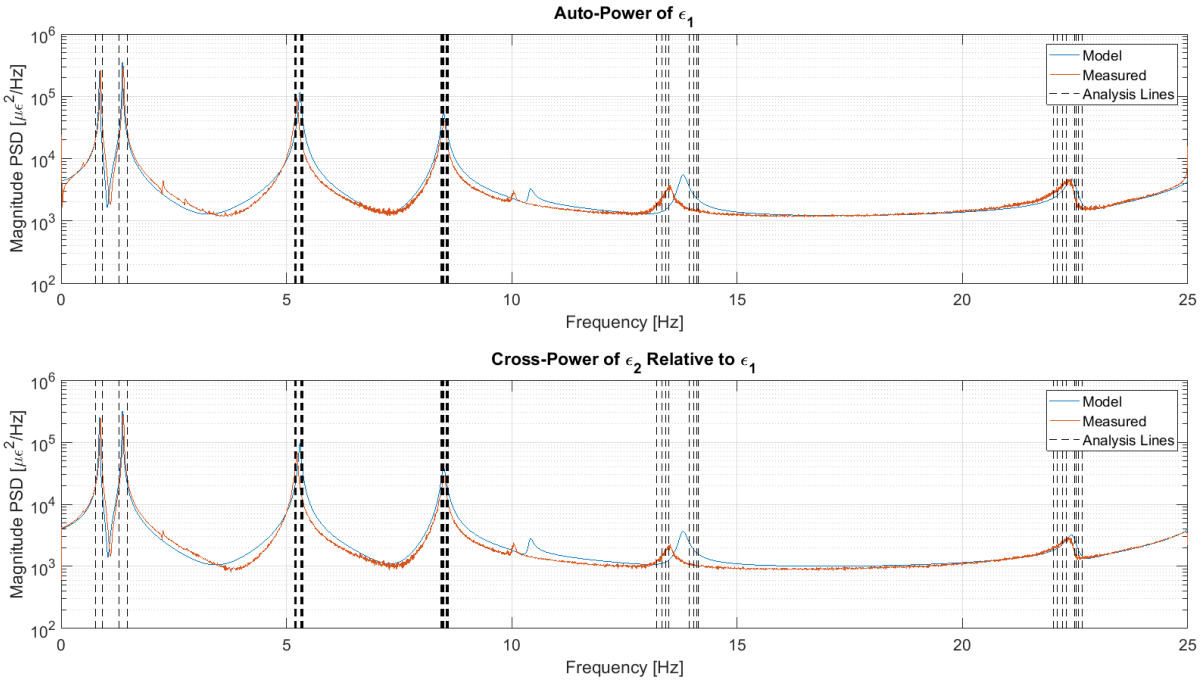

Figure 7-37: Comparison of the strain PSD for the correlated model PSD and damage case two PSD as well as the frequency lines chosen for the analysis.

Observation of Figure 7-37 yields the result that the damage inflicted in case two has caused very little change in the PSD peaks associated with bending in the stiff plane and the majority of the damage has manifested around the peaks related to the soft bending modes. This

effect is due to the majority of the material being removed on the face furthest from the soft bending axis which is nearly collocated with the neutral axis of the stiff bending plane.

In the same manner as that used for damage case one, the analysis was first run using DOF one as the reference. A set of converged damage scale factors were found for each of the 36 update parameters using DOF one as the reference. Using this converged set of damage scale factors as the initial parameter set for subsequent analysis, the damage identification algorithm was iteratively run for all 17-quality reference DOF. The mean values of the damage scale factors obtained by averaging each of the 36 parameters are given in Figure 7-38 along with the 95% confidence intervals.

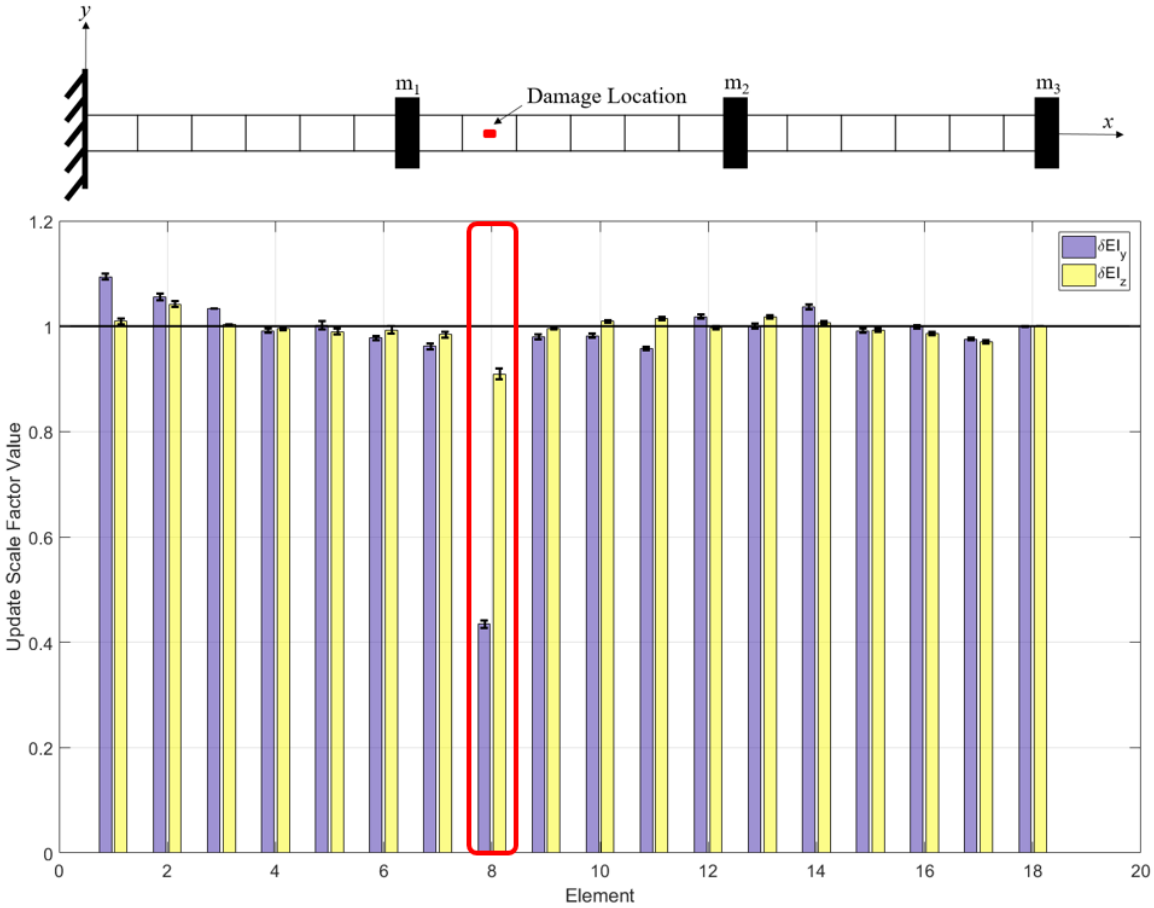

Figure 7-38: Bar plot of mean update parameter scale factors and 95% confidence intervals for each of the bending stiffness scale factors associated with damage case two.

Using the parameters given in Figure 7-38 the correlated model for damage case two was computed. A plot of the converged damage case two model is shown overlaid with the measurement PSD in Figure 7-39. It is observed that the modeled and measured PSD are in good agreement as desired, providing an assurance of the accuracy of the identified parameters. As was demonstrated using damage case one in the previous section, additional refinement runs may be conducted, as needed, in an effort to reduce the distribution of the update scale factors in elements believed to be free of damage and obtain a better estimate of the actual damage scenario.

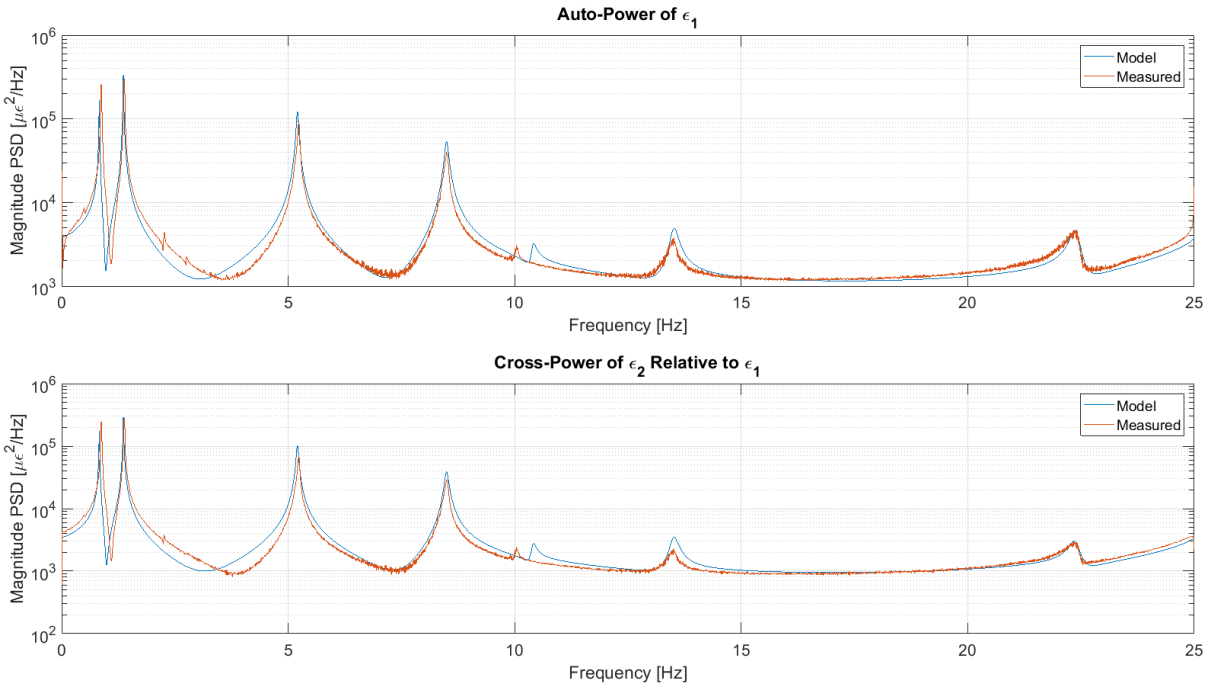

Figure 7-39: Comparison of the strain PSD for the correlated model PSD and damage case two PSD.

With the presence of damage correctly detected and localized the question again becomes how accurate is the severity estimate given by the current update parameter set. In order to provide the most accurate estimate of the "true" damage scale factors associated with element eight, the analysis was rerun starting with the same input information (as given in Figure 7-37) holding all parameters fixed with the exception of the two bending stiffness update scale factors associated

with element eight. Using this approach, the estimates of the true damage scale factors were found to be $\delta EI_{y,8} = 0.4784$ and $\delta EI_{z,8} = 0.9685$. While it is known these estimated true values contain the variation caused by both the damage event and the irreducible model error, it is the best estimate of the anticipated response under the current beam model framework. Comparing the converged values given in Figure 7-38 to the estimated true values yields an error of 9.2 percent in the estimate of the damage scale factor associated with bending stiffness about the y-axis and 6.1 percent in the estimate of the damage scale factor associated with bending stiffness about the z-axis for the initial parameter estimates. These estimates are far more accurate than the initial parameter estimates obtained for damage case one. It is believed some of the reduction in the error of the estimate can be attributed to the irreducible model error absorbed into the update parameter set associated with damage case one which was used as the baseline for damage case two. Furthermore, the use of the relatively simplistic FEM of the current test article limits the type of update scale factors such that complex damage modes are confined to impact only the bending stiffness. In practice, it is probable the effects the damage has on the orthotropic material properties, mass, damping, and more all play a role in the converged system error.

As was done for damage case one, the converged model parameters were used to generate a set of model PSD across all eighteen DOF. These model PSD were plotted with their experimental counterparts in Figure 7-40 to provide confidence in the global accuracy of the converged parameter set. All of the DOF are in good agreement with the exception of the tip location, which as previously discussed suffered from optical interference and as such was determined to be an inaccurate measurement.

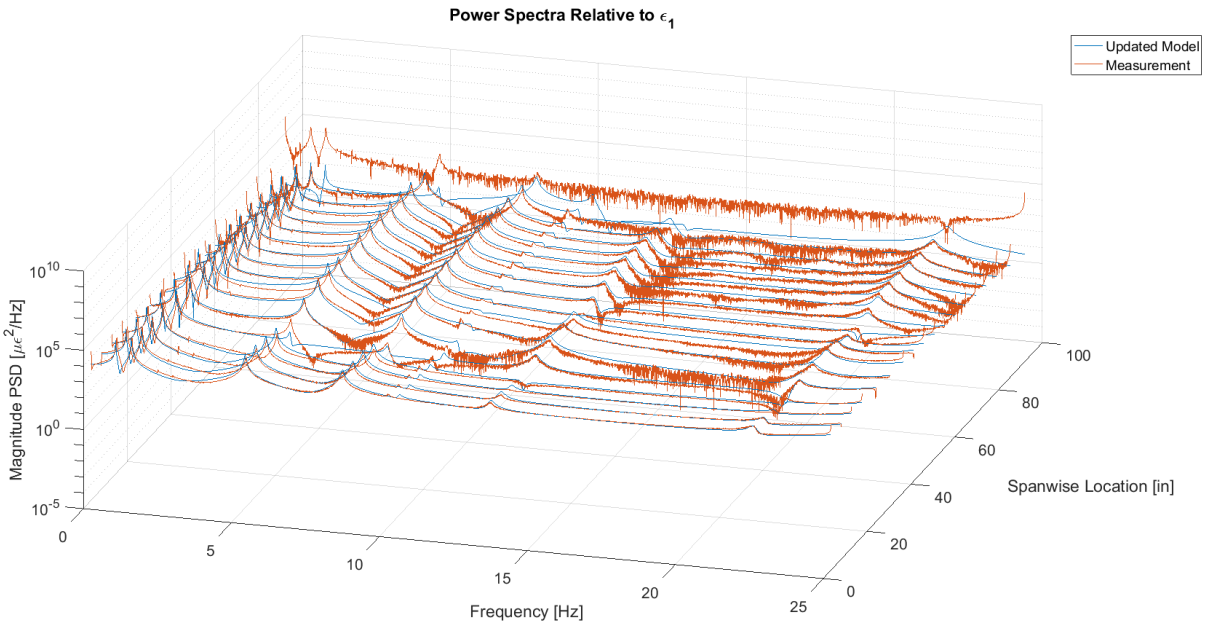

Figure 7-40: Correlated model PSD response of damage case two (blue) overlaid with the experimental data (red) across all 18 DOF for damage case two.

7.4.6 Experimental Damage Identification – Multiple Damage Sites

Through the previous two sections the ability of the algorithm to successfully detect and locate damage within a specific element has been presented in addition to providing an estimate of the type and severity of the damage. The predominant case in the SHM of aerospace structures would be for a single damage event to occur, be detected by the SHM system, and then determined to need repair or be safe to resume operation. If returned to operation, it is conceivable that an additional damage event could occur at another location and necessitate another SHM iteration, as was presented in the previous examples. It is also possible however that a single damage event causes damage in a number of elements, possibly in regions of the structure that are not adjacent to one another.

In order to demonstrate the algorithm's ability to detect multiple damage sites which have occurred since the time of the last model correlation both damage cases one and two were studied

simultaneously. In this case it was assumed that the correlated model presented in Figure 7-25 was the last known reference state prior to the measurement set associated with damage case two being taken (skipping the identification of damage case one as presented above). In this event, for successful identification to occur, the algorithm must simultaneously identify the damage scale factors associated with element five for damage case one and element eight associated with damage case two. A comparison between the correlated baseline (healthy) model and damage case two measured response (containing the damage associated with cases one and two) is given in Figure 7-41 along with the 44 frequency lines chosen for the analysis.

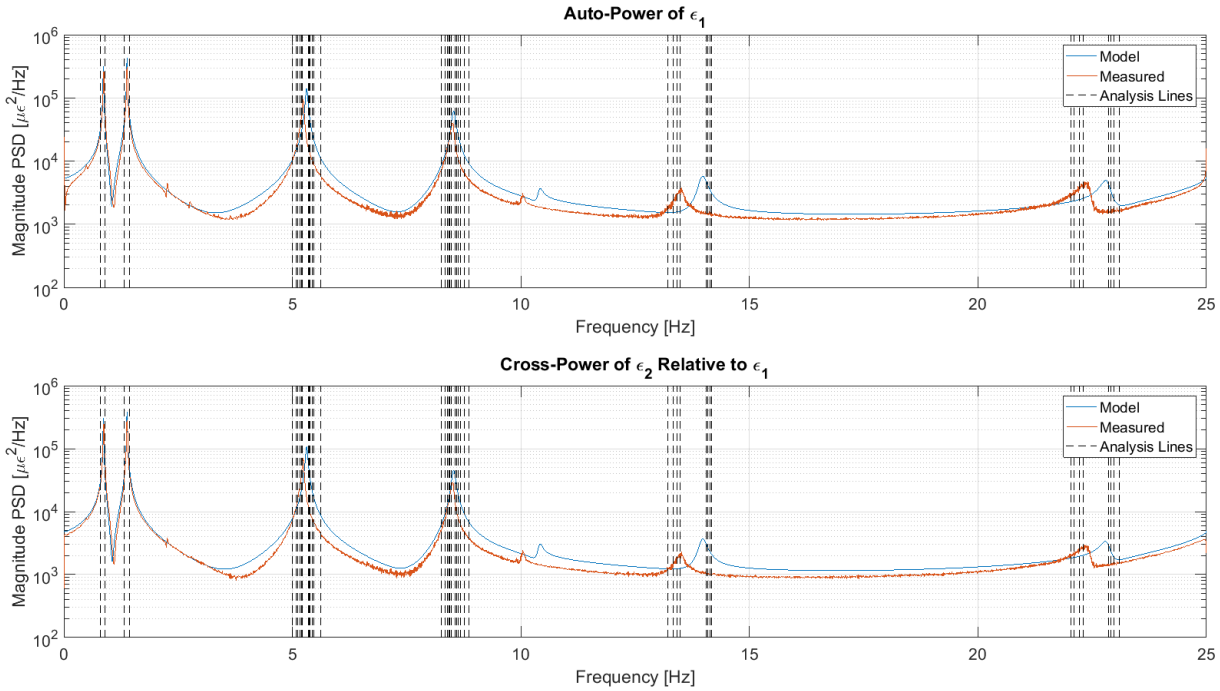

Figure 7-41: Comparison of the strain PSD for the baseline correlated model PSD and damage case two PSD. Note that the difference between modeled and measured PSD now contain the changes associated with both damage cases.

The same procedure outlined in the prior sections was repeated whereby DOF one was used as the reference in the initial damage identification run. Once a set of candidate parameters were returned, the analysis was repeated using these candidate parameters as the starting point for

each of the 17-quality reference DOF. The resulting refined damage parameters associated with the combined damage identification case are plotted in Figure 7-42 along with their respective 95% confidence intervals.

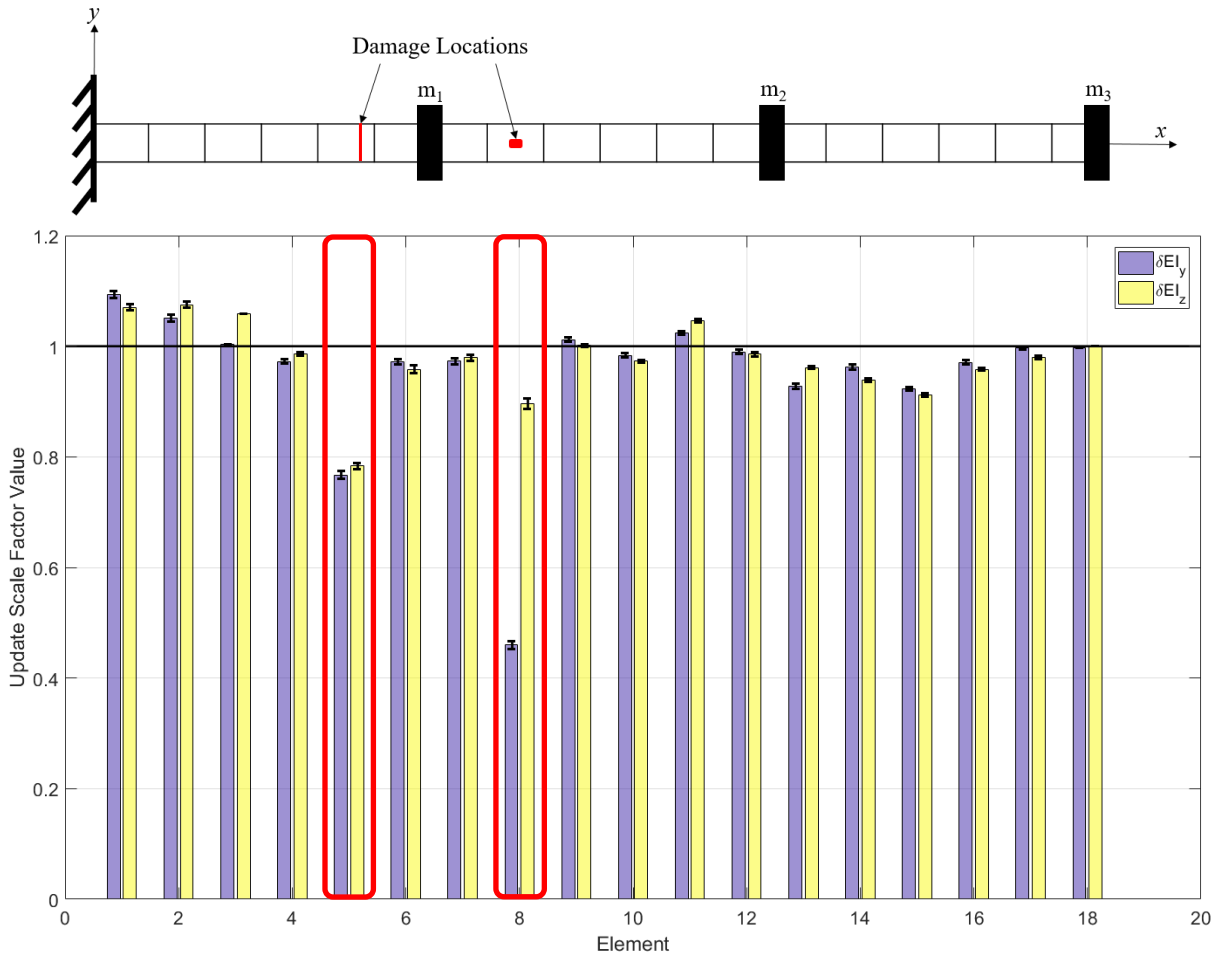

Figure 7-42: Bar plot of mean update parameter scale factors and 95% confidence intervals for each of the bending stiffness scale factors associated with the combined damage case.

Comparing the results from Figure 7-42 with those given in Figure 7-33 and Figure 7-38 yield the analysis was able to successfully identify both damage cases simultaneously, to approximately the same accuracy as each case individually. As was the case for damage case one, the combined damage detection results indicated a damage event in element five however the

magnitude is approximately half of the estimated true damage parameter values. Likewise, the damage level determined in element eight was found to be within ten percent of the estimated true damage parameter values found via damage case two. The average error in the undamaged parameters is also on the order of the undamaged errors found in damage cases one and two. These damaged parameter values can be seen as the values in the red boxes in Table 7-7 along with their undamaged counterparts.

Table 7-7: Converged engineering parameters of the 36 update parameters for the baseline (undamaged) testbed as well as the three damage scenarios studied. The red boxes indicate the parameters associated with the damaged elements in the respective cases.

	Healthy		Damage Case 1				Damage Case 2				Combined Damage			
Element	EI_y	EI_z	EI_y	Δ (%)	EI_z	Δ (%)	EI_y	Δ (%)	EI_z	Δ (%)	EI_y	Δ (%)	EI_z	Δ (%)
1	242.1	576.4	263.6	8.9	613.1	6.4	288.4	9.4	618.9	1.0	264.6	9.3	616.6	7.0
2	238.3	597.5	247.0	3.7	630.0	5.4	260.7	5.5	656.5	4.2	250.5	5.1	642.4	7.5
3	246.6	583.4	238.5	-3.3	593.1	1.7	246.4	3.3	594.8	0.3	247.3	0.3	617.8	5.9
4	239.9	579.6	223.3	-6.9	567.9	-2.0	221.4	-0.9	565.1	-0.5	233.2	-2.8	571.7	-1.4
5	239.5	527.2	193.5	-19.2	417.7	-20.8	193.9	0.2	413.6	-1.0	183.7	-23.3	413.0	-21.7
6	239.8	546.7	226.1	-5.7	521.1	-4.7	221.0	-2.2	517.3	-0.7	233.0	-2.8	523.9	-4.2
7	233.1	534.0	228.0	-2.2	521.0	-2.4	219.2	-3.8	512.7	-1.6	226.8	-2.7	522.8	-2.1
8	227.9	522.3	227.9	0.0	521.0	-0.2	99.0	-56.6	473.8	-9.1	104.7	-54.0	468.2	-10.4
9	227.0	555.6	229.9	1.3	549.8	-1.0	225.2	-2.0	547.4	-0.4	229.8	1.2	556.2	0.1
10	224.8	533.0	222.5	-1.0	536.4	0.6	218.5	-1.8	541.5	1.0	221.1	-1.7	518.6	-2.7
11	224.2	544.9	236.4	5.4	564.9	3.7	226.2	-4.3	573.1	1.5	229.6	2.4	569.8	4.6
12	222.3	559.3	215.8	-2.9	552.7	-1.2	219.7	1.8	551.2	-0.3	220.1	-1.0	551.2	-1.5
13	219.0	586.0	208.4	-4.8	518.6	-11.5	208.6	0.1	527.8	1.8	203.1	-7.2	563.3	-3.9
14	221.4	560.4	209.6	-5.3	509.5	-9.1	217.2	3.6	512.7	0.6	213.2	-3.7	525.9	-6.2
15	226.6	573.3	210.7	-7.0	563.8	-1.6	208.9	-0.9	559.4	-0.8	209.1	-7.7	522.6	-8.8
16	227.4	618.8	219.3	-3.6	583.6	-5.7	219.0	-0.1	575.4	-1.4	220.8	-2.9	592.9	-4.2
17	240.1	563.7	234.9	-2.2	564.4	0.1	229.1	-2.4	547.3	-3.0	239.3	-0.3	552.3	-2.0
18	230.4	562.0	230.3	-0.1	562.1	0.0	230.1	-0.1	562.0	0.0	229.8	-0.3	561.9	0.0

Note: Bending Stiffness values are given in units of ksi-in^4

Through the values of the undamaged parameters given in Table 7-7, it is observed that the threshold for false detection events is on the order of a ten percent parameter change. It is believed that with more advanced modeling, and better initial correlation, this threshold can be reduced further. As a final step, the mean model parameters generated for the combined damage case were

used to update the FEM. Comparisons between the correlated updated model and the measured PSD are given in Figure 7-43 where good agreement is shown between the modeled and measured responses.

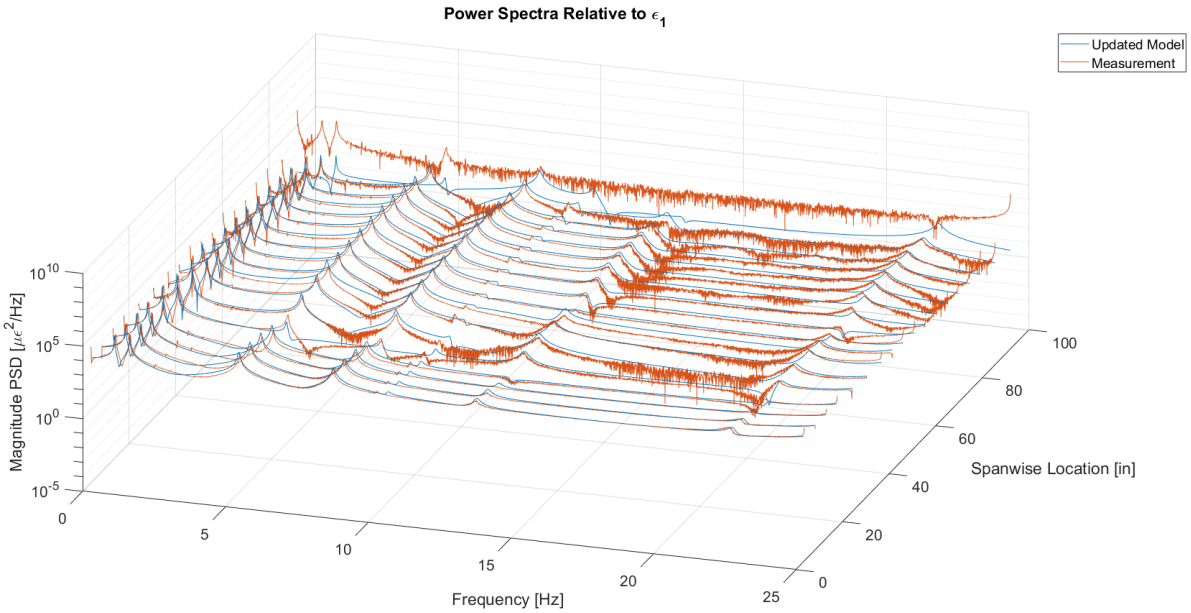

Figure 7-43: Correlated model PSD response (blue) overlaid with the experimental PSD (red) of all 18 sensors relative to sensor one for the combined damage case.

Chapter 8: Conclusions and Recommendations

Structural health monitoring (SHM) technologies continue to be pursued for aerospace structures in the interests of increased safety and, when combined with prognosis, efficiency in life-cycle management. The current work focused on developing and validating a method for in-situ health monitoring of aerospace structures. In particular, the current framework was developed for use with response only vibration data using natural operating turbulence to provide the means of excitation. While the framework is general so as to work with a wide suite of sensor options, particular emphasis was placed on fiber optic strain sensors as a lightweight, low cost, non-intrusive means of monitoring the vibration response.

At its core, the developed SHM system actively monitors a network of fiber optic strain sensors and uses the transient response data to calculate their associated power spectral densities (PSD). These PSD serve as the fundamental input to the developed SHM algorithm presented in the dissertation whereby comparisons between previously correlated model PSD and the current measured PSD are made. If anomalies between the correlated model and the measured data sets are detected, the developed SHM algorithm seeks to minimize the difference via updating of structural parameters underlying the structural model of interest (in the case of the presented work a finite element model of the structure).

The SHM algorithm itself is an adaption of a statistical least-squares minimization based in concepts of non-linear parameter estimation and model correlation. The algorithm developed uses power spectra based residual error vectors derived from distributed vibration measurements to update a structural finite element model through statistically weighted least-squares minimization. The output of the algorithm is a correlated finite element model which inherently produces estimates of the location, type, and severity of any detected damage as well as the

uncertainty associated with these estimates. While prognosis is not directly addressed in the current dissertation, all of the work was developed such that prognosis could be directly implemented using the correlated model parameters and expected future loads. Furthermore, while the current dissertation is focused on applications to aerospace structures, the method is generally applicable to civil and offshore structures as well.

Throughout the dissertation the developed algorithm was shown, both analytically and experimentally, to successfully detect, locate, and quantify damage present in a structural system. In the analytical studies presented in Chapters 4 and 5, it was shown that the algorithm is capable of accurately differentiating changes in mass from changes in stiffness and resolving damage features to negligible error even under extreme noise environments. Also presented in Chapter 5 was a comparison with contemporary model updating based SHM methodologies where the algorithm was shown to perform favorability to the alternative methods in all cases tested. These analytical results were further validated by the experimental work presented in Chapter 7, which provides an experimental demonstration of the damage detection algorithm on a composite structure.

The remainder of the current chapter highlights the novel contributions resulting from this work as well as provides recommendations for future development stemming from the current research.

8.1 Novel Contributions

Over the course of the research related to this dissertation a number of technical advancements were made and are presented below, in the order they appear within the dissertation.

- Developed the equations for the strain power spectral density which incorporate damage scale factors into the analytical model allowing for SHM to be performed on the scale factors (Sections 3.1 – 3.3).
- Formulated a residual error based objective function derived from response only strain vibration data for the purpose of SHM (Section 3.4).
- Adapted a Bayesian least-squares approach to parameter estimation via strain power spectral density modeling and measurements (Section 3.4).
- Derived the residual error covariance matrix as it relates to measurement noise present on strain power spectral density signals (Section 3.5).
- Presented a method by which the non-linear, power spectral density based objective function is linearized and minimized in an iterative fashion (Section 3.6).
- Utilized the statistics of the damage scale factors stemming from the use of multiple reference DOF in a single power spectral density measurement set to provide a confidence estimate on the identified update parameters (Section 3.6).
- Integrated a frequency line updating scheme which maintains a high level of parameter sensitivity throughout the iteration process leading to increased accuracy and convergence rates (Section 3.9).
- Conducted an evaluation of the impact frequency line selection has on algorithm performance coupled with the development of enhanced frequency line selection techniques (Sections 3.9, 4.5, 5.4.1).
- Implemented an automated adaptive step size control which promotes convergence to the best possible solution while minimizing the number of iterations to convergence (Section 3.10).

- Automated selection of frequency lines based on their locations relative to the peaks of the strain PSD curves (Section 4.5).
- Introduced active parameter sensitivity screening which monitors parameter sensitivity levels and fixes any parameter not currently contributing to the solution on an iteration-by-iteration basis. Implementation of such screening promotes convergence to meaningful solutions while simultaneously maximizing the parameters in the solution space (Sections 5.4.2 and 5.4.3).
- Designed, fabricated, and implemented an automatic impact hammer to provide repeatable impulse excitations for use in vibration testing (with specific applications to power spectral density modeling) (Section 6.2.3).
- Developed an optical frequency domain reflectometry-based interrogation system to return relatively high sample rate raw interferograms to be collected for further processing (Section 6.4).
- Enhanced data processing methods which provide a better wavelength estimate for the computation of strain using optical frequency domain reflectometry (Section 6.4).
- Fabricated, modeled, and correlated a composite testbed for use in experimental testing and validation of structural health monitoring routines (Section 7.1).
- Performed experimental implementation and validation of a stochastic SHM model updating algorithm which utilizes strain power spectral density measurements and modeling to accurately determine the presence, location, type, and severity of damage present in a composite aerospace structure (Section 7.4).

8.2 Recommendations for Future Work

While the dissertation has presented a novel approach to performing an in-situ health evaluation of aerospace structures there are still a number of topics in which more in-depth work would likely enhance the utility of the method. In the current section a number of the areas for future research are addressed and recommendations given based on the experience gained over the course of the presented work.

8.2.1 Optical Frequency Domain Reflectometry (OFDR) Based Sensing

One of the limiting factors in the current dissertation's experimental implementation was the limited sampling rate of the OFDR sensing system. While great advancements in both the hardware and the data processing of ODFR strain sensors were made in relation to this work there are still large gains to be had. The relatively low sample rate of the OFDR system is due in large part to a mechanical armature within the laser which provides the swept wavelength interrogation needed to evaluate the optical fibers. At present, the armature sweeps a prism over a range of motion to produce a predefined range of wavelengths at which the sensors are interrogated. Currently, the data is collected while the prism sweeps from low to high wavelengths however on the return sweep no data is collected. In the short-term the data collection routine could be modified to collect data on both the forward and reverse sweeps, nearly doubling the available sample rate.

In the long-term, research is underway to develop solid-state, narrow-band, swept, tunable lasers for use in OFDR interrogation. These solid-state lasers have the potential to increase the available sweep rates, and in turn sample rates, orders of magnitude. Once online, these solid-state lasers, coupled with advanced computational power, will provide ample frequency range to greatly increase the ability of the algorithm to resolve smaller damage features over larger structural areas.

8.2.2 Programming Language

Throughout the dissertation MATLAB has been used for all modeling and computations largely out of convenience in rapid development and implementation. While MATLAB was suitable for development and basic implementation, migration to a more efficient programming language is recommended. Currently, restrictions on the way MATLAB stores and processes data is a limiting factor in the number of elements contained within the generated PSD models. Furthermore, advancements in the processing of optical frequency domain reflectometry data within the dissertation have slowed the data processing down from real-time to a factor of approximately two-to-one when sampling at 100Hz. Migration from MATLAB to a suitable C language would likely bring the processing speeds back to real-time for sample rates well in excess of 100Hz.

8.2.3 Advancements in Test Article and Finite Element Formulation

The test article used within the current dissertation was developed to represent an aerospace structure, yet be economical and commercially available (so that destructive testing was possible). The limited dynamic range of the OFDR system was such that airfoil masses had to be incorporated to lower a reasonable number of frequencies under 25Hz. While the airfoil masses did an excellent job of shifting the frequencies, as well as adding system complexity and bend-twist coupling, they made studying any mass variations within the system impractical (the mass, and in turn density, of the beam was dominated by the airfoil masses and as such inclusion of mass properties in the experimental demonstration were not possible). With the presented SHM approach now experimentally validated, it is recommended a new test article be designed which includes several bending and torsion frequencies within the detectable range of the OFDR system while eliminating the mass loading.

Since the chosen test article was indeed a beam, modeling it using Timoshenko beam elements was a natural progression. The beam element formulation utilized equivalent laminate properties of the beam for simplicity and was shown to be effective in estimating the damage using the available beam properties. It is however believed that more advanced modeling would allow for a refined estimate of damage to be calculated and ultimately a more accurate model returned. It is further speculated that enhanced modeling techniques would greatly reduce the irreducible modeling error and in turn reduce the size of detectable damage features.

8.2.4 Excitation Studies

In the presented work, a series of excitation studies were performed to develop a means to collect the requisite experimental PSD data for the SHM algorithm. While the implementation of impulse response testing proved to be adequate for the purpose of demonstrating the algorithm, it is speculated that base excitation would better resemble atmospheric excitation on an aerospace structure. As such, it is recommended that the next generation of testing be done under base excitation. Incorporation of such an excitation would not only more closely resemble the dynamic loads seen in flight conditions but also allow the effects the variation of such loads have on the response power spectral densities to be studied. Ultimately the algorithm should be implemented on an aerospace structure placed into a wind tunnel and/or used in a flight test program to validate the algorithm's performance in a realistic flight environment.

Appendix A: Finite Element Modeling using Timoshenko Beam Elements

In order to utilize the analytical response PSD, the dynamic stiffness matrix for the system must be developed. Developing the dynamic stiffness matrix requires formulation of a mass, stiffness, and damping model of the system or structure of interest. Although the SHM framework has been developed for use with any set of generic elements comprising the finite element model of the structure, it is demonstrated throughout the dissertation using Timoshenko beam elements. The derivation of mass and stiffness matrices using Timoshenko beam elements is well documented and will be forgone in this dissertation. Instead the key results will be highlighted below for completeness. For a full derivation the reader is referred to Wu's book on the subject [109].

A.1 Finite Element Formulation – Timoshenko Beam Model

Consider a generic three-dimensional beam element as shown in Figure A-1.

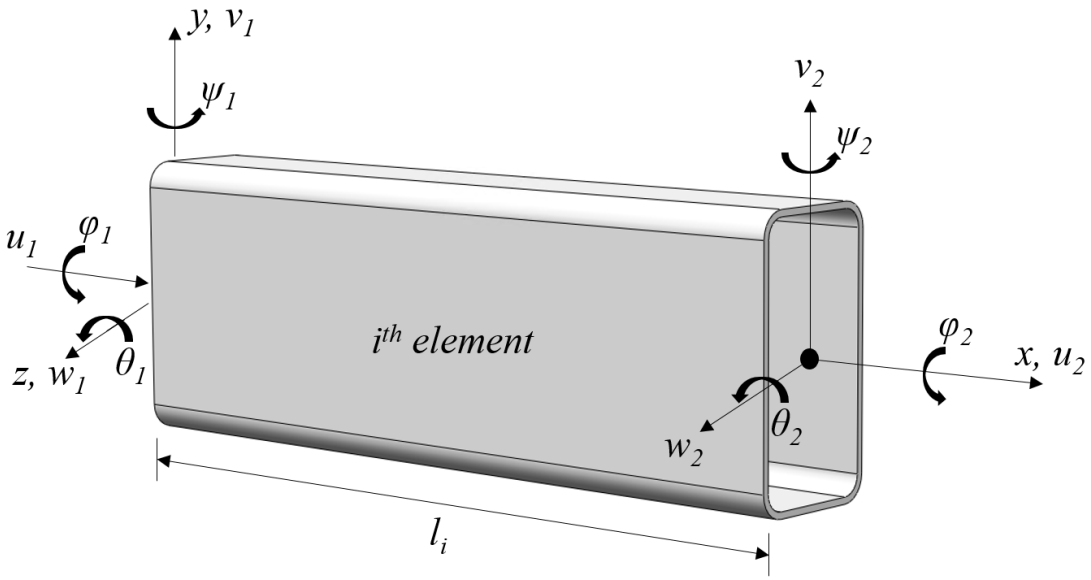

Figure A-1: Generic 3-D Timoshenko beam element used to formulate the system matrices.

As shown in Figure A-1, the elements under consideration are two-node, six degree-of-freedom (DOF) per node elements capable of modeling bending in two planes, axial deformation, and torsion. Since the elements are defined using principal coordinates, the axial, bending, and torsion responses are all decoupled from one another. While the vibrational modes associated with the axial modes are orders of magnitude higher in frequency than the OFDR optical sensors can currently monitor, they have been included for completeness. Should higher frequency content information be available (i.e. WDM sensors), or elemental coordinate transformations desired, the existing development could be directly applied.

Following the development presented in Wu [109], the elemental shape functions [a] in the isoperimetric domain can be defined by the relationship between the elemental displacement vector and the nodal displacement vector $\{d\}$:

$$\{u\} = [a]^T \{d\} \tag{A-1}$$

where,

$$\{u\} = \{u_x \quad u_y \quad u_z\}, \tag{A-2}$$

$$\{d\} = \{u_1 \quad v_1 \quad w_1 \quad \varphi_1 \quad \psi_1 \quad \theta_1 \quad u_2 \quad v_2 \quad w_2 \quad \varphi_2 \quad \psi_2 \quad \theta_2\}, \tag{A-3}$$

$$[a] = [\{a_x\} \quad \{a_y\} \quad \{a_z\}]. \tag{A-4}$$

Enforcing equilibrium allows for the explicit calculation of the shape function matrix [a]:

$$[a]=\begin{bmatrix}
1-\xi & 0 & 0 \\
C_{sy}\left(6\xi-6\xi^2\right)\eta & C_{sy}\left(1-3\xi^2+2\xi^3+(1-\xi)\Phi_y\right) & 0 \\
C_{sz}\left(6\xi-6\xi^2\right)\zeta & 0 & C_{sz}\left(1-3\xi^2+2\xi^3+(1-\xi)\Phi_z\right) \\
0 & (\xi-1)l\zeta & (1-\xi)l\eta \\
C_{sz}\left(1-4\xi+3\xi^2+(1-\xi)\Phi_z\right)l\zeta & 0 & -C_{sz}\left(\xi-2\xi^2+\xi^3+\frac{1}{2}\left(\xi-\xi^2\right)\Phi_z\right)l \\
C_{sy}\left(-1+4\xi-3\xi^2-(1-\xi)\Phi_y\right)l\eta & C_{sy}\left(\xi-2\xi^2+\xi^3+\frac{1}{2}\left(\xi-\xi^2\right)\Phi_y\right)l & 0 \\
\xi & 0 & 0 \\
-C_{sy}\left(6\xi-6\xi^2\right)\eta & C_{sy}\left(3\xi^2-2\xi^3+\xi\Phi_y\right) & 0 \\
-C_{sz}\left(6\xi-6\xi^2\right)\zeta & 0 & C_{sz}\left(3\xi^2-2\xi^3+\xi\Phi_z\right) \\
0 & -l\xi\zeta & l\xi\eta \\
C_{sz}\left(-2\xi+3\xi^2+\xi\Phi_z\right)l\zeta & 0 & -C_{sz}\left(-\xi^2+\xi^3-\frac{1}{2}\left(\xi-\xi^2\right)\Phi_z\right)l \\
C_{sy}\left(2\xi-3\xi^2-\xi\Phi_y\right)l\eta & C_{sy}\left(-\xi^2+\xi^3-\frac{1}{2}\left(\xi-\xi^2\right)\Phi_y\right)l & 0
\end{bmatrix}$$

(A-5)

where l is the element length, ξ is the isoperimetric parameter in the x-direction and varies from zero to one along the element length ($\xi = x/l$), ζ is the location of interest in the z-direction, measured relative to the neutral axis ($\zeta = z/l$), and η is the location of interest in the y-direction, measured relative to the neutral axis ($\eta = y/l$). Furthermore, C_{sy}, C_{sz}, Φ_y and Φ_z are nondimensionalize shear deformations parameters as defined below:

$$\Phi_y = \frac{12EI_z}{GA_{sy}l^2}, \tag{A-6}$$

$$C_{sy} = \frac{1}{1+\Phi_y}, \tag{A-7}$$

$$A_{sy} = k_y A, \tag{A-8}$$

$$\Phi_z = \frac{12EI_y}{GA_{sz}l^2}, \tag{A-9}$$

$$C_{sz} = \frac{1}{1+\Phi_z}, \tag{A-10}$$

$$A_{sz} = k_z A, \tag{A-11}$$

where E is the elastic modulus, G the shear modulus, A the elemental cross sectional area, I_y the bending inertia about the y-axis, I_z the bending inertia about the z-axis and k_y and k_z are the Timoshenko shear correction coefficients (in the x-y and x-z planes, respectively) determined by the element's cross section geometry.

Using the shape function matrix given in (A-5) the elemental mass and stiffness matrices can be determined using the force-displacement relationship as shown by Wu. The resulting elemental mass and stiffness matrices follow and are used throughout the dissertation to formulate the dynamic stiffness matrices where required:

$$[m_e] = \begin{bmatrix}
m_{1,1} & 0 & 0 & 0 & 0 & 0 & m_{1,7} & 0 & 0 & 0 & 0 & 0 \\
0 & m_{2,2} & 0 & 0 & 0 & m_{2,6} & 0 & m_{2,8} & 0 & 0 & 0 & m_{2,12} \\
0 & 0 & m_{3,3} & 0 & m_{3,5} & 0 & 0 & 0 & m_{3,9} & 0 & m_{3,11} & 0 \\
0 & 0 & 0 & m_{4,4} & 0 & 0 & 0 & 0 & 0 & m_{4,10} & 0 & 0 \\
0 & 0 & m_{5,3} & 0 & m_{5,5} & 0 & 0 & 0 & m_{5,9} & 0 & m_{5,11} & 0 \\
0 & m_{6,2} & 0 & 0 & 0 & m_{6,6} & 0 & m_{6,8} & 0 & 0 & 0 & m_{6,12} \\
m_{7,1} & 0 & 0 & 0 & 0 & 0 & m_{7,7} & 0 & 0 & 0 & 0 & 0 \\
0 & m_{8,2} & 0 & 0 & 0 & m_{8,6} & 0 & m_{8,8} & 0 & 0 & 0 & m_{8,12} \\
0 & 0 & m_{9,3} & 0 & m_{9,5} & 0 & 0 & 0 & m_{9,9} & 0 & m_{9,11} & 0 \\
0 & 0 & 0 & m_{10,4} & 0 & 0 & 0 & 0 & 0 & m_{10,10} & 0 & 0 \\
0 & 0 & m_{11,3} & 0 & m_{11,5} & 0 & 0 & 0 & m_{11,9} & 0 & m_{11,11} & 0 \\
0 & m_{12,2} & 0 & 0 & 0 & m_{12,6} & 0 & m_{12,8} & 0 & 0 & 0 & m_{12,12}
\end{bmatrix}$$

(A-12)

where $m_{i,j} = m_{j,i}$ and the nonzero upper diagonal entries are explicitly given as:

$$m_{1,1} = m_{7,7} = \frac{1}{3}\rho Al, \quad m_{1,7} = \frac{1}{6}\rho Al$$

$$m_{2,2} = \overline{c}_m\left(\left(\frac{13}{35} + \frac{7}{10}\Phi_y + \frac{1}{3}{\Phi_y}^2\right) + \frac{6{r_{gz}}^2}{5l^2}\right)$$

$$m_{2,6} = \overline{c}_m\left(\left(\frac{11}{210} + \frac{11}{120}\Phi_y + \frac{1}{24}{\Phi_y}^2\right)l + \left(\frac{1}{10} - \frac{1}{2}\Phi_y\right)\frac{{r_{gz}}^2}{l}\right)$$

$$m_{2,8} = \overline{c}_m\left(\left(\frac{9}{70} + \frac{3}{10}\Phi_y + \frac{1}{6}{\Phi_y}^2\right) - \frac{6{r_{gz}}^2}{5l^2}\right)$$

$$m_{2,12} = \overline{c}_m\left(-\left(\frac{13}{420} + \frac{3}{40}\Phi_y + \frac{1}{24}{\Phi_y}^2\right)l + \left(\frac{1}{10} - \frac{1}{2}\Phi_y\right)\frac{{r_{gz}}^2}{l}\right)$$

$$m_{3,3} = \hat{c}_m\left(\left(\frac{13}{35} + \frac{7}{10}\Phi_z + \frac{1}{3}{\Phi_z}^2\right) + \frac{6{r_{gy}}^2}{5l^2}\right)$$

$$m_{3,5} = \hat{c}_m\left(-\left(\frac{11}{210} + \frac{11}{120}\Phi_z + \frac{1}{24}{\Phi_z}^2\right)l - \left(\frac{1}{10} - \frac{1}{2}\Phi_z\right)\frac{{r_{gy}}^2}{l}\right)$$

$$m_{3,9} = \hat{c}_m\left(\left(\frac{9}{70} + \frac{3}{10}\Phi_z + \frac{1}{6}{\Phi_z}^2\right) - \frac{6{r_{gy}}^2}{5l^2}\right)$$

$$m_{3,11} = \hat{c}_m\left(\left(\frac{13}{420} + \frac{3}{40}\Phi_z + \frac{1}{24}{\Phi_z}^2\right)l - \left(\frac{1}{10} - \frac{1}{2}\Phi_z\right)\frac{{r_{gy}}^2}{l}\right)$$

$$m_{4,4} = m_{10,10} = \frac{1}{3}\rho I_x l, \quad m_{4,10} = \frac{1}{6}\rho I_x l$$

$$m_{5,5} = \hat{c}_m\left(\left(\frac{1}{105} + \frac{1}{60}\Phi_z + \frac{1}{120}{\Phi_z}^2\right)l^2 + \left(\frac{2}{15} + \frac{1}{6}\Phi_z + \frac{1}{3}{\Phi_z}^2\right){r_{gy}}^2\right)$$

$$m_{5,9} = \hat{c}_m\left(-\left(\frac{13}{420} + \frac{3}{40}\Phi_z + \frac{1}{24}{\Phi_z}^2\right)l + \left(\frac{1}{10} - \frac{1}{2}\Phi_z\right)\frac{{r_{gy}}^2}{l}\right)$$

$$m_{5,11} = \hat{c}_m\left(-\left(\frac{1}{140} + \frac{1}{60}\Phi_z + \frac{1}{120}{\Phi_z}^2\right)l^2 + \left(-\frac{1}{30} - \frac{1}{6}\Phi_z + \frac{1}{6}{\Phi_z}^2\right){r_{gy}}^2\right)$$

$$m_{6,6} = \overline{c}_m\left(\left(\frac{1}{105} + \frac{1}{60}\Phi_y + \frac{1}{120}{\Phi_y}^2\right)l^2 + \left(\frac{2}{15} + \frac{1}{6}\Phi_y + \frac{1}{3}{\Phi_y}^2\right){r_{gz}}^2\right)$$

$$m_{6,8} = \overline{c}_m\left(\left(\frac{13}{420} + \frac{3}{40}\Phi_y + \frac{1}{24}{\Phi_y}^2\right)l - \left(\frac{1}{10} - \frac{1}{2}\Phi_y\right)\frac{{r_{gz}}^2}{l}\right)$$

$$m_{6,12} = \overline{c_m}\left(-\left(\frac{1}{140} + \frac{1}{60}\Phi_y + \frac{1}{120}\Phi_y{}^2 \right) l^2 + \left(-\frac{1}{30} - \frac{1}{6}\Phi_y + \frac{1}{6}\Phi_y{}^2 \right) r_{gz}{}^2 \right)$$

$$m_{8,8} = \overline{c_m}\left(\left(\frac{13}{35} + \frac{7}{10}\Phi_y + \frac{1}{3}\Phi_y{}^2 \right) + \frac{6r_{gz}{}^2}{5l^2} \right)$$

$$m_{8,12} = \overline{c_m}\left(-\left(\frac{11}{210} + \frac{11}{120}\Phi_y + \frac{1}{24}\Phi_y{}^2 \right) l - \left(\frac{1}{10} - \frac{1}{2}\Phi_y \right) \frac{r_{gz}{}^2}{l} \right)$$

$$m_{9,9} = \hat{c}_m\left(\left(\frac{13}{35} + \frac{7}{10}\Phi_z + \frac{1}{3}\Phi_z{}^2 \right) + \frac{6r_{gy}{}^2}{5l^2} \right)$$

$$m_{9,11} = \hat{c}_m\left(\left(\frac{11}{210} + \frac{11}{120}\Phi_z + \frac{1}{24}\Phi_z{}^2 \right) l + \left(\frac{1}{10} - \frac{1}{2}\Phi_z \right) \frac{r_{gy}{}^2}{l} \right)$$

$$m_{11,11} = \hat{c}_m\left(\left(\frac{1}{105} + \frac{1}{60}\Phi_z + \frac{1}{120}\Phi_z{}^2 \right) l^2 + \left(\frac{2}{15} + \frac{1}{6}\Phi_z + \frac{1}{3}\Phi_z{}^2 \right) r_{gy}{}^2 \right)$$

$$m_{12,12} = \overline{c_m}\left(\left(\frac{1}{105} + \frac{1}{60}\Phi_y + \frac{1}{120}\Phi_y{}^2 \right) l^2 + \left(\frac{2}{15} + \frac{1}{6}\Phi_y + \frac{1}{3}\Phi_y{}^2 \right) r_{gz}{}^2 \right)$$

with, $\overline{c_m} = \dfrac{\rho A l}{(1+\Phi_y)^2}$, $r_{gy} = \sqrt{I_y / A}$, $\hat{c}_m = \dfrac{\rho A l}{(1+\Phi_z)^2}$, and $r_{gz} = \sqrt{I_z / A}$.

Likewise, the elemental stiffness matrix is shown to be:

$$[k_e] = \begin{bmatrix}
k_{1,1} & 0 & 0 & 0 & 0 & 0 & k_{1,7} & 0 & 0 & 0 & 0 & 0 \\
0 & k_{2,2} & 0 & 0 & 0 & k_{2,6} & 0 & k_{2,8} & 0 & 0 & 0 & k_{2,12} \\
0 & 0 & k_{3,3} & 0 & k_{3,5} & 0 & 0 & 0 & k_{3,9} & 0 & k_{3,11} & 0 \\
0 & 0 & 0 & k_{4,4} & 0 & 0 & 0 & 0 & 0 & k_{4,10} & 0 & 0 \\
0 & 0 & k_{5,3} & 0 & k_{5,5} & 0 & 0 & 0 & k_{5,9} & 0 & k_{5,11} & 0 \\
0 & k_{6,2} & 0 & 0 & 0 & k_{6,6} & 0 & k_{6,8} & 0 & 0 & 0 & k_{6,12} \\
k_{7,1} & 0 & 0 & 0 & 0 & 0 & k_{7,7} & 0 & 0 & 0 & 0 & 0 \\
0 & k_{8,2} & 0 & 0 & 0 & k_{8,6} & 0 & k_{8,8} & 0 & 0 & 0 & k_{8,12} \\
0 & 0 & k_{9,3} & 0 & k_{9,5} & 0 & 0 & 0 & k_{9,9} & 0 & k_{9,11} & 0 \\
0 & 0 & 0 & k_{10,4} & 0 & 0 & 0 & 0 & 0 & k_{10,10} & 0 & 0 \\
0 & 0 & k_{11,3} & 0 & k_{11,5} & 0 & 0 & 0 & k_{11,9} & 0 & k_{11,11} & 0 \\
0 & k_{12,2} & 0 & 0 & 0 & k_{12,6} & 0 & k_{12,8} & 0 & 0 & 0 & k_{12,12}
\end{bmatrix} \quad \text{(A-13)}$$

As was the case for the mass matrix, the stiffness matrix is symmetric (i.e. $k_{i,j} = k_{j,i}$) and the nonzero upper diagonal entries are explicitly given as:

$$k_{1,1} = k_{7,7} = -k_{1,7} = \frac{EA}{l},$$

$$k_{2,2} = C_{sy}\frac{12EI_z}{l^3}, \quad k_{2,6} = k_{2,12} = C_{sy}\frac{6EI_z}{l^2}, \quad k_{2,8} = -C_{sy}\frac{12EI_z}{l^3}$$

$$k_{3,3} = k_{9,9} = C_{sz}\frac{12EI_y}{l^3}, \quad k_{3,5} = k_{3,11} = -C_{sz}\frac{6EI_y}{l^2}, \quad k_{3,9} = -C_{sz}\frac{12EI_y}{l^3}$$

$$k_{4,4} = k_{10,10} = \frac{GI_x}{l}, \quad k_{4,10} = \frac{-GI_x}{l}$$

$$k_{5,5} = k_{11,11} = C_{sz}\frac{(4+\Phi_z)EI_y}{l}, \quad k_{5,9} = k_{9,11} = C_{sz}\frac{6EI_y}{l^2}, \quad k_{5,11} = C_{sz}\frac{(2-\Phi_z)EI_y}{l}$$

$$k_{6,6} = k_{12,12} = C_{sy}\frac{(4+\Phi_y)EI_z}{l}, \quad k_{6,8} = -C_{sy}\frac{6EI_z}{l^2}, \quad k_{6,12} = C_{sy}\frac{(2-\Phi_y)EI_z}{l}$$

$$k_{8,8} = C_{sy}\frac{12EI_z}{l^3}, \quad k_{8,12} = -C_{sy}\frac{6EI_z}{l^2}$$

A.2 Strain-Displacement Transformation

In order to transform the model PSD from the displacement to the strain domain, the strain-displacement transformation matrix is required in accordance with equation (3-21). The transformation to the strain domain is necessary to allow for comparisons between the experimentally measure strain PSD obtained via the fiber optic strain sensors and the analytical model given in (3-14). Since the fiber optic sensors will be monitoring axial strain, the goal of the transformation matrx is to convert the displacement based analtyical PSD to axial strain. Assuming a linear strain field, the strain can be written in terms of the displacement as:

$$\varepsilon_{xx} = \frac{\partial u}{\partial x}. \tag{A-14}$$

Recalling from (A-1) the expression relating the global displacement vector to the nodal displacement vector and isolating the axial deformation:

$$\{u_x\} = \{a_x\}^T \{d\}. \tag{A-15}$$

Substituting (A-15) into (A-14) to obtain the strain requires use of the chain rule where:

$$\frac{du_x}{dx} = \frac{du_x}{d\xi}\frac{d\xi}{dx}. \tag{A-16}$$

Using the definition of the isoperimetric domain (i.e. $\xi = x / l$):

$$\frac{du_x}{dx} = \frac{1}{l}\frac{du_x}{d\xi} \tag{A-17}$$

which implies:

$$\varepsilon_{xx} = \frac{1}{l}\frac{du_x}{d\xi} = \frac{1}{l}\frac{d}{d\xi}\left(\{a_x\}^T \{d\}\right). \tag{A-18}$$

Defining the strain-displacement transformation for the n^{th} element $\{B_n\}$ as the vector which transforms the nodal displacements and rotations to axial strain:

$$\varepsilon_n = \{B_n\}\{d\} \tag{A-19}$$

leads to the result:

$$\{B_n\} = \frac{1}{l}\frac{d\{a_x\}^T}{d\xi}. \tag{A-20}$$

Substituting (A-5) into (A-20) yields the final form of the elemental strain-displacement transformation vector:

$$\left\{B_n\right\}^T = \frac{1}{l}\begin{Bmatrix} -1 \\ C_{sy}(6-12\xi)\eta \\ C_{sz}(6-12\xi)\zeta \\ 0 \\ C_{sz}(-4+6\xi-\Phi_z)l\zeta \\ C_{sy}(4-6\xi+\Phi_y)l\eta \\ 1 \\ C_{sy}(-6+12\xi)\eta \\ C_{sz}(-6+12\xi)\zeta \\ 0 \\ C_{sz}(-2+6\xi+\Phi_z)l\zeta \\ C_{sy}(2-6\xi-\Phi_y)l\eta \end{Bmatrix}. \tag{A-21}$$

This elemental transformation vector, whose transpose is given in (A-21), can be stacked row wise at multiple locations within a single element as well as across multiple elements to form the transformation matrix [*B*]. The final step in developing the strain-PSD analytical model is to convert from the displacement domain representation given in (3-14) to the strain domain. Defining the strain transfer function in terms of the displacement-PSD and strain-displacement transformation matrix:

$$[H_\varepsilon(r,\omega)] \equiv [B(r)][H(r,\omega)]. \tag{A-22}$$

Substituting (A-22) into (3-14):

$$[S_{\varepsilon\varepsilon}(r,\omega)] = [B(r)]\left([H^*(r,\omega)][S_{ff}(\omega)][H^T(r,\omega)]\right)[B(r)]^T \tag{A-23}$$

Or equivalently:

$$[S_{\varepsilon\varepsilon}(r,\omega)] = [B(r)][S_{xx}(r,\omega)][B(r)]^T . \quad \text{(A-24)}$$

Appendix B: Damping Models

With the equations related to the mass and stiffness matrices developed, the damping matrix must be estimated in order to fully characterize the system for calculation of the PSD. The sections below summarize the theory related to the damping models explored in this dissertation. All of the methods utilize proportionally damped approximations since the structures being studied allow for such models (lightly damped without interconnected components). As the structures being evaluated increase in complexity the current SHM framework allows for the inclusion of more sophisticated damping models, such as structural damping demonstrated in Chapter 5, where required.

Proportional viscous damping relates damping to the velocity of the degrees-of-freedom through proportionality to the mass and/or stiffness matrices of the system. A major benefit of using proportional viscous damping is the fact the damped equation of motion remains uncoupled in the modal domain, resulting in normal (non-complex) modes that simplify the analysis. Proportional damping can accurately model the damping present in structural materials which are directly related to the mass and stiffness but struggles to capture the effects of damping caused by things such as boundaries and joints. Since the beam being modeled is largely free of connections a proportional damping model is capable of providing a realistic estimate.

Transforming the equation of motion given in (3-1) from the displacement domain into the modal domain via the introduction of generalized coordinates allows for the derivation of the proportional viscous damping model. By definition, generalized coordinates $\{q(t)\}$ are related to the displacement domain coordinates $\{x(t)\}$ via the mode shape matrix $[\Phi]$ by [94]:

$$\{x(t)\} = [\Phi]\{q(t)\} \tag{B-1}$$

where the mode shape matrix is comprised of the stacking of individual mode shapes column-wise to yield a matrix:

$$[\Phi] = \begin{bmatrix} \{\phi_1\} & \{\phi_2\} & \cdots & \{\phi_n\} \end{bmatrix}. \tag{B-2}$$

Taking the appropriate derivatives, substituting (B-1) into (3-1), and pre-multiplying by the transpose of the modal vector yields the equation of motion in generalized coordinates:

$$[\Phi]^T [M][\Phi]\{\ddot{q}(t)\} + [\Phi]^T [C][\Phi]\{\dot{q}(t)\} + [\Phi]^T [K][\Phi]\{q(t)\} = [\Phi]^T \{f(t)\} \tag{B-3}$$

where the orthogonality between the mass and stiffness matrices and the mode shape leads to the diagonalizing of the modal mass and modal stiffness matrices such that:

$$\{\phi\}_m^T [M]\{\phi\}_n = \begin{cases} M_n, \text{ if } m = n \\ 0 \text{ , if } m \neq n \end{cases} \tag{B-4}$$

$$\{\phi\}_m^T [K]\{\phi\}_n = \begin{cases} K_n \text{ , if } m = n \\ 0 \text{ , if } m \neq n \end{cases} \tag{B-5}$$

Under the assumption that the damping matrix is proportional to mass and stiffness, the damping matrix will also be decoupled in the modal coordinate domain such that:

$$\{\phi\}_m^T [C]\{\phi\}_n = \begin{cases} C_n \text{ , if } m = n \\ 0 \text{ , if } m \neq n \end{cases} \tag{B-6}$$

where C_n is defined in terms of the modal damping ratio (ζ_n) and natural frequencies (ω_n) as:

$$C_n = 2\omega_n \zeta_n . \tag{B-7}$$

The determination of [C] is ultimately dependent on the method chosen to estimate such parameters. Four common methods for generating the proportional damping matrix are given in the following sections including the most common, Rayleigh damping, as well as Extended Rayleigh, Modal, and Caughey damping models.

B.1 Rayleigh Damping

Rayleigh damping is the most commonly used form of proportional viscous damping. Rayleigh damping seeks to relate the damping matrix to the mass and stiffness matrices through two proportionality constants (α and β) such that:

$$[C] = \alpha[K] + \beta[M] \tag{B-8}$$

Under this formulation, the damping in the system is presumed to be linearly proportional to both the mass and stiffness. This implies that larger elements will have an increased mass, stiffness, and damping. Rayleigh damping is often used not only for its simplicity but also due to the fact that it preserves the sparsity of the dynamic stiffness matrix.

In the case where no experimental information is known, [C] is approximated using experience or engineering intuition as to the proportionality constants α and β. If some information regarding the system's true damping and frequency parameters are available, an estimate of the proportionality constant can be solved for using (B-9). From the relationships given in (B-6) through (B-8), an explicit equation for the estimated damping ratios in terms of α and β is given as:

$$\zeta_n = \frac{1}{2}\left(\alpha\omega_n + \frac{\beta}{\omega_n} \right). \tag{B-9}$$

It is observed that a choice of two experimental modes would lead to a system of linear equations in which α and β could be solved for explicitly. Rayleigh damping models of this type do an excellent job at estimating the damping of the two modes used to solve for the proportionality constants. The major downside of the Rayleigh model stems from the fact that no information outside of the two modes are included in the damping model hence making extrapolation to other modes typically largely in error. To circumvent this limitation, researchers have used techniques such as least-squares fit to solve for an α and β which fit many modes well. If the damping of all the modes are similar in magnitude the results of the least-squares fit are usually acceptable however cases such as these tend to be the exception.

B.2 Extended Rayleigh Damping

In an effort to overcome the two-mode limitation in the traditional Rayleigh damping approach, the Extended Rayleigh Damping method was developed. The major advantage of the Extended Rayleigh Damping model is the ability to incorporate modal information of as many modes of interest as desired into the damping matrix. The inclusion of information from these additional modes comes in the form of performing a summation of the scaled mass and stiffness matrices over the desired modes. Many researchers have proposed various means for scaling the mass and stiffness matrices and one such way is that proposed by Clough and Penzien [110] in which the mode shapes, frequencies, and damping ratios of the system are used for the scaling such that:

$$[C]=\left(\frac{2\zeta_c}{\omega_c}\right)[K]+[M]\left[\sum_{n=1}^{c-1}2\left(\zeta_n-\zeta_c\left(\frac{\omega_n}{\omega_c}\right)\right)\frac{\omega_n}{M_n}\{\phi_n\}\{\phi_n\}^T\right][M] \quad \text{(B-10)}$$

where c corresponds to the number of modes to be included in the damping estimation.

The use of equation (B-10) can be carried out using experimental or modeled frequencies and mode shapes or a combination of the two. Of course, the accuracy of the developed damping matrix will depend on the accuracy of the input parameters. In the current work, experimental damping ratios and natural frequencies were obtained from accelerometer testing. Since the DOF of the experimental data were limited to six single axis accelerometers, a correlated FEM was used to extract the mode shapes at each model DOF to be used in the generation of the Extended Rayleigh Damping model presented in the dissertation.

B.3 Direct Modal Damping

An alternative approach to the application of Rayleigh's method to forming the damping matrix is the direct modal damping matrix formulation. The modal damping matrix is formed using experimental modal data in which the frequencies and damping ratios are known a priori. In the direct modal formulation the modes are considered decoupled in the modal domain. The damping matrix in modal coordinates can be represented as a diagonal matrix with each diagonal term proportional to a natural frequencies and damping ratio of the system [111].

$$[C_n]=\begin{bmatrix}\ddots & & \\ & 2\zeta_n\omega_n & \\ & & \ddots\end{bmatrix}. \quad \text{(B-11)}$$

Using either experimental or analytical mode shapes of the system, the modal damping matrix in physical coordinates is written as:

$$[C] = [\Phi]^{-T} [C_n] [\Phi]^{-1}. \tag{B-12}$$

For the vast majority of cases, the number of modes of interest will not match the number of degrees of freedom in the model and hence the mode shape matrix will be non-square and not invertible. In these cases, the rectangular mode shape matrix will require the use of the pseudo-inverse to solve (B-12). Calculation of the pseudo-inverse is numeric in nature, essentially arising from a least-square error minimization, and as such can introduce unquantified errors into the damping matrix. These errors tend to manifest themselves with the inclusion of higher frequency modes and are not of concern for the current work.

B.4 Caughey Damping

The final type of proportional damping model considered in the current dissertation is Caughey Damping. The Caughey damping matrix is a generalization of Rayleigh damping in which a series representation of the damping matrix is formed using calculated coefficients [112]. First proposed by Caughey [113] and later proved by Caughey and O'Kelly [114], the series representation of the damping model given in (B-13) is a necessary and sufficient condition for the existence of normal modes for a system without repeated roots. This series representation is now known as the Caughey series and is possibly the most general form of a damping matrix which still results in normal modes [111]. The Caughey damping matrix can be expressed in terms of the global mass and stiffness matrices as well as the unknown coefficients (α_n) as:

$$[C] = [M] \sum_{n=0}^{c-1} \alpha_n \left([M]^{-1} [K] \right)^n \tag{B-13}$$

where c is the number of modes of interest.

The advantage of using the Caughey series to represent the damping matrix is that it includes a mechanism to model damping over the entire set of modes of interest while not requiring the use of the mode shapes. The major drawback of the method is the computation of the coefficients can be numerically unstable, particularly when computed over a wide frequency domain. The computation of the parameters was outlined by Gerain and Rixen [112] whereas a linear system of equations is solved such that:

$$[\Omega]\{\alpha\} = \{\zeta\} \tag{B-14}$$

where the experimental natural frequencies and damping ratios of the *c* modes of interest are considered in the matrix [Ω] and vector {ζ}, respectively, as:

$$[\Omega] = \frac{1}{2}\begin{bmatrix} \frac{1}{\omega_1} & \omega_1 & \omega_1^3 & \cdots \omega_1^{2c-3} \\ \frac{1}{\omega_2} & \omega_2 & \omega_2^3 & \cdots \omega_2^{2c-3} \\ \vdots & \vdots & \vdots & \vdots \\ \frac{1}{\omega_c} & \omega_c & \omega_c^3 & \cdots \omega_c^{2c-3} \end{bmatrix}, \quad \{\zeta\} = \begin{Bmatrix} \zeta_1 \\ \zeta_2 \\ \vdots \\ \zeta_c \end{Bmatrix}. \tag{B-15}$$

B.5 Computation of Damping Matrices

In order to implement the damping models discussed in Appendix B, a set of experimental data taken with a set of six accelerometers on the thin-walled cantilever carbon beam being utilized. Using the experimental modal data collected for model correlation discussed in Chapter 7, the modal parameters were extract using the commercially available curve fitter, ME'Scope by Vibrant Technology. Table B-1 summarized the experimentally derived modal parameters used in the formulation of the damping matrices.

Table B-1: Experimental natural frequencies and damping ratios used in the computation of the damping models.

Mode Description	Frequency (Hz)	Damping Ratio (%Critical)
1st Bending -Soft	5.11	0.500
1st Bending -Stiff	7.61	0.932
2nd Bending -Soft	31.58	0.579
2nd Bending -Stiff	48.23	0.076
3rd Bending -Soft	86.29	0.784
3rd Bending -Stiff	133.30	0.907
4th Bending -Soft	163.90	0.500
1st Torsion	252.19	1.180
1st Axial	535.26*	0.829
4th Bending -Stiff	258.79	0.100
2nd Torsion	279.99	0.784
2nd Axial	1869.88*	0.977

* = Not measured and instead supplemented with correlated finite element model data

In all cases where the mode shapes were required to estimate the damping matrix, analytical mode shapes of the modes of interest where taken from a correlated finite element model of the structure. This allows for the mode shapes to be estimated at all DOF being modeled and the appropriate dimensions of the damping matrix be calculated directly.

B.5.1 Calculation of the Damping Matrix for Chapter 4 Analytical Studies

In the instance of the single beam element cases studied in Chapter 4, a proportional viscous damping model was implemented using available experimental modal data from the beam being modeled and studied in this dissertation. With the given set of extracted natural frequencies and damping ratios, the modal damping matrix was calculated using (B-7) [111] where the diagonal modal damping matrix $[C_n]$ is define as:

$$[C_n] = \begin{bmatrix} \ddots & & \\ & 2\zeta_n\omega_n & \\ & & \ddots \end{bmatrix}. \tag{B-16}$$

Using the analytical mode shapes $[\Phi]$, experimental damping factors $\{\zeta_n\}$, and experimental natural frequencies $\{\omega_n\}$ the damping matrix $[C]$ for the carbon beam in physical coordinate space was calculated as:

$$[C] = [\Phi]^{-T}[C_n][\Phi]^{-1}. \tag{B-17}$$

Since the measurements were made using single axis accelerometers at a limited number of sensing locations (six accelerometers) a complete set of experimental mode shapes were not available. Instead the finite element model (FEM) was correlated using static strain and dynamic accelerometer data and then the correlated FEM was used to generate analytical mode shapes to be used in the conversion from generalized coordinates to physical coordinates using equation (B-17). The extracted analytical mode shapes corresponding to the twelve modes listed in Table B-1 are:

$$[\Phi] = \begin{bmatrix} 0 & 0 & 0 & 0 & 0 & 0 & 0 & 0 & 20.33 & 0 & 0 & -29.42 \\ 13.13 & 0 & -28.16 & 0 & 4.42 & 0 & 18.52 & 0 & 0 & 0 & 0 & 0 \\ 0 & -13.13 & 0 & -28.15 & 0 & -4.44 & 0 & 0 & 0 & 18.43 & 0 & 0 \\ 0 & 0 & 0 & 0 & 0 & 0 & 0 & 28.73 & 0 & 0 & -41.57 & 0 \\ 0 & 0.49 & 0 & -0.19 & 0 & -3.60 & 0 & 0 & 0 & -4.12 & 0 & 0 \\ 0.49 & 0 & 0.19 & 0 & -3.60 & 0 & 4.13 & 0 & 0 & 0 & 0 & 0 \\ 0 & 0 & 0 & 0 & 0 & 0 & 0 & 0 & 28.75 & 0 & 0 & 41.60 \\ 38.66 & 0 & 38.96 & 0 & 43.36 & 0 & 72.36 & 0 & 0 & 0 & 0 & 0 \\ 0 & -38.65 & 0 & 38.93 & 0 & -43.26 & 0 & 0 & 0 & 71.66 & 0 & 0 \\ 0 & 0 & 0 & 0 & 0 & 0 & 0 & 40.63 & 0 & 0 & 58.79 & 0 \\ 0 & 0.58 & 0 & -2.04 & 0 & 4.54 & 0 & 0 & 0 & -15.15 & 0 & 0 \\ 0.58 & 0 & 2.04 & 0 & 4.54 & 0 & 15.27 & 0 & 0 & 0 & 0 & 0 \end{bmatrix}$$

where the reader is reminded that the columns of the mode shape matrix correspond to each of the twelve modes listed in Table B-1 and the rows correspond to the six DOF per node as organized in equation (A-3). Before calculating the modal damping matrix, and ultimately the proportional damping matrix, the mode shapes, frequencies, and damping ratios must be sorted such each column of the mode shape matrix has the shape corresponding to the degree of freedom having the same row number. With the sorting completed the proportional damping matrix is calculated as:

$$[C] = \begin{bmatrix} 8.64 & 0 & 0 & 0 & 0 & 0 & -1.53 & 0 & 0 & 0 & 0 & 0 \\ 0 & 0.437 & 0 & 0 & 0 & -1.80 & 0 & -0.090 & 0 & 0 & 0 & 0.998 \\ 0 & 0 & 0.079 & 0 & 2.15 & 0 & 0 & 0 & -0.217 & 0 & -1.93 & 0 \\ 0 & 0 & 0 & 0.639 & 0 & 0 & 0 & 0 & 0 & -0.171 & 0 & 0 \\ 0 & 0 & 2.15 & 0 & 172.1 & 0 & 0 & 0 & 1.20 & 0 & 0.287 & 0 \\ 0 & -1.80 & 0 & 0 & 0 & 135.2 & 0 & -0.664 & 0 & 0 & 0 & -12.7 \\ -1.53 & 0 & 0 & 0 & 0 & 0 & 4.319 & 0 & 0 & 0 & 0 & 0 \\ 0 & -0.090 & 0 & 0 & 0 & -0.664 & 0 & 0.110 & 0 & 0 & 0 & -0.996 \\ 0 & 0 & -0.217 & 0 & 1.20 & 0 & 0 & 0 & 0.174 & 0 & 1.83 & 0 \\ 0 & 0 & 0 & -0.171 & 0 & 0 & 0 & 0 & 0 & 0.319 & 0 & 0 \\ 0 & 0 & -1.93 & 0 & 0.287 & 0 & 0 & 0 & 1.83 & 0 & 50.9 & 0 \\ 0 & 0.998 & 0 & 0 & 0 & -12.7 & 0 & -0.996 & 0 & 0 & 0 & 28.4 \end{bmatrix} x10^{-2}$$

Lastly, removing the rows and columns associated with the unused and fixed DOF (since the examples in Chapter 4 utilize in-plane bending with the first node fixed) leaves the damping matrix given in (4-4) and repeated here for clarity as:

$$[C] = \begin{bmatrix} 1.74x10^{-3} & 1.83x10^{-2} \\ 1.83x10^{-2} & 5.09x10^{-1} \end{bmatrix} \tag{B-18}$$

References

[1] Speckmann, H. (2007) Structural Health Monitoring: Focal Point for SHM, Airbus, International Maintenance Review Board Policy Board, European Union Aviation Safety Agency Meeting.

[2] Oliver, J. A. (2015) *Frequency Response Function Based Damage Identification for Aerospace Structures*, University of California, San Diego.

[3] LeckLider, T. (2016) Even More About Strain Gages, Evaluation Engineering.

[4] Higgins, S. (1895) Inspection of Steel-Tired Wheels, *Proceedings of New York Railroad Club*, 988-989.

[5] Farrar, C. R., and Worden, K. (2012) *Structural health monitoring: a machine learning perspective*, John Wiley & Sons.

[6] Ikegami, R. (2000) Structural health monitoring: assessment of aircraft customer needs, *Structural Health Monitoring*, 12-23.

[7] Begg, R. D., Mackenzie, A. C., Dodds, C. J., and Loland, O. D. (1976) Structural integrity monitoring using digital processing of vibration siqnals, In *Offshore Technology Conference*, Offshore Technology Conference.

[8] Coppolino, R., and Rubin, S. (1980) Detectability of structural failures in offshore platforms by ambient vibration monitoring, In *Offshore Technology Conference*, Offshore Technology Conference.

[9] Wojnarowski, M. E., Stiansen, S. G., and Reddy, N. E. (1977) Structural integrity evaluation of a fixed platform using vibration criteria, In *Offshore Technology Conference*, Offshore Technology Conference.

[10] Heng, A., Zhang, S., Tan, A. C., and Mathew, J. (2009) Rotating machinery prognostics: State of the art, challenges and opportunities, *Mechanical systems and signal processing 23*, 724-739.

[11] Rogers, L. (1979) The application of vibration signature analysis and acoustic emission source location to on-line condition monitoring of anti-friction bearings, *Tribology international 12*, 51-58.

[12] Mba, D., and Rao, R. B. (2006) Development of Acoustic Emission Technology for Condition Monitoring and Diagnosis of Rotating Machines; Bearings, Pumps, Gearboxes, Engines and Rotating Structures.

[13] Urban, L. A. (1973) Gas path analysis applied to turbine engine condition monitoring, *Journal of Aircraft 10*, 400-406.

[14] Goranson, U. (1997) Jet transport structures performance monitoring, *Structural Health Monitoring Current Status and Perspectives*, 3-17.

[15] Kosmatka, J., and Oliver, J. (2006) Development of an in-flight structural health monitoring system for composite unmanned aircraft, In *47th AIAA/ASME/ASCE/AHS/ASC Structures, Structural Dynamics, and Materials Conference 14th AIAA/ASME/AHS Adaptive Structures Conference 7th*, p 1881.

[16] Fan, W., and Qiao, P. (2011) Vibration-based damage identification methods: a review and comparative study, *Structural health monitoring 10*, 83-111.

[17] Gobbato, M., Conte, J. P., Kosmatka, J. B., and Farrar, C. R. (2012) A reliability-based framework for fatigue damage prognosis of composite aircraft structures, *Probabilistic Engineering Mechanics 29*, 176-188.

[18] Staszewski, W., Mahzan, S., and Traynor, R. (2009) Health monitoring of aerospace composite structures–Active and passive approach, *composites Science and Technology 69*, 1678-1685.

[19] Michaels, J. E., Lee, S. J., Chen, X., Shi, F., and Michaels, T. E. (2011) Understanding and exploiting applied loads for guided wave structural health monitoring, In *2011 Aircraft Airworthiness & Sustainment Conference, San Diego, CA*.

[20] Roy, S., Chang, F., Lee, S., Pollock, P., and Janapati, V. (2013) A novel machine-learning approach for structural state identification using ultrasonic guided waves, *Safety, Reliability, Risk and Life-Cycle Performance of Structures and Infrastructures; CRC Press: Boca Raton, FL, USA*, 321-328.

[21] Mendoza, E., Prohaska, J., Kempen, C., Esterkin, Y., and Sun, S. (2013) In-flight fiber optic acoustic emission sensor (FAESense) system for the real time detection, localization, and classification of damage in composite aircraft structures, In *Photonic Applications for Aerospace, Commercial, and Harsh Environments IV*, p 87200K, International Society for Optics and Photonics.

[22] Velazquez, E., and Kosmatka, J. (2012) Acoustic Emission Structural Health Monitoring of Laminated Composite Aircraft Structures, In *53rd AIAA/ASME/ASCE/AHS/ASC Structures, Structural Dynamics and Materials Conference 20th AIAA/ASME/AHS Adaptive Structures Conference 14th AIAA*, p 1788.

[23] Clarke, T., Simonetti, F., and Cawley, P. (2010) Guided wave health monitoring of complex structures by sparse array systems: Influence of temperature changes on performance, *Journal of Sound and Vibration 329*, 2306-2322.

[24] Crane, R. M., and Ratcliffe, C. P. (2005) SIDER Testing of Impact Damaged Sandwich Panels, NAVAL SURFACE WARFARE CENTER CARDEROCK DIV BETHESDA MD.

[25] Davis, C. E., Norman, P., Ratcliffe, C., and Crane, R. (2012) Broad area damage detection in composites using fibre Bragg grating arrays, *Structural Health Monitoring: An International Journal 11*, 724-732.

[26] Cawley, P., and Adams, R. (1979) The location of defects in structures from measurements of natural frequencies, *The Journal of Strain Analysis for Engineering Design 14*, 49-57.

[27] Cawley, P., and Adams, R. D. (1979) A vibration technique for non-destructive testing of fibre composite structures, *Journal of Composite Materials 13*, 161-175.

[28] Ganeriwala, S. N., Yang, J., and Richardson, M. (2011) Using modal analysis for detecting cracks in wind turbine blades, *Sound and Vibration 45*, 10.

[29] Humar, J., Bagchi, A., and Xu, H. (2006) Performance of vibration-based techniques for the identification of structural damage, *Structural Health Monitoring 5*, 215-241.

[30] Lorenzo, E. D., Petrone, G., Manzato, S., Peeters, B., Desmet, W., and Marulo, F. (2016) Damage detection in wind turbine blades by using operational modal analysis, *Structural Health Monitoring: An International Journal 15*, 289-301.

[31] Sung, S. H., Koo, K. Y., and Jung, H. J. (2014) Modal flexibility-based damage detection of cantilever beam-type structures using baseline modification, *Journal of Sound and Vibration 333*, 4123-4138.

[32] Mendrok, K., and Uhl, T. (2010) The application of modal filters for damage detection, *Smart structures and systems 6*, 115-133.

[33] Martins, B. L., and Kosmatka, J. B. (2015) Detecting damage in a UAV composite wing spar using distributed fiber optic strain sensors, In *56th AIAA/ASCE/AHS/ASC Structures, Structural Dynamics, and Materials Conference*, p 0447.

[34] Ricles, J., and Kosmatka, J. (1992) Damage detection in elastic structures using vibratory residual forces and weighted sensitivity, *AIAA journal 30*, 2310-2316.

[35] Napolitano, K. L., and Kosmatka, J. B. (1996) Damage detection of highly damped structures using direct frequency response measurements and residual force vectors, In *Smart Structures and Materials 1996: Passive Damping and Isolation*, pp 110-122, International Society for Optics and Photonics.

[36] Kosmatka, J. B., and Ricles, J. M. (1999) Damage detection in structures by modal vibration characterization, *Journal of Structural Engineering 125*.

[37] Seyedpoor, S. M., and Montazer, M. (2016) A two-stage damage detection method for truss structures using a modal residual vector based indicator and differential evolution algorithm, *Smart Structures and Systems 17*, 347-361.

[38] Esfandiari, A., Bakhtiari-Nejad, F., Sanayei, M., and Rahai, A. (2010) Structural finite element model updating using transfer function data, *Computers & Structures 88*, 54-64.

[39] Trendafilova, I. (2005) An Investigation on Vibration-Based Damage Detection in an Aircraft Wing Scaled Model, *Key Engineering Materials 293-294*, 321-328.

[40] HE, X., and TANG, H. (2015) Experimental Validation of Structural Damage Identification Using Vibration Transmissibility, *Structural Health Monitoring 2015*.

[41] Bayissa, W., and Haritos, N. (2007) Damage identification in plate-like structures using bending moment response power spectral density, *Structural Health Monitoring 6*, 5-24.

[42] Wang, L., Yang, Z., and Waters, T. P. (2010) Structural damage detection using cross correlation functions of vibration response, *Journal of Sound and Vibration 329*, 5070-5086.

[43] Li, J., Hao, H., and Lo, J. V. (2015) Structural damage identification with power spectral density transmissibility: numerical and experimental studies, *Smart Structures and Systems 15*, 15-40.

[44] Zheng, Z. D., Lu, Z. R., Chen, W. H., and Liu, J. K. (2015) Structural damage identification based on power spectral density sensitivity analysis of dynamic responses, *Computers & Structures 146*, 176-184.

[45] Khoa, N., Alamdari, M. M., Runcie, P., and Nguyen, V. (2016) Damage identification on bridges using ambient vibration testing, In *Life-Cycle of Engineering Systems: Emphasis on Sustainable Civil Infrastructure: Proceedings of the Fifth International Symposium on Life-Cycle Civil Engineering (IALCCE 2016), 16-19 October 2016, Delft, The Netherlands*, p 69, CRC Press.

[46] Nitesh, G., Augustin, M., Sakthi Sathya, P., Saransh, J., Viswamurthy, S., Kotresh, G. M., and Ramesh, S. (2013) Structural health monitoring of composite aircraft structures using fiber Bragg grating sensors, *Journal of the Indian Institute of Science 93*, 735-750.

[47] Sohn, H., Dutta, D., Yang, J., DeSimio, M., Olson, S., and Swenson, E. (2011) Automated detection of delamination and disbond from wavefield images obtained using a scanning laser vibrometer, *Smart Materials and Structures 20*, 045017.

[48] Staszewski, W., Lee, B., Mallet, L., and Scarpa, F. (2004) Structural health monitoring using scanning laser vibrometry: I. Lamb wave sensing, *Smart Materials and Structures 13*, 251.

[49] Kosmatka, J., and Valdes, A. (2005) Using ground vibration testing to correlate the Hunter UAV structural model, *SAMPE journal 41*, 5-13.

[50] Bernasconi, O., and Ewins, D. (1989) Application of strain modal testing to real structures, In *Proceedings of the 7th international modal analysis conference*, pp 1453-1464.

[51] Foss, G., and Haugse, E. (1995) Using modal test results to develop strain to displacement transformations, In *Proceedings-SPIE The International Society for Optical Engineering*, pp 112-112, SPIE INTERNATIONAL SOCIETY FOR OPTICAL.

[52] Agneni, A., Crema, L. B., and Coppotelli, G. (2016) Modal Parameters Directly Estimated from Power Spectral Densities or Correlation Functions in Output-Only Analysis, *Experimental Techniques 40*, 311-321.

[53] Xu, Z.-D., Zeng, X., and Li, S. (2013) Damage detection strategy using strain-mode residual trends for long-span bridges, *Journal of Computing in Civil Engineering 29*, 04014064.

[54] Pedram, M., Esfandiari, A., and Shadan, F. (2014) Finite Element Model Updating Using Power Spectral Density of Structural Response, In *EWSHM-7th European Workshop on Structural Health Monitoring*.

[55] Imai, H., Yun, C.-B., Maruyama, O., and Shinozuka, M. (1989) Fundamentals of system identification in structural dynamics, *Probabilistic Engineering Mechanics 4*, 162-173.

[56] Åström, K. J., and Eykhoff, P. (1971) System identification—a survey, *Automatica 7*, 123-162.

[57] Berman, A., and Flannelly, W. G. (1971) Theory of incomplete models of dynamic structures, *AIAA journal 9*, 1481-1487.

[58] Ibrahim, S. R. (1988) Correlation of analysis and test in modeling of structures: assessment and review, In *Structural Safety Evaluation Based on System Identification Approaches*, pp 195-211, Springer.

[59] Lin, R., and Ewins, D. (1994) Analytical model improvement using frequency response functions, *Mechanical Systems and Signal Processing 8*, 437-458.

[60] Imregun, M., Sanliturk, K., and Ewins, D. (1995) Finite element model updating using frequency response function data: II. Case study on a medium-size finite element model, *Mechanical Systems and Signal Processing 9*, 203-213.

[61] Imregun, M., Visser, W., and Ewins, D. (1995) Finite element model updating using frequency response function data: I. Theory and initial investigation, *Mechanical systems and signal processing 9*, 187-202.

[62] Dos Santos, J. A., Soares, C. M., Soares, C. M., and Maia, N. (2005) Structural damage identification in laminated structures using FRF data, *Composite Structures 67*, 239-249.

[63] Marwala, T., Boulkaibet, I., and Adhikari, S. (2016) *Probabilistic finite element model updating using bayesian statistics: applications to aeronautical and mechanical engineering*, John Wiley & Sons.

[64] Boulkaibet, I., Mthembu, L., Marwala, T., Friswell, M., and Adhikari, S. (2017) Finite element model updating using Hamiltonian Monte Carlo techniques, *Inverse Problems in Science and Engineering 25*, 1042-1070.

[65] Ching, J., Muto, M., and Beck, J. L. (2006) Structural model updating and health monitoring with incomplete modal data using Gibbs sampler, *Computer-Aided Civil and Infrastructure Engineering 21*, 242-257.

[66] Martinez-Luengo, M., Kolios, A., and Wang, L. (2016) Structural health monitoring of offshore wind turbines: A review through the Statistical Pattern Recognition Paradigm, *Renewable and Sustainable Energy Reviews 64*, 91-105.

[67] Gura, I. A. (1968) Extension of Linear Estimation Techniques to Nonlinear Problems, *Journal of the Astronautical Sciences 15*, 194-205.

[68] Collins, J. D., Hart, G. C., Haselman, T., and Kennedy, B. (1974) Statistical identification of structures, *AIAA journal 12*, 185-190.

[69] Tarantola, A., and Valette, B. (1982) Generalized nonlinear inverse problems solved using the least squares criterion, *Reviews of Geophysics 20*, 219-232.

[70] Keil, S. (2017) *Technology and practical use of strain gages: with particular consideration of stress analysis using strain gages*, John Wiley & Sons.

[71] Ward, J. F. (1960) Structural-loads surveys on two tilt-wing VTOL configurations.

[72] Harting, D. R. (1966) The—S/N—Fatigue-life gage: A direct means of measuring cumulative fatigue damage, *Experimental Mechanics 6*, 19A-24A.

[73] Sanayei, M., and Saletnik, M. J. (1996) Parameter estimation of structures from static strain measurements. I: Formulation, *Journal of Structural Engineering 122*, 555-562.

[74] Sanayei, M., and Saletnik, M. J. (1996) Parameter estimation of structures from static strain measurements. II: Error sensitivity analysis, *Journal of structural Engineering 122*, 563-572.

[75] Schweikhard, K. A., Richards, W. L., Theisen, J., Mouyos, W., and Garbos, R. (2001) Flight demonstration of X-33 vehicle health management system components on the F/A-18 systems research aircraft.

[76] Richards, W. L., Lee, D. G., Piazza, A., Stewart, A. K., and Carman, G. P. (2004) Characterization of embedded fiber optic sensors in advanced composite materials for structural health monitoring, In *Smart Structures and Materials 2004: Smart Structures and Integrated Systems*, pp 505-513, International Society for Optics and Photonics.

[77] Richards, W. L., Parker Jr, A. R., Ko, W. L., Piazza, A., and Chan, P. (2012) Application of fiber optic instrumentation.

[78] Pena, F., Martins, B. L., and Richards, W. L. (2018) Active In-Flight Load Redistribution Utilizing Fiber-Optic Shape Sensing and Multiple Control Surfaces.

[79] Murayama, H., Kageyama, K., Kamita, T., and Igawa, H. (2002) Structural health monitoring of a full-scale composite structure with fiber-optic sensors, *Advanced Composite Materials 11*, 287-297.

[80] Richards, W. L., Madaras, E. I., Prosser, W. H., and Studor, G. (2013) NASA Applications of Structural Health Monitoring Technology.

[81] Zou, Y., Tong, L., and Steven, G. P. (2000) Vibration-based model-dependent damage (delamination) identification and health monitoring for composite structures—a review, *Journal of Sound and vibration 230*, 357-378.

[82] Hwang, J. S., Loendersloot, R., and Tinga, T. (2016) Modal Strain Energy Based Structural Health Monitoring on Rib Stiffened Composite Panels, In *The 3rd International Conference on Advances in Structural Health Management and Composite Structures*, Chonbuk National University.

[83] Guan, H., and Karbhari, V. M. (2008) Improved damage detection method based on element modal strain damage index using sparse measurement, *Journal of sound and vibration 309*, 465-494.

[84] Esfandiari, A., Sanayei, M., Bakhtiari-Nejad, F., and Rahai, A. (2010) Finite element model updating using frequency response function of incomplete strain data, *AIAA journal 48*, 1420-1433.

[85] Esfandiari, A. (2014) Structural model updating using incomplete transfer function of strain data, *Journal of Sound and Vibration 333*, 3657-3670.

[86] Brincker, R., and Ventura, C. (2015) *Introduction to operational modal analysis*, John Wiley & Sons.

[87] Martins, B. L., and Kosmatka, J. B. (2018) Ambient Excitation Based Model Updating for Structural Health Monitoring via Dynamic Strain Measurements, In *2018 AIAA/ASCE/AHS/ASC Structures, Structural Dynamics, and Materials Conference*, p 0455.

[88] Reynders, E. (2012) System identification methods for (operational) modal analysis: review and comparison, *Archives of Computational Methods in Engineering 19*, 51-124.

[89] Rainieri, C., and Fabbrocino, G. (2014) Operational modal analysis of civil engineering structures, *Springer, New York 142*, 143.

[90] Siesakul, B. T., Gkoktsi, K., and Giaralis, A. (2015) Compressive power spectrum sensing for vibration-based output-only system identification of structural systems in the presence of noise, In *Compressive Sensing IV*, p 94840K, International Society for Optics and Photonics.

[91] Martins, B. L., and Kosmatka, J. B. (2016) Evaluation of Fiber Optic Strain Sensors for Applications in Structural Health Monitoring, In *57th AIAA/ASCE/AHS/ASC Structures, Structural Dynamics, and Materials Conference*, p 0708.

[92] Pedram, M., Esfandiari, A., and Khedmati, M. R. (2016) Finite element model updating using strain-based power spectral density for damage detection, *Structural Control and Health Monitoring 23*, 1314-1333.

[93] Pedram, M., Esfandiari, A., and Khedmati, M. R. (2017) Damage detection by a FE model updating method using power spectral density: Numerical and experimental investigation, *Journal of Sound and Vibration 397*, 51-76.

[94] Rao, S. S. (2004) *Mechanical Vibrations*, Pearson Prentice Hall.

[95] Champeney, D. C. (1987) *A handbook of Fourier theorems*, Cambridge University Press.

[96] Ang, A. H. S., and Tang, W. H. (2007) *Probability Concepts in Engineering: Emphasis on Applications to Civil and Environmental Engineering*, Wiley.

[97] Chapra, S. C., and Canale, R. P. (2010) *Numerical methods for engineers*, Boston: McGraw-Hill Higher Education.

[98] Alamdari, M. M., Li, J., and Samali, B. (2014) FRF-based damage localization method with noise suppression approach, *Journal of Sound and Vibration 333*, 3305-3320.

[99] Ewins, D. (2000) Modal testing: theory, practice and application (mechanical engineering research studies: engineering dynamics series), *Research studies Pre, 2nd ed., ISBN-13*, 978-0863802188.

[100] Reuter, M. G., and Hill, J. C. (2012) An efficient, block-by-block algorithm for inverting a block tridiagonal, nearly block Toeplitz matrix, *Computational Science & Discovery 5*, 014009.

[101] Roberson, W. (2015) Error using ==> mupadmex Error in MuPAD command: Out of memory?

[102] MathWorks. MATLAB 2017a.

[103] Allemang, R. J., and Brown, D. L. (1987) Experimental Modal Analysis and Dynamic Component Synthesis. Volume 6. Software User's Guide, CINCINNATI UNIV OH DEPT OF MECHANICAL AND INDUSTRIAL ENGINEERING.

[104] Rao, S. S. (2007) *Vibration of continuous systems*, John Wiley & Sons.

[105] Kabe, A. M. (1985) Stiffness matrix adjustment using mode data, *AIAA journal 23*, 1431-1436.

[106] Zimmerman, D., Simmermacher, T., and Kaouk, M. (2005) Model correlation and system health monitoring using frequency domain measurements, *Structural health monitoring 4*, 213-227.

[107] Zang, C., and Imregun, M. (2003) Structural damage detection and localization using FRF-based model updating approach, In *Key Engineering Materials*, pp 191-202, Trans Tech Publ.

[108] Materials, A. (2013) Application of Interferometer Technology to Achieve Accurate Optical Wavelength Measurements, https://www.azom.com/article.aspx?ArticleID=9502.

[109] Wu, J. S. (2014) *Analytical and Numerical Methods for Vibration Analyses*, Wiley.

[110] Clough, R. W., and Penzien, J. (1993) Dynamics of structures. 1993, *Copyright of Applied Mechanics & Materials*.

[111] Adhikari, S., and Phani, A. S. (2004) Rayleigh's Classical Damping Revisited.

[112] Géradin, M., and Rixen, D. J. (2014) *Mechanical vibrations: theory and application to structural dynamics*, John Wiley & Sons.

[113] Caughey, T. (1960) Classical normal modes in damped linear dynamic systems, *Journal of Applied Mechanics 27*, 269-271.

[114] Caughey, T., and O'Kelly, M. E. (1965) Classical normal modes in damped linear dynamic systems, *Journal of Applied Mechanics 32*, 583-588.